From the past to the future: Influences of solar variability and volcanic activity on Earth's climate

A dissertation submitted to the
ETH ZURICH

for the degree of
Doctor of Sciences

presented by
JULIEN GÉRARD ANET

Master of Science ETH in Atmospheric and Climate Science
born 27 November 1986
citizen of Genève (GE)

accepted on the recommendation of
Prof. Dr. T. Peter, examiner
Prof. em. Dr. Dr. h.c. H. Wanner, co-examiner
Dr. E. Rozanov, co-examiner

2013

Die Naturwissenschaft macht die Menschen nicht zu geschäftigen Prahlern und Schwätzern und nicht zu solchen, die die von der Menge hochgeschätzte Bildung zur Schau stellen, sondern zu Selbstbewussten und Selbstgenügsamen, die nicht auf den Wert der äusseren Dinge, sondern auf ihre eigenen Güter stolz sind.

Epikur von Samos, 341 - 271 v. Chr.

Contents

Abstract

Climate on Earth is strongly linked to solar activity and volcanic eruptions. Both factors imply several ways to influence not only climate, but also atmospheric chemistry over time scales from months to tenths of years. It goes without saying that past short-range climatic changes on Earth were linked to risk of famine for civilizations. Although the last most severe cold period, the Dalton Minimum (DM) including the "year without summer" in 1816, was most probably linked to combined solar decline and major volcanic activity in 1809 and 1815, it is the uncertainty of the solar contribution and the possibility of a solar decline in near future, which raised the awareness of the scientific community in the recent past. Conjectures that the Sun may enter a new "Grand Solar Minimum" during the second half of the 21st century are based on statistical analyses of the past solar activity and by an extraordinarily weak current solar maximum. Speculations are that future anthropogenic climate change might be partly compensated if a strong decline in solar activity were to occur.

It is a well-known fact that the Sun not only undergoes a regular 11-year cycle, but also varies periodically in intensity over timescales of seconds to hundreds of years. In the last millennium, five so-called "grand minima" were found in proxies: The Oort, Wolf, Spörer, Maunder and Dalton Minima. All of them have been made responsible for strong regional to global changes in surface temperatures and precipitation. Linked to solar activity there are changes in the penetration of energetic particles (among them galactic cosmic rays, coming from outer space, as well as solar energetic protons and low energetic electrons, originating from the Sun), leading to varying ionization rates of basic atmospheric constituents such as nitrogen or oxygen in the upper and middle atmosphere creating NO_x and HO_x. These chemical compounds are both involved in the ozone destruction cycle in the stratosphere and are precursors for the ozone production cycles in the troposphere.

The first and major aim of this thesis is to perform a climate simulation extending from

the 17th century to the year 2100. For this task, a new coupled atmosphere-ocean climate chemistry model (AO-CCM) is developed based on the chemistry-climate model (CCM) SOCOL3 and the ocean model MPIOM. Energetic particle parameterizations have been implemented and the model spin-up has been carefully investigated. Driven by the strong solar forcing reconstruction of Shapiro et al. (2011), a transient simulation is then launched, spanning the period from 1600 AD to 2100 AD, with embedded scenarios and ensemble calculations starting i) in 1780 AD to investigate the DM (1780-1840) and ii) in 2000 AD to investigate the impact of a potential grand solar minimum in the 21st century.

The second aim of this thesis is to separate, attribute and quantify the impact on global and regional climate of solar irradiance decreases, energetic particles and volcanic eruptions during the DM, and the third aim is doing about the same for the 21st century with a hypothetical new grand solar minimum, focusing especially on the solar contribution of the probable climate change. For both periods the state of the climate and atmospheric chemistry are compared to an "unperturbed" state of the climate forced by a constant forcing factors.

The first part of this thesis based on two simulations modeling the climate change over the last 400 and the future 100 years. The analysis of the results revealed that our model did not well represent the Maunder Minimum, however very well reproduced the volcanic and solar-induced cooling period during the DM. As well, the anthropogenic warming of the last hundred years is well recreated, although the sensitivity to increasing greenhouse gas concentrations in the beginning of the 20th century seems to be on the higher edge. Yet, when simulating the 21st century by using IPCCs RCP 4.5 scenario, we find a similar global warming of surface temperatures by around 2 K than the CMIP5 reference simulations.

For the period of the DM, a series of sensitivity experiments ("scenario runs") is carried out, varying independently either the solar ultra-violet (UV) irradiance, the solar visible and near infrared irradiance (VIS, NIR), the EPP and the stratospheric aerosol burden due to volcanic eruptions. We show that while the changes in the UV spectrum of the Sun and volcanic eruption have a strong effect on stratospheric chemistry and dynamics, the changes in VIS and NIR irradiance and EPP do not. Conversely, tropospheric climate is rather influenced by the VIS and NIR solar spectrum decrease and by the volcanic eruptions than by changes in the UV solar spectrum. Again,

EPP do not show a significant impact on tropospheric chemistry or climate. In the stratosphere, a reduction of UV irradiance by 15% causes a global ozone decrease below the stratopause reaching 8% in the midlatitudes at 5 hPa and a significant stratospheric cooling of up to 2 K in the midstratosphere and to 6 K in the lower mesosphere. Volcanic aerosols heat the tropical lower stratosphere and tropopause allowing more water vapor to enter the tropical stratosphere, which, via HO_x reactions, decreases upper stratospheric and mesospheric ozone by roughly 4%. Conversely, heterogeneous chemistry on aerosols reduces stratospheric NO_x, leading to a 12% ozone increase in the tropical lower and middle stratosphere, whereas a decrease in ozone of up to 5% is found over Antarctica in boreal winter. On the Earth's surface, the calculated decrease of 0.3% of the VIS and NIR irradiance causes a drop of global temperatures by 0.2 K and a drop of north hemispheric temperatures by up to 0.4 K. The global ocean heat content (OHC) of the uppermost 300 meters of depth drops by nearly 2% when reducing only the VIS and NIR irradiance. Reduction of the UV irradiance or change in the energetic particle precipitation does not influence global temperatures. However, small seasonal changes are visible in the polar regions. Volcanic eruptions have a significant influence on the tropospheric climate by inducing a global cooling of up to 0.6 K and a drop in the OHC of the uppermost 100 meters of depth by up to 2.5% over 2 years after the eruptions. However, the eruptions do not explain the long-lasting cold period following the period after 1817 AD. As well, we show that volcanic eruption can significantly modify the global circulation, altering the precipitation patterns globally, but also locally over Europe. We thus conclude that volcanic eruptions "kicked-in" the cool DM period, which then was sustained by the lower solar irradiance.

For the 21st century, the constant and declined solar activity scenarios reveals that about 20% or 0.4 K of the expected future greenhouse warming might become compensated by a grand solar minimum. However, the climate for the solar activity minimum case still would be warmer by 1.4 K near the end of the century when being forced by the optimistic IPCC RCP 4.5 scenario. We show that the anticipated total column ozone recovery would be delayed or even cancelled in some parts of the globe mostly by the decreased UV radiation, possibly leading to an increase of skin cancer in the equatorial and subtropical region and thus requiring stronger limitations on the ozone depleting substances regulated by the original Montreal protocol.

Résumé

Le climat de la Terre est fortement lié à l'activité solaire et aux éruptions volcaniques. Ces deux facteurs impliquent différentes façons d'influencer non seulement le climat, mais aussi la constitution chimique de l'atmosphère sur des échelles de temps s'étendant de quelques mois a des dixaines d'années. Il va de soit que les derniers changements climatiques avaient pour conséquences des risques de famine pour les civilisations. La dernière période froide, dénommée le minimum de Dalton (MD), incluant "l'année sans été" de 1816, était très probablement lié à un déclin solaire et à une activité volcanique majeure en 1809 et 1815. C'est surtout l'incertitude de la contribution solaire exacte et - de plus - la possibilité d'une nouvelle baisse d'activité solaire dans l'avenir proche qui ont sensibilisé la communauté scientifique ces dernières années. Les spéculations qu'un nouveau minimum solaire puisse se passer durant la deuxième partie du 21$^{\text{ème}}$ sciècle sont basés sur des analyses statistiques de l'activité solaire historique et sur le maximum solaire actuel étant plutôt faible. Basées sur ces faits, des hypothèses existent que le réchauffement climatique pourrait être partiellement compensé par une nouvelle période de faible activité solaire.

C'est un fait connu que le Soleil subit non seulement un cycle d'activité régulier de 11 ans, mais aussi des cycles d'intensité ayant une période de quelques secondes a plusieurs centaines d'années. Durant le dernier millénaire, cinq "grands minimums solaires" ont pu être reconstruit à partir d'indicateurs climatiques ("proxy"): Les minimums de Oort, de Wolf, de Spörer, de Maunder et de Dalton. Tous ont été rendu responsables pour des changements de température et de précipitation globaux. Liée aux changements d'activité solaires, une variation de la pénétration des rayons cosmiques et des particules énergétiques solaires, menant à des variations du taux d'ionisation des constituents basiques de notre atmosphère (comme l'azote ou l'oxygène) est observée. Les produits, parmis d'autres surtout de l'oxide d'azote et de l'hydroxyle, sont des réactifs efficaces dans les réactions de destructions d'ozone dans la stratosphère et de production d'ozone dans la troposphère.

L'objectif primaire de cette thèse est d'accomplir une simulation du climat de la période de 1600 à 2100 ap. J.-C.. Pour effectuer cette simulation, d'abord, un nouveau modèle couplé océan-atmosphère de chimie-climat (AO-CCM) basé sur le modèle de chimie-climat (CCM) SOCOL3 et sur le modèle océan MPIOM a été développé. Les paramétrisations pour les particules énergétiques ont été implémentées et une analyse de la stabilisation du climat simulé par le modèle a été faite. Entrainé par la reconstruction de l'irradiance solaire d'une haute amplitude de Shapiro et al. (2011), une simulation transitoire a été lancée, simulant la période de 1600 à 2100 ap. J.-C., contenant des scénarios débutants en i) 1780 ap. J.-C. pour l'investigation du MD (1780-1840) et en ii) 2000 ap. J.-C. pour examiner l'impact d'un minimum solaire dans le courant du 21ème siècle sur notre climat.

Le deuxième but de cette thèse est de séparer, d'attribuer et de quantifier l'impact global et régional d'un grand minimum solaire, des particules énergétiques et d'éruptions volcaniques sur le climat terrestre pendant le MD. Le troisième but est de faire la même chose pour le 21ème sciècle, en admettant le scénario d'un nouveau grand minimum solaire, en focussant surtout l'aspect du ralentissement éventuel du réchauffement climatique. Pour ces deux périodes, l'état du climat terrestre est comparé à un état "non-perturbé", forcé par des facteurs externes (volcans, irradiation solaire, ionisation par les particules énergétiques) gardés constants.

La première partie de la thèse est basée sur deux simulations simulant le changement de climat sur les dernières 400 et les futures 100 années. L'analyse de ces résultats a révélé que notre modèle n'a pas réussi à représenter le minimum de Maunder correctement. Par contre, la période froide pendant le MD induite par un minimum solaire et par deux violentes éruptions volcaniques a bien été reproduite. De même, le réchauffement anthropogénique des dernières 100 années est correctement simulée, même si la sensibilité de notre modèle à une augmentation de la concentration des gaz à effet de serre est relativement haute. Malgré cela, la simulation du 21ème sciècle suivant le scénario du GIEC RCP 4.5 démontre que nos résultats - notamment un réchauffement global de 2 K - sont tout à fait comparables à ceux trouvés par les simulations de référence du CMIP5.

Pour la période du MD, une série d'expériences ("scénarios") est simulée, permettant de varier indépendemment soit l'irradiance solaire dans l'ultra-violet (UV), dans le

visible et l'infra-rouge proche (VIS, IRP), l'intensité des particules énergétiques ainsi que les éruptions volcaniques. Nous démontrons que si les variations dans le spectre UV du Soleil et des éruptions volcaniques ont un effet majeur sur la chimie et la dynamique de la stratosphère, cela n'est pas le cas avec les variations dans le spectre VIS/IRP du soleil et des particules énergétiques. Inversement, le climat de la troposphère est plutôt influencée par le spectre VIS et IRP du Soleil et par les éruptions volcaniques que par les variations dans l'UV. A nouveau, les particules énergétiques sont sans action dans la troposphère. Dans la stratosphère, une réduction de l'UV de 15% cause une baisse globale de l'ozone sous la stratopause, atteignant une perte d'ozone de jusqu'à 8% dans les latitudes moyennes, à 5 hPa de hauteur. De même, un refroidissement de la stratosphère de près de 2 K à la hauteur de la couche d'ozone et de près de 6 K dans les régions de la basse mesosphère.

Les aérosols volcaniques réchauffent la région de la tropopause tropicale, permettant une augmentation du transport de vapeur d'eau de la troposphère dans la stratosphère. Cette vapeur d'eau va - via diverses réactions - diminuer la concentration d'ozone dans la haute stratosphère et la mésosphère d'environ 4%. Inversement, des réactions hétérogènes sur les aérosols volcaniques réduisent la concentration stratosphérique de l'oxide d'azote, permettant une hausse de 12% d'ozone dans les régions tropicales. Sur la surface de la Terre, la diminution de l'irradiance du spectre VIS/IRP de 0.3% cause un refroidissement global de 0.3 K et une baisse de températures sur la partie hémisphèrique du nord de 0.4 K. La chaleur globale des premiers 300 mètres de profondeur des océans diminue de près de 2% en réduisant seulement le rayonnement VIS/IRP. La baisse de température est négligeable si le modèle n'est forcé que par la baisse du rayonnement UV. Par contre, les éruptions volcaniques ont un éffet signifiant en induisant un refroidissement global de près de 0.3 K et une baisse de la chaleur océanique des premiers 100 mètres de profondeur de jusqu'à 2.5% sur les deux années qui suivent les éruptions. Malgré cela, les éruptions volcaniques pour elles-mêmes ne peuvent pas expliquer la longue période froide qui suit l'année 1817 ap. J.-C.. De plus, les éruptions volcaniques sont capables de modifier la circulation globale, menant à des anomalies de précipitations globales, mais aussi régionales (Europe). De ce fait, nous concluons que les éruptions volcaniques ont initié la période froide du MD, laquelle a été soutenue par une baisse d'irradiance solaire.

Pour le 21ème sciècle, la comparaison des scénarios d'un soleil gardant une activité constante et d'un soleil entrant dans un nouveau grand minimum révèle que environ 20% - ou 0.4 K - du réchauffement climatique prédit pourrait être compensé par un

nouveau minimum solaire. Cependant, le climat se réchaufferait quand-même de 1.4 K d'ici la fin de ce siècle, en suivant le scénario optimiste RCP 4.5 du GIEC. Additionelle-ment, nous démontrons que la récupération de la couche d'ozone sera retardée ou même anihilée dans ceraines régions du globe, à cause de la réduction de l'irradiance UV. Cela pourrait impliquer une augmentation du risque du cancer de la peau dans le régions équatoriales; une limitation encore plus stricte des substances détruisant la couche d'ozone, réglée par le protocole de Montréal, serait nécessaire.

Chapter 1

Introduction

1.1 Motivation

Although climate on Earth has been in continuous transition for the last 400'000 years and is highly correlated with solar activity (Milanković, 1930; Petit et al., 1999; Shackleton, 2000), the very rapid changes in climate during the 20th century cannot be explained solely by solar variability (Intergovernmental Panel on Climate Change, IPCC, Climate change 2007, 2007). Recent reports by the IPCC, as well as studies such as those by Karl and Trenberth (2003) and Oreskes (2004), strongly indicate that anthropogenic greenhouse gas (GHG) emissions are responsible for the warming observed over the last 80 years. However, as the IPCC noted in the last Assessment Report Four (AR4), scientific understanding of the influence of solar irradiance, cosmic energetic particles, and volcanic aerosols on Earth's climate is low (Table 2.11 [a]). This also means that future variations of any one of the three factors might lead to largely unknown climatic changes. The Sun, which is currently at the maximum of solar cycle 24, has not reached the same levels of activity as it did during solar cycles 22 or 23.

What does the Earth's history tell us about climate changes? Research focusing on the recent (100 to 1000 years) past can help to understand the effect of these influences on Earth's climate: So called proxies, i.e. measured variables used to infer the value of a variable of interest in climate or palaeo-climate research (e.g., ice cores, tree rings, sub-fossil pollen, boreholes, corals, and lake and ocean sediments) can be used for backtracking global temperatures, solar and volcanic activity. For instance, during the formation of ice, small bubbles of ambient air are trapped and then conserved over

---

[a]http://www.ipcc.ch/publications_and_data/ar4/wg1/en/ch2s2-9-1.html#table-2-11

tens of thousands to hundreds of thousands of years (e.g., Lorius et al., 1990, and ref. therein). By extracting such ice cores and examining the air bubbles trapped within, information about the past atmospheric trace gas constitution (e.g., carbon dioxide, methane and nitrous oxide) can be gathered. Currently, the "history of our atmosphere" has been reconstructed up to 650'000 years before present in finer resolution using ice cores extracted at the Vostok drilling site in Antarctica (Petit et al., 1999; Spahni et al., 2005) and up to several millions of years in coarser resolution for certain gases (alkenone-based, Pagani et al., 1999) or temperature (using geological sources from the ocean drilling project, e.g. Zachos et al., 2001; Lisiecki and Raymo, 2005). However, the temporal resolution gets rougher over time due to the compression of ice with depth and the uncertainty of precipitation rates in the polar regions. Volcanic influences on climate can also be reconstructed using ice core records (Gao et al., 2008; Arfeuille et al., 2013a), as can the galactic cosmic ray intensity, which has been extracted from beryllium-10 (^{10}Be) records in ice cores (e.g., Raisbeck et al., 1990). Both, however, are limited in resolution and accuracy by the changes the ice undergoes over the long time spans. All reconstructions tell us that there were repetitive climate warmings and coolings in the past hundreds to thousands of years (ky), which however were all linked to either solar activity changes, volcanic eruptions, or to Earth orbital changes (see later).

Coming back to the decreasing solar activity, some critical voices have suggested that an imminent solar minimum might offset or weaken the amplitude of the anticipated anthropogenic climate change: Some peer-reviewed articles (e.g., Mörner, 2010; Lüdecke et al., 2011a; Lüdecke, 2011b) as well as several non peer-reviewed publications (e.g., Clark, 2006; Whitehouse, 2007; Easterbrook, 2010; Ewert, 2011), which are not necessarily trustworthy, can be found and should be considered attentively to avoid any overhasty reasoning and conclusion concerning future climate change. "Climate-skeptic" publications claim that ongoing global warming were largely unrelated to anthropogenic activities, but rather were related to internal variabilities of the Earth's system (Pacific Decadal Oscillation (PDO) Mörner, 2010). Also, Lüdecke et al. (2011a) and Lüdecke (2011b) have analyzed different time series of NASA-GISS temperature records of the northern hemisphere and concluded that the anthropogenic effect was minor and that positive trends in climate were mainly related to artifacts of "hot islands" formed in urban areas or to solar influence, using sun spot numbers as solar activity proxy data. Such publications have received almost no recognition from their international peers, possibly due to an alleged limited in-depth-analysis, and thus should be considered with care. They - even if only partly true - may have

a high impact on political and socio-economical decisions. Other authors (e.g., Clark, 2006; Whitehouse, 2007) have suggested that a new grand solar minimum could give more time to the global community for adapting to ongoing anthropogenic global warming. This is partly true. But should an argumentation not rather point at the greater chance to keep up the original plans to reduce even more anthropogenic global warming than just "taking more time" in order to reach "only" the 2 °C goal? However, most - if not all - recent publications looking at a new hypothetical grand solar minimum, like Jones et al. (2012) or Meehl et al. (2013), both using a climate model, concluded that a future global warming would indeed have a certain effect on climate warming, but could possibly only decelerate anthropogenic global warming and reduce its amplitude by 0.1 K to 0.2 K - which is a small fraction! A major point of discussion in the two latter publications is that the amplitude of the solar forcing in certain spectra (such as the UV part of the solar spectrum) applied to their climate models did only vary by a small fraction, whereas other approaches suggest a far stronger decrease in the UV spectrum. This point is taken up by the present thesis.

To better understand how and to what degree the Sun and volcanoes influence Earth's climate, this study develops and executes a climate simulation of the last 400 years. This period includes the two most recent grand solar minimum periods (the Maunder Minimum [MM] and the Dalton Minimum [DM]) thus allowing us to explore the possible influence of significant solar variability on Earth's climate. A future scenario of a new DM-like solar activity decrease in the 21st century was also simulated in response to the abovementioned critical discussion of compensation or partial compensation of anthropogenic warming by solar changes. In short, the aim of this thesis is to reduce the uncertainty of solar and energetic particle influence on climate in order to better predict future climate change in the 21st century and, ultimately to provide a stronger basis for climate change mitigation.

This study was conducted within the SNF Sinergia project FUPSOL (FUture and Past SOLar influences on climate) as collaboration of the following institutions:

- The PMOD/WRC was in charge of the reconstruction of the solar forcing.

- EAWAG's Surface Waters Department delivered the forcing data for the cosmic ray intensity.

- The University of Bern's Geography Institute (GIUB) provided the data for atmospheric boundary conditions, indlucing GHGs, and stratospheric or tropospheric

aerosols.

- The University of Bern's Climate Physics group and the Institute for Atmosphere and Climate (IAC) at ETH Zürich, collaborated in assembling the data, developing the model, designing the model run environment, running the model and analyzing the data.

1.2   Objectives

The main objectives of this thesis are the:

1. **Implementation of the energetic particle parameterization of Calisto (2011) into the chemical climate model (CCM) SOCOL3.** The primary task was a parallelization of the routines, as they had to be rewritten from the single-processor SOCOLv2 (Schraner et al., 2008) to the multi-processor SOCOL3 version (Stenke et al., 2013).

2. **Coupling of the CCM SOCOL3 with the ocean model MPIOM to the AO-CCM SOCOL3-MPIOM.** This step was very important in order to be able to run long transient simulations of 500 years. Of course, the state of the ocean has to be dynamic and not prescribed in order to capture the climate response to the extreme climate scenarios.

3. **Spin up of the ocean in order to get a stable, non-drifting set of restart files as a basis for the 500-year long climate simulations.** Without this step, an undefined drift in the ocean could have interfered with the temperature anomaly responses originating from varying solar irradiances, volcanic aerosols or energetic particles.

4. **Transient forcing climate simulation from the year 1600 AD to the year 2100 AD. Two sets of solar forcings from Shapiro et al. (2011) were used.** These simulations included 4 run members that will be discussed further in Section 3.8. The Shapiro forcings show a particularly strong modulation of solar variability, therefore facilitating the detection and attribution of a solar signal in the model output.

5. **In-depth analysis of the Dalton Minimum (DM). This was accomplished by performing sensitivity studies in which solar irradiance, volcanic or ener-**

getic particle activity have been varied independently. The aim of these sensitivity studies is to reduce the uncertainty regarding the extent to which each of these factors influence Earth's climate, and all scenario runs were performed as ensemble calculations.

6. **In-depth analysis of the 21st century including a scenario that hypothesizes a new Dalton Minimum-like decrease in solar activity that reaches its minimum around 2090.** This simulation allowed to determine to what degree future anthropogenic warming is indeed pared back by a decrease in solar activity.

1.3 Structure

This thesis is structured as follows:

- Chapter 2 gives an extensive overview of the state of the research, of the model and of the design of the experiments.

- Chapter 3 presents the model framework, the forcing data and the experiments.

- Chapters 4 and 5 focus on the influence of the different forcings on Earth's climate during the Dalton Minimum (DM), a period of very low solar activity lasting from around 1780 AD to 1840 AD. The effects on the stratosphere are described in the first of these two chapters, while the second chapter presents the effects of the different forcing factors on the troposphere during the DM.

- Chapter 6 is dedicated to the possible effects on future climate of a new grand solar minimum, reaching the lowest irradiance values in 2090 AD.

- The seventh and final chapter of this thesis presents the most important conclusions of this work and provides a brief outlook regarding possible future research questions.

Chapter 2

State of the research

This chapter provides an overview of the generally accepted findings of the recent past. First, a short introduction about the structure of the Earth's atmosphere and about the basic chemical reactions steering ozone chemistry are given. In Section 2.2, the influence of solar activity on the Earth's climate is explained. In Section 2.3, a description of the influence of energetic particle precipitation (EPP) on Earth is given. Finally, 2.4 provides a description of volcanic activity on Earth.

2.1   The Earth's atmosphere

The Earth's atmosphere consists of different "shells", characterized by their stratification and chemical composition: The troposphere, extending to 11 km above the Earth's surface at the poles and up to 18 km above at the equator, contains what we call "weather". Thunderstorms, fair weather cumulus or monsoon rain - everything happens in the troposphere. Temperatures decrease linearly from the ground up to the tropopause, where they reach as low as -90° C at the tropics. Because of this linear decrease and the relatively high amount of moisture, the stratification of the troposphere is rather unstable; vertical mixing through convection occurs easily.

The second "shell" is the stratosphere. The stratosphere, which is between $\sim$15 and 50 km above the Earth's surface, contains the very important ozone layer, which makes life on Earth possible by absorbing hazardous UV radiation. The stratosphere heats up following a vertical gradient, reaching $\sim$0° C at the top, the stratopause, located at 50 km above the Earth's surface. Due to its positive temperature gradient, the stratosphere is stably stratified - hence its name. This suppresses vertical motion like

convection efficiently.

The third "shell", the mesosphere, reaches up to 90 km height above the Earth's surface. Here, oxygen, the second most abundant gas of the Earth's atmosphere, exists mostly as atoms and no longer as molecules due to the very energetic radiation coming from the Sun. Nevertheless, the bottom of the mesosphere is the coldest part of the Earth's atmosphere, reaching temperatures as low as -100° C. This is also the atmospheric layer most influenced by energetic particles, which will be discussed in greater detail in section 2.3.

The most important interactions that will be discussed on the following pages are illustrated in Figure 2.1.

2.1.1 Dynamics

Simplified to the maximum, the Earth is nothing more than a heat engine, transforming parts of the incoming solar radiation to a large degree into infrared radiation and heat (i.e. molecular motion), to a smaller degree into latent heat, yet smaller degree into thermals, and finally to a very small degree - namely corresponding to the more energetic fraction of the incoming UV - into chemical energy. All these energy forms to
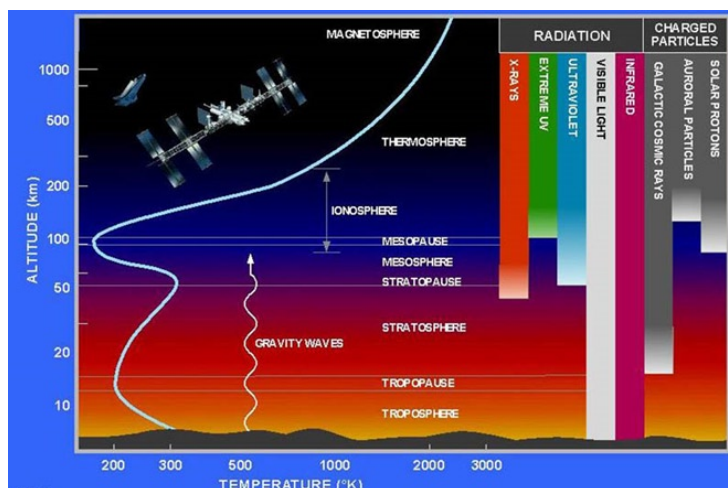

Figure 2.1: Structure of the Earth's atmosphere, including penetration depths of X-rays, UV and visible and infrared radiation. The approximate heights of the atmosphere reached by the three different classes of energetic particles are also illustrated. Source: http://www.theozonehole.com/atmosphere.htm

some degree power the atmospheric dynamics, i.e. kinetic energy of air masses. Only the continuous radiative heating by the Sun allows the atmosphere to be in ongoing motion, although radiative cooling persistently extracts energy from the system.

The atmosphere is heated up more intensely at the equator than at the poles. This energy imbalance represents a reservoir of available potential energy as described by Lorenz (1954), seven years before he accidentally discovers the chaos theory when working on numerical weather prediction. This imbalance will induce a pressure force from the equator to the poles, converting the available potential energy into kinetic energy. Due to the rotation of the Earth, a general deflection to the east will be the consequence for air parcels traveling polewards from the equator (Coriolis, 1835), so that the predominant zonal motion in midlatitudes is from west to east ("westerlies"). This leads to a good mixing of all atmospheric constituents, which is especially visible after volcanic eruptions, as the volcanic ash is dispersed all over the globe with a zonal gradient. With time, the volcanic ash gets dispersed also more and more uniformly, weakening the zonal gradient. The latter observation is due to the continuous equator-to-pole gradient, which allows also efficient meridional mixing.

Stratification in the troposphere is weak, facilitating processes of vertical mixing like convection. The natural boundary of an air parcel with vertical motion is reached at the tropopause. In contrast, the changing of the vertical temperature gradient from a negative to a positive sign due to the increasing temperature in the stratosphere induces a very stable stratification, preventing any convective vertical motion (except some overshooting above the most vigorous convection cells). So, if no convection is possible in the stratosphere - how does vertical and meridional mixing occur there?

Due to the thermal imbalance that exists in both the troposphere and the stratosphere, a measurable equator-to-pole circulation prevails throughout the year. During polar winter, strong radiative cooling over the winter pole occurs, resulting in the subsidence of air masses. In the stratosphere, this supports the equator-to-pole residual circulation, also known as "Brewer-Dobson-circulation" (BDC). However, the BDC is not primarily thermal-wind driven, but rather gravity-wave driven. Vertically propagating gravity waves and planetary waves eventually break when they enter the stratosphere due to the decreasing air density. There, the breaking disturbs the zonal mean flow due to the deposition of momentum. This momentum deposition represents an anomaly in the zonal mean flow that is partly compensated for by the BDC, correcting the anomaly

of the total momentum. In such a way, the ozone-rich air can be slowly transported into areas with less energetic radiation at the high latitudes.

The strong temperature gradient in winter also has severe consequences on zonal winds, which are accelerated via the thermal wind relation, leading to a strong stratospheric polar vortex at a height between 20 and 50 km. The vortex isolates air masses very efficiently, leading to extremely low temperatures at which stratospheric clouds can form, hosting certain heterogeneous reactions (see section 2.1.2). As well, significant subsidence occurs, accelerating the BDC equator-to-pole branch in the winter hemisphere. However, so-called sudden stratospheric warmings (SSW) regularly occur, breaking up the vortex and sometimes even inversing the zonal wind field. These SSWs can be initiated by vertically propagating gravity waves, which mostly originate from orographic sources (e.g. Rocky Mountains, Himalaya, Scandinavian Mountains). As such, SSWs are more likely to happen in the northern hemisphere than in the southern hemisphere. Upon breaking, gravity waves can decelerate the polar vortex, frequently leading to its splitting. This is concomitant with a strong sudden warming of the stratospheric polar region after mixing of extratropical and polar air masses. Sometimes, a thermal gradient reversal can happen, inversing the zonal mean wind circulation.

In the following sections, the chemical and dynamical processes in the three aforementioned atmospheric shells will be presented (Brasseur and Solomon, 2005; Holton and Hakim, 2012).

2.1.2 Chemistry

In order to understand the dynamics behind the temperature gradients in the stratosphere, the basic ozone chemistry first needs to be presented. Due to the high complexity of atmospheric chemistry, a complete overview in this thesis would be too extensive. Hence, only the reactions most relevant to the work done during the thesis will be explained.

2.1.3 Ozone chemistry

The formation of the ozone layer during the Earth's history was a crucial development that allowed creatures and plants to transition from the sea to the land. Without the

protecting ozone layer, UV-C and UV-B radiation with wavelengths below 320 nm would reach the ground, ionizing even water and producing cancer or other genetic defects that would make life outside the water impossible (Setlow, 1974; Norval et al., 2007).

The ozone layer was first explained by Chapman (1930), who identified the following reactions. Still valid today, these reactions are known as the "pure oxygen chemistry":

$$O_2 + h\nu \longrightarrow 2O(^3P) \qquad\qquad \lambda < 242\,\text{nm} \qquad (2.1)$$
$$O(^3P) + O_2 + M \longrightarrow O_3 + M \qquad\qquad\qquad\qquad (2.2)$$
$$O_3 + O(^3P) \longrightarrow 2O_2 \qquad\qquad\qquad\qquad (2.3)$$
$$O_3 + h\nu \longrightarrow O(^3P) + O_2 \qquad\qquad \lambda \gtrsim 310\,\text{nm} \qquad (2.4)$$
$$O_3 + h\nu \longrightarrow O(^1D) + O_2 \qquad\qquad \lambda \lesssim 310\,\text{nm} \qquad (2.5)$$

The starting reaction is 2.1, which represents the photolysis of oxygen and requires radiation with wavelengths below 242 nm. In the stratosphere and mesosphere, the created $O(^3P)$ can react with oxygen and a third body to ozone (2.2). Both - $O(^3P)$ and ozone - are member of the odd oxygen "O_x" family. Ozone however, can be destroyed by reacting with $O(^3P)$ (2.3) and thus creating two oxygen molecules, or by photolysis. Depending of the radiation, either $O(^3P)$ (2.4, lower part of the atmosphere) and oxygen or $O(^1D)$ (2.5, upper part of the atmosphere) and oxygen are the products. The reactions responsible for the increase in temperature in the stratosphere are the reactions 2.2, 2.4 and 2.5.

The reaction rate of 2.1 increases with increasing atmospheric height and decreasing air density. This leads to an ozone production maximum at around 40 km of height. However, the maximum number densities of ozone at the equator is found between at around 25 km height, as illustrated in Figure 2.2. The discrepancy between the two heights can be explained by looking at Figure 2.3 which illustrates the mean ozone and O_x life-time. Most of the ozone at 40 km is readily photolyzed (short life-time) or reacts with $O(^3P)$ back to oxygen. This reaction pathway becomes less important with decreasing height due to increasing O_x life-times, as less $O(^3P)$ is available. This implies an increasing ozone life-time, and thus a higher ozone concentration.

The annual cycle of the total ozone column over the pre-ozone hole years (before $\approx$1940) is illustrated in Figure 2.4. Contour units are in Dobson Units (DU) and represent the height of the ozone layer in hundredths mm assuming one would bring down
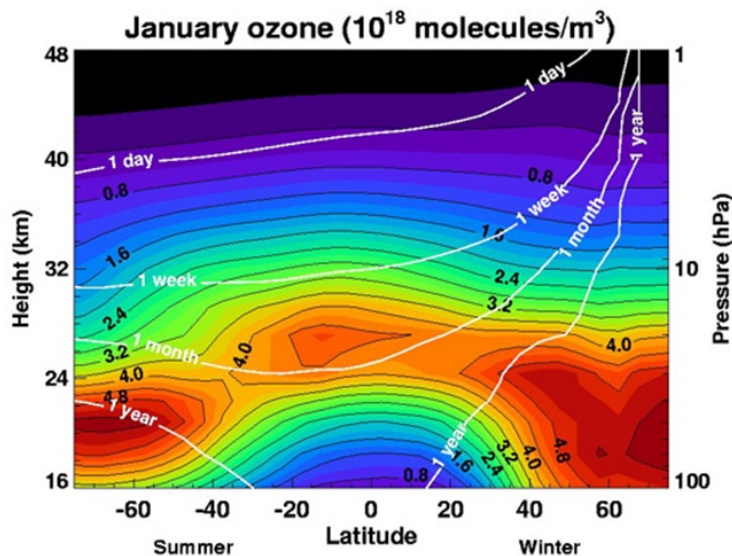
Figure 2.2: Mean January ozone profile, shown as the zonal mean. Colored areas show the ozone molecule number density in 10^{18} particles per m^3. White lines illustrate the photochemical ozone replacement time, or the time that is needed to reproduce the amount of ozone at this particular location after an assumed complete removal of ozone. Source: E. Smith, CCPO, `http://www.ccpo.odu.edu/~lizsmith/SEES/ozone/` `class/Chap_8/8_Js/8-02.jpg`, last access 16.06.2013

to the surface the total ozone column. Hence, assuming the atmosphere would show a value of 100 DU, this would represent a layer of ozone of 1 mm thickness of pure ozone gas at standard conditions. The lowest ozone column values are observed in the hemispheric fall over the poles and generally throughout the year over the equator. In the extratropics, following the yearly minimum column values, ozone recovers to maximum values of 400 to 460 DU in spring. However, since the 1970s, the yearly cycle of the ozone layer has substantially changed due to the emissions of anthropogenic ozone depleting substances (ODSs). Above all, ODS like CFCl$_3$ or halons get photolyzed and a free halogen - especially chlorine and bromine - atom will react with ozone in different chemical reactions, as will be shown in the next section. These reactions occur mainly in the cold polar winter season and lead to an accelerated ozone depletion during the spring season. Presently, the ozone chemistry has been modified in such a way that the lowest values are reached over the southern polar region in October and over the northern polar region in March. Values as low as 85 DU have been recorded, although the frequency of such alarmingly low values has decreased thanks to the Montreal Protocol on Substances that Deplete the Ozone Layer (1989), which limits the use of ODS. The scientific community agrees that ozone values will likely reach pre-1960s levels in
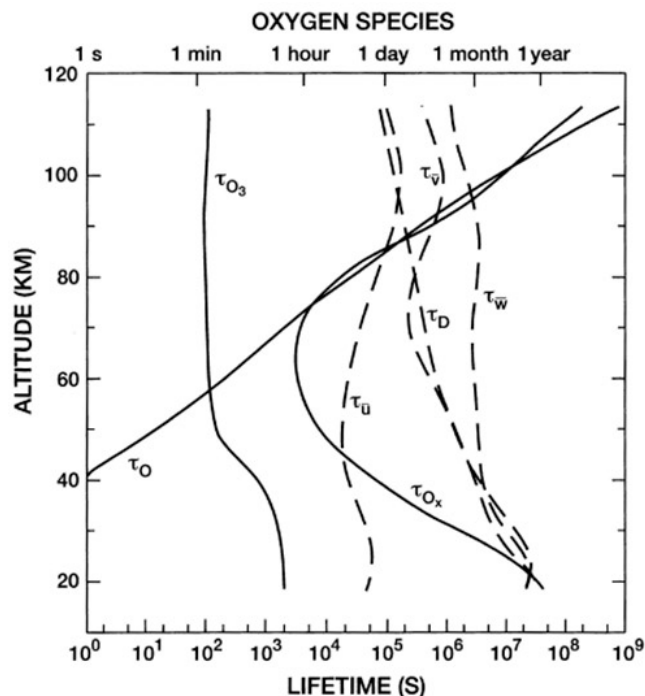
Figure 2.3: Illustration of the different lifetimes of oxygen species in the atmosphere. τ_{O_3} = Ozone, τ_O = Molecular oxygen, τ_{Ox} = All oxygen species (ozone, O(^{1}D) and O(^{3}P)), τ_D = vertical diffusivity life-time, $\tau_{\bar{u}}$ = characteristic time needed for a meridional distance of 1000 km, $\tau_{\bar{v}}$ = same for the zonal component, $\tau_{\bar{w}}$ = same for the vertical component. Source: Brasseur and Solomon (2005)

2050 and will even face a "superrecovery" later on in some regions of the globe.

2.1.4 Ozone production and destruction chemistry

The ozone production mechanism suggested by Chapman (1930) was accepted for a long time as the sole ozone-forming mechanism. However, the reaction rate of 2.3 was reestimated in the 1950s and found to be much lower than previously assumed (Hunt, 1966). Bates and Nicolet (1950) suggested that OH and HO$_2$ - often summarized as HO$_x$ - could modify the ozone concentrations. This was confirmed by Hampson (1964), who was the first to describe the process by using chemical reactions. Crutzen (1969), however, realized that the additional HO$_x$ mechanism did not sufficiently explain the stratospheric ozone concentration and suggested a catalytic destruction cycle of ozone by the oxidized family of the most abundant chemical element in the Earth's atmosphere: nitrogen (Crutzen, 1970). Molina and Rowland (1974) later suggested a
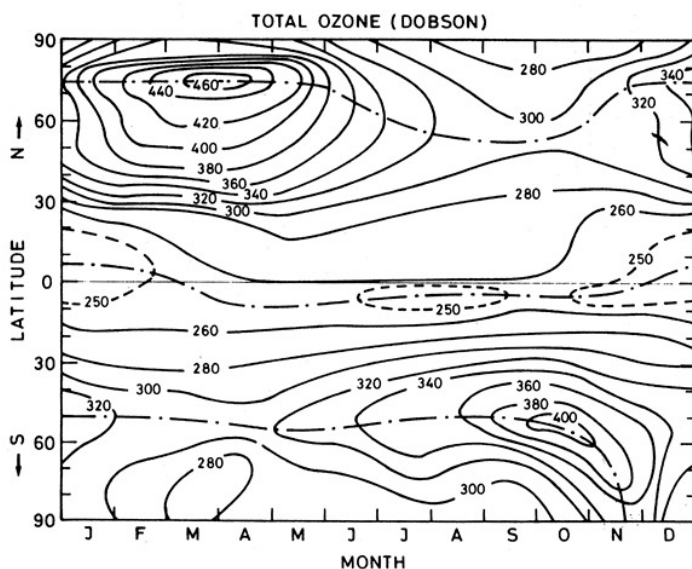
Figure 2.4: Total ozone column in DU during preindustrial times (London, 1980).

similar chlorine-induced destruction cycle, and Wofsy et al. (1975) presented an additional bromine destruction cycle. For all cycles, the radical chain reaction cycle is very similar, following the basic catalytic ozone destruction reactions:

$$X + O_3 \longrightarrow XO + O_2 \tag{2.6}$$
$$XO + O \longrightarrow X + O_2 \tag{2.7}$$

where X stands for any available catalyser, such as H, NO, Cl or Br. In the preindustrial atmosphere, only NO and H were available in noteworthy concentrations. Cl and Br were only minor constituents of the stratosphere, as long-lived natural bromine and chlorine emissions are very low. In the following sections, the detailed NO_x, HO_x and halogen chemistries will be presented, followed by a short overview of the heterogenous chemistry that occurs during volcanic events. The summarized ozone destruction rates are illustrated in Figure 2.5.

2.1.4.a NO_x-cycle

The NO_x-family consists of two chemical components: NO and NO_2. In the stratosphere, their only significant source is nitrous oxide (N_2O), which comes from bacterial emissions in natural soils and oceans, and further from agriculture, where the use of nitrogen fertilizers and animal waste stimulate naturally occurring bacteria to produce

more N_2O. With an atmospheric lifetime of 98 years (Ravishankara et al., 2009), most of the emitted N_2O needs to enter the stratosphere, where it undergoes the following reactions:

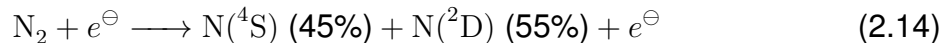$$N_2O + h\nu \longrightarrow N_2 + O(^1D) \qquad \lambda < 200\,nm, \sim 90\,\% \qquad (2.8)$$

$$N_2O + O(^1D) \longrightarrow 2NO \qquad \sim 5.8\% \qquad (2.9)$$

$$N_2O + O(^1D) \longrightarrow N_2 + O_2 \qquad \sim 4.2\% \qquad (2.10)$$

After formation via reaction 2.8, NO is ready to start the ozone destruction cycle, which mostly occurs between 35 to 45 km altitude:

$$NO + O_3 \longrightarrow NO_2 + O_2 \qquad (2.11)$$

$$NO_2 + O \longrightarrow NO + O_2 \qquad (2.12)$$
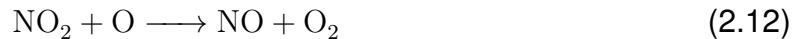
Below 35 km altitude, this cycle loses importance because of the lack of $O(^1D)$ atoms, and at altitudes above 45 km, the thinning of the air density and of all of its constituents leads to a reduction of the destruction rate.

Via a secondary, less important pathway, NO is also produced through the ionization of nitrogen by energetic particles following the reactions described in Aikin (1994) and Egorova et al. (2011). Each incoming energetic particle (e.g. relativistic electron or proton) collides with air molecules and ionizes them, i.e. produces "ion pairs". These ion pairs will be highly energetic, leading to further ionization and dissociation of air molecules. Important reactions include

$$N_2 + e^\ominus \longrightarrow N^+ + N + 2e^\ominus \qquad (2.13)$$

$$N_2 + e^\ominus \longrightarrow N(^4S)\ (45\%) + N(^2D)\ (55\%) + e^\ominus \qquad (2.14)$$

$$N^+ + N_2 \longrightarrow N_2^+ + N(^4S) \qquad (2.15)$$

where $N(^4S)$ is the electronic ground state and $N(^2D)$ is the electronic first excited state of the nitrogen atom. Almost all of the excited $N(^2D)$ atoms react immediately with O_2, producing nitric oxide,

$$N(^2D) + O_2 \longrightarrow NO + O, \qquad (2.16)$$

whereas collisional quenching of $N(^2D)$ plays only a minor role. Conversely, the ground state $N(^4S)$ can undergo a "cannibalistic" reaction with NO,

$$N(^4S) + NO \longrightarrow N_2 + O, \tag{2.17}$$

leading to the destruction of NO_x, which is the dominant pathway under sunlit conditions with high NO concentrations. In the absence of NO, e.g. during night when all NO reacted with ozone to NO_2 and oxygen, the $N(^4S)$ atoms react slowly with oxygen,

$$N(^4S) + O_2 \longrightarrow NO + O. \tag{2.18}$$

Obviously, reactions 2.16 and 2.17 are two very opposing pathways, one leading to NO_x production, the other to NO_x destruction. Therefore, within our modeling approach, $N(^2D)$ is immediately converted into NO, while $N(^4S)$ is a regular species in the CCM, which is subject to a full kinetic treatment. Following Brasseur and Solomon (2005), when dissociation of molecular nitrogen yields one $N(^4S)$ and one $N(^2D)$ atom, the net odd nitrogen production is extremely small: almost every $N(^2D)$ atom produces one NO molecule, but almost every $N(^4S)$ atom immediately destroys one at these altitudes. Net production is provided only by the very small fraction of $N(^4S)$ atoms which react via reaction 2.18

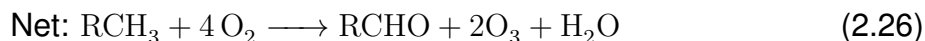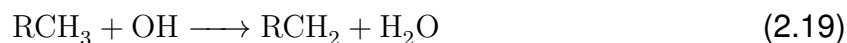Therefore, a reliable quantification of the $N(^2D)$:$N(^4S)$ branching ratio is required. Following Porter et al. (1976), 1.25 N atoms (or N^+ ions) are produced per ion pair, of which 55% are $N(^2D)$ and 45% are $N(^4S)$ (see Table V in Porter et al., 1976). In SOCOL, the first excited state, $N(^2D)$, is assumed to convert instantaneously to NO. The ground state atom, $N(^4S)$, may undergo the cannibalistic reaction with the produced NO, i.e. $N(^4S) + NO \longrightarrow N_2 + O$, or may react, though much more slowly, with molecular oxygen to generate NO.

In essence, the circumstances above mean that 1 ion pair produces often much less than 1 molecule NO, e.g. as little as 1.25 $\times$ (55% - 45%) = 0.125 NO under sunlit conditions. Conversely, in the absence of light, most NO will react with O_3 and not be available for the cannibalistic reaction. Our model contains all these processes (Calisto et al., 2011).

While NO_x induces ozone losses in the stratosphere and mesosphere, it is a precursor for ozone in the troposphere. Amongst the natural sources (35%) are biomass burning,

soil emissions and lightning; amongst the anthropogenic sources ($\backsim$65%) various forms of combustion processes (fossil fuel and biomass). Ozone production is often observed in urban areas in summer, when so-called "photosmog" occurs. Photosmog can only exist if both volatile organic carbons (VOC) - among them carbon monoxide, methane or benzene - and NO_x coexist. As example we use "RCH_3" as VOC:

$$RCH_3 + OH \longrightarrow RCH_2 + H_2O \tag{2.19}$$
$$RCH_2 + O_2 \longrightarrow RCH_2O_2 \tag{2.20}$$
$$NO + RCH_2O_2 \longrightarrow NO_2 + RCH_2O \tag{2.21}$$
$$RCH_2O + O_2 \longrightarrow RCHO + HO_2 \tag{2.22}$$
$$NO + HO_2 \longrightarrow NO_2 + OH \tag{2.23}$$
$$2NO_2 + h\nu \longrightarrow 2NO + 2O \tag{2.24}$$
$$2\times(O_2 + O + M \longrightarrow O_3 + M) \tag{2.25}$$

$$\text{Net: } RCH_3 + 4O_2 \longrightarrow RCHO + 2O_3 + H_2O \tag{2.26}$$

Hence, the VOC is oxidized, creating ozone. In a pristine atmosphere, e.g. the Antarctic troposphere, NO_x concentrations can also be influenced by ionization through galactic cosmic rays following reactions 2.13 to 2.18 (Calisto et al., 2011).

2.1.4.b HO$_x$-cycle

The HO$_x$-family consists of OH and HO$_2$. Photolysis of ozone is responsible for the initiation of the HO$_x$-cycle:
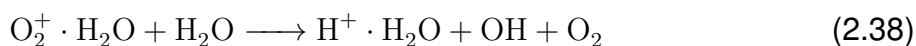
$$O_3 + h\nu \longrightarrow O_2 + O(^1D) \tag{2.27}$$
$$O + H_2O \longrightarrow 2OH \tag{2.28}$$

In the stratosphere, one discerns between "low HO$_x$" and "high HO$_x$" regimes. In the low HO$_x$ regime, which is especially active below 20 km, the following reactions destroy ozone:

$$OH + O_3 \longrightarrow HO_2 + O_2 \tag{2.29}$$

$$HO_2 + O_3 \longrightarrow OH + 2O_2 \tag{2.30}$$

$$\text{Net: } 2O_3 + h\nu \longrightarrow 3O_2 \tag{2.31}$$

In high HO_x regimes which are found above 45 km due to the high availability of $O(^1D)$ and intense radiation, the following cycle is dominant:

$$OH + O_3 \longrightarrow HO_2 + O_2 \tag{2.32}$$

$$HO_2 + O \longrightarrow OH + O_2 \tag{2.33}$$

$$O_3 + h\nu \longrightarrow O + O_2 \tag{2.34}$$

$$\text{Net: } 2O_3 + h\nu \longrightarrow 3O_2 \tag{2.35}$$

At very high altitudes - mainly in the mesosphere - HO_x can also be produced by ionization through energetic particles. The following reactions, established in various laboratories, are summarized as follows (e.g., Aikin, 1994):

$$O_2 + e^{\ominus} \longrightarrow O_2^+ + 2e^{\ominus} \tag{2.36}$$

$$O_2^+ + H_2O \longrightarrow O_2^+ \cdot H_2O \tag{2.37}$$

$$O_2^+ \cdot H_2O + H_2O \longrightarrow H^+ \cdot H_2O + OH + O_2 \tag{2.38}$$

$$H^+ \cdot H_2O + e^{\ominus} \longrightarrow H + H_2O \tag{2.39}$$

$$H + O_2 \longrightarrow HO_2 \tag{2.40}$$

The last two reactions are only important at heights above 70 km, were dissociative recombination matters due to further ionization. Below, thanks to the formation of negative ions like nitrates, the recombination reaction 2.46 is far more likely to happen:

$$H^+ \cdot H_2O + NO_3^- \longrightarrow HNO_3 + H_2O \tag{2.41}$$
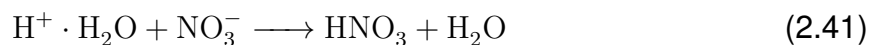
and subsequently the HNO_3 can photolyze:

$$HNO_3 + h\nu \longrightarrow OH + NO_2. \tag{2.42}$$
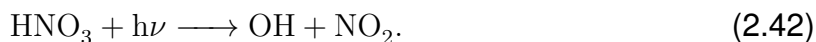
Alternative pathways exist with negatively ionized oxygen molecules. This process will not be covered in this thesis.

In contrast to NO_x lifetimes, the lifetimes of HO_x in the stratosphere and lower mesosphere are very short, ranging on the order of hours to days (Figure 5.27 in Brasseur and Solomon, 2005). As such, HO_x is not transported over long distances in the stratosphere, but its continuous resupply by $H_2O + O(^1D)$ and EPP still lets it have a significant local impact on the ozone layer.

2.1.4.c ClO_x- and BrO_x-cycles

As found by Molina and Rowland (1974) and Molina and Molina (1987), the ClO_x-cycles (ClO_x = Cl + ClO) play major roles in ozone depletion in the modern atmosphere. Before any anthropogenic influence, naturally emitted CH_3Cl was the only source for creating atomic chlorine, which was then able to interfere with stratospheric ozone chemistry:
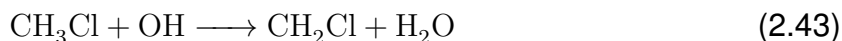
$$CH_3Cl + OH \longrightarrow CH_2Cl + H_2O \tag{2.43}$$
$$CH_3Cl + h\nu \longrightarrow CH_3 + Cl \tag{2.44}$$
$$\tag{2.45}$$

Nowadays, due to anthropogenic ODS emissions, a majority of atomic chlorine is produced from photolysis of $CFCl_3$:

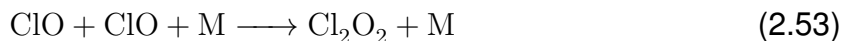$$CFCl_3 + h\nu \longrightarrow CFCl_2 + Cl \qquad\qquad \lambda < 226\,nm \tag{2.46}$$

The two ClO_x cycles can run freely until the termination 2.61 or 2.62 sets in.
Cycle I, midlatitudes, upper stratosphere:

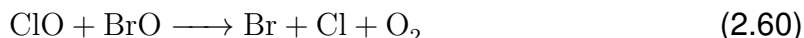$$Cl + O_3 \longrightarrow ClO + O_2 \tag{2.47}$$
$$ClO + O \longrightarrow Cl + O_2 \tag{2.48}$$
$$O_3 + h\nu \longrightarrow O + O_2 \tag{2.49}$$

$$\text{Net: } 2O_3 + h\nu \longrightarrow 3O_2 \tag{2.50}$$

Cycle II, lower polar winter stratosphere (ozone hole):

$$Cl + O_3 \longrightarrow ClO + O_2 \tag{2.51}$$
$$Cl + O_3 \longrightarrow ClO + O_2 \tag{2.52}$$
$$ClO + ClO + M \longrightarrow Cl_2O_2 + M \tag{2.53}$$
$$Cl_2O_2 + h\nu \longrightarrow 2Cl + O_2 \tag{2.54}$$
$$\text{Net: } 2O_3 + h\nu \longrightarrow 3O_2 \tag{2.55}$$

The only way to interrupt the destruction cycle is to create so-called reservoir species, disabling both the NO_x and ClO_x species at once:

$$NO_2 + ClO + M \longrightarrow ClONO_2 + M \tag{2.56}$$
$$\text{Or: } CH_4 + Cl \longrightarrow HCl + CH_3 \tag{2.57}$$
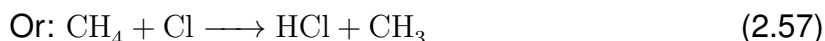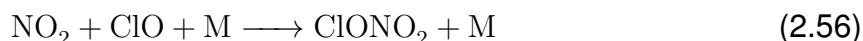
Similarly, BrO_x (BrO_x = Br + BrO) also efficiently destroys ozone. The only natural bromine which is emitted is methyle bromide (CH_3Br), but nowadays other ODS have become more important. The chlorine cycle 2.52-2.55 can simply be substituted by bromine, as was found by Wofsy et al. (1975). More important is a cycle found by Yung et al. (1980), which couples together chlorine and bromine species:

$$Cl + O_3 \longrightarrow ClO + O_2 \tag{2.58}$$
$$Br + O_3 \longrightarrow BrO + O_2 \tag{2.59}$$
$$ClO + BrO \longrightarrow Br + Cl + O_2 \tag{2.60}$$
$$\text{Net: } 2O_3 + h\nu \longrightarrow 3O_2 \tag{2.61}$$

The different rates of ozone destruction due to the six cycles (chlorine-bromine-, low HO_x-, high HO_x-, NO_x-, ClO_x-, and BrO_x-cycles) are illustrated in Figure 2.5.

2.2   Influence of the Sun on Earth's climate

The Sun is the most important driver of the climate system. There are many different ways in which solar radiation can be changed on its way to planet Earth.
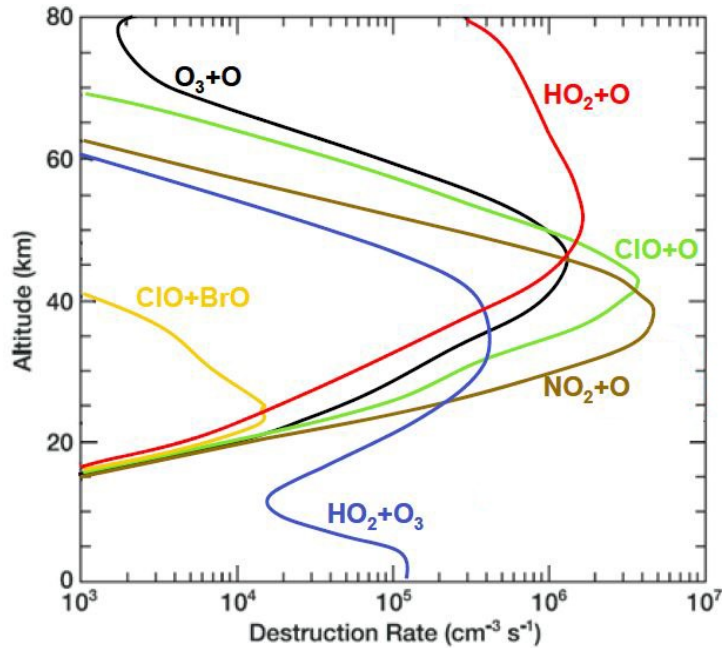
Figure 2.5: Daytime averaged rates of destruction of ozone at 40°N in winter by a range of chemical processes for 1998 levels of reactive chemicals, from the numerical model of Garcia and Solomon. Yellow = chlorine-bromine-cycle, blue = low HO_x cycle, red = high HO_x cycle, green = ClO_x cycle, brown = NO_x cycle, black = O_x cycle. From Garcia and Solomon (1983, 1994), edited by T. Peter, ETHZ.

Let's first focus on the Sun itself: Oversimplified, the Sun is nothing more than a fusion reactor, transforming hydrogen into helium, which, following Einstein's relativity theory, generates the amount of energy

$$E = mc^2 \qquad (2.62)$$

where m is the loss of mass from the conversion from 4 hydrogen atoms (4 protons: $_0^1$H) to one helium atom (2 protons, 2 neutrons: $_2^4$He). This loss is on the order of 4.28 million tons of solar matter per second. By multiplying this number by the square of the speed of light, the resulting energy amounts to roughly 3.85×10^{26} Watts (Sackmann 1993). This power is radiated more or less isotropically, so that only a tiny amount reaches the top of the Earth's atmosphere (TOA). This power is expressed in W/m^2 as S_0, the so-called "solar constant". However, as will be explained later, S_0 is anything but constant.

First, the Sun slightly increases its luminosity and temperature (at a rate of 0.00657 percent per million years [Ga]) in order to maintain its core pressure, which decreases due to hydrogen depletion. This increase is significant over aeons (e.g. it is 30 % brighter now than 4.6 Ga ago) but is insignificant over climatological time scales of some thousands of years (Lang, 2001). The energy transport from the core of the Sun through the radiative and convection zones can be altered on a time-scale of some years to hundreds of thousands of years by magnetic disturbances (Nesme-Ribes et al., 1994). Finally, the photosphere - the main zone from which radiation is being emitted from the Sun - is constantly undergoing changes in its structure and surface coverage. Sunspots cover parts of the photosphere following an 11-year cycle, during which they move from the magnetic poles slowly towards the equator of the Sun. The Sun achieves a maximum of sunspots during the mean of this 11 year period (Maunder, 1904). The 11-year cycle has been recognized since the early 19th century (Schwabe, 1844; Wolf, 1850, 1861) and is very regular, as can be seen in Figure 2.6.

This cycle originates from a regular inversion of the solar magnetic field due to the differential rotational period on the sun, reaching 33.4 days at the poles and 25.6 days at the equator (Kosovichev et al., 1997). Like a string, the magnetic field is wound up around the Sun, as the equator has a lower rotational period than the poles. Over time, the magnetic streamlines must break through the photosphere, releasing the tension of the field and forming bipolar sunspots at the location of exit and entrance of the field. At the end of the solar cycle, the slightly toroidal magnetic field is broken up and starts a new cycle, with the poles becoming the opposite of what they were during the last cycle. These modifications of the photosphere significantly change S_0 by up to 0.4%, as has been observed by several satellite radiometers (HF, ACRIM, DIARAD, Figure 2.7), although the exact value differs from instrument to instrument (see Figure 2.7).

In addition to this 11-year solar cycle, periodicities of 22 years (Hale-cycle), 88 years, 208 years (Sonett and Suess, 1984) and maybe even 2000 years (Mayewski et al., 1997) are known. The Sp$\acute{\text{o}}$rer (SM, 1415-1530), Maunder (MM, 1645-1715) and Dalton (DM, 1780-1840) Minima illustrated in Figure 2.8 were discovered with the help of cosmogenic nucleides like ^{10}Be (Beer et al., 1994; Hoyt and Schatten, 1998; Steinhilber et al., 2008) and are evidence that such grand solar minima happen regularly - and will probably occur again in the near future (Abreu et al., 2008, 2010).

Finally, scientists since Milanković (1930) have recognized that the Earth follows complex variations in its orbit around the Sun (see Figure 2.9). The Earth's rotational axis changes its tilt angle slightly with a periodicity of 41 kyrs (obliquity). Moreover, the Earth's rotational axis wobbles regularly (precession), performing one complete rotation
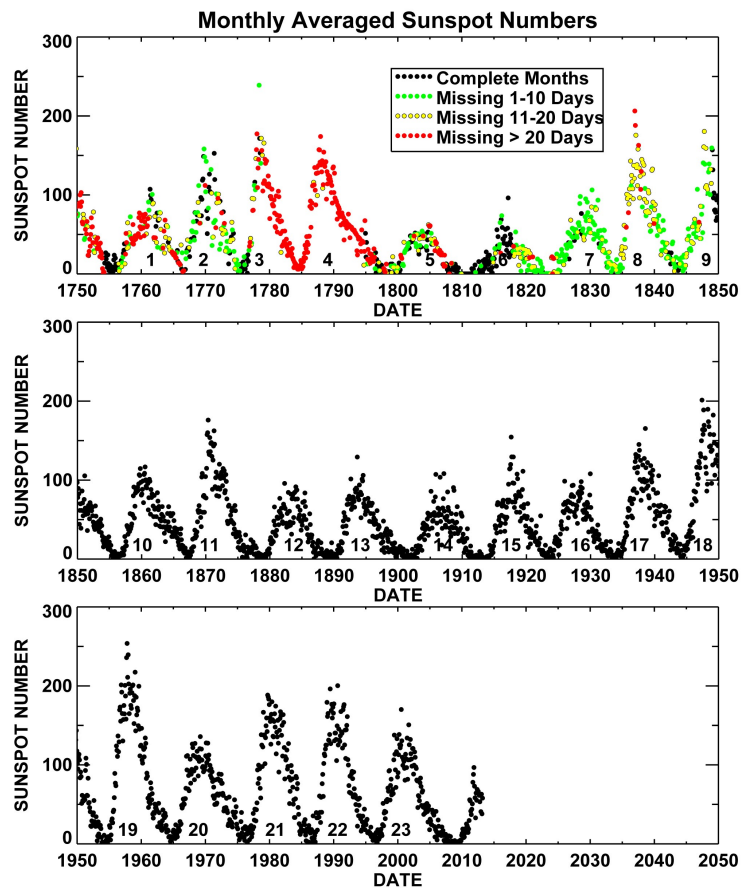
Figure 2.6: Average monthly Zürich sunspot numbers from 1750 to present. Source: HATHAWAY/NASA/MSFC 2013/2014, `http://solarscience.msfc.nasa.gov/images/Zurich_Color_Small.jpg`, last access 17.06.2013

every 21 kyrs. The Earth's eccentricity, or the "deformation" of the ellipse of the Earth's orbit around the Sun, also varies with an average periodicity of 93 kyrs. Together, these three variations constitute the "Milanković-cycle" (shown as "Solar Forcing" in Figure 2.9), which is held responsible for glacial and interglacial records in deep-sea sediments (see Hays et al., 1976; Imbrie et al., 1993; Beer et al., 2000) and also in ice core records (Figure 2.9, lowest panel).

All of these factors significantly affect the amount of solar power reaching the highest layers of the Earth's atmosphere, the TOA. The amount of incoming power is usually expressed in Watts per meter squared at TOA height and is currently believed to be about 1360.8 +/- 0.5 W/m^2 (Kopp and Lean, 2011). Until 2011, the canonical value was of 1365.4 +/- 1.3 W/m^2 although the exact value was - and still is - difficult to estimate due to the different measurement techniques and values of the HF, ACRIM, VIRGO,
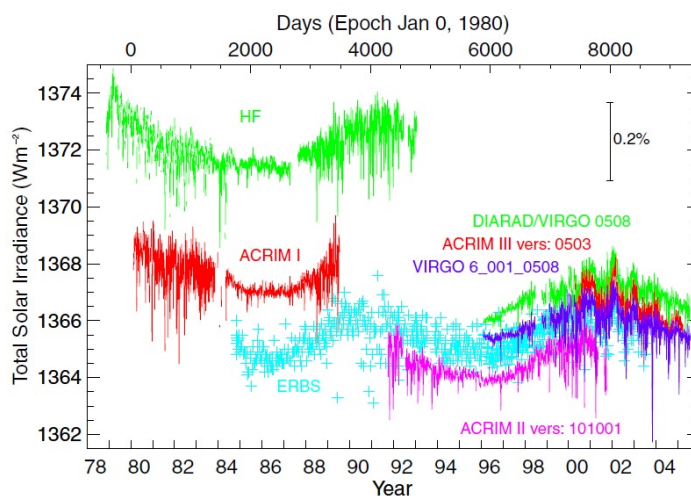
Figure 2.7: TSI measurements from different radiometers on different space platforms from November 1978 to December 2003 (Fröhlich, 2006).
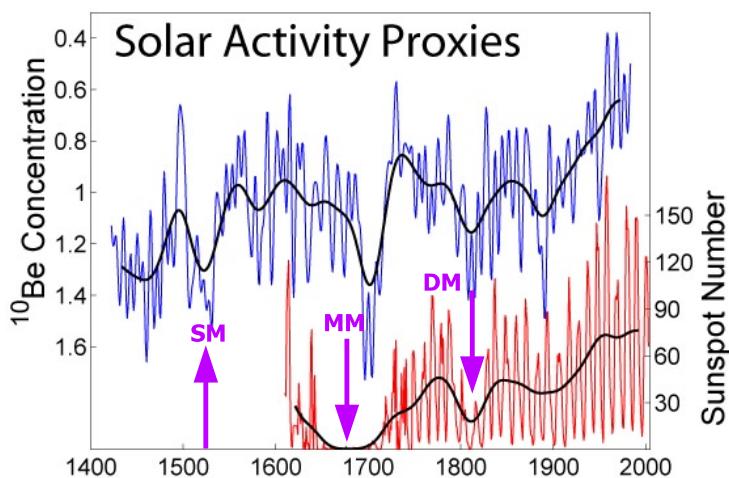

Figure 2.8: Illustration of the solar activity derived from reconstructed sunspot number data from Hoyt and Schatten (1998) (red) and ^{10}Be isotope concentration from measurements in the Dye-3 ice core from Beer et al. (1994). Image adapted from Robert A. Rohde / Global Warming Art, `http://www.globalwarmingart.com/images/6/60/Solar_Activity_Proxies.png`, last access 17.06.2013

.

PREMOS/SOVAP, and TIM/SIM radiometers. S_0 therefore varies from composite to composite (PMOD, ACRIM, SORCE/TIM).

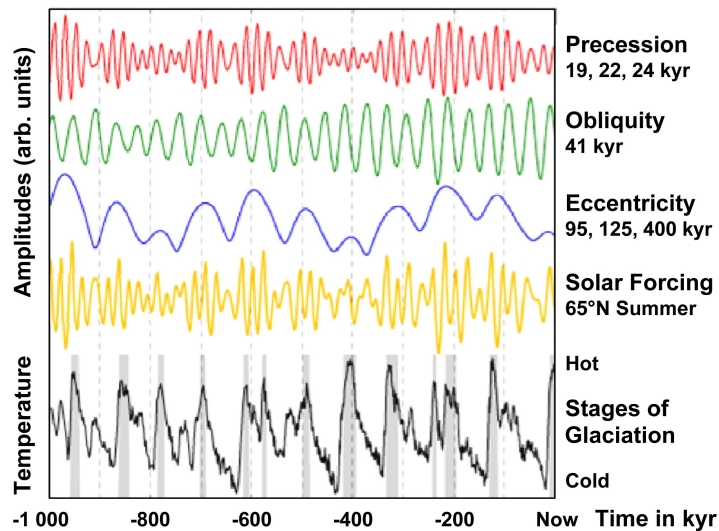The overall variation of the solar constant induced by the different processes of solar

Figure 2.9: Milanković cycles over the last 1 million years. In black, the observed glacial cycles from Lisiecki and Raymo (2005) are plotted above the grey shaded areas illustrating interglacial periods. Image created by Robert A. Rohde / Global Warming Art, `http://www.globalwarmingart.com/images/7/7e/Milankovitch_Variations.png`, last access 17.06.2013, modified by Prof. T. Peter, ETHZ

.

physics and orbital parameters is about 0.3 % for those variations with low periodicities (hundreds of years). For the grand minimum periodicities, the variation accounts for 0.8% and for around 0.06% for the 11-year solar cycle (PMOD composite, Fröhlich, 2006).

These changes might appear to be small, but they might be amplified due to different interactions in the Earth's atmosphere and on the Earth's surface. It has been known for some time that small variations in the TSI create much higher irradiance changes in some parts of the globe, especially over the western Pacific region. For the recent past (Shindell et al., 1999; Kodera and Kuroda, 2002; Haigh, 2003), these anomalies are explained by two main mechanisms, known as "top-down" and "bottom-up" (Meehl et al., 2009).

2.2.1   Top-Down mechanism

The top-down mechanism consists of seven main steps, all of which are illustrated in Figure 2.10. First, assume that a small positive UV spectral anomaly occurs and propagates down from the TOA to the mid-stratosphere (1). There, ozone not only absorbs the surplus UV radiation and heats the surrounding atmosphere (2,3), but is also produced at a higher rate (2). The supplementary heating, always more pronounced in the equatorial region than in the extratropics, implies a strengthening of the temperature gradient (4) and thus an acceleration of the subtropical and polar jets (5). The strengthened horizontal shear due to the greater wind speed gradient increases the potential vorticity and hinders the ability of planetary waves coming from the troposphere to penetrate the tropopause. The waves are deflected toward lower latitudes, changing the Hadley cell circulation (6) and modifying the energy transport in such a way that a significant increase in convergence at the intertropical convergence zone (ITCZ) happens. The result is an increase in precipitation (7) especially in the western Pacific region.

2.2.2   Bottom-Up mechanism

The bottom-up-mechanism is also a chain reaction of different atmospheric modifications, illustrated in Figure 2.11. As with the top-down mechanism, a small anomaly in the visible spectrum of the TSI (1) propagates down through the atmospheric window to the ocean (2). Let us focus specifically on the western Pacific. There, the nearly cloudless atmosphere permits an efficient warming of the sea surface (2), enhancing evaporation (3) and thus also ocean upwelling. The moist air masses are then transported by trade winds in the direction of the ITCZ (4), where convergence occurs (5), leading to increased precipitation. The accelerated Hadley-cell is then
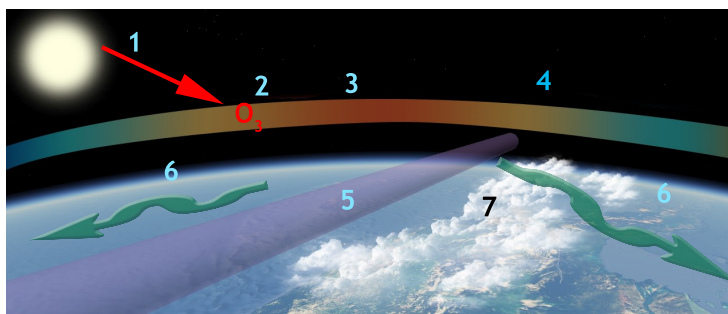

Figure 2.10: Top-Down mechanism, illustrated in 7 steps. Earth surface picture from Google Earth

.

responsible for a positive feedback. That is, the subsidence in the subtropical regions is strengthened (6), which suppresses cloud formation there even more, permitting an unrestrained penetration of the solar anomaly down to the sea surface.

Both mechanisms are coupled, amplifying one another and finally leading to locally much larger radiative anomalies than observed at the top of atmosphere (Meehl et al., 2009). Thus, at solar maximum conditions, the observed sea surface temperature and precipitation anomalies look very much like a weakened La Niña event, with the same patterns of ocean upwelling regions and mild winters in North America (Meehl et al., 2003) followed by a weak El Niño event some years later (e.g., White and Liu, 2008).

2.3 Influence of energetic particles on Earth's climate

Closely related to the science of the solar activity is the science of energetic particles. Energetic particles come either from outside the planetary system or from the Sun. Parker (1957), Warneck (1972), Swider and Keneshea (1973), Crutzen et al. (1975), and Usoskin et al. (2004) studied in detail the ionization of the atmosphere by cosmic and other energetic particles. A classification of different sources of ionization has been developed over time, categorized by the particle energies and their frequency of occurrence.

Cosmic particles or, more precisely, galactic cosmic rays (GCR), are formed primarily by high-energy sources like supernovae and quasars. They travel nearly at the speed of light and are thus highly energetic particles, reaching energies in the range of several
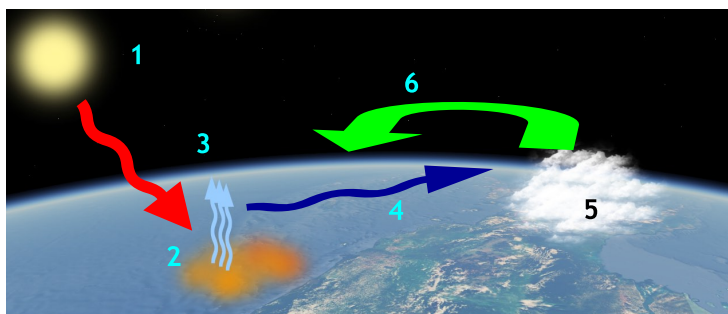

Figure 2.11: Bottom-Up mechanism, illustrated in 6 steps. Earth surface picture from Google Earth

.

GeVs (1 GeV = 1.602×10^{-10} J, Bazilevskaya et al., 2008). GCRs are composed of about 87% protons (^{1}H$^+$), 12% alpha particles ($^4_2$He^{2+}) and 1% heavier atoms. The latter can consist of basically all elements in the periodic table as their observed frequencies are very similar to the elemental distribution in the Sun (Hoerandel, 2003). Exceptions are greater amounts of lithium, beryllium or boron, all of which can exist in concentrations up to 500'000 times greater than the remaining elements due to the spallation of cosmic rays penetrating interstellar matter (mostly C, N, O, Ne, and H, Mitler, 1972).

The GCR flux is dependent on solar activity. As the Earth is shielded from GCRs by the solar magnetic field, minimum GCR penetration occurs when solar magnetic activity is at a maximum (Forbush, 1954).

When GCRs penetrate the Earth's atmosphere, a so-called "cosmic ray shower" consisting of ion pairs is triggered. Secondary energetic particles are released following the interaction of the cosmic ray particle with an atmospheric constituent, mostly nitrogen or oxygen. The secondary rays further ionize atmospheric constituents, forming nitrogen oxides, hydrogen oxides and Beryllium 7 (^{7}Be). While the first two species mainly remain in the stratosphere and eventually leave it with the BDC as HNO$_3$, the elemental ^{7}Be is water soluble, attaches to aerosol particles and can be transported downward into the troposphere, where it is finally rained out. Due to its short half-life (53.22 days), ^{7}Be is a rather bad tracer. However, a second beryllium product from spallation of nitrogen or oxygen exists, ^{10}Be. ^{10}Be is a far better tracer for GCR activity (e.g., Beer et al., 1991) and can also be used also for solar activity reconstructions (Figure 2.8) as it is very stable. GCR ionization reaches a maximum between 15 and 20 km (which constitutes basically the Bragg peak in the stopping power).

Another source of EPP are solar energetic particles (SEP), previously called "solar cosmic rays (SCR)" or "solar proton events (SPEs)". SEPs originate from explosive solar activity. Irregularly, but especially during periods of high solar activity, coronal mass ejections (CMEs), also called flares when they are less intense, can be observed. Their frequency of occurrence ranges from several times per day under solar active conditions to less than one per week in solar quiescent conditions (Gosling, 1993).

The exact origin of CMEs is not yet fully understood. A relatively well-accepted theory is that CMEs occur when two twisted magnetic streamlines encounter each other. The

energy released during the magnetic reconnection is transformed into kinetic energy, accelerating charged particles to very high velocities. Sometimes, CMEs have enough kinetic energy to expel large amounts of solar plasma. Huge plasma parcels may then travel in the direction of the Earth, reaching it after 1-4 days, carrying with it the magnetic field and accelerating other charged particles in front of it. The energy of those particles may be as high as 1 GeV (Kahler, 1992). Near the Earth, the charged particles are directed toward the polar regions, following geomagnetic streamlines. However, with enough kinetic energy, the particles largely ignore the Earth magnetic field and can penetrate the Earth's atmosphere, sometimes even propagating down to the stratosphere in cases of energies above 500 MeV (Shea et al., 2006; Jackman et al., 2008). As shown by Bazilevskaya et al. (2008), most protons only penetrate the atmosphere between from $60°$ and $90°$ geomagnetic latitude, as the geomagnetic shielding is strong at lower latitudes. CMEs not only ionize atmospheric constituents, generating nitrogen and hydrogen oxides, but are also a threat to every object orbiting around the Earth. Satellites can be destroyed and astronauts killed if they are not sufficently shielded against the charged particles.

The third class of energetic particles are so-called energetic electrons, which originate from the solar wind. The solar wind is a very regular and rather slow flow of protons and electrons. Parts of this solar plasma are trapped in the magnetosphere of the Earth. In times of turbulent heliospheric magnetic periods and especially during CME directed towards the Earth, this plasma is accelerated along the Earth's magnetic streamlines to the poles, where some of the particles penetrate the ionosphere. Strong evidence for their existence are the regularly occurring aurorae, which peak in activity during solar active periods. The red colors originate from excited nitrogen molecules or oxygen atoms, green colors from excited oxygen atoms and violet to purple colors from nitrogen ions.

Low energetic electrons (LEE) have energies of some 100 keV. Exceptionally highly energetic electrons (HEE) can have energies of up to 2 MeV (Gaines et al., 1995), but these are rather rare (1 to 10% Callis et al., 1991).

All classes of energetic particles lead to the formation of nitrogen oxides following the ratio found by Porter et al. (1976): 1.27 nitrogen atoms are produced per ion pair impacting on nitrogen molecules (see Formula 2.13 and 2.14). Of those 1.27 nitrogen atoms, 45% yield the $N(^4S^0)$ ground state and 55% the excited $N(^2D^0)$ state. The latter
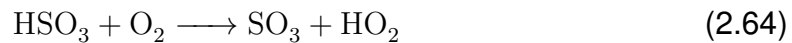
readily reacts with oxygen to form NO. Similarly, hydrogen oxide is formed with HO_x production rates following the P_{HO_x}/Q ratio of around 1.8, where P_{HO_x} is the production rate of HO_x and Q the total ionization rate (Solomon et al., 1981). All of these products interact substantially with the other chemical constituents of the atmosphere, as detailed in the previous section.

2.4   Influence of volcanic activity on Earth's climate

Volcanoes are one - if not the most - important cause of natural climate change over timescales ranging from 1 to 100 years. Depending on the size of the volcanic eruption, modifications are either constrained to the regional scale (ash cloud) or occur globally (big volcanic ash plume). Volcanoes emit gases when they erupt, particularly water vapour (H_2O), carbon dioxide (CO_2) and sulfur dioxide (SO_2) (Halmer et al., 2002). It is known that H_2O and CO_2 are two greenhouse gases able to substantially modify global temperatures. However, the amount of H_2O and CO_2 emitted during a volcanic eruption is so small compared to global total concentrations that their effect is negligible. Only in periods of massive volcanic activity and magmatism (e.g. during the Cretaceous, 145 - 66 Ma BP) did CO_2 outgassing raise atmospheric CO_2 levels so much that a greenhouse warming effect occurred (Kerrick, 2001). Hence, the most important climatically active gas species erupted in the present and recent past volcanic activities is SO_2.

One measure to classify the intensity of a volcanic eruption is the so-called "volcanic explosivity index" VEI (Newhall and Self, 1982). Most volcanic activity classified as "small" ranges from 0-3 VEI; examples of such eruptions are those happening regularly on Mounts Etna and Stromboli, or the 1995 Soufrière. Those volcanoes do not erupt explosively enough for their plume to reach the tropopause; they therefore only influence the troposphere. However, there has been discussion since very recent time whether or not also the low to moderate volcanic eruptions - at primarily tropical latitudes - could inject sulfur directly to altitudes between 18 and 20 km, from where it is lofted by the BDC (Vernier et al., 2011), exerting a negative radiative forcing of up to -0.1 W/m^2 (Solomon et al., 2011).

SO_2 is oxidized with OH and water to form H_2SO_4 which is very soluble (Stockwell and Calvert, 1983; Margitan, 1984):

$$SO_2 + OH + M \longrightarrow HSO_3 + M \tag{2.63}$$

$$HSO_3 + O_2 \longrightarrow SO_3 + HO_2 \tag{2.64}$$

$$SO_3 + H_2O \longrightarrow H_2SO_4 \tag{2.65}$$

Most of the sulfuric acid that forms in the troposphere is then rained out or removed by dry deposition (e.g., Casadevall et al., 1984) on time scales of hours to weeks.

Volcanic eruptions reaching VEIs of 4 or more will inject part of their plume matter directly into the lower stratosphere. Examples are the El Chichón eruption in 1980 and the Mount Pinatubo eruption in 1991. Due to advection and mixing processes, the H_2SO_4 aerosols will be equally distributed zonally. H_2SO_4 aerosols in the stratosphere are able to influence climate in several ways.

First, they host heterogeneous chemical reactions and thus change the composition of the stratosphere. Second, they absorb a part of the outwelling IR radiation, thus heat the stratosphere and change its dynamics. Both effects lead effectively to ozone destruction, roughly in similar amounts (Pitari and Rizi, 1993).

The heterogeneous reactions taking place on sulfuric acid droplets allow chemical transformations, which would otherwise not be possible in the gas phase. Primarily the N_2O_5 hydrolysis

$$N_2O_5 + H_2O \xrightarrow{\text{het}} 2\,HNO_3 \tag{2.66}$$

occurs on the surface of aerosol particles almost independently of temperature throughout the troposphere and the stratospheric aerosol layer (Hanson and Ravishankara, 1991). Under volcanically perturbed conditions the surface area density of the stratospheric aerosol can increase by an order of magnitude, leading to a massive enhancement of nitrogen deactivation and HNO3 gain (Fahey et al., 1993). The consequences are that the NO_x-induced ozone destruction (reactions 2.11-2.12) will decrease, while the ClO_x-induced ozone destruction will increase. The latter is the result of a reduction in ClO_x deactivation via

$$NO_2 + ClO + M \longrightarrow ClONO_2 + M. \tag{2.67}$$
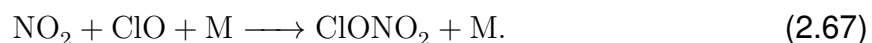
In the modern stratosphere with massive ClO_x loading, the net effect is therefore ozone loss. Conversely, in the preindustrial stratosphere with much less stratospheric ClO_x, the volcanic aerosols led to a slowing of the NO_x-induced loss cycle and hence to reduced ozone loss, i.e. increased ozone mixing ratios as will be shown in Chapter 4.

Besides N_2O_5 hydrolysis, other heterogeneous reactions are the chlorine activation reactions, which are known from heterogeneous chemistry on Polar Stratospheric Clouds (PSCs). However, these reactions require very low temperatures, thus they typically do not occur under midlatitude conditions. The reaction, which still occurs at highest temperatures, is

$$ClONO_2 + H_2O \xrightarrow{het} HOCl + HNO_3. \tag{2.68}$$

The reaction probability of reaction 2.68 increases exponentially with decreasing temperature, becoming equal to that of reaction 2.66 below 200 K (Sander et al., 2011). Therefore, globally reaction 2.66 dominates the effect on the ozone column, while 2.68 dominates under polar winter conditions (Granier and Brasseur, 1992).

In the stratosphere, under cold polar winter conditions the aerosols take up water, dilute, hence increasing the solubility of HCl, which enables the two following reactions on cold aerosol particles (Drdla and Müller, 2012) or PSCs:

$$ClONO_2 + HCl \xrightarrow{het} Cl_2 + HNO_3 \tag{2.69}$$

$$HOCl + HCl \xrightarrow{het} Cl_2 + H_2O \tag{2.70}$$

These reactions further enhance ozone destruction, as the chlorine molecule can then be photolyzed into chlorine radicals, which readily react with ozone, creating ClO and oxygen (see reactions 2.69-2.70).

Conversely, in preindustrial times the halogen-free atmosphere led to an increase in ozone in the stratospheric aerosol layer. This is due to the deactivation of NO_x into relatively passive reservoir species on the surface of H_2SO_4 aerosols. This resulted in an increase in ozone of up to 10% over the tropical tropopause region after the 1815 Tambora eruption (Anet et al., 2013a).

In terms of affecting stratospheric and tropospheric dynamics, sulfate aerosols both absorb and reflect radiation: On one hand, incoming solar radiation is backscattered and only partly absorbed, which leads to a cooling of on the surface below the aerosols. On the other hand, longwave radiation emitted from the Earth's surface is absorbed, leading to a strong warming in the aerosol layer, and back-radiated to the Earth's surface. The overall effect is probably a slight warming at the equator right after the eruption due to the additional downwelling of LW radiation. In extratropical regions, the situation is a bit more complicated. The additional heating that occurs in the tropopause changes the temperature gradient and leads to modifications in monsoon intensity and storm track patterns (e.g., Oman et al., 2005). El Niño-like anomalies are also more likely to occur right after an explosive volcanic eruption, leading to temperature and precipitation anomalies over the whole globe (e.g., Adams et al., 2003).

Chapter 3

Model description and evolution of the coupling

3.1 Atmosphere

The model framework that was designed for the study is based on the chemistry-climate model (CCM) SOCOL3 (Stenke et al., 2013) and the Max-Plank-Institute ocean model (MPIOM) (Marsland et al., 2003), coupled by the Ocean Atmosphere Sea Ice Soil (OASIS3) module (Valcke, 2013). SOCOL3 consists of the middle atmosphere (MA) general circulation model ECHAM5 (Roeckner et al., 2003; Manzini et al., 2006) and of a modified version of the chemistry-transport model (CTM) MEZON (Model for Evaluation of oZONe trends, Rozanov et al. (1999, 2001); Egorova et al. (2003); Schraner et al. (2008)).

3.1.1 GCM

The MA-ECHAM5 climate model emerged from an early version (cycle 17, 1985) of the ECMWF weather forecast model (Roeckner et al., 1989) and has been modified for climate modeling purposes by the Max Plank Institute in Hamburg (**EC**MWF **HAM**burg). Its dynamical core is based on the vorticity and divergence form of the primitive equations, forecasting the temperature, vorticity, divergence, surface pressure, humidity and cloud water. The vertical resolution of the model version used in this study consists of 39 hybrid sigma-pressure levels (L39) ranging from the surface to 0.01 hPa. The chosen horizontal resolution is a triangular truncation of the spherical harmonics to 31

wave-numbers, mostly shortened to T31.

The parameterization of the incoming shortwave radiation is based on the ECMWF radiation code. The spectrum is resolved into six bands: One UV band (185-250 nm), one band in the transition region from near UV to visible radiation (250-440 nm), one visible band (440-690 nm) and three near- to short-wavelength infrared (IR) bands (690-1190 nm, 1190-2380 nm, 2380-4000 nm). A shortcoming of this parameterization is the rather narrow first band, extending only down to 185 nm. This has implications for the radiative heating by ozone and oxygen at shorter wavelengths, as they are underestimated. In addition, the treatment of the solar irradiation forcing by the standard ECHAM5 radiation code does not work properly (Forster et al., 2011). Thus, corrective radiative heating parameterizations from the absorption of oxygen and ozone in the Lyman-alpha line (121.6 nm), the Schumann-Runge bands (175-200nm), the Hartley and Huggins bands (200-300 nm) and the Herzberg continuum (240-260 nm) were implemented in the model following Zhu (1994) and Egorova et al. (2004). The radiative transfer for longwave radiation follows the rapid radiation transfer model (RRTM) scheme of Mlawer et al. (1997) with 16 spectral intervals. This is the same scheme used in the cycle 23 weather model of the ECMWF. The whole radiation scheme is called every two hours.

For stratiform cloud parameterization, two different schemes are available. The prognostic equations for vapor, liquid, ice phase and a cloud microphysical scheme are from Lohmann and Roeckner (1996). A statistical cloud cover scheme including prognostic equations for the distribution of moments is based on Tompkins (2002). Cumulus convection is parameterized following Tiedtke (1989), with minor modifications for penetrative convection according to Nordeng (1994).

3.1.2   Modified CCM

The GCM and the chemical part of the CTM are coupled together to create the chemistry climate model (CCM) SOCOL3. Every two hours, the GCM passes temperature fields to the chemical module, which computes the chemical transformations of 41 gas species participating in 200 gas phase reactions, 16 heterogeneous reactions and 35 photolytic reactions. These tendencies are then handed back to the GCM, which handles the advection of the species. The GCM also takes into account the radiative

forcing from carbon dioxide, water vapor, methane, nitrous oxide, chlorofluorocarbons (CFCs) and hydrochlorofluorocarbons (HCFCs) and ozone.

Important changes were made to the base version of the model code in order to implement an ionization routine identical to that of Calisto (2011), as no explicit ion chemistry is included. However, the code of Calisto (2011) was written for SOCOL2, which is a single-processor model. Hence, all routines needed to be parallelized. In the same step, additional changes were done:

- Implementation of the GCR ionization parameterization from Usoskin and Kovaltsov (2006) and Usoskin et al. (2010), and parallelization of the data import routines.

- Implementation of the SEP ionization parameterization from Jackman et al. (1990) and Jackman (2006), and parallelization of the data import routines.

- Implementation of the LEE ionization parameterization from Baumgaertner et al. (2009) and parallelization of the data import routines.

- Implementation of a routine to allow variations in the position and strength of the geomagnetic field.

- Implementation of a routine similar to Heikkilä (2007) that permits the simulation of the ^{10}Be and ^{7}Be transport and deposition rates in SOCOL3. As the existing routines had to be transposed from the ECHAM5-HAM to the SOCOL3-MPIOM model, tiny adjustments were made, especially concerning wet deposition, which is not available natively in SOCOL3. Hence, wet deposition was replaced by a coupling of the ^{10}Be and ^{7}Be concentrations to the precipitation rate. Final results were very similar to the fields produced by ECHAM5-HAM.

- Implementation of a passive tracer for computing the mean age of air.

The GCR parameterization of Usoskin and Kovaltsov (2006) and Usoskin et al. (2010) is based on the CRAC:CRII (Cosmic RAy induced Cascade: application for Cosmic Ray Induced Ionization) model. A lookup table for the ionization rates of energetic particles is given. With the help of three coordinates - the geomagnetic latitude, the height and the solar modulation potential Φ - the ionization rate at every point of the SOCOL3 atmosphere can be computed. Using the relation of 1.27 nitrogen atoms formed per ion pair, N and NO production rates are computed and added to the global

N and NO tracer tendencies of the SOCOL3 model.

The SEP parameterization also starts using the same assumptions about NO_x and HO_x production as are used for the GCRs. However, due to the far less energetic characteristics of the solar protons as compared to GCRs, a strong cutoff eliminating any ionization is defined at geomagnetic latitudes below $60°$.

Finally, the LEE parameterization is based on formula 3 from Baumgaertner et al. (2009) and produces only NO_x. The deficiency of our SOCOL-MPIOM is that it does not have any treatment for the upper mesosphere nor the ionosphere- or thermosphere-heights, at which ionization by low energetic electrons occurs most intensively. Hence, the simple but generally accepted solution was to inject an A_p-index dependent NO_x-flux into the two highest model levels at geomagnetic latitudes above $55°$.

The dynamical timestep of the atmosphere is set to 15 minutes.

3.2   Ocean

The ocean model MPIOM is derived from the HOPE model series (Hamburg Ocean Primitive Equation) and is based on a staggered Arakawa-C grid. With its orthogonal curvilinear grid, MPIOM does not possess a regular latitude-longitude grid. This allows the user to "hide" the poles over land areas, which overcomes the numerical pole problem. This also allows for regional modeling with a locally finer model grid, thus overcoming the difficult choice of suitable boundary conditions by retaining the global modeling possibility (see Figure 3.1). Like the atmospheric model, the ocean model is based on the primitive equations. An extensive description of the model is given in Marsland et al. (2003). The dynamical timestep of the ocean is set to 144 minutes.

3.3   Coupling

Both models can work independently from one another, if suitable boundary conditions are provided for the "missing part" (ocean prescribed for a run with atmosphere
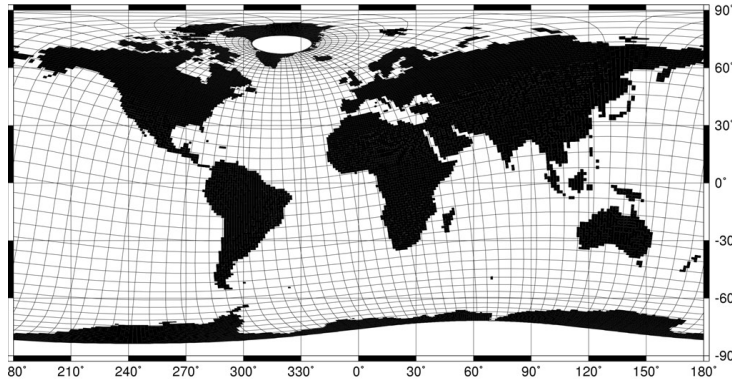
Figure 3.1: Illustration of the grid used for the ocean model. Note that the poles are located over Antarctica and Greenland, permitting a high resolution over the north Atlantic basin and overcoming the pole problem. Figure from the ISS-ESM presentation (J. Jungclaus, MPI-Hamburg)

.

model only, and atmosphere prescribed for a run with ocean model only). Much more interesting and necessary for our experiment is an interactive coupling of both model parts. For this purpose, we used the coupler OASIS3, which is implemented in the COSMOS model framework. As a standard, the exchange timestep between ocean and atmosphere was set to one day. After 24 hours of simulation, the 2-D fields of sea surface temperature, sea ice concentration, sea ice thickness, snow depth and ocean surface velocities are passed from the ocean to the atmosphere using first order conservation remapping. In exchange, the atmosphere passes the eastward and northward wind stress vector components over water and ice, the snow flux over ice, the heat flux over water and ice, the residual heat flux, the surface shortwave flux, the wind speed at 10m, and the water flux in the ocean (computed by the hydrology discharge model of Hagemann and Dümenil (1997) to the ocean.

3.4 Setbacks

Although the access to the basic model framework "COSMOS" (Budich et al., 2010) - which includes the atmosphere model MA-ECHAM5, the ocean model MPIOM and the coupler OASIS3 - was easily provided to us, compilation and subsequent execution was unfruitful using our standard compiler (Intel Fortran Compiler version 10.1.018, henceforth called IFORT) despite some major changes in the compilation (different

standard compilers, different model architecture) and run scripts (different libraries, different model architecture). We hoped to overcome this problem by integrating the chemical part in the standard COSMOS framework and by modifying slightly the provided standard models. Two approaches were possible:

- Implement MEZON into COSMOS.

- Implement MPIOM and the coupling routines of MA-ECHAM5 with OASIS3 into SOCOL3.

We tackled the first approach with the help of the programming framework "Eclipse", which simplified the merging task of the two model versions MA-ECHAM5 and SOCOL3 largely, as a very handy "compare" feature highlighted all the differences. However, on account of overly complex changes (ECHAM5 model version 5.3 in COSMOS compared to 5.4.01 in SOCOL3) and programming peculiarities in the downloaded MPIOM version, we still failed to make the ocean model compilable with IFORT on the second attempt. Hence, the first approach was aborted.

In a strong and fruitful collaboration with the ocean team at the MPI Hamburg (J. Junclaus, H. Haak) and the climate physics group of the University of Bern, a new start was undertaken by aquiring the newest MPIOM-ECHAM5 framework[a] used during the EaSyMS2011 (Earth System Modelling School 2011) and by implementing the coupling routines of MA-ECHAM5 into SOCOL3. This second approach was much more successful, although several attempts had to be made to find the correct compilation flags in order to compile and run the new model framework SOCOL3-MPIOM.

The first run of the new model version showed that the radiation balance (incoming radiation versus outgoing radiation at TOA) was different than the one of the SOCOL3 version. The reason is most probably found in the prescribed sea surface temperatures and sea ice coverage fields (SST/SIC) in SOCOL3, which are computed interactively in the new model version. This radiation inequilibrium problem became very apparent when the models were started in order to "spin-up" the simulation (see later). After initialization of the model from restart files of the millennium simulations[b] (Jungclaus et al., 2010) from the year 1600, a strong negative trend in ocean temperatures was

---

[a]MPIOM: Version 1.5, ECHAM5: Version 5.4

[b]Transient simulations of the years from 800 AD to 2005 AD, http://www.mad.zmaw.de/service-support/consortium-model-runs/millennium-experiments/index.html

observed due to a positive radiation balance anomaly at the TOA of 1.5 W/m^2. This triggered a strong increase in sea ice and a subsequent change of the albedo, inducing a negative feedback effect on temperatures. However, a stabilization in temperatures after around 200 model years was observed.

The next major difficulty to overcome was a strongly decreasing Atlantic meridional overturning circulation (AMOC). The analysis of the problem showed that a freshwater correction routine implemented in the most recent coupling module was overlooked during the merging process of the two models[c]. This lead to a significant improvement in the AMOC, which was further improved by applying a new land surface mask to the atmosphere model containing less ocean surface.

After these corrections and a harmonization of the model namelists, a new cooling effect was observed, leading to a rapid formation of sea ice until latitudes of 60° N. It became apparent that we erroneously selected the standard stratiform cloud parameterization of SOCOL3 (Tompkins, 2002) instead of the older Lohmann and Roeckner (1996) parameterization, which should be used for SOCOL-MPIOM. The switch to the correct parameterization reduced the cloud coverage dramatically, stabilizing temperatures at a much higher and more realistic level.

However, the precipitation pattern was still not satisfactory, showing a strong northward shift of the ITCZ and a general precipitation overestimation in the subtropics and an underestimation at the equator. The pattern very much resembled a systematic reduction of the incoming solar radiation at the equator, mirrored to a minor extent in the sub- and extratropics. It was only after an in-depth look at the boundary condition files that an erroneous volcanic forcing was found, which perpetually repeated the strong eruption of the year 1600 instead of prescribing the background stratospheric aerosol conditions. This lead to El Niño-like conditions and to a redistribution of tropical precipitation into the subtropics.

Due to the abovementioned bugs, the spin-up simulations were completed about a month later. Yet, they showed a reasonable stabilization of the ocean, which let us start the transient simulations. Unfortunately, a last but severe bug in the land surface

---

[c]This freshwater correction routine performed a calculation of the precipitation, evaporation and runoff fluxes into the ocean and - if the sum is not zero - redistributes the surplus of freshwater equally over all oceans.

forcing data forced us to stop all simulations in the 20th century due to an exaggerated surface warming. It later became apparent that the preprocessing of the land use (LU) boundary condition datasets was done erroneously after inverting a matrix row with a matrix line, therefore excluding "C4 natural grass", "tundra", "C3 pasture" and "C4 pasture" from the datasets. The temporally changing LU entails a change in albedo, and hence also of the cloud cover and global temperatures. This set the whole FUPSOL project back 5 months, but was also an opportunity for us to understand the impacts of varying boundary conditions on the model framework itself and on global climate.

After the correction of this last bug, all simulations were - successfully - ran a second time.

3.5 Available modeling environments and harddisk space

We initially planned to run all experiments on the proprietary "Brutus" cluster of the ETH. However, it became soon clear that the required CPU time, the overall CPU-burden and the subsequent risk of a very high queuing time would lead to an overbooking of the cluster by our group. As a result, applications were sent to the Swiss National Supercomputing Centre CSCS, located in Manno, to get additional computing power. The CSCS approved a wall time of 300 khrs over a project time of one year. Just after receiving confirmation from CSCS, a third cluster - Ubelix, located at the University of Bern - became available. In addition, the multiprocessor machine CALC2 was purchased by the PMOD/WRC in late 2011, and was released for the FUPSOL simulations. CALC2 first had to be configured to our needs, which included installing and testing different constellations of libraries and compilers. In the end, IFORT was chosen with the parallel computing library OpenMPI, which delivered the best and most stable results.

Unfortunately, the very complex architecture of the different machines at the CSCS hampered a quick operability of our model framework. Frequent changes in the compiler and library versions, as well as a major upgrade of the infrastructure (upgrade from Cray-XT5 to Cray-XE6) also delayed our simulations. Problems like the unability to run so-called Multiple-Program Multiple-Data (MPMD) frameworks on a single

node/blade on the main Cray-XE6 forced us to run our model on a postprocessing machine. But even there, despite the best efforts of the CSCS helpdesk, we had no success in running our model framework. Thus, we decided to shift our runs from the CSCS to Ubelix.

There, the model framework was very quickly put into operation, allowing us to run all necessary simulations simultaneously. We noticed that the computing time needed for one simulated model year varied depending on the usage of the cluster. Overall, however, calculations were done with approximately the same speed on Ubelix as on Brutus. On CALC2, due to the lesser amount of CPUs, the average speed was around 20% slower than on the Brutus and Ubelix clusters. However, as we were the only users of this machine, there was no queuing time. Table 3.1 illustrates the different configurations and speeds of the three environments.

The project was allocated 50 TB of harddisk space on a RAID 6 with twenty 3 TB disks, mounted on a postprocessing node (hydro.ethz.ch) at the IAC as well as 50 TB of backup space with the same RAID configuration on another postprocessing node (kryo.ethz.ch). The security of the data storage was thus maximized, at the expense of available space, which was reduced to 50 TB of the 100 TB available. To compensate, another 100 TB of space was allocated on Climstor, located at the University of Bern at the GIUB. However, the data were not saved redundantly on Climstor, as no backup was available (only RAID safety level).

3.6 Dataflow

A well-tailored and stable set of run- and postprocessing scripts was provided by the MPI Hamburg in the EaSyMS2011 package. However, the scripts had to be substan-

Table 3.1: Cluster configurations and average speed

Cluster	Configuration	Speed
Ubelix	AMD Opteron 2354, 16 GB RAM, RHEL6	5.5 h / year @ 64 CPU
Ubelix	Intel Xeon E5450, 16 GB RAM, RHEL6	5.5 h / year @ 64 CPU
Brutus	AMD Opteron 8380, 32 GB RAM, CentOS6	5.7 h / year @ 64 CPU
Brutus	AMD Opteron 8384, 32 GB RAM, CentOS6	5.7 h / year @ 64 CPU
CALC2	AMD Opteron 6180, 132 GB RAM, Debian 6	7.4 h / year @ 48 CPU

tially modified to our needs in order to get the chemistry part of the model both running and postprocessed. In order to securely archive all the simulation data from the production platforms Brutus and Ubelix to Hydro and finally to Kryo and Climstor, a proven dataflow following Figure 3.2 was set up.

- Step one: In the optimal case, the runscripts on Brutus and Ubelix are submitted manually to the queue once per experiment. The runscript is then responsible for the creation of the namelist, the adaptation of the next dates simulation, the linking of the input data to the "work" folder, and the simulation. In addition, the raw output from the model is handed over to the postprocessing script, which is also automatically launched by the runscript. The runscript re-submits itself for the next simulation period. The postprocessing handles the selection of the desired variables, the interpolation from model to pressure levels and finally also the computation of some diagnostic variables like the EP-fluxes or the residual mean circulation.

- Step two: Data are uploaded from Brutus/Ubelix to Hydro. On Hydro, all analysis and plotting routines are stored and used to classify the huge amount of data from the simulations. NCL scripting (NCAR/CISL/VETS, 2012) was preferred, but a quick analysis with FERRET, IDL or R was also done.

- Step three: Once per day, an incremental backup was done from Hydro to Kryo with rsync in order to keep a backup of all needed simulation data. The two systems are physically separated from each other, which increases the data security.

- Step four: Unused simulation data was regularly moved from Zürich to Bern via secure rsync onto the data tank of Climstor. The risk of data loss originating from a severe hard disk or RAID failure was accepted in favor of additional disk space.

3.7   Model forcing

In order to be able to run the model as a transient simulation from 1600 AD to 2100 AD, different datasets were needed. The challenge was to choose assumptions for anthropogenic and natural forcing data that were as realistic as possible. One one hand, for greenhouse gases (GHGs) or ozone depleting substances (ODSs), this is done relatively easily thanks to proxy reconstructions from ice cores (e.g., Petit et al., 1999). Stratospheric aerosol forcing data can also be traced back using ice core proxy
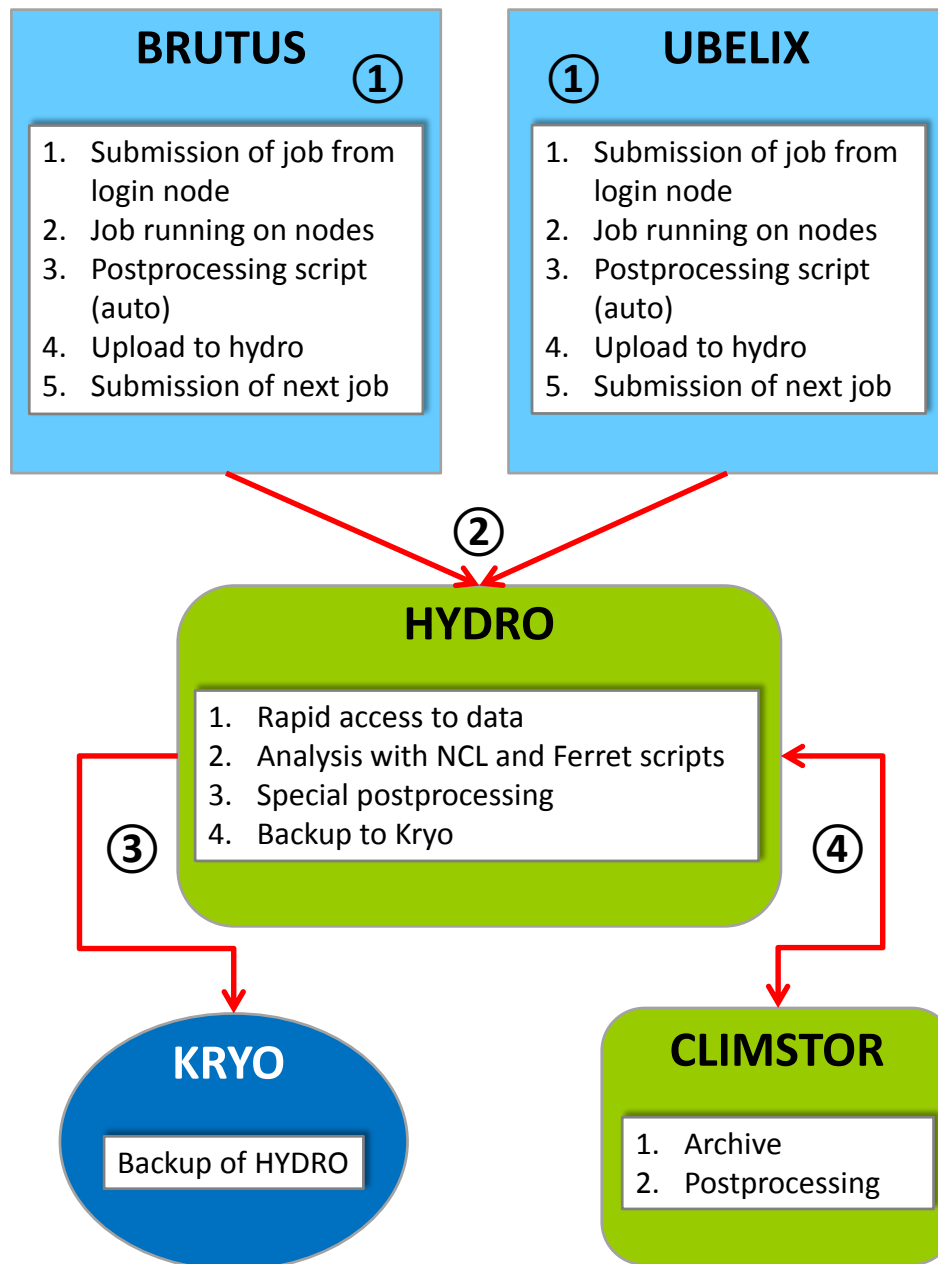
Figure 3.2: Dataflow and sequence of operations on the Brutus and Ubelix clusters, as well as on the hydro, kryo and climstor systems.

.

data, as after a strong volcanic eruption, the volcanic ash is spread over the entire globe. Over the poles, as the ash is deposited, it slowly gets compressed and isolated from the atmosphere during the ice formation process, making the reconstruction of past events possible. On the other hand, historic datasets for tropospheric aerosols,

land use data or wind fields of the quasi-biennal oscillation (QBO) need to be created by making various assumptions linked to the global population, for instance, as no other reliably proxies exist. The following sections provide a short overview of the different boundary conditions used in the simulations.

3.7.1 Solar forcing

Two total solar irradiance (TSI) reconstructions were available from our collaborators: The Steinhilber et al. (2009) reconstruction and the Shapiro et al. (2011) reconstruction, where the latter has recently been criticized for being too strong in amplitude (Feulner, 2011a). During the planning phase, the modelers estimation was that the Steinhilber et al. (2009) forcing could be too weak for our model, which led to the possibly courageous decision to force the simulations by using the middle and lowest amplitude values of the Shapiro et al. (2011) forcing. This forcing is based on the solar modulation potential (Φ) reconstructions, produced by ^{10}Be analysis from ice cores. The radiative forcing data is plotted in Figure 3.3 for the six bands of the SOCOL3-MPIOM radiation code. The amplitudes of the chosen forcing are indeed very high compared to other reconstructions like Lean et al. (1995), Bard et al. (2000) or Feulner (2011b). Moreover, the changes in UV over the grand minima and the 11-year solar cycle are some of the strongest (Ermolli et al., 2013). Yet, our choice proved to be the good one, as the model response to solar irradiance variations shows in Chapters 4 and 5.

For the photolysis rates, look-up tables which have been generated from the spectral solar irradiance (SSI) of Shapiro et al. (2011) are used.

3.7.2 Greenhouse gases and ozone depleting substances

The GHG and ODS forcings up to the year 1859 AD were taken form the Paleoclimate Modelling Intercomparison Project Phase III (PMIP3) protocol (Etheridge et al., 1996, 1998; MacFarling-Meure, 2004; Ferretti et al., 2005; MacFarling-Meure et al., 2006) data repository. CO_2 and CH_4 was reconstructed from the Law Dome Ice data (MacFarling-Meure et al., 2006), while N_2O was reconstructed from a spline fit through different ice cores, among them Dome C, GRIP, EUROCORE and H15 (Machida et al., 1995; Flückiger et al., 1999, 2002). All data can be found in the dataset from F. Joos,
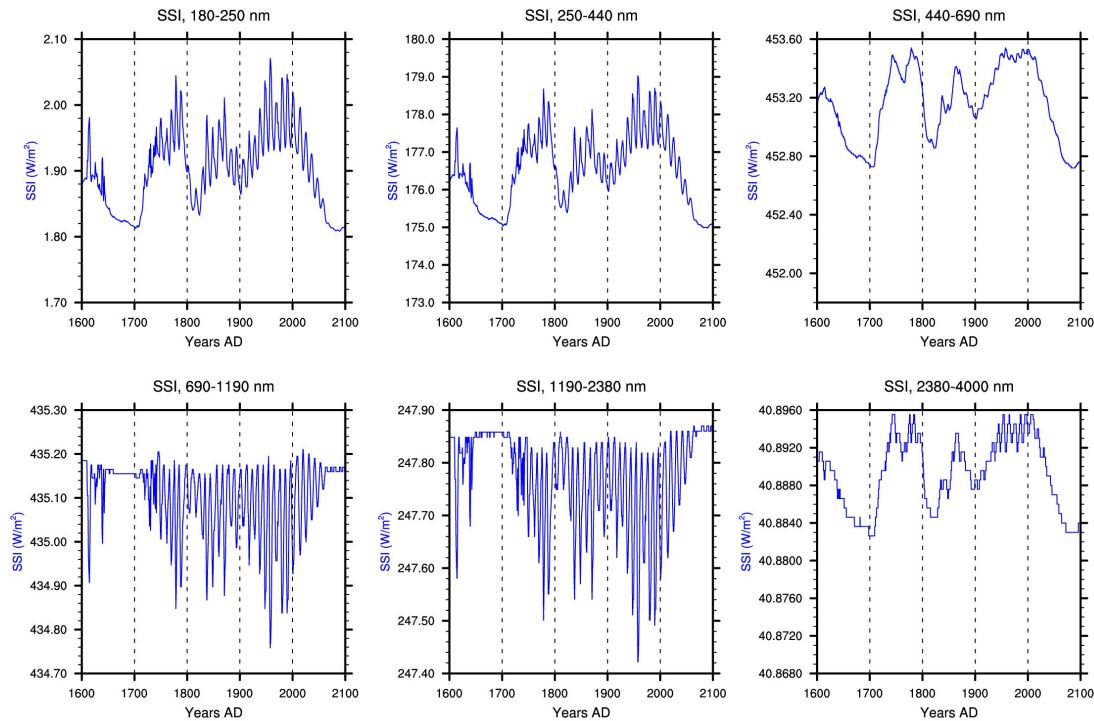
Figure 3.3: Spectral solar irradiance from 1600 AD to 2100 AD from Shapiro et al. (2011). From left to right, top to bottom: hard UV (185-250 nm, band 1), soft UV (250-440 nm, band 2), visible (440-690 nm, band 3), near IR (690-1190 nm, band 4), short-wavelength IR1 (1190-2380 nm, band 5) and short-wavelength IR2 (2380-4000 nm, band 6).

2007[d]. From the year 1859 AD until 2000 AD, the NASA GISS repository input data of the 2004 GCM simulation was used.

ODS were set to preindustrial values until the year 1930 AD and followed the NASA GISS recommendations until the year 2000 AD.

After the year 2000 AD, CMIP5 forcing data from IPCC's relative concentration pathway (RCP) 4.5 scenario were used for both GHG and ODS.

The GHG forcing is illustrated in Figure 3.4a.

---

[d]http://climate.uvic.ca/EMICAR5/data/ghg_lawdome_giss_merge_c5mip_24jul09.1-2000.txt
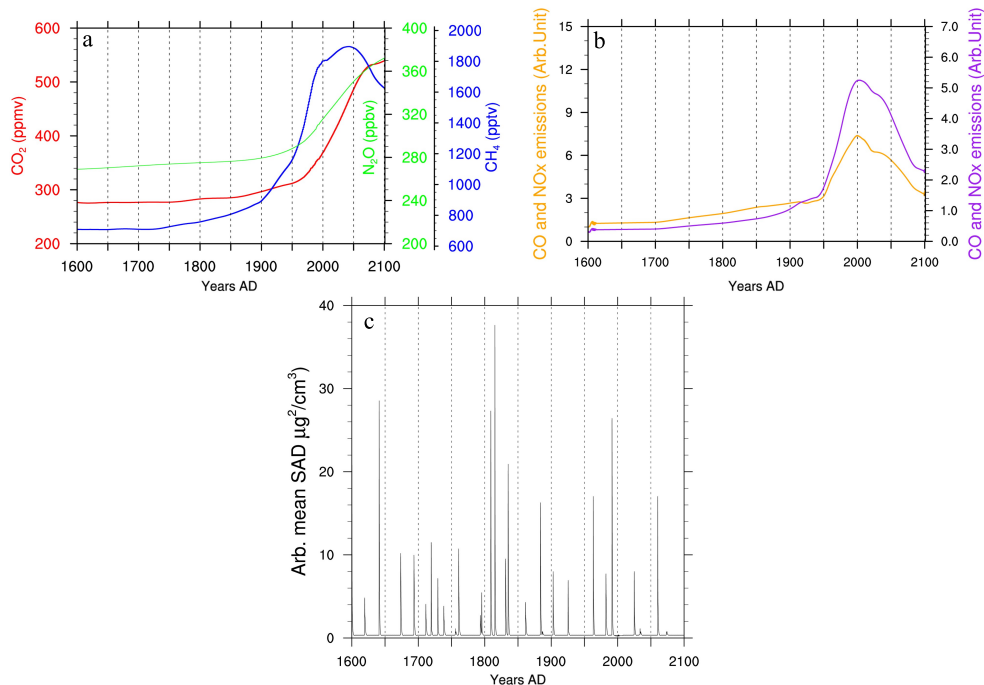
Figure 3.4: (a) Greenhouse gases CO_2, CH_4 and N_2O, (b) CO and NO_x, and (c) volcanic aerosol forcing from 1600 AD to 2100 AD

3.7.3 CO and NO_x emissions

Apart from the anthropogenic greenhouse gases, emissions like carbon monoxide and NO_x from activities such as international shipping, and aviation, as well as from biogenic sources, needed to be taken into account. The forcing data were taken from the CMIP5 datasets for the years after 1850 AD (Buhaug et al., 2009; Eyring et al., 2010; Lee et al., 2009; Lamarque et al., 2010). A linear phase-out of shipping emissions from 1850 AD backwards to the year 1800 AD was assumed, as no steamships existed before 1850 AD. For the CO and NO_x coming from biomass burning, it was assumed that 10% of the 1990 AD biomass burning is natural while the rest is anthropogenic. Thus the natural part was kept constant for the whole simulation period, while the anthropogenic part was scaled with the world population. The emissions (in arbitrary units) are illustrated in Figure 3.4b

For NO_x produced by lightning, the average NO_x production in an air column (Turman and Edgar, 1982) was distributed vertically with the vertical lightning profile from Pickering et al. (1998) and injected into the model.

3.7.4 Volcanic aerosols

For the forcing of the model from 1600 AD until 2000 AD, the well-established dataset from Gao et al. (2008, 2012) was used. These data were combined with information on the eruption column height (mostly based on existing literature on tephra dispersal, in some cases including estimations based on a simple 1D model of the volcanic plume). Gao et al. (2008) derived volcanic aerosol loadings from 54 ice cores, 32 from the Arctic and 22 from Antarctica. From this aerosol loading, aerosol optical depths (AOD) and other optical factors mapped on a latitude height grid were calculated by Arfeuille et al. (2013a) using the Atmospheric and Environmental Research Inc. (AER) model (Weisenstein et al., 1997).

For the 21st century, the volcanic forcing was chosen to mimic the natural variability. A Fuego-like eruption in 2024, a smaller eruption in 2033, an Agung-like eruption in 2060 and another small eruption in 2073 were set. The forcing data are illustrated in Figure 3.4c.

3.7.5 Tropospheric aerosols

Tropospheric aerosol datasets were produced following a two-step process. First, aerosol properties were produced by scaling existing CAM3.5 simulations with a bulk aerosol model driven by the CCSM3 (CMIP4) sea-surface temperatures and the 1850-2000 CMIP5 emissions (S. Bauer, pers. comm., 2011). As no reliable proxies are available for data before 1850, scaling had to be done using some assumptions. First, 10% of the 1990 emissions were believed to be natural and were kept constant over the whole simulation range. Moreover, a backward extrapolation was done from the year 1850 to the year 1600, scaling the emissions as a function of the world population.

3.7.6 Land surface

Land surface data were mapped from a reconstruction by Pongratz et al. (2008). Potential vegetation classes from Ramankutty and Foley (1999) were used in regions that are not anthropogenically influenced. Elsewhere, the vegetation was changed to crop or grassland according to the land-use (LU) reconstruction of (Pongratz et al., 2008). Following Hagemann et al. (1999) and Hagemann (2002), the vegetation classes were then converted to land surface parameters for ECHAM. From the initial T63 resolution,
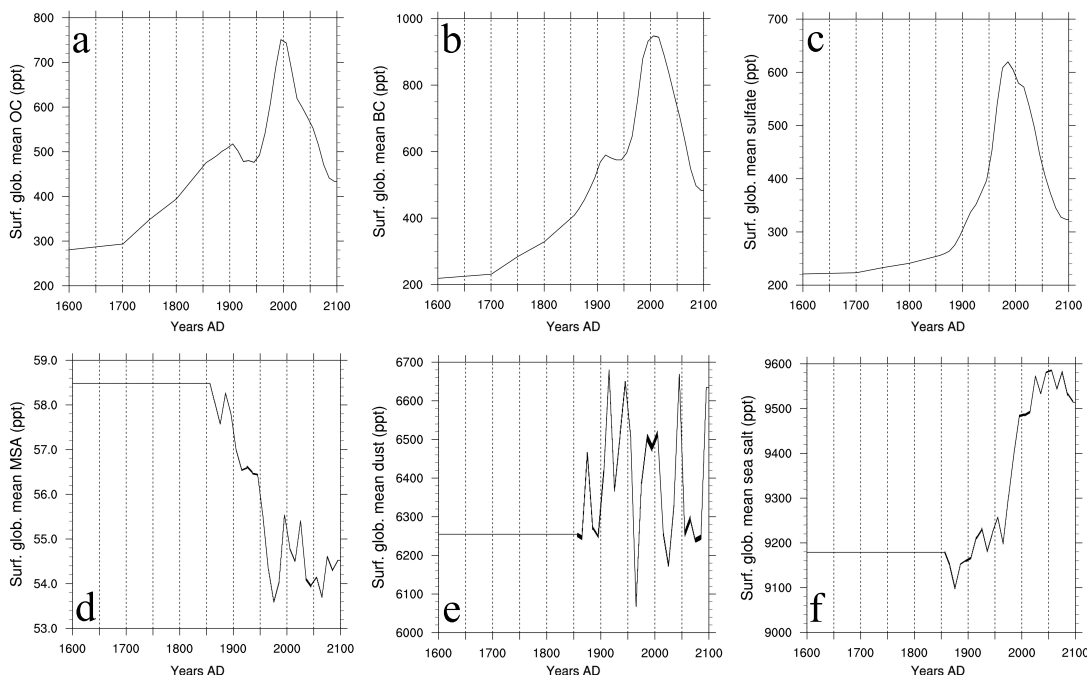
Figure 3.5: Tropospheric aerosol forcing from 1600 AD to 2100 AD, globally averaged on the lowest model level in ppt. (a) Organic carbon, (b) black carbon, (c) sulfate, (d) methane sulfonate, (e) mineral dust (0-2 μm), and (f) sea salt (0-10 μm)

all derived quantities such as albedo, roughness length, or leaf-area-index were then interpolated to the SOCOL3-MPIOM T31 model grid and linearly interpolated between the different times for which land-use reconstructions are available (see Pongratz et al., 2008, for further details).

3.7.7 QBO

Due to a relatively coarse vertical resolution of 39 levels, the model does not reproduce the quasi-biennial oscillation autonomously. To compensate this, reconstructed equatorial zonal mean wind fields are nudged to the model. These data were produced back to 1900 by Brönnimann et al. (2007). Using historical upper-level wind data, total ozone data from sonds and surface pressure data, Brönnimann et al. (2007) determined the QBO phase. Prior to 1909, however, the phase was not reconstructible due to lacking measurements. To produce QBO data for earlier periods, we decided to perpetually repeat an idealized QBO cycle (extracted from recent data), with an overlaid averaged annual cycle. The same approach was taken for the extension into the future

(Brönnimann et al., 2007).

3.7.8 Energetic particles

For the EPP parameterization, four datasets were needed, one for GCRs, one for SEPs, one for LEEs and one for the geomagnetic field position and strength.

Galactic cosmic rays are based on Φ, which was reconstructed by Steinhilber et al. (2008) using ^{10}Be proxy data. The dataset compares well with the neutron monitor measurements available since the year 1950. Using Φ, the pressure-latitude ionization rates by galactic cosmic rays are computed using the lookup tables from Usoskin et al. (2010). Φ is illustrated in Figure 3.6a.

For the parameterization of the LEE following the Baumgaertner et al. (2009) approach, the A_p index was used. An indicator for geomagnetic disturbances, the A_p index can be reconstructed back to the year 1932. For data before 1932, the A_p index was correlated with the A_a index, which has a longer history but is based on only two stations. The A_a index is available from 1868 to present. Using sunspot numbers, the A_a and A_p indexes can be reconstructed further back to the year 1600 via correlation. The A_p index is illustrated in Figure 3.6b.

For the period from 1963 to 2008, SEPs were prescribed using the Jackman data (see Jackman et al., 2009). However, due to their very short-lived nature, such events cannot be reconstructed before the satellite era from ^{10}Be or other proxies. Although Shea et al. (2006) presented a solution for reconstructing big events like the Carrington event from nitrate proxies, we did not use the method for our work because it is quite controversial (e.g., Wolff et al., 2012). We decided instead to use randomized SEPs for the years before 1963 by using a return period-based analysis of the last 45 years. The forcing data are illustrated in Figure 3.6c.

The paleo-magnetic datasets for the position and the strength of the geomagnetic field was provided by C. Finlay, 2011 at the request of F. Steinhilber. The included Schmidt Quasi- Normalized Spherical Harmonic (QNSH) (Jackson et al., 2000; Korte et al., 2009; Finlay et al., 2010) coefficients for the dipole and the quadruple at 5 year intervals 1600-2100 are required for computing the eccentric dipole model SOCOL3-MPIOM uses. The data were applied to the model in order to take into account the geomagnetic

dependency of the ionization. Changes in strength and position are illustrated in Figure 3.6 d, e and f.
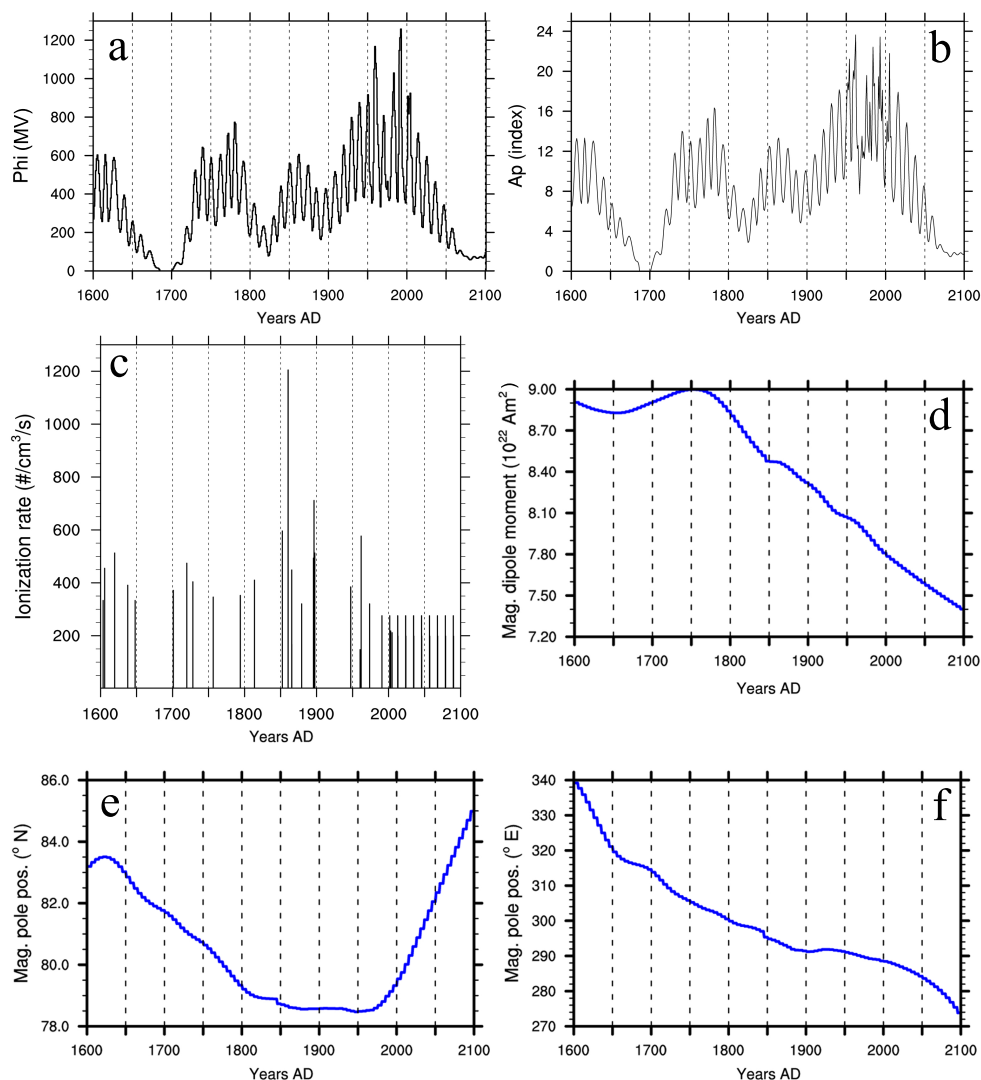
Figure 3.6: Forcing due to energetic particle precipitation from 1600 AD to 2100 AD. a) Φ in Megavolts, b) A_p index, c) ionization rate from solar proton events at 1 hPa height, d) magnetic dipole moment, e) latitudinal magnetic pole position, f) longitudinal magnetic pole position

3.8 Experiments

The intention of the original FUPSOL proposals was to perform 4 series of experiments in order to answer to these questions:

- Spin-up of the model framework: How long does it take to equilibrate the ocean of the new model?

- Transient simulation from 1600 AD to 2100 AD: Are the global temperature minima during the grand solar minima well represented? Do we succeed in reproducing the modern warming?

- Sensitivity studies for the Dalton minimum (DM): Which forcing (solar, energetic particles or volcanic) had the greatest influence on climate during the DM?

- Sensitivity studies for the 21st century: What effect will variations in all three forcing factors have on future climate, especially in view of a future grand solar minimum?

However, due to the difficulties discussed in section 3.3, the original plan had to be slightly modified. The future sensitivity runs in particular were reformulated. Instead of four different sensitivity experiments for the future, three experiments focused on solar variability were run, which will be explained later.

3.8.1 Spin-up

The general aim of a spin-up is as follows: When starting the model on a defined date, initial conditions are needed for the different fields like wind, temperature, humidity, ozone concentration and others. To avoid wasting memory, only a few dates, such as "preindustrial", "last glacial minimum" or "present time" are available for the initial conditions. The model therefore needs time to adapt to the period in which it has been "put" and will first need a "spin-up": The model spins-up in the sense that all atmospheric variables undergo a very strong drift in the first years of simulation and only stabilize several years into the simulation. The ocean, having a much longer life-time, needs incomparably more time to reach an approximate equilibrium in the temperature fields. We noticed that 200 years were the minimum spin-up time (equivalent to 12,800 CPU-hours).

Two nearly identical spin-up runs were done, their only difference being the solar forcing (and hence the photolysis rates). One run ("Bestguess") was forced by the average Shapiro et al. (2011) solar forcing, while the other run ("Scaled") was run with the upper uncertainty values of the Shapiro et al. (2011) solar forcing data. The Scaled run was forced with a TSI value about 2 W/m^2 higher than the Bestguess run during the spin-up.

3.8.2   Transient simulation from 1600 AD to 2100 AD

Four defined states, each with two members per forcing (Bestguess/Scaled) were chosen to start the transient runs. After 205 years of spin-up, the first members of Bestguess/Scaled were launched. The second members were launched 10 years later, after 215 years of spin-up.

Once again, the two experiments were identical to one another with the exception of the intensity of the solar forcing of Shapiro et al. (2011) (averaged reconstructed value versus lowest amplitude value of the entire uncertainty range). Both experiments were forced by the reconstructed solar forcing until the year 2000 AD and by a new grand solar minimum in the 21st century following the description in Section 3.8.4.

3.8.3   Sensitivity studies, Dalton Minimum

All DM sensitivity experiments, simulating the DM from 1780 AD to 1840 AD, were restarted using the first member of the Bestguess experiment from the transient simulations. In order to have a minimum amount of information regarding the uncertainty of the different sensitivity experiments, each experiment had three members, restarted with an ocean from the year 1779, 1780 or 1781[e].

The sensitivity runs were designed in the following way:

- In the control experiment, DM-CTRL1780, all forcing factors except GHG, ODS and tropospheric aerosols were kept to constant 1780 AD conditions.

- In the reference experiment, DM-ALL, all forcing factors varied over time.

---

[e]This is the standard procedure to disturb a AO-CCM, compared to the disturbances induced in a A-CCM only. There, to create such disturbances, the initial CO_2 concentrations are varied slightly during the first months of the run.

- The first solar sensitivity experiment, DM-TD (where TD means "Top-Down"), kept all forcing factors constant except for the first SSI band, the extra-heating parameterizations and the photolysis rates, which were allowed to vary over time.

- The second solar sensitivity experiment, DM-BU (where BU means "Bottom-Up"), kept all forcing factors kept constant except for the second to sixth SSI bands, which were allowed to vary over time.

- The volcanic sensitivity experiment, DM-VOLC, kept all forcing factors constant except for the stratospheric aerosols, which were allowed to vary over time.

- The EPP sensitivity experiment, DM-EPP, kept all forcing factors constant except for the energetic particle precipitation rates, which were allowed to vary over time.

3.8.4 Sensitivity studies, 21st century

The future sensitivity studies were, as already mentioned, redimensioned significantly due to the time lost in the beginning. Hence, apart from the two base runs Scaled and Bestguess, only one additional experiment was performed, called CONST. In contrast to the transient Bestguess and Scaled runs, which both simulated a strong decrease in solar irradiance due to a new grand solar minimum (see Figure 3.3), the solar forcing in the CONST run was kept constant from the year 2010 AD to the year 2100 AD, mimicking the solar cycles 22 and 23 perpetually.

Chapter 4

Forcing of stratospheric chemistry and dynamics during the Dalton Minimum

J.G. Anet[1], S. Muthers[2,3], E. Rozanov[1,4], C.C. Raible[2,3], T. Peter[1], A. Stenke[1], A.I. Shapiro[4], J. Beer[5], F. Steinhilber[5], S. Brönnimann[3,6], F. Arfeuille[3,6], Y. Brugnara[3,6], W. Schmutz[4]

[1]Institute for Atmospheric and Climate Science ETH, Zurich, Switzerland
[2]Climate and Environment Physics, Physics Institute, University of Bern, Bern, Switzerland
[3]Oeschger Centre for Climate Change Research, University of Bern, Bern, Switzerland
[4]Physikalisch-Meteorologisches Observatorium Davos and World Radiation Center (PMOD/WRC), Davos, Switzerland
[5]Eawag, Surface Waters group, Switzerland
[6]Institute of Geography, University of Bern, Bern, Switzerland

4.1 Abstract

The response of atmospheric chemistry and dynamics to volcanic eruptions and to a decrease in solar activity during the Dalton Minimum is investigated with the fully coupled atmosphere-ocean-chemistry general circulation model SOCOL-MPIOM covering the time period 1780 to 1840 AD. We carried out several sensitivity ensemble experiments to separate the effects of (i) reduced solar ultra-violet (UV) irradiance, (ii) reduced solar visible and near infrared irradiance, (iii) enhanced galactic cosmic ray intensity as well as less intensive solar energetic proton events and auroral electron precipitation, and (iv) volcanic aerosols. The introduced changes of UV irradiance and volcanic aerosols significantly influence stratospheric dynamics in the early 19th century, whereas changes in the visible part of the spectrum and energetic particles have smaller effects. A reduction of UV irradiance by 15 %, which represents the presently discussed highest estimate of UV irradiance change caused by solar activity changes, causes global ozone decrease below the stratopause reaching 8 % in the midlatitudes at 5 hPa and a significant stratospheric cooling of up to 2 °C in the midstratosphere and to 6 °C in the lower mesosphere. Changes in energetic particle precipitation lead only to minor changes in the yearly averaged temperature fields in the stratosphere. Volcanic aerosols heat the tropical lower stratosphere allowing more water vapor to enter the tropical stratosphere, which, via HO_x reactions, decreases upper stratospheric and mesospheric ozone by roughly 4 %. Conversely, heterogeneous chemistry on aerosols reduces stratospheric NO_x leading to a 12 % ozone increase in the tropics, whereas a decrease in ozone of up to 5 % is found over Antarctica in boreal winter. The linear superposition of the different contributions is not equivalent to the response obtained in a simulation when all forcing factors are applied during the DM – this effect is especially well visible for NO_x/NO_y. Thus, this study also shows the non-linear behavior of the coupled chemistry-climate system. Finally, we conclude that especially UV and volcanic eruptions dominate the changes in the ozone, temperature and dynamics while the NO_x field is dominated by the EPP. Visible radiation changes have only very minor effects on both stratospheric dynamics and chemistry.

4.2 Introduction

The fourth assessment report of the Intergovernmental Panel on Climate Change (Forster et al., 2007) noted that while the scientific understanding of the greenhouse gas (GHG) emissions and volcanic effects on climate is rather high, this is not the case

for changes in solar activity. The combined forcings of GHG and tropospheric aerosols is predicted to increase until possible stabilization is reached in the second half of the 21st century. The volcanic effect is unpredictable. Concerning solar activity, it is hypothesized that solar activity will – after a long period of high activity – drop to a new grand minimum in the 21st century (Abreu et al., 2008, 2010; Lockwood et al., 2011b; Steinhilber and Beer, 2013). Given this, an assessment of periods in the past containing grand solar minima is helpful to understand the mechanism and its implications. As an example, the Dalton Minimum (DM) was a time period lasting from 1790 to 1830 which was characterized by a significant cooling in Europe (Luterbacher et al., 2004) and the extratropical Northern Hemisphere (Ljungqvist, 2010; Auchmann et al., 2012). This unusually cold time coincides with the period of very low solar activity as expressed in low sunspot numbers (Hoyt and Schatten, 1998) and high volcanic activity due to two major volcanic eruptions in 1809 and in 1815. The exact causes of this cooling are not well defined. Some part of it can be explained by downward propagating stratospheric perturbations (e.g. Ineson et al., 2011). We thus decided to study this period and address the solar and volcanic effects on stratospheric climate and chemistry. Up to now, studies of the DM were done to a major part with climate models with coupled interactive oceans. The novelty of our experiment setting was to include interactive chemistry to a GCM coupled to a deep layer ocean. We succeeded thus to include the most important natural forcing in a climate model simulation during the DM: (a) solar irradiance changes, which can be decomposed into a ultraviolet (UV), visible and infrared (IR) part of the spectrum, (b) explosive tropical volcanic eruptions and (c) energetic particle precipitation (EPP).

Solar activity has been monitored for a long time (Wolf, 1861; Hoyt and Schatten, 1998). The influence of the Sun on time scales of up to hundreds of years can first be divided in two temporal classes: there is a regular, well established 11 yr cycle (Wolf, 1861; Schwabe, 1844) – which can vary in its intensity – and on the longer time scale there are grand minimum and maximum states of the solar activity.

Solar influence can be further classified in terms of where the biggest effects can be observed in the Earth's atmosphere. This is strongly linked to the part of the spectrum with the largest variability. Kodera and Kuroda (2002) investigated the effects of the 11 yr solar cycle on atmospheric dynamics, focusing on the UV part of the spectrum. Their work suggests a downward propagation of the response in the middle atmosphere caused by heating through UV absorption and ozone increase. In solar active conditions, this additional heating leads to an increasing pole-to-equator temperature gradient, influencing also the stratospheric zonal winds (Kodera and Kuroda, 2002). This process is known as the top-down-mechanism (e.g. Meehl et al., 2009;

Gray et al., 2010). A different aspect is to focus rather on the visible spectrum and to follow a bottom-up-approach (Meehl et al., 2009): during solar active conditions more evaporation occurs in the subtropics. This in turn leads to an increase in the precipitation amount, which accelerates the Hadley and Walker cells (Labitzke et al., 2002), finally leading to ENSO-like anomalies and influencing stratospheric circulation. Using reconstructions of the solar irradiance like the ones from Lean et al. (1995), these two processes have been studied extensively in the last years using models of different complexity (see Gray et al., 2010 and references therein).

The fact that volcanoes can influence global climate has already been recognized in Franklin (1784) and Milham (1924). While Franklin (1784) mainly focused on the effect on the troposphere, which, after the Lakagigar (Laki) eruption, was polluted by a large amount of particles, partly leading to a constant haze, Milham (1924) focused on the Tambora eruption and the uncommon weather pattern following the eruption. In the twentieth century, partly because of four major volcanic eruptions (Agung in 1963, Fuego in 1974, El Chichón in 1982, Pinatubo in 1991), more intense scientific research was done, focusing especially on the radiative effects of stratospheric aerosols (see Hansen et al., 1992; Stenchikov et al., 1998; Robock, 2000, and references therein). The plume of powerful volcanic eruptions reaches the stratosphere (Halmer et al., 2002). There, SO_2 is transformed through a number of chemical reactions to sulfate aerosols. Aerosols at lower stratospheric altitudes (Whitten et al., 1980) are mostly spherical (Tratt and Menzies, 1994) and scatter back to space part of the incoming solar short-wave radiation. On the other hand, sulfate aerosol absorb thermal radiation. The aerosol particles also provide a media for heterogeneous reactions facilitating the removal of reactive nitrogen oxides and activation of halogen radicals. Thus, volcanic aerosols are important for both radiative and chemical processes in the atmosphere.

Reconstructions of the volcanic forcing (Gao et al., 2008) have been used to model past and modern influences of volcanic events on global climate. Generally, following observations and modeling studies, while the lower stratosphere is heated by absorption of infrared radiation by the aerosols, the troposphere and the surface usually experiences a significant cooling after major volcanic eruptions (Dutton and Christy, 1992; Minnis et al., 1993; Stenchikov et al., 1998; Arfeuille, 2012). The interaction with chemistry is more complex due to the effects of enhanced halogen loading in modern times (Tie and Brasseur, 1995). In a clean preindustrial atmosphere, a significant globally averaged increase of total column ozone can be expected within one to three years after a volcanic eruption, whereas at the equator, ozone column depth is decreasing slightly (Arfeuille, 2012). In a halogen-contaminated atmosphere of today, global ozone concentration drops significantly after a volcanic eruption. The resulting heating leads to major

changes in the atmospheric dynamics and large-scale oscillation patterns like El Niño, Arctic Oscillation (AO) or North Atlantic Oscillation (NAO) (Robock, 2000; Stenchikov et al., 2002; Yoshimori et al., 2005; Wagner and Zorita, 2005; Christiansen, 2007; Fischer et al., 2007; Spangehl et al., 2010).

The influence of EPP on climate is – compared to the other two aforementioned factors – a rather new subject to science and has been investigated increasingly often during the last twenty years. Its effect is still not well known and a quite controversial issue in the climate change discussion (Marsh and Svensmark, 2000; Laut, 2003; Lockwood and Fröhlich, 2007; Erlykin et al., 2013). This disagreement is also a reason why EPP have not been included in important climate model simulation campaign in support of WMO and IPCC assessments (WMO, 2011; Forster et al., 2007). The EPP can be divided into three main categories: galactic cosmic rays (GCRs), solar protons and high- and low energetic electrons (HEE, LEE). All of them can ionize neutral molecules in the Earth's atmosphere.

The GCRs are highly energetic charged particles. They originate from supernova explosions in our galaxy and their flux and energy spectrum at the entry of the heliosphere is very stable over millenial timescales, only being modulated by the solar activity, which is shielding the Earth from them via magnetospheric deflection (see e.g. Scherer et al., 2004). The observed GCR flux variability thus follows the cycles of the solar magnetic activity. GCRs are highly energetic particles, often relativistic with energies reaching several GeVs (Bazilevskaya et al., 2008), being capable in influencing our atmosphere in important ways: GCRs dissipate their energy mainly by ionization processes. Following a Bragg-peak (Bragg and Kleeman, 1905), the maximal ionization rate by GCR is reached between 15 km and 20 km altitude (Usoskin et al., 2010). The ionization is largest in the polar regions (poleward of $\pm 60°$) where the geomagnetic field has the weakest shielding effect (lowest cut-off rigidity).

Solar protons events (SPEs) emerge from coronal mass ejections of the sun, which occur very irregularly and are rarely directed towards the Earth. Hence, SPEs are very sporadic and hardly predictable. The solar wind plasma usually reach the Earth's atmosphere within 1–2 days after the ejection (Kahler, 1992). The charged particles are directed towards the poles, where they follow the lines of the geomagnetic field into the atmosphere. Only in extreme cases – when their energies reach 500 MeV or more – they can propagate down to the stratosphere (Jackman et al., 2008). As a result of the magnetic shielding, the effect of SPEs is strongly latitude dependent with a minimum equatorward of $\pm 20°$ and a maximum poleward of $\pm 60°$.

LEEs and HEEs originate from the interaction of the Earth's magnetospheric plas-

masheet with the solar wind (Brasseur and Solomon, 2005). Solar plasma is kept trapped in the magnetosphere of the Earth and can be accelerated during periods of higher solar wind speeds. The accelerated electrons then rapidly travel along the magnetic field lines to the poles and partly penetrate the uppermost layers of the atmosphere (Bazilevskaya et al., 2008). The best evidence for their existence are the aurorae, formed by the excitation of nitrogen and oxygen atoms.

Ionization of oxygen and nitrogen lead to NO_x and HO_x production.

In the stratosphere, while HO_x has a short life-time in the range of minutes to hours and thus affects atmospheric chemistry only locally, reactive nitrogen (NO_y) and its members nitric acid or chlorine nitrate have lifetimes comparable to or even longer than the characteristic times for vertical and horizontal mixing occurring for instance via the Brewer-Dobson circulation (BDC). In the stratosphere, NO_x and HO_x interact with ozone in a significant way, as was found by analyzing important ionization events (Callis et al., 1998; Funke et al., 2011). Changes in ozone concentration inside the polar vortex modify the pole-to-equator temperature gradient and thus can have a significant influence on circulation and weather patterns (Gray et al., 2010). Different modeling studies demonstrated the influence of EPP not only on chemistry (Jackman et al., 2008; Baumgaertner et al., 2009; Egorova et al., 2011; Calisto et al., 2011; Rozanov et al., 2012b) but also on dynamics (Baumgaertner et al., 2009; Calisto et al., 2011; Rozanov et al., 2012b).

Climate during the DM minimum has already been simulated with general circulation models (GCM) in a number of studies (Bauer et al., 2003; Wagner and Zorita, 2005; Ammann et al., 2007; Spangehl et al., 2007; Arfeuille, 2012). While Bauer et al. (2003) only used a simplified model, Wagner and Zorita (2005) and Spangehl et al. (2007) exploited a coupled atmosphere–ocean GCM (AO-GCM). Arfeuille (2012) used the chemistry-climate model (CCM) SOCOL to simulate the effects of the Tambora volcanic eruption in 1815 on climate and found a strong geopotential height gradient anomaly (around 250 gpm) between 55°N and 75°N at 50 hPa in the first winter after the eruption (November–April) as well as a net radiative forcing anomaly reaching -8 W/m^2 (60°S–60°N) during the first five months following the eruption. Thus, volcanic influences and solar Grand Minima are generally accepted as main drivers for global climate cooling. Wagner and Zorita (2005) also investigated the contribution of the slightly increasing GHG concentrations during the DM and did not find any significant impact.

In this paper, we investigate the effect of different natural factors on global stratospheric climate during the DM with a fully interactive atmosphere–ocean-chemistry climate model (AO-CCM). To the best of our knowledge, no coupled AO-CCM with EPP

parametrization has yet been used for an in-depth analysis of the climate and chemistry state during the DM so far. This is also a reason why a comparison and a validation of our model simulation is nearly impossible to do: Although investigations of the influence of EPP on modern climate have been done (Calisto et al., 2011; Rozanov et al., 2012b), the far higher CFC content nowadays makes it difficult to compare the effect on the chemistry and especially on ozone. Concerning the effects of volcanic eruptions, e.g. the work of Arfeuille (2012) can give some hints how an other model (the former model version SOCOLv2 without interactive ocean) has simulated the Tambora eruption. Yet, exact numbers in ozone disturbance are sparse and thus also here, a validation of our results is difficult.

The description of the model framework is done in Sect. 4.3. In Sect. 4.4 we describe the chemical and dynamical changes in the stratosphere. In the last chapter, we discuss and summarize the findings of this work.

4.3 Description of the model and experimental setup

4.3.1 AO-CCM SOCOL3-MPIOM

The AO-CCM SOCOL3-MPIOM emerges from the coupling of the CCM SOCOL3 (Stenke et al., 2013) and the ocean model MPIOM (Marsland et al., 2003) with the OASIS3 coupler (Valcke, 2013). SOCOL3 consists of the chemistry module MEZON (Model for Evaluation of oZONe trends, Rozanov et al., 1999; Egorova et al., 2003; Schraner et al., 2008) which is coupled to the GCM MA-ECHAM5 (Roeckner et al., 2003). Atmospheric temperature fields are passed to MEZON, which computes the tendencies of 41 gas species, taking into account 200 gas phase, 16 heterogeneous, and 35 photolytical reactions. Once computed, the chemical tendencies are handed back to ECHAM5, which then takes care of the transport of species. The simulations were run in T31 spectral resolution, which is equivalent to a grid spacing of around 3.75°. The vertical spacing is irregular, as the model uses hybrid sigma pressure coordinates on 39 levels from 1000 hPa up to 0.01 hPa (80 km). The chemistry scheme is only called every two hours – simultaneously with the radiative scheme – in order to be computationally efficient.

Due to this relatively coarse vertical resolution the Quasi-Biennial-Oscillation (QBO) is not reproduced autonomously by the GCM. To reproduce the QBO, the equatorial zonal wind field is nudged to reconstructed data in the same manner as described in Giorgetta

(1996).

The original ECHAM5 radiation code does not properly treat solar spectral irradiation forcing (Forster et al., 2011), therefore extra-heating correction factors (Zhu, 1994) for the Lymann-α line, the Schumann–Runge, Hartley and Huggins bands as well as for the Herzberg continuum were implemented. The radiation code was also modified in such a way that ECHAM5 reads in spectrally resolved solar irradiance in the six ECHAM5 short-wave bands with varying distribution instead of the standard fixed distribution of the varying total solar irradiance into the six bands.

Parametrization of the different EPPs was done identically to Rozanov et al. (2012b) and ref. therein, with the only difference that the code has been modified for use in SOCOLv3. Highly energetic electrons (HEE) was not included in the model. To include the magnetic dependency of the ionization by EPP, a temporal, locally changing dipole magnetic field was implemented in the model using geomagnetic proxy data as input.

4.3.2   Boundary conditions

The model is forced by several boundary conditions described in the following section.

The GHG concentrations for the 1780 to 1840 period of carbon dioxide, methane and nitrous oxide are based on the Paleoclimate Modelling Intercomparison Project Phase III (PMIP3) protocol (Etheridge et al., 1996, 1998; MacFarling-Meure, 2004; Ferretti et al., 2005; MacFarling-Meure et al., 2006). Halogen containing species were kept constant to preindustrial levels.

All forcings influenced by the activity level of the Sun were based on the solar modulation potential reconstructions produced from ^{10}Be records from ice cores: for the spectral solar irradiance forcing we use the reconstruction of Shapiro et al. (2011). In Fig. 4.1, the radiative forcing data is plotted for the six bands of ECHAM5 radiation code. The main difference between this reconstruction and the former ones like Lean et al. (1995) or Bard et al. (2000) is the amplitude of the variability. For example, the difference between the maximum and the minimum TSI value during the DM is roughly 6 W/m^2 whereas in e.g. Lean et al. (1995), the drop was only by 2 W/m^2. For the photolysis rates, look-up tables are used which have been generated from the spectral solar irradiance (SSI) of Shapiro et al. (2011).

Several different datasets were used for the energetic particles. For the parameterization of NO$_x$ influx, Baumgaertner et al. (2009) used the A$_p$ index which can be reconstructed until the year 1932. The A$_p$ index can be correlated with the A$_a$ index,
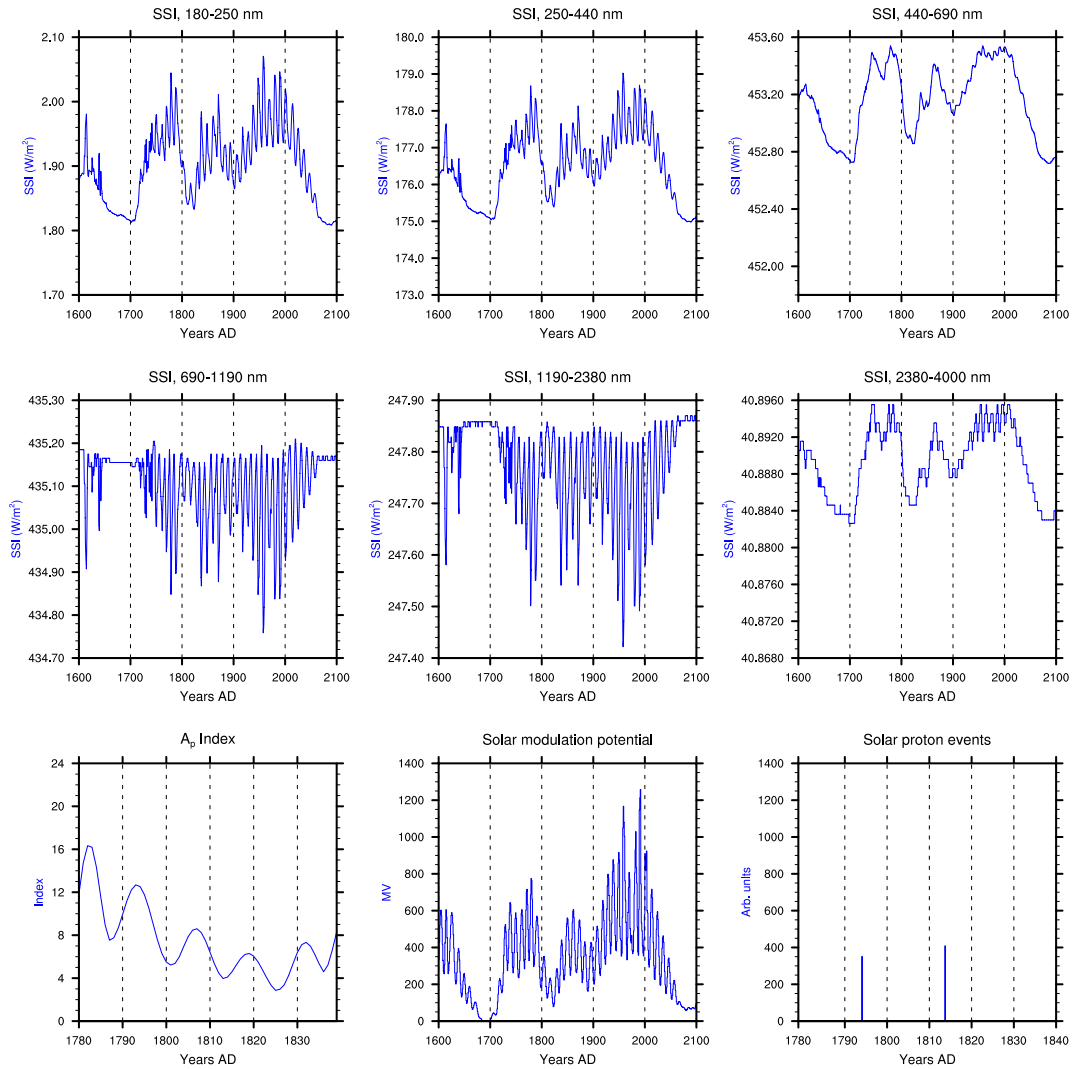
Figure 4.1: Shapiro et al. (2011) and A_p-index, solar modulation potential and SPE during the DM. From left to right, top to bottom: hard UV (185–250 nm, band 1), soft UV (250–440 nm, band 2), visible (440–690 nm, band 3), IR-A (690–1190 nm, band 4), IR-B (1190–2380 nm, band 5), IR-C (2380–4000 nm, band 6), A_p-index, Solar modulation potential (Φ), and SPEs.

which has a longer history but is only based on two stations. It is available from 1868 to present. Based on sunspot numbers, the A_a and A_p indexes can be reconstructed via correlation until the year 1600. SPEs were prescribed from an existing SPE data set (provided by Charles Jackman and covering the period 1963–2008, see Jackman et al., 2009). SPEs are very short-lived (in the order of days), thus such events cannot be reconstructed from proxies like ^{10}Be, which are usually used. Shea et al. (2006)

presented a solution to reconstruct big events like the Carrington event from nitrates deposited in ice cores. This method is however very controversial (Wolff et al., 2008; Schrijver et al., 2012). In our work, SPEs are randomized for the years before 1963 by using a return-period based analysis of the last 45 yr, and weighted this result with the A_p index. Cosmic rays are based on the solar modulation potential (Φ), which has been reconstructed by Steinhilber et al. (2008). The dataset compares well with the neutron monitor measurements which are available since the year 1950. Φ is an index which describes the solar modulation of the cosmic ray flux, which can be converted into pressure-latitude ionization rates using lookup tables from Usoskin et al. (2010). Paleo-magnetic datasets (C. Finlay, personal communication, 2010) are applied to the model in order to take into account the geomagnetic dependency of the ionization.

Stratospheric aerosol properties are prescribed according to the approach applied by Arfeuille et al. (2013a) who used the Atmospheric and Environmental Research Inc. (AER) model (Weisenstein et al., 1997) constrained with ice core-based estimates of sulphate aerosol mass (Gao et al., 2008, 2012). From those simulations, zonally averaged aerosol optical properties (spectrally resolved) and surface area density forcing data for SOCOL3-MPIOM were extracted. The most important volcanoes during the DM period where two weak eruptions (1 and 3 Mt SO_2) in 1794 and 1796 with unknown locations (probably extra-tropical), a strong unknown tropical eruption of 27 Mt SO_2 in 1809, the 55 Mt SO_2 Tambora eruption in 1815 and two eruptions (8.5 Mt and 20 Mt SO_2) – the Babuyan Claro in 1831 and the Cosiguina in 1835.

Uncertainties in historical long-term volcanic aerosol datasets can be large, with more challenges than for the representation of the well observed Pinatubo 1991 eruption. Indeed, the lack of atmospheric observations leads to uncertainties arising from ice-core measurements and calibrations, and from the implementations of volcanic dataset, which generally involve further assumptions (e.g. altitude and size distributions of the aerosols). The volcanic forcing applied here is based on an aerosol model for the calculation of these variables, and the strengths of this method for the depiction of the aerosol latitude/altitude/size distributions for eruptions in the pre-satellite period are described in Arfeuille et al. (2013a). As many CCMs, also SOCOL tends to overestimate the stratospheric warming following the Pinatubo eruption (Eyring et al., 2006; Lanzante, 2007), and the AER-based SOCOL simulation of the Pinatubo eruption (Arfeuille et al., 2013b) suggests that AER-SOCOL might also overestimate the stratospheric warming due to the eruptions in the Dalton minimum. While this issue is one of the current uncertainties for the representation of volcanic impacts in the pre-satellite period, it can be noted that in the important tropical tropopause region, SOCOL forced by AER leads to a good representation of temperature after the Pinatubo eruption, even in

better agreement with observations than many GCMs forced by satellite-based aerosol datasets.

Tropospheric aerosol properties were constructed by scaling the existing CAM3.5 simulations with a bulk aerosol model driven by CCSM3 (CMIP4) sea-surface temperatures and the 1850–2000 CMIP5 emissions (S. Bauer, personal communication, 2011). For data before the year 1850, the applied scaling is a function of the world population except for 10 % of the presumed 1990 biomass burning aerosols which were considered natural.

The model was forced by the standard (Hagemann et al., 1999; Hagemann, 2002) land surface datasets provided with the ECHAM5 package.

Finally, equatorial zonal mean zonal winds for nudging the QBO were generated from backward extension of the Brönnimann et al. (2007) reconstructions using an idealized QBO cycle plus a seasonal anomaly cycle.

4.3.3   Experiments

To investigate the influence of solar, volcanic and the EPP forcings, we perform a series of three-members ensemble sensitivity experiments described in Table 4.1. We initialize our runs in the year 1780 from a transient simulation starting in 1388 AD. While the first ensemble member is run with unperturbed initial 1780 conditions, the two following members are initialized with an ocean field of the year 1781 and 1779. Every experiment covers 60 yr to reach December 1840. The analyzed period is chosen from 1805 to 1825 in order to reduce the noise and strengthen the signal from volcanic, solar

Table 4.1: Experiments for DM sensitivity runs: CONST values are 1780 monthly mean values. BCKGRD means that only background aerosol emissions were enabled while volcanic eruptions were turned off. TRANS means transient forcing.

Name	UV	VIS	Volcanic	EPP	Photolysis	Extra Heating
DM-CTRL1780	CONST	CONST	BCKGRD	CONST	CONST	CONST
DM-ALL	TRANS	TRANS	TRANS	TRANS	TRANS	TRANS
DM-TD	TRANS	CONST	BCKGRD	CONST	TRANS	TRANS
DM-BU	CONST	TRANS	BCKGRD	CONST	CONST	CONST
DM-VOLC	CONST	CONST	TRANS	CONST	CONST	CONST
DM-EPP	CONST	CONST	BCKGRD	TRANS	CONST	CONST

and particle forcings. The small number of ensemble members is chosen to reduce the computational time needed for the simulations.

To address the relative roles of the UV, visible and infrared radiation as well as the extra heating and the photolysis rates, the two experiments called DM-TD (top-down) and DM-BU (bottom-up) are designed. In DM-TD, all forcing data is kept constant except (i) the first radiation band (UV) of ECHAM5 radiation code, (ii) the coefficients of extra-heating parameterization as well as (iii) the photolysis rates. Hence, all forcing comes from the stratosphere only because the response of the heating rate in the second band of ECHAM5 radiation code (250–440 nm) to the solar variability is very small (Forster et al., 2011). The opposite experiment, DM-BU, is designed in a way that all forcing is kept constant except in the 2–6 bands of the ECHAM5 radiation code. Hence, DM-BU does not include any stratospheric heating or ozone production changes, meaning that all extra radiation is absorbed mostly in the troposphere and by the surface. In turn, the DM-VOLC runs are driven with all forcings kept to constant 1780 conditions except the volcanic forcing. The DM-CTRL1780 runs are performed with perpetual 1780 conditions, whereas the DM-ALL runs are driven with all forcings in transient conditions. To address the effect of energetic particles, we carry out the DM-EPP experiment which is forced only by the parameterizations for GCR, SPE and LEE, while all other forcings are set constant or switched to background aerosol concentrations (volcanic forcing).

4.3.4   Method of comparison

In the next section we analyze 60 yr long time series of annual zonal mean quantities constructed from the results of three 20 yr long ensemble runs for each experiment. The statistical significances were calculated using the two-tailed Student's t test using the 5 % significance level, comparing all 60 yr long time series for each experiment. All figures illustrate the relative or absolute deviation of the results of the experiment runs relative to the control run (DM-CTRL1780). On all plots, the yellow line indicates the height of the dynamical WMO tropopause. The nonlinearities are computed in a following way: Differences of DM-TD, DM-BU, DM-VOLC and DM-EPP relative to DM-CTRL1780 are computed and added. This field is then compared to the difference field between DM-ALL and DM-CTRL1780. A positive value in the nonlinearity plot would mean, that the stacked relative differences are greater than the combined from DM-ALL. Nonlinearities are only discussed when the sum of the contributions and the combined modelled effect are significantly different.

If not noted differently, the upper left figure of every panel illustrates the overall effect of

all factors (DM-ALL), followed by the effects of UV solar irradiance (DM-TD), volcanic aerosols (DM-VOLC) and energetic particle precipitation (DM-EPP). As a reduction of the visible and infrared radiation in the DM-BU experiment has small effects on the stratospheric chemistry, these results are not shown in the chemical section.

4.4 Results

4.4.1 Atmospheric chemistry

In this section, we focus on four species: ozone, water vapor, HO_x and NO_x, as they show the most pronounced response to the considered factors.

4.4.1.a Ozone

Figure 4.2a shows the relative effect of DM-ALL including all factors – namely reduction of solar radiation, volcanic eruptions and EPP – with respect to the control simulation (DM-CTRL1780). Substantial ozone depletion is found almost everywhere reaching its maximum (-8%) in the upper tropical mesosphere and middle stratosphere over the high latitudes. However, the opposite response is simulated in the polar upper mesosphere and tropical upper troposphere/lower stratosphere (UT/LS) regions where the ozone mixing ratio increases by up to 15%.

Figure 4.2b shows that mainly the effects of the solar UV reduction in DM-TD are responsible for the ozone loss at ozone layer height and for the gain of ozone in the polar upper mesosphere. These ozone changes in the atmosphere can be explained mostly by three factors:

1. The decrease in solar UV irradiance which reduces the ozone production via oxygen photolysis in the stratosphere and NO_2 photolysis in the troposphere,

2. The increase of NO_x (see Fig. 4.5, Sect. 3.1.3), which facilitates the intensification of the NO_x cycle of ozone oxidation (Reactions 1–3),

$$NO + O_3 \longrightarrow NO_2 + O_2 \tag{R1}$$

$$NO_2 + O \longrightarrow NO + O_2 \tag{R2}$$
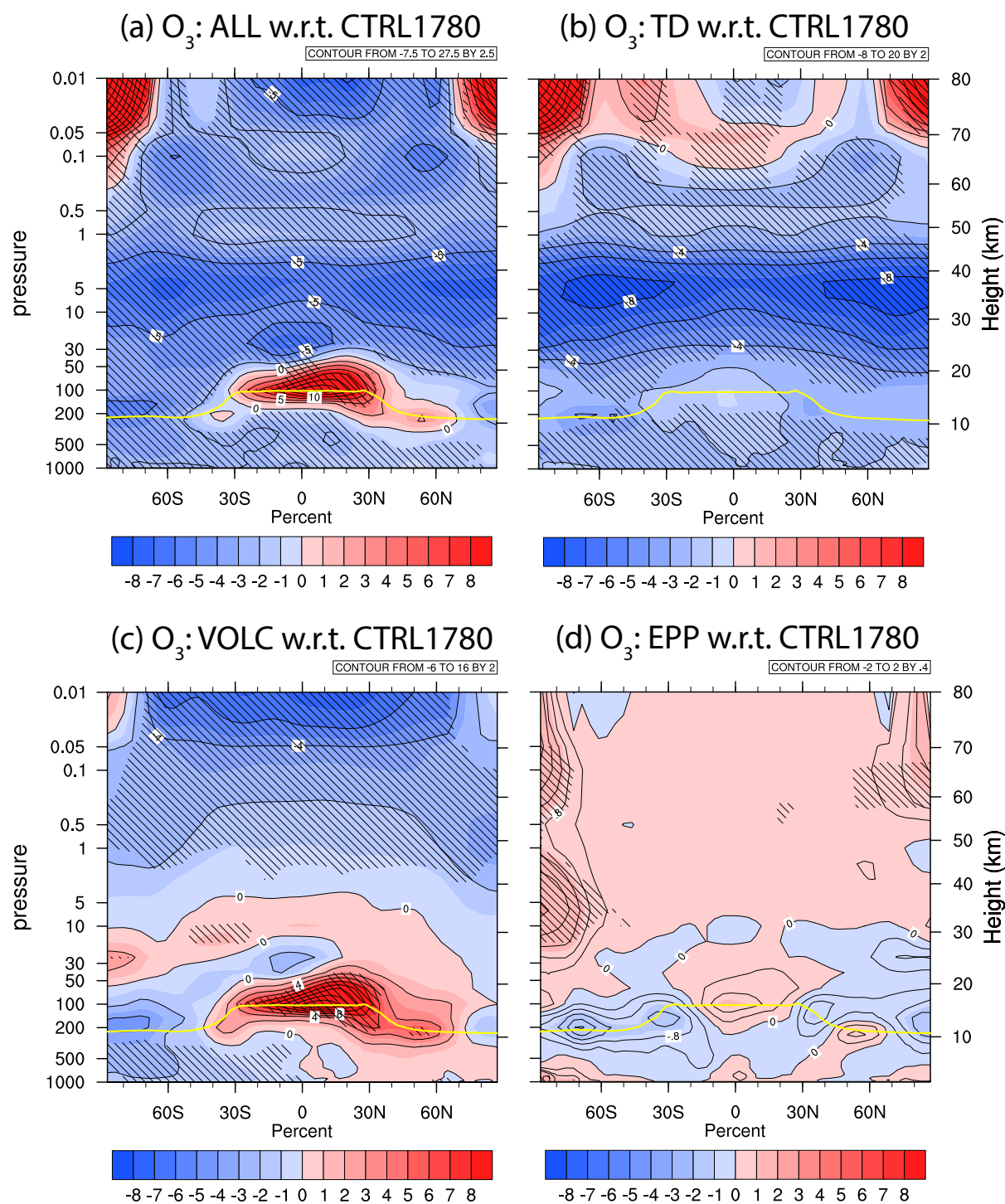
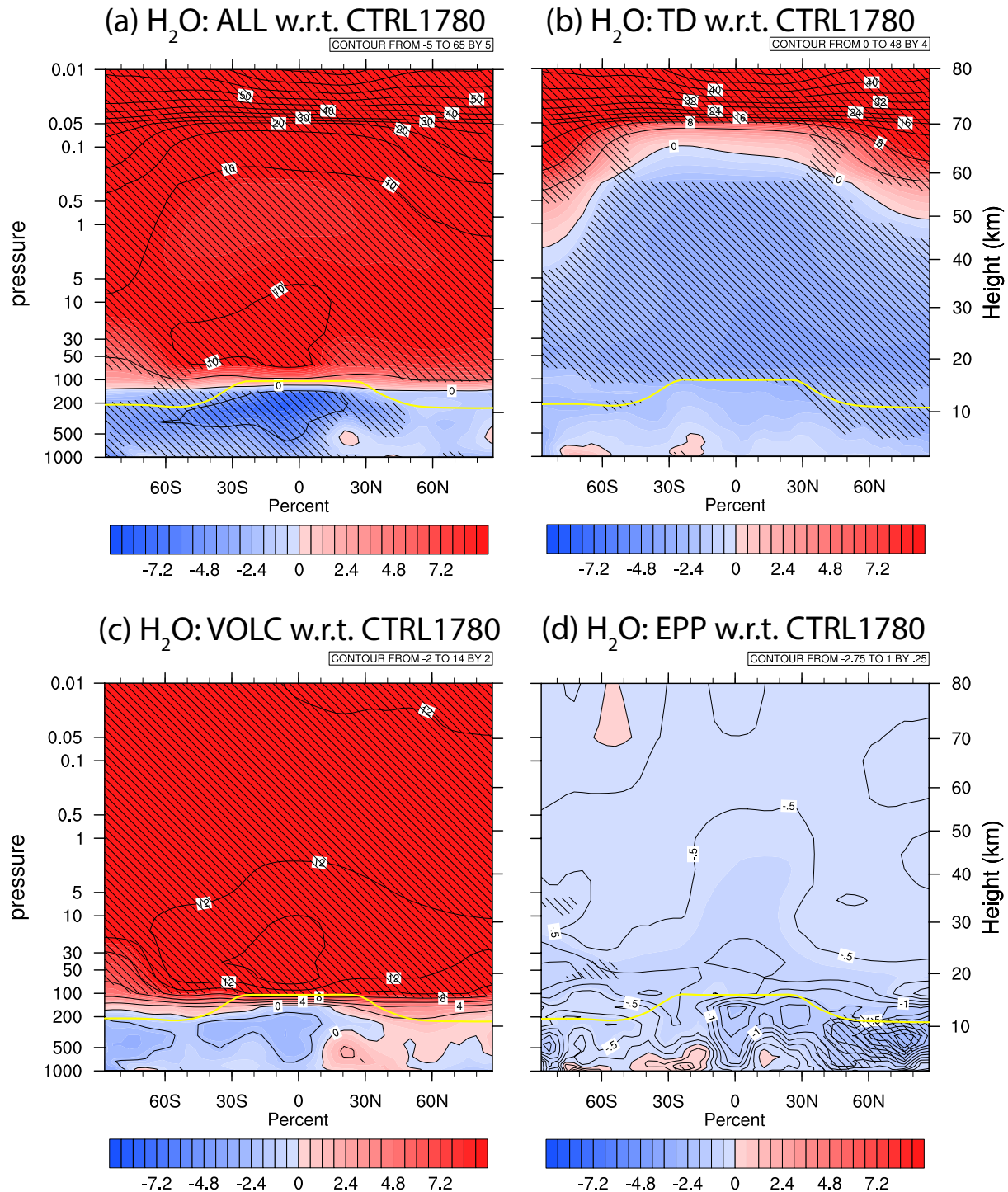Figure 4.2: Relative differences of yearly mean ozone of the DM-ALL, DM-TD, DM-VOLC and DM-EPP experiments with relation to the DM-CTRL1780 forcing run. Hatched areas are significantly different on a Student's t test with $\alpha = 5\,\%$. The yellow line illustrates the height of the WMO tropopause.

Net:

$$O_3 + O \longrightarrow 2\,O_2 \tag{R 3}$$

3. The slight compensation of the abovementioned ozone depletion processes due to the stratospheric cooling caused by reduced solar UV and ozone mixing ratio, slowing down the ozone destruction cycles (see Sect. 3.2.1).

At the poles in lower mesospheric height (60–80 km) a surplus of ozone by up to 20 % is explained by the fact that at these heights, the UV radiation acts like a sink rather than a source of ozone. Thus, with less UV radiation, near the mesopause, ozone destruction is supressed.

The surplus of ozone at the tropical tropopause can be explained by volcanic effects with the DM-VOLC experiment (see Fig. 4.2c). The main reason for the ozone increase in the tropical UT/LS after volcanic eruptions is the transformation of NO_x to N_2O_5 and the subsequent hydrolysis of N_2O_5 to HNO_3 via heterogeneous reactions on/in the sulfuric acid particles, formed in the stratosphere from the products of the volcanic eruptions. In the present day atmosphere, ozone depletion was observed after major volcanic eruptions and attributed to catalytic reactions involving reactive halogens. However, a potentially significant background of natural chlorine and bromine existed. The effect of this background, to cause ozone depletion, would have been dominated by nitrogen deactivation on sulphate aerosol. Therefore the heterogeneous conversion of HO_x and NO_x to relatively passive reservoir species leads to ozone increase to up to 16 %. The decrease of ozone in the mesosphere is related to the strong increase of the HO_x species at that height (see Sect. 3.1.2.) leading to an acceleration of the ozone depletion cycle.

Energetic particles can influence the ozone concentration, as shown in Rozanov et al. (2012b). Although our NO_x field looks very similar to the one from the cited work (see Sect. 3.1.3), the ozone response to EPP in the polar mesosphere is much weaker in our simulations. The main reason for this finding is that background temperatures in the involved regions are different in SOCOLv3 from SOCOLv2. Though, the reaction of nitrogen with oxygen is highly temperature dependent (Funke et al., 2011). Thus, only a minor part of the signal seen in Fig. 4.2a can be attributed to EPP: the annual mean ozone anomaly shows an ozone decrease of up to 2 % in the southern extra-tropics, which is due to the ionization of nitrogen by GCRs. The change is however only significant on a 10 % level. Over the poles, in the lower mesosphere, a significant

increase of ozone of up to 2 % is simulated due to the lower ionization rates of both SPEs and LEEs, leading to less NO_x (see later). Seasonal variations are visible. The biggest effect is modeled in austral spring (SON, see Figure S 4.1 in the appendix), where significant losses of ozone at UT/LS level of up to 4 % are found in the southern polar latitudes.

The temporal evolution of ozone at 70 hPa (Figure S 4.2 in the appendix) and at 1 hPa (Figure S 4.3 in the appendix), averaged between 20°N–20°S, are illustrated in the supplement. They show that while at the tropical tropopause height, especially the volcanic events dominate in the overall signal, it is the solar signal which dominates over all at 1 hPa height (blue curve of DM-TD experiment inducing a negative anomaly visible in the pink DM-ALL curve). Other forcing factors which are not of importance at 70 hPa height have not been plotted.

4.4.1.b HO_x and water vapor

In Figs. 4.3a and 4.4a the differences in water vapor and HO_x between DM-ALL and DM-CTRL1780 are illustrated. While water vapor concentration increases dramatically above the tropopause, HO_x is experiencing an increase in tropical UT/LS and a decrease in the mesosphere and middle tropical stratosphere.

The results of the DM-TD experiment illustrated in Fig. 4.3b and Fig. 4.4b help to attribute the H_2O increase and HO_x loss in the mesosphere to the introduced decrease of solar UV irradiance. A strong (by up to 25 %) HO_x decrease in the mesosphere coinciding with pronounced increase of H_2O is driven by less intensive water vapour photolysis in Lyman-alpha line and Schumann–Runge bands. When looking at the highest levels of the model atmosphere, one recognizes that HO_x decreases less in the lower mesosphere than at stratopause levels (see Fig. 4.4b). This can be explained by looking at the increase of the water vapour content in Fig. 4.3b. As water vapour is more prominent in periods of decreasing UV radiation above 60 km, due to the decrease in photodissociation, production of OH via reaction with $O(^1D)$ is more likely. Moreover a cooling of the upper troposphere/lower stratosphere (UT/LS) of 0.1 K decreases the stratospheric water content by 2 %. Hence, as the mean decrease of temperature at UT/LS height (shown in the dynamics section) in our DM-TD run is of around 0.2 K, a decrease of roughly 4 % of the stratospheric water content is to be expected – and modeled. This drop is the reason for the observed decrease in HO_x below 65 km down to the tropopause of 4 % on average.

To explain the strong increase of water vapour above the tropopause, a look at the

Figure 4.3: Relative differences of yearly averaged water vapour of the DM-ALL, DM-TD, DM-VOLC and DM-EPP experiments with relation to the DM-CTRL1780 forcing run. Hatched areas are significantly different on a Student's t test with α = 5%. The yellow line illustrates the height of the WMO tropopause.
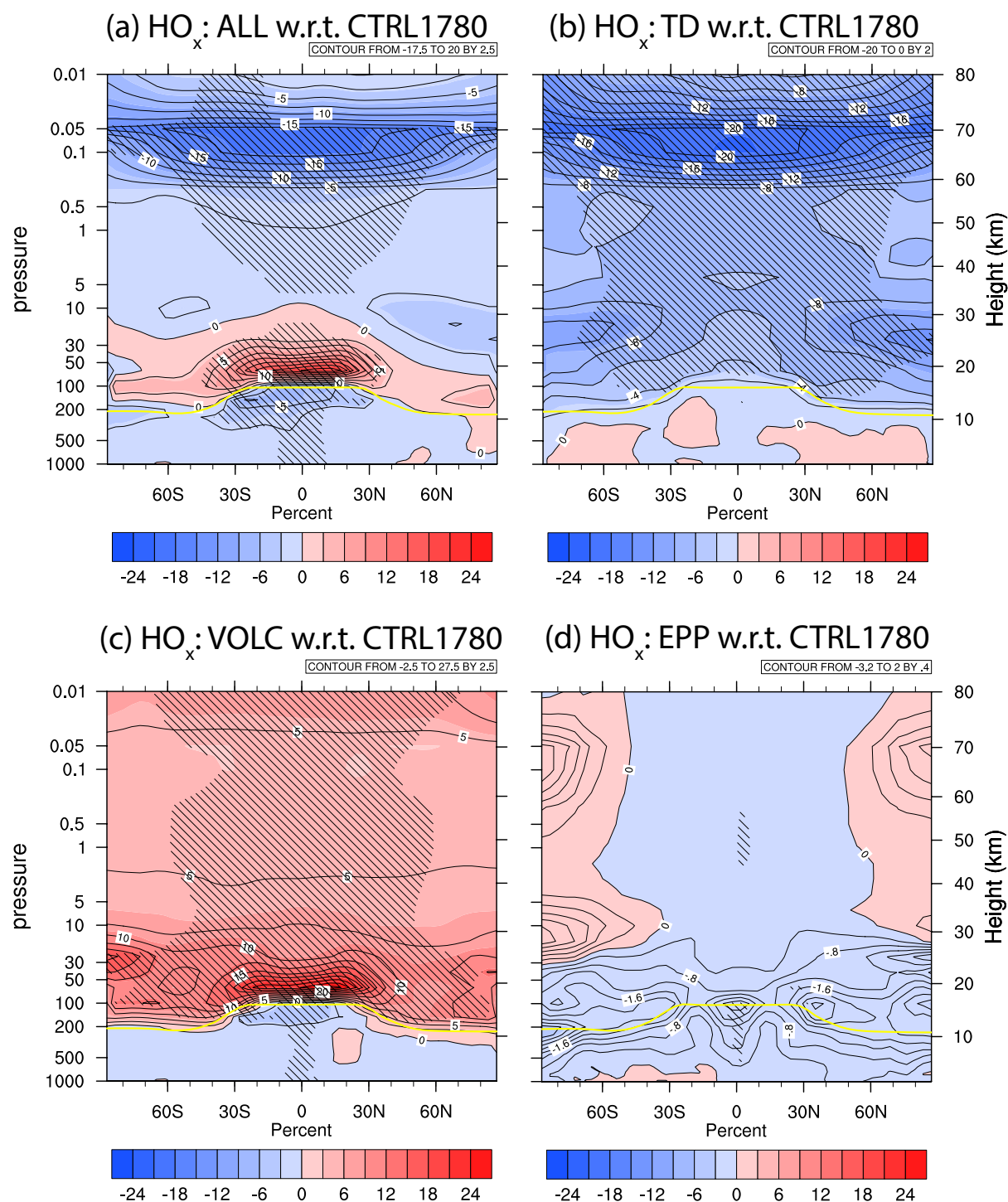
Figure 4.4: Relative differences of yearly averaged HO$_x$ of the DM-ALL, DM-TD, DM-VOLC and DM-EPP experiments with relation to the DM-CTRL1780 forcing run. Hatched areas are significantly different on a Student's t test with α = 5%. The yellow line illustrates the height of the WMO tropopause.

results of the DM-VOLC experiment (see Fig. 4.3c) is needed. Due to a warming signal (which will be shown in Section "Temperature"), a strong (of up to 14 %) increase in the stratospheric water content is modelled even when the results are averaged over 20 yr long period (see Robock, 2000). It is interesting to note that in the two years after Tambora, simulated water vapor contents raised by up to 60 % at the tropical tropopause. Such a strong increase in water vapor content leads to an acceleration of reactions

$$H_2O + O(^1D) \longrightarrow OH + OH \tag{R4}$$

$$H_2O + h\nu \longrightarrow H + OH \tag{R5}$$

in the lower mesosphere and stratosphere. Hence, an increase in HO$_x$ throughout the whole stratosphere and mesosphere (see Fig. 4.4c) is observed, with peak increases over the equatorial tropopause. The increase in HO$_x$ leads to a speed-up in oxidation of long-lived species like methane or CO.

In a clean and unpolluted atmosphere, a surplus of nitrogen oxides automatically leads to the drop of HO$_x$ concentrations. In Fig. 4.4d the additional NO$_x$ produced (see next subsection) from the GCRs decrease the amount of HO$_x$ slightly. These changes are marginally significant on a 5 % level but highly significant on a 10 % level in the tropical regions of the largest ionization rates (around 100 hPa). A decrease of HO$_x$ of up to 3 % – during the absolute minimum of the DM even of up to 8 % – is simulated by our model. This decrease is supported by the slight additional decrease of 0.5 to 1 % in the stratospheric water vapour content (Fig. 4.3d).

4.4.1.c NO$_x$

In the DM-ALL experiment, the NO$_x$ mixing ratio dramatically decreases in the polar mesosphere by up to 70 % and – with a much smaller magnitude – also in the tropical middle stratosphere. In the tropical upper troposphere and in the stratosphere, increase in NO$_x$ is found (see Fig. 4.5a) reaching its maximum in the upper tropical stratosphere/lower mesosphere. The latter can be explained by the smaller solar UV forcing in the DM-TD experiment (see Fig. 4.5b). The reduction in the solar UV irradiance leads to a pronounced decrease of the photolysis rates for all species including nitrogen oxide (NO). The NO absorption bands overlap with the oxygen Schumann–Runge bands
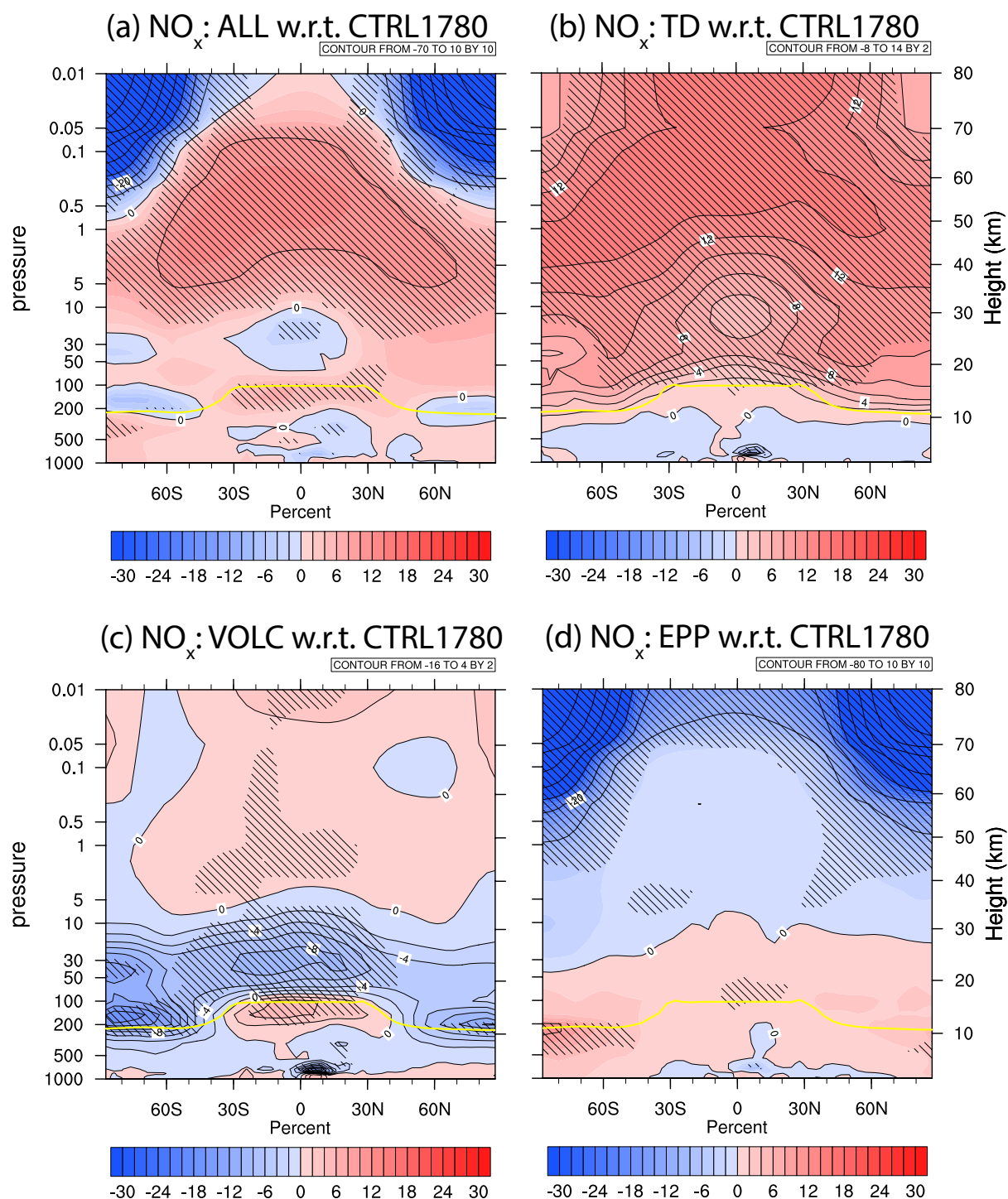
Figure 4.5: Relative differences of NO_x of the DM-ALL, DM-TD, DM-VOLC and DM-EPP experiments with relation to the DM-CTRL1780 forcing run. Hatched areas are significantly different on a Student's t test with α = 5%. The yellow line illustrates the height of the WMO tropopause.

(170–200 nm) and the introduced decline of the solar irradiance in this interval is one of the most pronouned (Shapiro et al., 2011). The NO photolysis ($NO + h\nu \rightarrow N + O$) plays a crucial role in the NO_y budget providing pure loss of NO_y via the subsequent cannibalistic reaction ($N + NO \rightarrow N_2 + O$) which explain the overall NO_x increase in the DM-TD experiment.

The dipole structure in the tropical UT/LS is explained by the influence of the volcanic eruptions. The volcanic sulfate aerosols provide a media for a number of fast heterogeneous reactions. For the clean stratosphere during the DM, the most important reactions was the N_2O_5 hydrolysis which facilitates the conversion of active nitrogen oxides to rather passive nitric acid. This effect is shown in Fig. 4.5c which illustrates the results of the DM-VOLC experiment. A significant NO_x decrease over the DM period is observed in this experiment above the tropopause over the tropics and high latitudes where the aerosol abundance is at maximum. The causes for a small NO_x increase in the tropical upper troposphere are not clear, probably it is related to the ozone increase in this area which leads to an enhanced NO_x production via $N_2O + O(^1D) \rightarrow NO + NO$.

As expected, most of the changes in NO_x seen in Fig. 4.5a is dominated by energetic particles (see Fig. 4.5d). The NO_x influx parameterized as the function of A_p index weakened in intensity during the DM leading to NO_x decrease by up to 80 %. Particles with higher energies – to a large part GCRs, whose flux was higher during the DM – penetrate deeper into the atmosphere. At tropopause levels, up to 6 % more NO_x at the poles and of up to 2 % more NO_x at the equator is produced by GCRs. While an increase in NO_x concentrations above 50 km has only a small effect on the ozone layer, NO_x production at lower altitudes may lead to an acceleration of the destruction of ozone via reactions 1–3. This insight could be of high importance for the possible future decrease in solar activity in the current century (see Anet et al., 2013b). The NO_x-anomalies compare well to those found in Rozanov et al. (2012b). The reason why the positive change in NO_x is not reflected in Fig. 4.5a is that conversion to NO_y occurs due to the additional amount of stratospheric aerosols from the volcanic eruptions. In DM-ALL, a strong decrease in NO_y is seen over the whole tropopause region.

The NO_x field is a good example to show the non-linear behavior of atmospheric chemistry (see Fig. 4.6a). Superimposing all relative differences of all experiments, the mesospheric polar regions from the stacked DM-BU, DM-TD, DM-VOLC and DM-EPP result in significant differences of up to 15 % more NO_x compared to DM-ALL. The NO_x field in the lower stratosphere over the northern extratropics shows also a significant positive anomaly of 2–4 % more NO_x. The analysis of the NO_y field in Fig. 4.6b shows an even more pronounced anomaly when superimposing all differences of all contributions

(a) NO$_x$: Non-linearities   (b) NO$_y$: Non-linearities
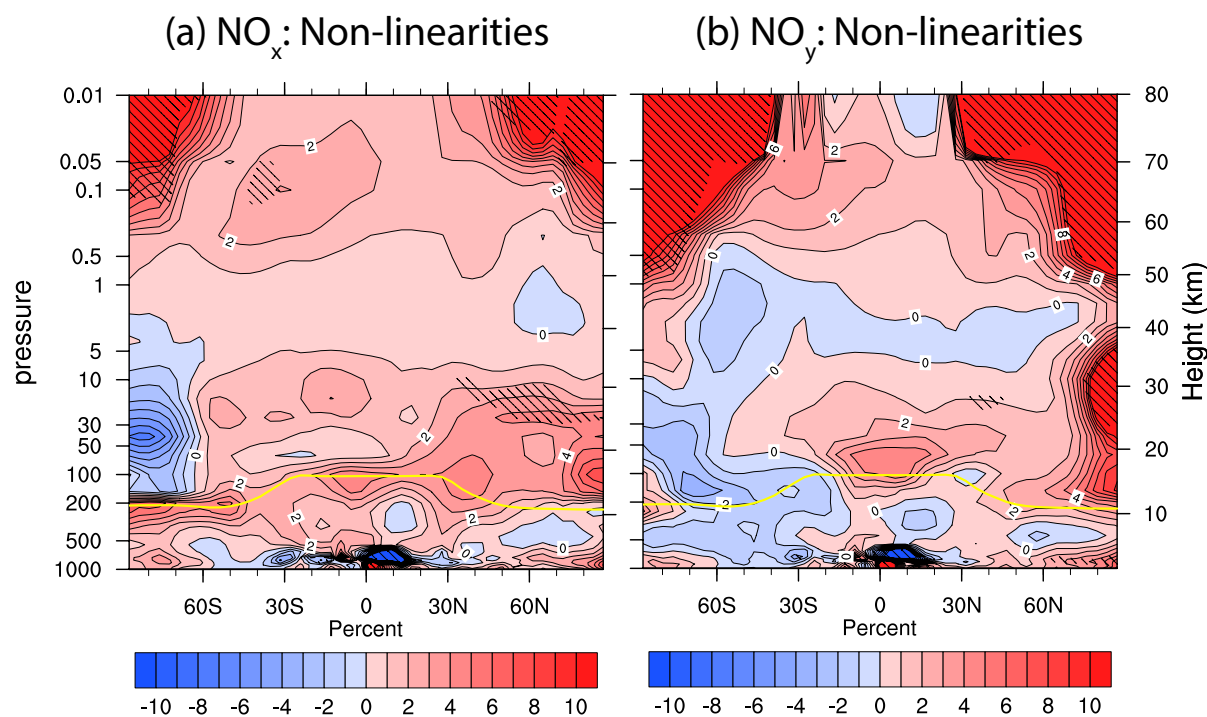
Figure 4.6: Differences between the DM-ALL vs. DM-CTRL1780 field and the (DM-TD + DM-BU + DM-VOLC + DM-EPP) vs. DM-CTRL1780 field. Positive values show a positive anomaly of the stacked differences over the DM-ALL difference field. Hatched areas are significantly different on a Student's t test with $\alpha = 10\%$. The yellow line illustrates the height of the WMO tropopause.

together and comparing this result to the DM-ALL field: values of up to 25 % more NO$_y$ in the mesospheric polar atmosphere and in the northern polar midstratospheric region are reached. These differences stem partly from the NO-photolysis, which was kept to constant 1780 values during the DM-EPP run. As well, the additional cooling during the DM-VOLC run resulted in NO$_x$ deactivation over the poles, which could not happen during the DM-TD run.

The temporal evolution of NO$_x$ at 70 hPa (Figure S 4.4 in the appendix) and at 1 hPa (Figure S 4.5 in the appendix), averaged between 20°N–20°S, are illustrated in the supplement. The main signal at 70 hPa height again – as for ozone – is dominated by the volcanoes. The remaining forcings are relatively unimportant at this height and have not been plotted. At 1 hPa height, it is the solar signal which is dominant, although spikes do appear in volcanic periods. The latter anomalies however go back to normal values 1–2 years after the volcanic eruptions. A negative NO$_x$ anomaly due to EPP is not yet visible at this altitude.

4.4.2 Stratospheric dynamics

In this section we present the changes of the stratospheric temperature and winds during the DM and identify the contribution of all considered factors.

4.4.2.a Temperature

As it is shown in Fig. 4.7a, during the DM the model simulates cooling in the entire atmosphere except the lower tropical stratosphere. The cooling gradually increases with altitude from 1 K in the middle stratosphere around 25 km up to 8 K near the mesopause. A slight enhancement of the cooling is also visible in the lower polar stratosphere. Weaker cooling of up to 0.6 K occurs below 100 hPa maximizing in the tropical upper troposphere.

Figure 4.7b shows the temperature changes due to implied decrease of visible and infrared solar irradiance (experiment DM-BU) and demonstrates that this factor is producing a weak cooling in the troposphere and in the upper stratosphere. The tropospheric cooling is explained by less energy income to the surface, while the cooling in the stratosphere is most likely caused by the decrease in available solar radiation for the ozone absorption in the Chappuis band. The temperature changes due to solar UV irradiance (experiment DM-TD) are illustrated in Fig. 4.7c which shows that this factor plays the dominant role in the cooling of the atmosphere above 25 km. The results shown in Fig. 4.7d demonstrate that the influence of volcanic eruptions has a more complicated spatial pattern. The volcanic aerosols produce a strong warming of up to 2 K at around 20 km in the tropical and subtropical region. The volcanic aerosol is able to absorb infrared solar and terrestrial radiation (Stenchikov et al., 1998, e.g.). The obtained strong warming in the lower tropical stratosphere means that the increased absorption of the terrestrial radiation by volcanic aerosols dominates over the absorption of the solar radiation, which should lead to a cooling due to the introduced decrease of the solar activity during the DM. As discussed in the introduction, this warming effect may be overestimated by our AO-CCM in the lower stratosphere, while at the tropopause there are good chances that our model – forced by AER data – reproduces an accurate warming right after the eruption. The warming in the UT/LS region explains the strong increase of water vapour in the stratosphere which was illustrated in Sect. 3.1.2 The cooling in the upper part of the model domain is explained by the blocking of the outgoing terrestrial radiation by the aerosol layer leading to a decrease of the energy incoming in these layers. The dipole-like structure of the temperature changes over the polar regions would hint on the intensification of the polar night jets: this suspicion is
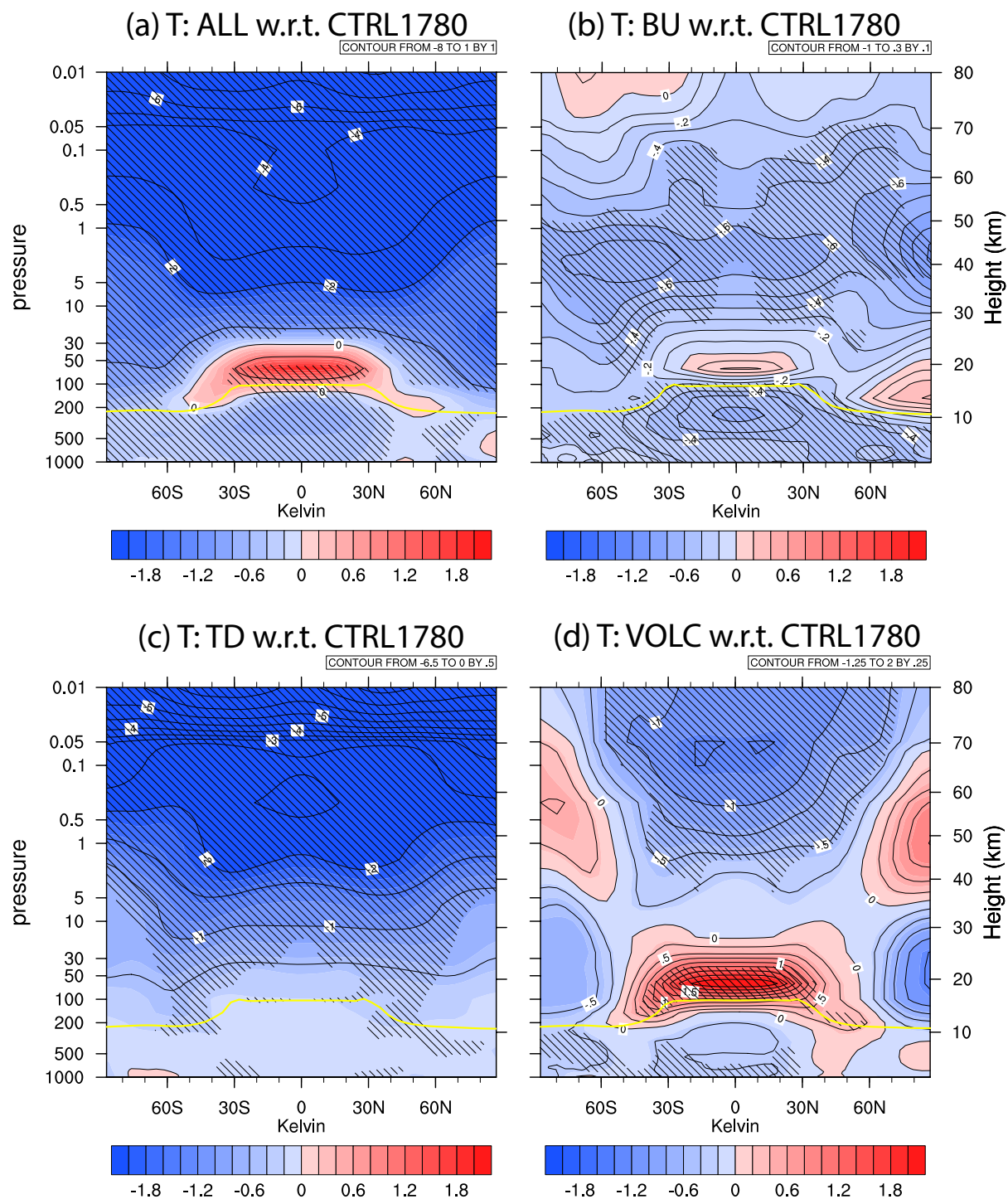
Figure 4.7: Absolute differences in temperatures of the DM-ALL, DM-BU, DM-TD and DM-VOLC experiments with relation to the DM-CTRL1780 forcing run. Hatched areas are significantly different on a Student's t test with α = 5%. The yellow line illustrates the WMO tropopause height.

confirmed when analyzing seasonal means, which show a strong statistical significant acceleration on the 5 % level of the north polar night jet and a significant increase on the 10 % level of the southern polar night jet (see Figure S 4.6 in the appendix). The blocking of the solar visible and infrared radiation by volcanic aerosols leads to a cooling in the troposphere.

Due to dilution and gravitational settling as well as washout processes, the volcanic aerosols concentration is decreasing over time. This has an implication on the temperature anomalies: we find that lower stratospheric temperatures revert to climatology, which is in agreement with (Robock, 2000).

The annual mean temperature changes from EPP are small and not statistically significant. Seasonal means however show significant differences: the austral winter seasonal mean show a dipole pattern over the South Pole (Fig. 4.10a). A significant drop in temperatures of up to 0.7 K between 100 hPa and 5 hPa is modeled in winter time, deepening in spring time to a cooling of up to 1 K. At the same time, a heating of approximately the same amplitude in a height between 1 hPa and 0.05 hPa is modeled. We explain the pattern over the southern pole by a strengthening of the polar vortex during austral winter (see next subsection) as well as a significant positive ozone anomaly of up to 3 % at 5 hPa (Fig. 4.2d). Ozone at these heights act as a radiative coolant. The positive temperature anomaly at mesosphere heights is due to a faster descent of air masses (BDC), leading to a increase in diabatic heating. No significant major changes in temperature can be observed during the boreal winter season.

The analyzed nonlinearities in temperatures are only significant in the troposphere and hence not shown here.

The temporal evolution of the temperatures at 70 hPa (Figure S 4.7 in the appendix) and at 1 hPa (Figure S 4.8 in the appendix), averaged between 20°N–20°S, are illustrated in the supplement. The main anomalies at 70 hPa height dominating over the analyzed period are triggered by volcanic eruptions (+24 K in 1815). Other effects can be neglected. At 1 hPa height, it is the solar signal which is dominant (blue line, DM-TD). But – as for NO_x – during the volcanic periods, slight, short-lived (1 year) negative temperature anomalies (negative peaks of 1–2 K) are modelled. EPP or BU radiation do not influence temperatures in such a way that it would be visible on the graphs at stratopause height.
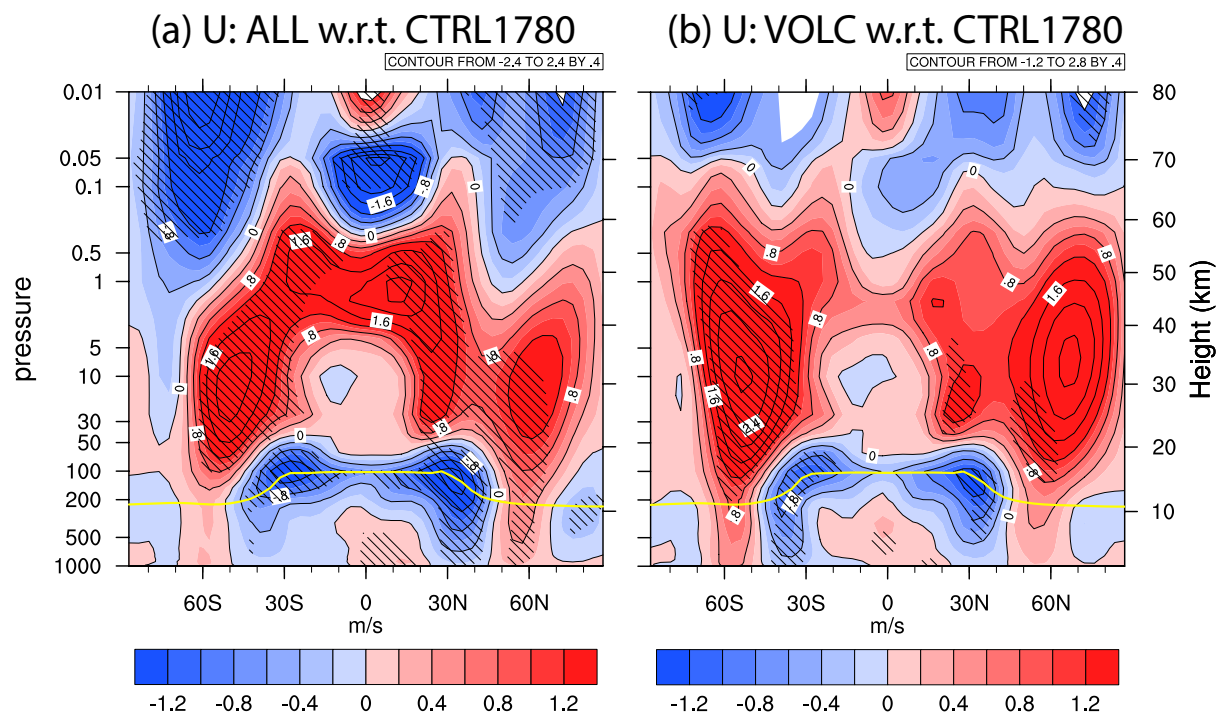
Figure 4.8: Absolute differences in mean zonal wind of the DM-ALL and the DM-VOLC experiments with relation to the DM-CTRL1780 forcing run. Hatched areas are significantly different on a Student's t test with α = 5%. The yellow line illustrates the WMO tropopause height.

4.4.2.b   Wind and general circulation

The combined effect of all considered factors shown in Fig. 4.8a consists of a strong although only partly significant acceleration of the zonal winds in the subtropical stratosphere from 20 to 60 km and in the tropical stratosphere at around 50 km height. On the other hand, a significant deceleration of the tropical jets and a decrease of the mesospheric extra-tropical zonal winds are found.

Because the introduced decrease of solar activity (DM-TD and DM-BU) does not have any wider significant influence on the annual mean zonal wind and only minor upper stratospheric influence at the southern polar region in austral winter time, the majority of the changes are attributed to the influence of the volcanic eruptions.

The model result shows a strong and significant deceleration of the zonal winds from the subtropical middle troposphere down to the surface of up to 0.8 ms^{-1}. The down-ward propagation of the signal is observed in both hemispheres. This effect comes from the strong, extended warming of the entire tropical lower stratosphere by volcanic aerosols
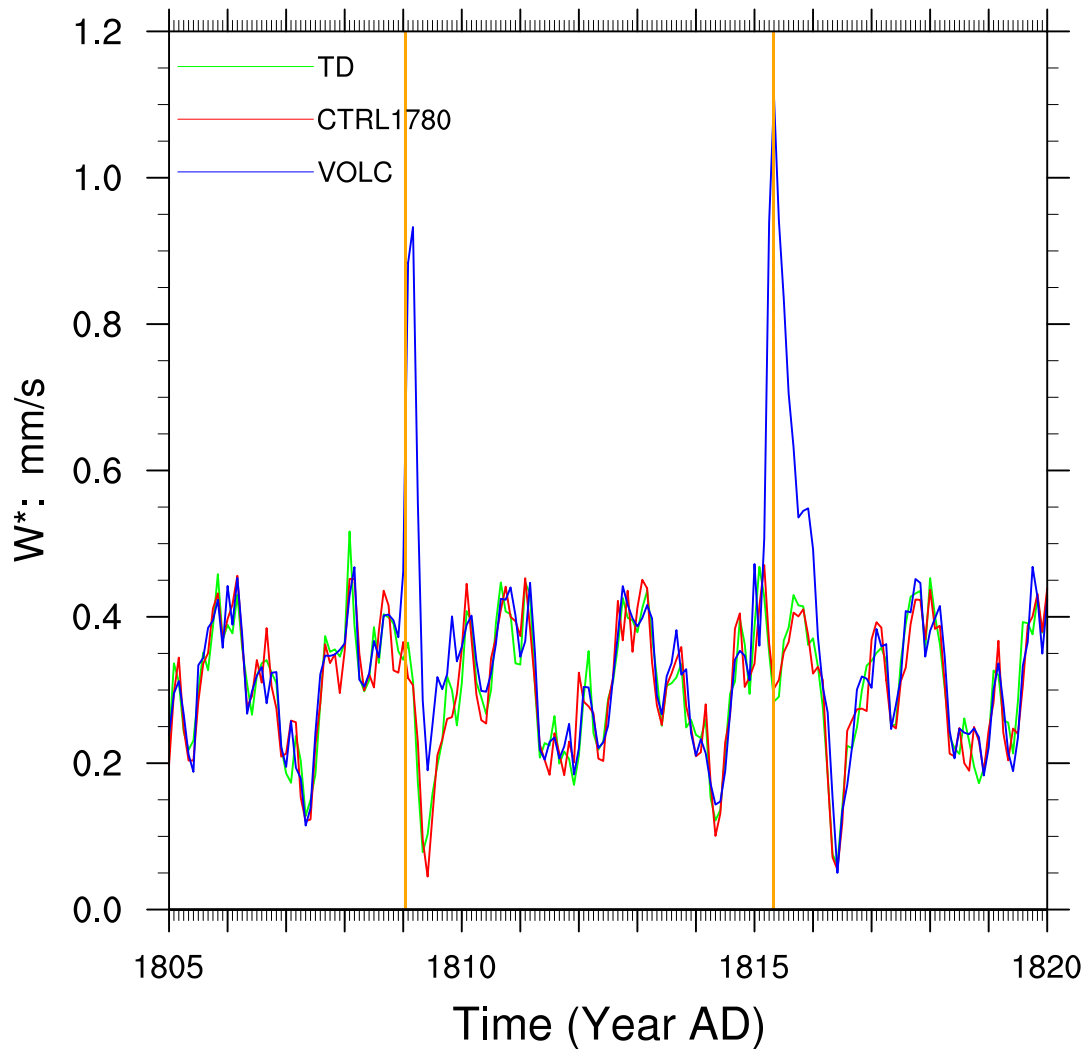
Figure 4.9: Residual vertical velocity (calculation as in Andrews et al. (1987), Eqs. 3.5.1 to 3.5.3) from 1805 to 1820 for the DM-CTRL1780, DM-VOLC and DM-TD simulations at 30 hPa height averaged from 20°N/20°S. The two major volcanic eruptions in 1809 (unknown) and 1815 (Tambora) are marked with two vertical orange lines. The data are averages of the three ensemble members and are not smoothed.

(see Fig. 4.8d), leading to a smaller temperature gradient from the equator to the extratropics. This weakens the subtropical jets. On the other hand, a significant strengthening of the polar jets up to 2.8 ms^{-1} is modeled, coming from the increased temperature gradient between the tropical tropopause and the polar tropopause ($\Delta T = 3.2K$). Moreover, in Fig. 4.9, a strong acceleration in vertical residual circulation (positive numbers are upwards) is observed after the 1809 and 1815 volcanic eruptions. Thus, the BDC

is accelerated right after major volcanic eruptions. We explain this result by the finding that immediately after the volcanic eruption, cooling in the upper troposphere occurs. This favors the dissipation of gravity waves through the tropopause, leading to an additional gravity wave drag in the lower stratosphere and hence an acceleration of the BDC. Following the heating of the lower stratosphere by the volcanic aerosols, the vertical residual circulation drops due to strengthening of the temperature gradient at the tropopause.

The DM-EPP experiment indicates positive – however not significant – changes in annual zonal mean winds of up to 0.8 ms^{-1} at the stratospheric southern polar extratropics. This anomaly becomes highly significant in austral winter seasonal mean (Fig. 4.10b) and reaches values of up to 1.2 ms^{-1}. The origin of this finding is the increase of adiabatic heating by descending air masses of the BDC in austral winter. The residual vertical circulation (not shown) shows a significant increase in down-ward motion of the air masses by up to 0.8 mm s^{-1}. This in turn forms a positive temperature anomaly, leading to an increase in the pole-to-equator gradient at 60 km of height.
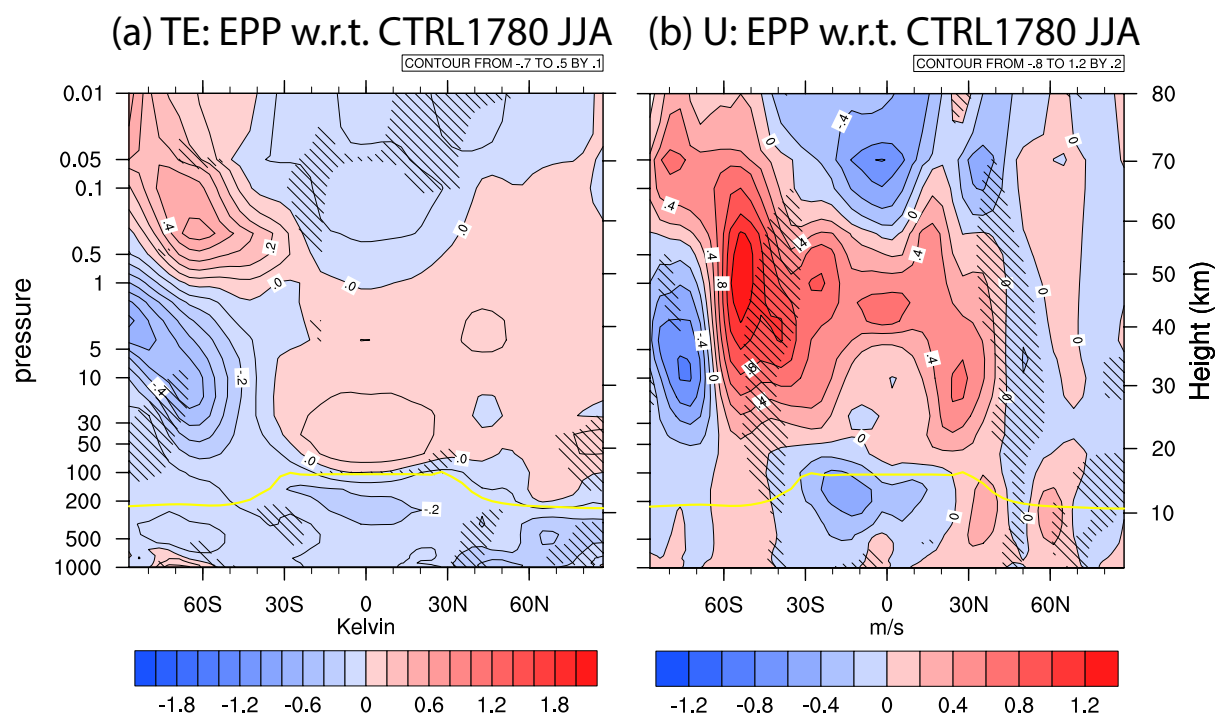
Figure 4.10: Absolute JJA seasonal differences in temperature (left) and mean zonal wind (right) of the DM-EPP experiments with relation to the DM-CTRL1780 forcing run. Hatched areas are significantly different on a Student's t test with $\alpha = 5\%$. The yellow line illustrates the WMO tropopause height.

As a consequence, the zonal wind increases. During boreal winter, a similar but less strong and non-significant pattern is found.

Nonlinearities in the zonal wind field are especially well visible at the southern extratropical stratopause, where a positive bias of up to 2 ms^{-1} is found (not shown). We assign this anomaly to the complex interaction between the DM-VOLC temperature gradient changes and the overall DM-TD negative temperature anomaly, which could have led to significant higher temperature gradient changes especially at the stratopause.

4.5 Conclusions

We present in this paper a modeling study of the different forcings which could have led to the dynamical and chemical changes in the stratosphere during the DM from 1805 to 1825 AD. The contributions, analyzed with four sensitivity experiments, include decrease in visible and near infrared radiation (DM-BU), UV radiation (DM-TD), volcanic eruptions (DM-VOLC) and energetic particles, the latter including an increase of galactic cosmic rays ionization and a decrease of solar proton events and low energetic electron precipitation (DM-EPP). A comparison of DM-TD, DM-VOLC and DM-EPP to the control run showed major significant changes. However, when comparing DM-BU to the control run, we did not succeed in identifying any noticeable changes neither in stratospheric chemistry nor in the stratospheric dynamics – except for the midstratospheric temperature field. This is mainly due to the drop of only 1 % in the radiation band 3 from the Shapiro et al. (2011) reconstruction.

The reconstructions of the solar irradiance for past times remain highly uncertain (Judge et al., 2012; Shapiro et al., 2013; Solanki et al., 2013) since no direct long-term measurements are available. We are aware of the fact that by using a strong solar forcing, the temperature, wind and chemical responses will be correspondingly strong, so that a comparison to a weaker forcing might be in place. However, in the recent work of Anet et al. (2013b), we compared the ozone response between the strong forcing of Shapiro et al. (2011) – applied here – and a weaker one. Differences were not high enough to warrant the repetition of all experiments with a weaker solar forcing.

When isolating the different contributions, our simulations show the following effects on temperatures: when reducing the solar radiation in the 185–250 nm band and the photolysis rates, a temperature drop, reaching higher negative anomalies at the mesosphere than at the tropopause is modeled. The anomalies reach 0.2 K at the tropopause and quasi-uniformly drop to values down to 6 K at the lower mesosphere.

The main reason is the lower absorption of radiation by ozone. A significant cooling of up to 0.6 K is observed in the middle stratosphere when reducing the irradiance of the bands 2 and 3 of the solar spectrum in our model (250–690 nm). In the volcanic scenario, the tropical tropopause is heated by up to 2.2 K due to radiative absorption by the aerosols while a significant cooling of up to 1.2 K is modeled around the stratopause. In the DM-EPP scenario, only a seasonal significant change in temperatures could be modeled in JJA, leading to a dipole-like structure: a cold anomaly of 0.5 K in the southern polar middle stratosphere and a warming of around the same amount in the southern polar lower mesosphere.

The zonal winds did not change significantly neither in the DM-BU nor in the DM-TD experiment. However, a strong significant change is modeled in the subtropics and extratropics in both hemispheres in the lower and upper stratosphere by up to 2.8 ms^{-1} when forcing the model only with volcanic aerosols. This effect is highest in the two years following an important volcanic eruption. Same as for the temperature, changes in zonal winds in the DM-EPP scenario are only significant in the JJA seasonal mean, showing a zonal wind increase of up to 1.2 ms^{-1} in the southern extratropical stratosphere, which is due to the dipole-like temperature anomalies.

The analysis of the stratospheric chemistry lead to following conclusions: ozone drops by up to 8 % in the ozone layer, HO_x decreases by up to 20 % at the stratopause and water vapour content decreases in the low stratosphere by up to 3.6 % but increases by up to 40 % at the lower mesosphere in the DM-TD scenario. In the DM-VOLC scenario, ozone increases by up to 16 % at the tropical tropopause but decreases by up to 6 % at the stratopause, HO_x increases all over by up to 25 % as does the water vapour amount by up to 14 %. These effects are highest in the two subsequent years after a major volcanic eruption (up to 60 % more water vapour in the lower stratosphere in the 2 yr after Tambora). The DM-EPP experiment showed highly significant changes in the NO_x field: while decrease of up to 80 % is modeled at the mesospheric poles, increase of up to 4 % is simulated at the polar tropopause. However, no or very low effects are modeled on ozone, HO_x and water vapour.

By considering the changes in dynamics and chemistry, we conclude that only due to the complex interaction of volcanic, UV solar spectral and EPP forcing, these contributions induce changes in dynamics and chemistry of the stratosphere during the DM. The reduction of the visible radiation plays only a minor role in most of the fields except for the temperature. Thus, for future modeling studies, including an interactive chemistry with separate treatment of the different spectral bands is of great importance in order to get the climate responses on solar- and volcanic forcing as realistic as possible.

Concluding, the ozone decrease was predominantly influenced by the decrease in UV radiation in the polar mesosphere and at ozone layer height, whereas the volcanic eruptions influenced ozone concentrations at tropical tropopause height. EPP influenced only in a minor part ozone concentrations in the polar mesosphere. HO_x and water vapor increase were affected primarily by volcanic eruptions in the stratosphere and by UV in the lower mesosphere. NO_x fields were most notably influenced by EPP in the polar mesosphere and by UV in the upper stratosphere. Stratospheric winds were influenced to a major part from volcanic eruptions. Temperatures were mainly influenced by volcanic eruptions and UV reduction, leading to a significant warming at the tropical tropopause and to a cooling in the remaining of the atmosphere.

With respect to a possible future grand solar minimum in the 21st century a drop of ozone column by up to 7 % due to the reduction of the UV radiation is a very significant finding. In combination with a similar decrease in the ozone layer thickness due to ozone depleting substances, this may become a possible health issue on Earth. As well, the effects of reduction of UV, volcanic eruptions and increase of oxidation by GCRs should be thoroughly investigated in future research of the 21st century with an AO-CCM. The evolution of the ozone layer remains an important scientific topic, as e.g. crop yields or health of living beings are subject to both anthropogenic and natural influences.

4.6 Acknowledgements

4.7 Appendix

Supplementary Material for ACP Manuscript "Forcing of stratospheric chemistry and dynamics during the Dalton Minimum" by J. G. Anet Institute for Atmospheric and Climate Science ETH, Zurich, Switzerland

S. Muthers Climate and Environment Physics, Physics Institute, University of Bern, Switzerland Oeschger Centre for Climate Change Research, University of Bern, Bern, Switzerland

E. Rozanov Physikalisch-Meteorologisches Observatorium Davos and World Radiation Center (PMOD/WRC), Davos, Switzerland

C. C. Raible Climate and Environment Physics, Physics Institute, University of Bern, Switzerland Oeschger Centre for Climate Change Research, University of Bern, Bern, Switzerland

T. Peter Institute for Atmospheric and Climate Science ETH, Zurich, Switzerland

A. Stenke Institute for Atmospheric and Climate Science ETH, Zurich, Switzerland

A. I. Shapiro Physikalisch-Meteorologisches Observatorium Davos and World Radiation Center (PMOD/WRC), Davos, Switzerland

J. Beer Eawag, Surface Waters group, Switzerland

F. Steinhilber Eawag, Surface Waters group, Switzerland

S. Broennimann Institute of Geography, University of Bern, Switzerland Oeschger Centre for Climate Change Research, University of Bern, Bern, Switzerland

F. Arfeuille Institute of Geography, University of Bern, Switzerland Oeschger Centre for Climate Change Research, University of Bern, Bern, Switzerland

Y. Brugnara Institute of Geography, University of Bern, Switzerland Oeschger Centre for Climate Change Research, University of Bern, Bern, Switzerland

and

W. Schmutz Physikalisch-Meteorologisches Observatorium Davos and World Radiation Center (PMOD/WRC), Davos, Switzerland

As supplementary electronic material, eight (8) PDF figures are published online.
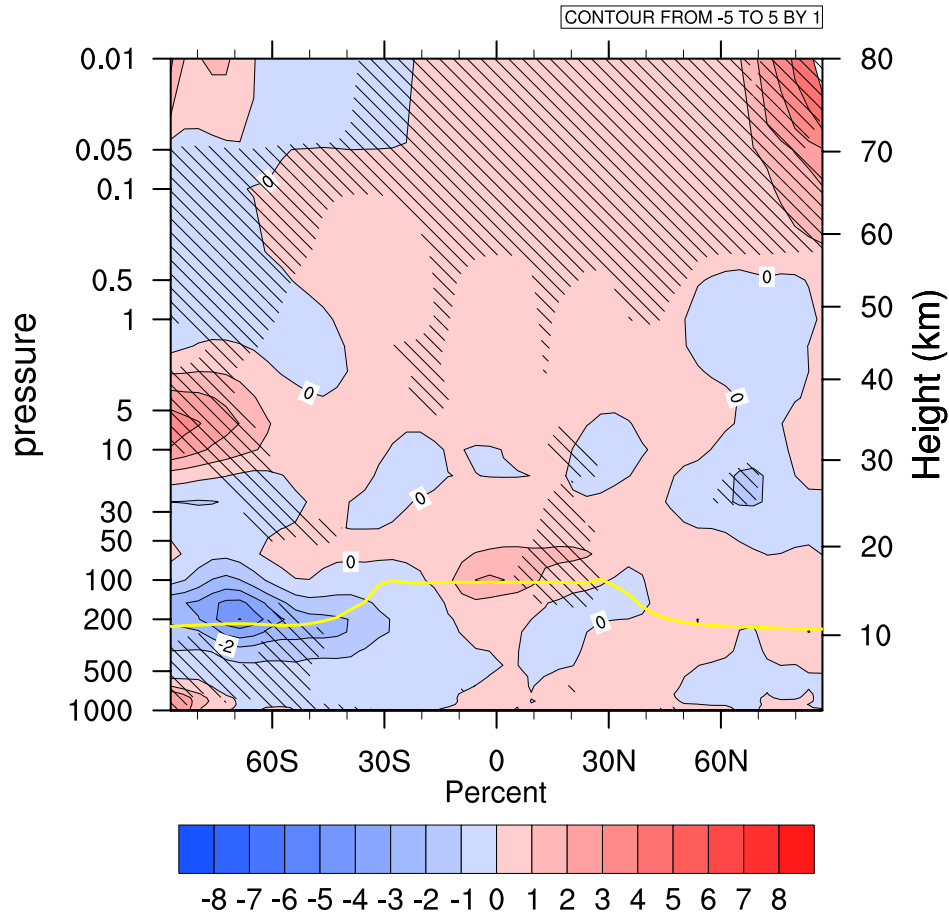
Figure S 4.1: Relative differences of ozone of the DM-EPP experiment with relation to the DM-CTRL1780 forcing run for the SON season. Hatched areas are significantly different on a Student's t-test with alpha = 5%. The yellow line illustrates the height of the WMO tropopause.
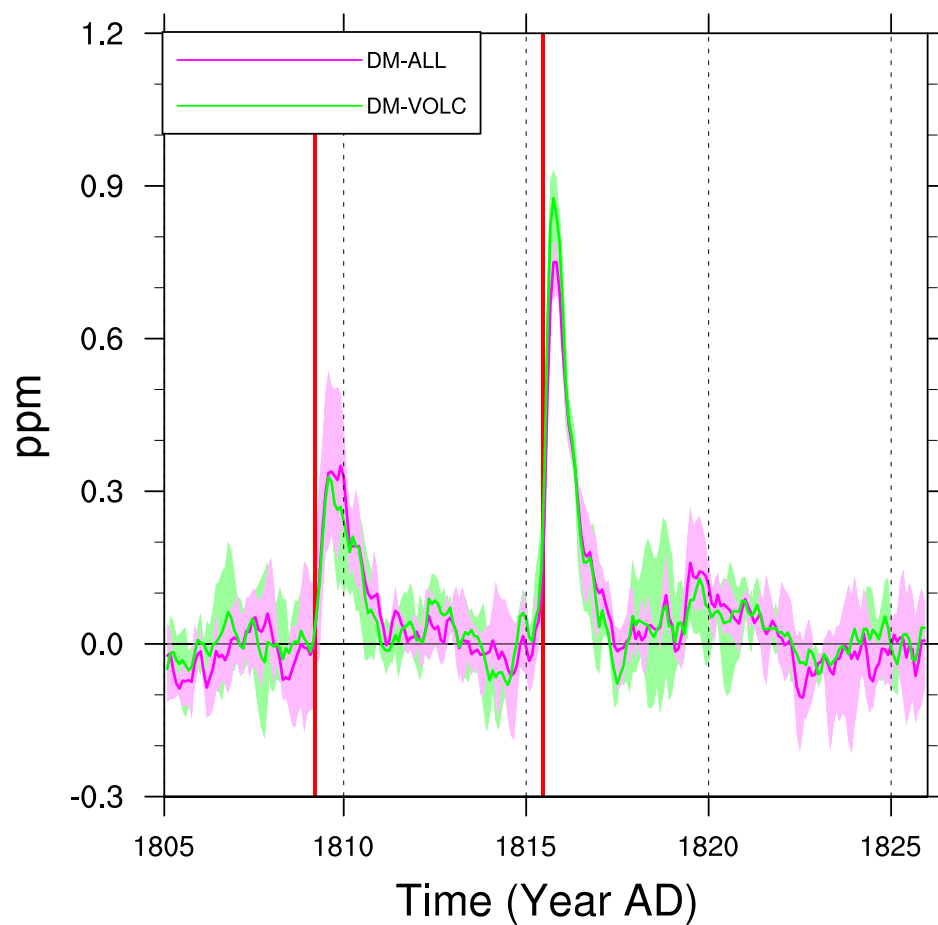
Figure S 4.2: Ozone mixing ratio anomalies, averaged from 20°N to 20°S, at 70 hPa height. Coloured curves show anomalies of experiments DM-ALL and DM-VOLC relative to DM-CTRL1780. The two major volcanic eruptions in 1809 (unknown) and 1815 (Tambora) are marked with two vertical red lines. The data are averages of the three ensemble members and are not smoothed.
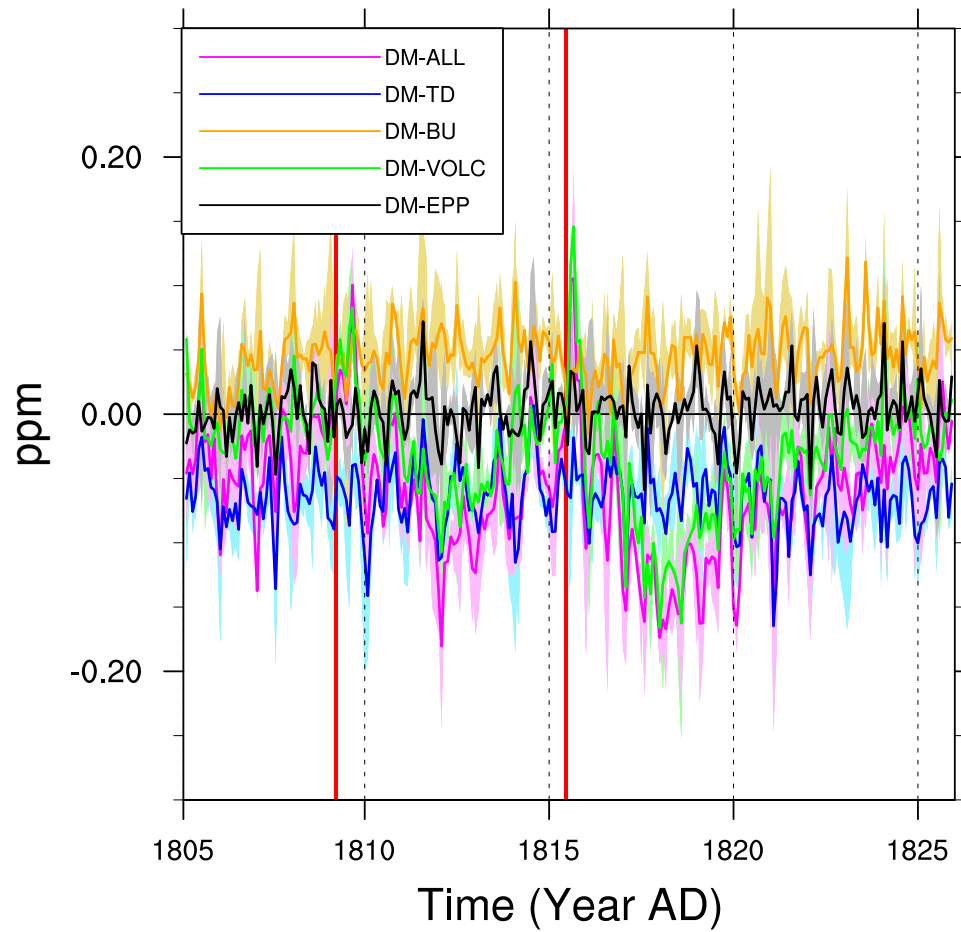
Figure S 4.3: Same as Figure S 4.2, but at 1 hPa of height and illustrating the anomalies of all experiments, relative to DM-CTRL1780.
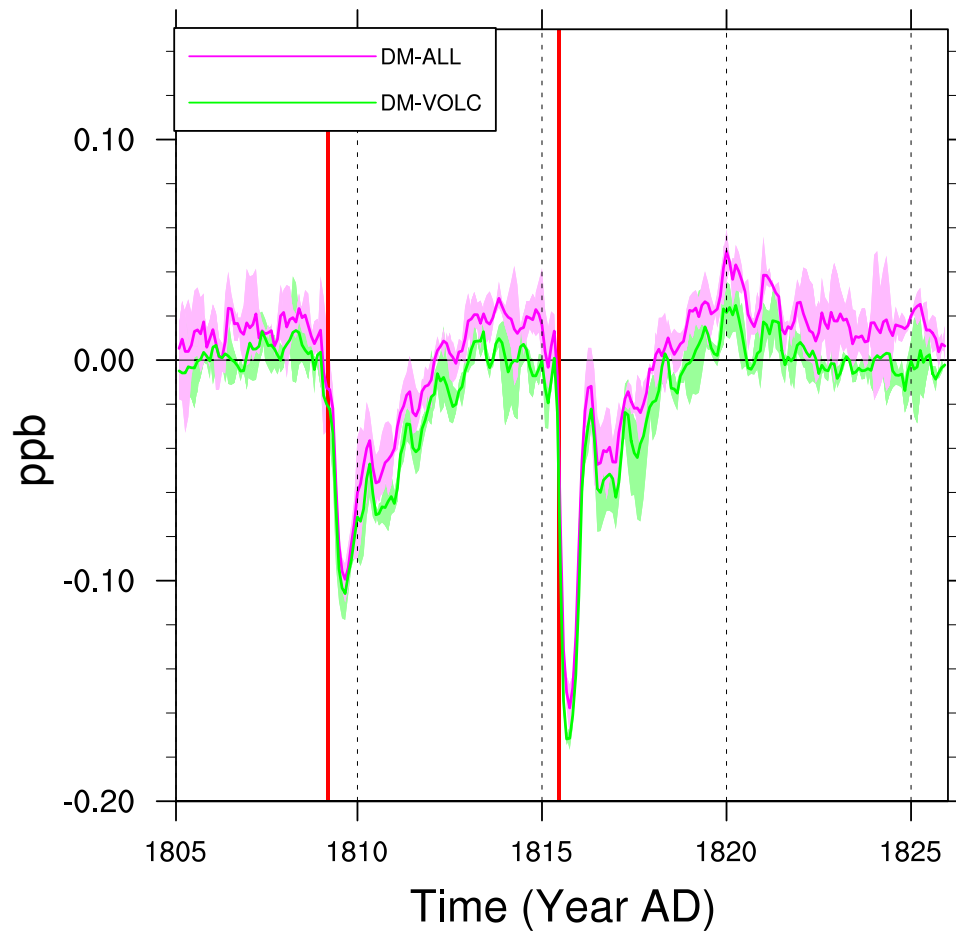
Figure S 4.4: Same as Figure S 4.2, but illustrating NOx anomalies relative to DM-CTRL1780.
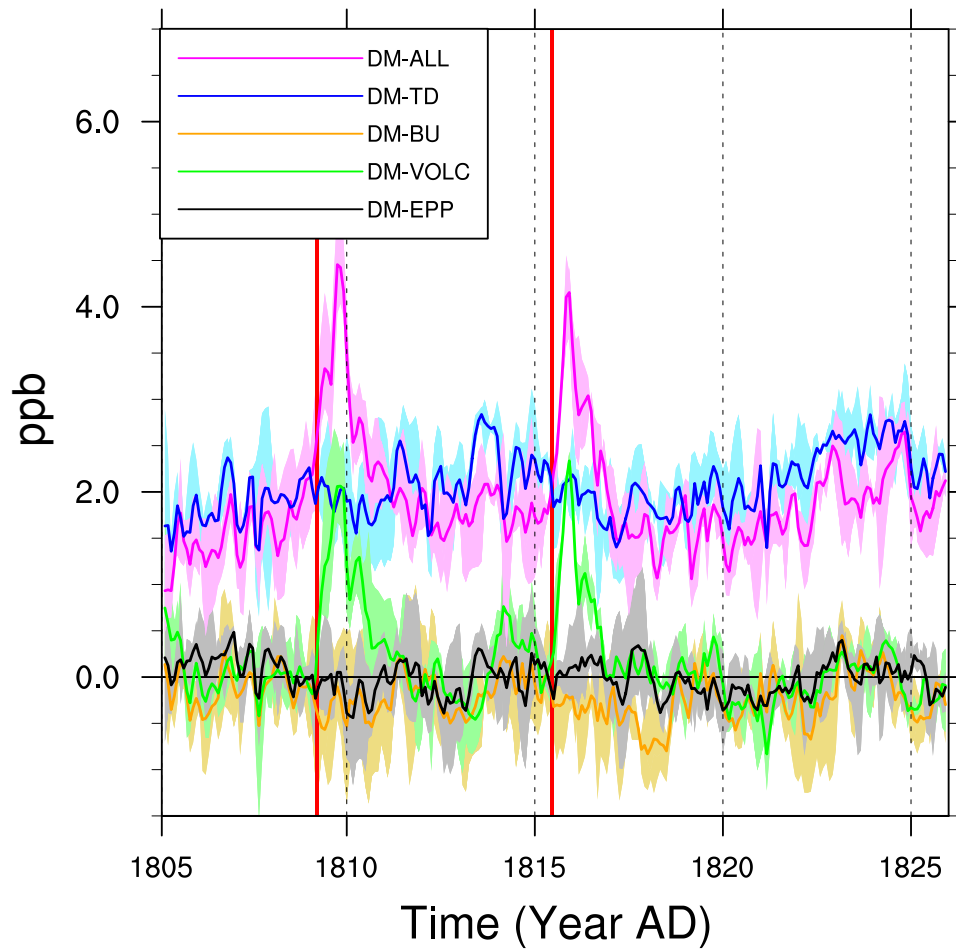
Figure S 4.5: Same as Figure S 4.4, but at 1 hPa of height and illustrating the anomalies of all experiments, relative to DM-CTRL1780.
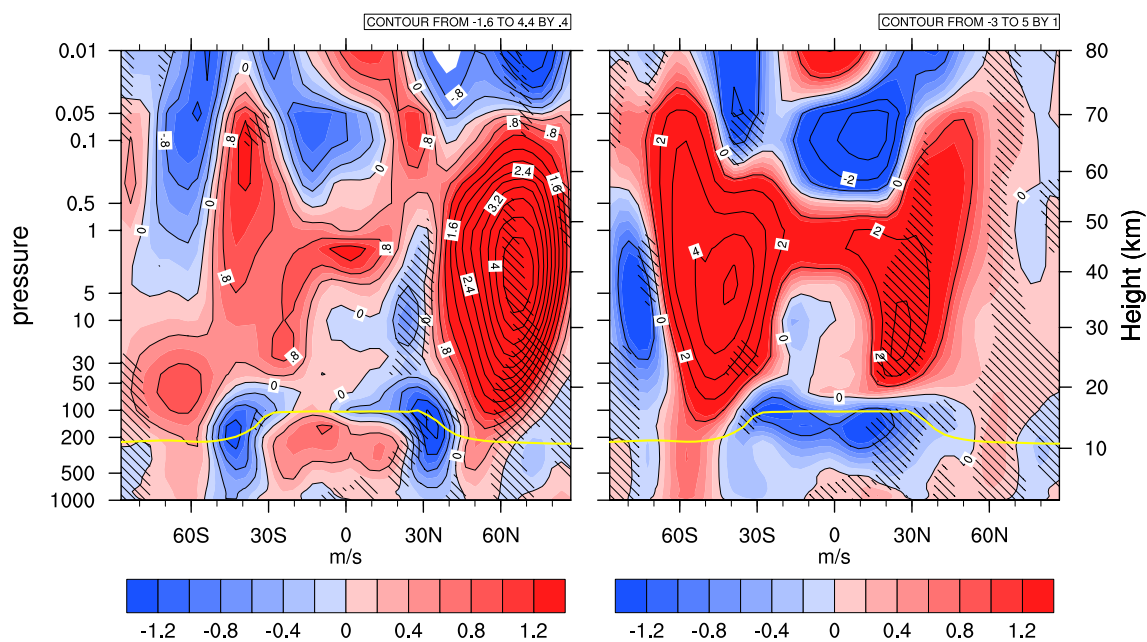
Figure S 4.6: Absolute differences of the zonal wind field of the DM-VOLC experiment with relation to the DM-CTRL1780 forcing run for the JJA (left) and DJF (right) season. Hatched areas are significantly different on a Student's t-test with alpha = 5% (left) and alpha = 10% (right). The yellow line illustrates the height of the WMO tropopause.
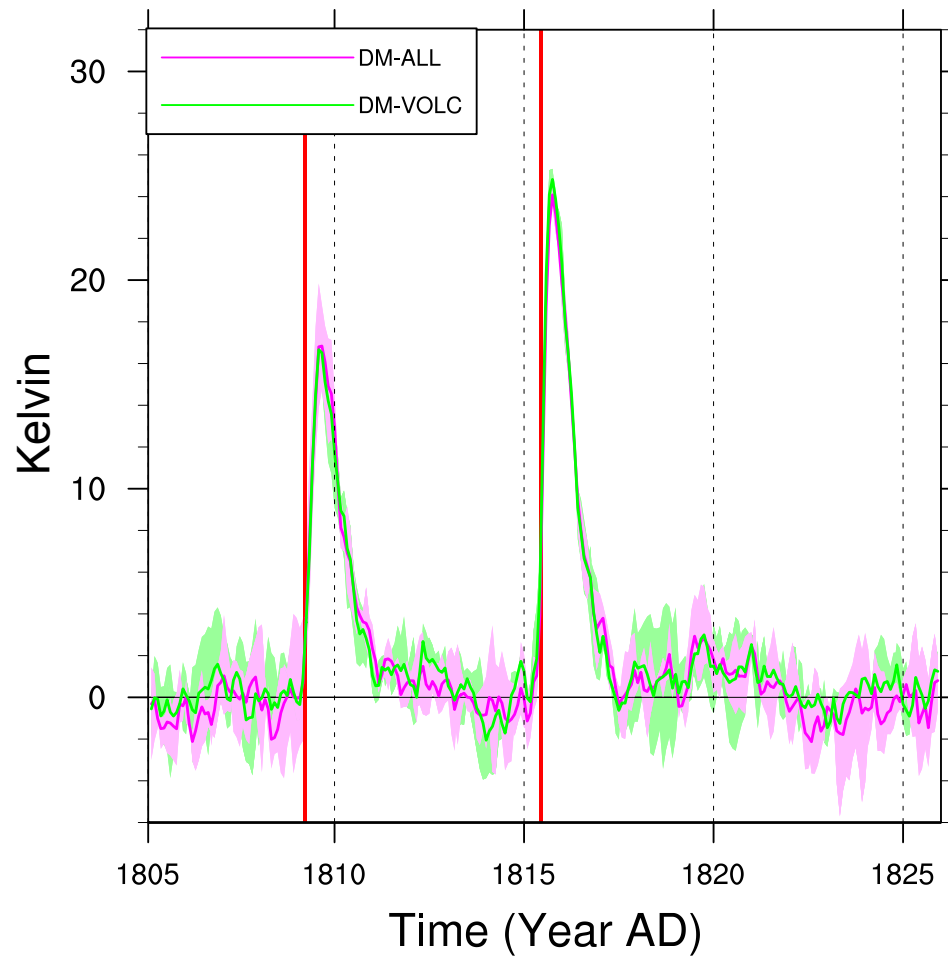
Figure S 4.7: Same as Figure S 4.2, but illustrating temperature anomalies relative to DM-CTRL1780.
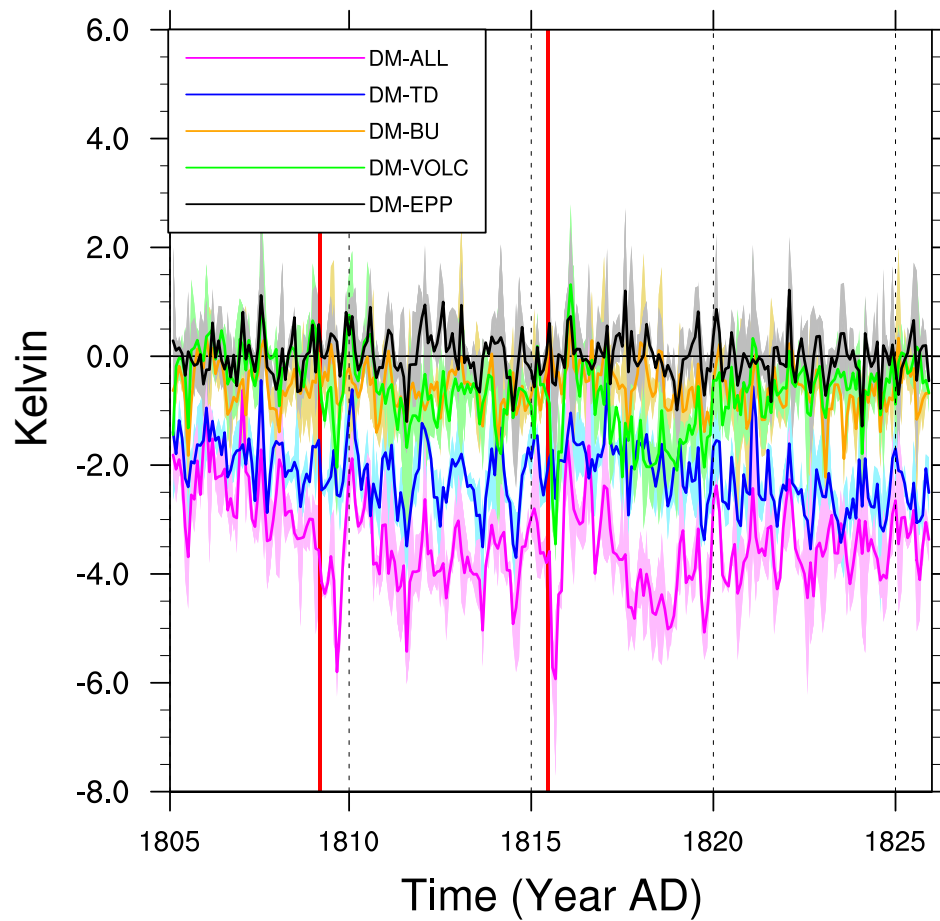
Figure S 4.8: Same as Figure S 4.7, but at 1 hPa of height and illustrating the anomalies of all experiments, relative to DM-CTRL1780.

Chapter 5

Impact of solar versus volcanic activity variations on tropospheric temperatures and precipitation during the Dalton Minimum

J.G. Anet[1], S. Muthers[2,3], E. Rozanov[1,4], C.C. Raible[2,3], A. Stenke[1], A.I. Shapiro[4], S. Brönnimann[3,5], F. Arfeuille[3,5], Y. Brugnara[3,5], J. Beer[6], F. Steinhilber[6], W. Schmutz[4], T. Peter[1]

[1] Institute for Atmospheric and Climate Science ETH, Zurich, Switzerland
[2] Climate and Environment Physics, Physics Institute, University of Bern, Bern, Switzerland
[3] Oeschger Centre for Climate Change Research, University of Bern, Bern, Switzerland
[4] Physikalisch-Meteorologisches Observatorium Davos and World Radiation Center (PMOD/WRC), Davos, Switzerland
[6] Institute of Geography, University of Bern, Bern, Switzerland
[5] Eawag, Surface Waters group, Switzerland

5.1 Abstract

The aim of this work is to elucidate the impact of changes in solar irradiance and energetic particles versus volcanic eruptions on tropospheric global climate during the Dalton Minimum (DM, 1780-1840 AD). Separate variations in the (i) solar irradiance in the UV-C with wavelengths λ <250 nm, (ii) irradiance at wavelengths λ >250 nm, (iii) in energetic particle spectrum, and (iv) volcanic aerosol forcing were analyzed separately, and (v) in combination, by means of small ensemble calculations using a coupled atmosphere-ocean chemistry-climate-model. Global and hemispheric mean surface temperatures show a significant dependence on solar irradiance at λ >250 nm. Also, powerful volcanic eruptions in 1809, 1815, 1831 and 1835 significantly decrease global mean temperature by up to 0.5 K for 2-3 years after the eruption. However, while the volcanic effect is clearly discernible in the Southern Hemispheric mean temperature, it is less significant in the Northern Hemisphere, partly because the two largest volcanic eruptions occurred in the SH tropics and during seasons when the aerosols were mainly transported southward, partly because of the higher northern internal variability. In the simulation including all forcings, temperatures are in reasonable agreement with the tree-ring-based temperature anomalies of the Northern Hemisphere. Interestingly, the model suggests that solar irradiance changes at λ <250 nm and in energetic particle spectra have only insignificant impact on the climate during the Dalton Minimum. This downscales the importance of top-down processes (stemming from changes at λ <250 nm) relative to bottom-up processes (from λ >250 nm). Reduction of irradiance at λ >250 nm leads to a significant (up to 2%) decrease of the ocean heat content (OHC) between the 0 and 300 meters of depth, whereas the changes in irradiance at λ <250 nm or in energetic particle have virtually no effect. Also, volcanic aerosol yields a very strong response, reducing the OHC of the upper ocean by up to 1.5%. In the simulation with all forcings, the OHC of the uppermost levels recovers after 8-15 years after volcanic eruption, while the solar signal and the different volcanic eruptions dominate the OHC changes in the deeper ocean and prevent its recovery during the DM. Finally, the simulations suggest that the volcanic eruptions during the DM had a significant impact on the precipitation patterns caused by a widening of the Hadley cell and a shift of the intertropical convergence zone.

5.2 Introduction

The Dalton Minimum (DM) was a 60 year-long period of low solar activity, lasting from 1780 AD to 1840 AD. In addition, early in the 19th century, two major volcanic eruptions took place, ejecting large amounts of sulfur dioxide into the stratosphere, which, after conversion to sulfate aerosols, increased planetary albedo affecting global climate. In 1816, an exceptionally cold summer was recorded in Western Europe. This year got known as the "year without summer" (Harington, 1992; Robock, 1994). While the scientific acceptance of a significant climate impact from volcanic eruptions is high, there is ongoing debate about the contribution of the solar variability to global temperature changes in the troposphere during the DM, see for example Table 2.11 of the last IPCC report (Intergovernmental Panel on Climate Change, IPCC, Climate change 2007, 2007).

It is well-known that solar activity varies over time. This is not only documented by the sunspot number datasets (Wolf, 1861), but also by the cosmogenic isotopes ^{10}Be conserved in ice sheets (Steinhilber et al., 2008, 2009). The past evolution of the solar irradiance has been reconstructed by a number of authors (see Solanki et al., 2013, and references therein). Recently, Shapiro et al. (2011) reconstructed the spectral solar irradiance (SSI) for the last 400 years using the solar modulation potential Φ as a proxy. Their results show that the decrease of the heavily absorbed UV-C during the DM reaches 15%, while it does not exceed 1% in the solar spectrum with $\lambda >$250 nm and is negligible in the solar near infrared (NIR). This disproportionate change in the spectral solar irradiance has complex effects on Earth's atmospheric chemistry and climate system: On one hand, a substantial decrease in the UV-C at $\lambda <$250 nm cools down the middle atmosphere and decreases the ozone production due to decelerated oxygen photolysis (Anet et al., 2013a), but is too small (only 0.3 W/m^2) to directly impact tropospheric climate. On the other hand, the decrease at $\lambda >$250 nm by 6.5 W/m^2 does not affect stratospheric chemistry, but directly influences surface temperatures.

A negative UV-C anomaly affects the state of the stratosphere and mesosphere (Rozanov et al., 2012a; Anet et al., 2013a), from where it may influence the tropo-sphere via a cascade of mechanisms: By cooling down the tropical and midlatitude stratosphere, it decreases the pole-to-equator temperature gradient, weakens the zonal winds and decelerates the Brewer-Dobson circulation. The latter is followed by a

cooling in the lower tropical stratosphere (Kodera and Kuroda, 2002), modulation of the Hadley cell (Haigh, 1996) and alteration of the tropospheric wave pattern (Brugnara et al., 2013), propagating down to the surface. This is also known as the "top-down" mechanism (Meehl et al., 2009). However, in the present set of simulations the top-down mechanism is shown to be of minor importance when comparing with other mechanisms discussed below.

Complementary to the top-down mechanism is the "bottom-up" mechanism, which we investigate here by separating the role of solar irradiance at $\lambda >$250 nm: As most of this radiation is able to pass through the stratosphere without major absorption, its anomalies directly impact the radiation fluxes, energy balance and temperatures on the ground. Depending on the surface albedo, a part of this radiation is absorbed and transformed to latent or sensible heat. It is known that during periods with weak solar activity, less radiation is available in the tropics for conversion to latent heat, leading to a decrease in the amount of precipitation (Meehl et al., 2008) and thus a weakening of the Ferrel and Hadley cells (Labitzke et al., 2002).

Besides electromagnetic radiation, a second major factor varying over time and influencing stratospheric and upper tropospheric chemistry and - regionally - tropospheric dynamics is energetic particle precipitation (EPP). These particles consist of galactic cosmic rays (GCRs), solar energetic particles (SEPs), low energy electrons (LEE) originating from the magnetosphere and high energy electrons (HEE) stemming from the Earths radiation belt. While SEP and LEE/HEE vary in phase with the solar activity, GCRs are partly deflected by the solar wind, and therefore are negatively correlated with solar activity. Ionization of neutral molecules like N_2 or O_2 by energetic particles facilitates the formation of NO_x and HO_x (see e.g. Sinnhuber et al., 2012) accelerating the ozone destruction followed by a cooling inside the polar vortex and an increase of pole-to-equator temperature gradients, which in turn can change the tropospheric climate. These processes were simulated by several CCM and significant response of the atmosphere to EPP was identified (Calisto et al., 2011; Semeniuk et al., 2011; Rozanov et al., 2012b). However, in our previous study (Anet et al., 2013a) the net effect of particles was found to be rather weak. This is seemingly contradictory, but can be partly explained by a compensating effect of decreasing LEE and increasing GCR intensity during the DM, which above-mentioned studies could not take into account because they either investigated only one sort of the energetic particles, or they compared model runs with all EPP included against a reference run without any EPP.

A third factor, which notably influenced the stratospheric and tropospheric climate and chemistry at least for a short time in the DM, are major volcanic eruptions, which are known for having ejected up to 60 Mt (Tambora volcanic eruption, year 1815) of sulfur dioxide into the atmosphere. Presumably, the plumes reached deep into the stratosphere, where the massive amounts of sulfur dioxide were converted to sulfate aerosols. As the result, the haze in the sky and colorful sunsets were reported during the period (see e.g. Olson et al., 2004). The aerosol particles efficiently scatter a fraction of the incoming solar radiation back to space, but also absorb a part of the outgoing terrestrial infrared (IR) and incoming solar near IR (NIR). The reduction in incoming visible or NIR radiation overwhelms the IR absorption, leading to an overall global cooling, except in the polar night, where sunlight is lacking and a small warming prevails (Robock, 2000). Generally, a significant cooling of the surface occurs in the first weeks after major volcanic eruptions, lasting for one to two years and leading to modified patterns of precipitation, surface pressure and the teleconnection patterns, such as the Arctic Oscillation (AO), North Atlantic Oscillation (NAO) (Shindell et al., 2000; Stenchikov et al., 2002; Fischer et al., 2007) or the El Niño Southern Oscillation (ENSO) (Robock and Mao, 1995; Adams et al., 2003).

Different modeling studies in the recent past show a large range of simulated climate responses to solar forcings. For instance, Wagner and Zorita (2005) showed with an atmosphere-ocean general circulation model (AO-GCM) without coupled chemistry that the combined effects of volcanic eruptions and solar irradiance decrease could significantly (by up to several tenths of a degree) modify global mean temperatures. They attributed most of this cooling to the volcanic effects, and their "solar-only" simulation without volcanic eruptions showed a decrease of global temperatures of only 0.1 K. Feulner (2011a) concluded from their experiment with an intermediate complexity model that the solar contribution to the cool period during the DM was likely a smaller one. They showed that the cold climate was explained mostly by volcanic forcing. Their application of the strong solar irradiance forcing proposed by Shapiro et al. (2011) led to a substantial disagreement of their simulated and the reconstructed temperature time series. Shindell et al. (2000) compared the long-term influence of volcanic eruptions to grand solar minimum conditions with focus on the DM and on the Maunder Minimum (MM) - which occurred about 150 years before the DM. They concluded that volcanic eruptions have rather strong but only short-lived effects on temperatures, while the reduction of the solar irradiance during the grand minimum affects temperatures on longer time scales. They estimated a solar induced cooling

during the MM of globally 0.6 to 0.8 K. For the same period, Varma et al. (2012) investigated the Southern Hemispheric wind field response to the MM solar irradiance decrease. They estimated the stratospheric ozone change due to the reduction of solar UV irradiance from a global scaling with total solar irradiance (TSI) variations, which could lead to a shift in the Southern Hemispheric westerly winds to the north via the "top-down" mechanism consisting of a chain of complex radiative-dynamical processes (Meehl et al., 2008; Haigh, 1996). In another paper, Varma et al. (2011) concluded that the "bottom-up" mechanism via a reduction of visible irradiance had a similar effect. However, these publications (Varma et al., 2011, 2012) do not provide detailed information on changes in tropospheric temperatures.

The influence of volcanic and solar forcing on ozone chemistry, stratospheric temperatures and global circulation has become of great scientific interest in the recent years. The aim of this work is to analyze the tropospheric climate changes during the DM with a fully coupled atmosphere-ocean chemistry-climate model (AO-CCM) driven by the state-of-the-art set of climate forcings and to disentangle the contributions from changes in solar spectral irradiance, energetic particles and volcanic eruptions. To the best of our knowledge so far, such a sophisticated model and climate forcing set have not been applied for the evaluation of the tropospheric climate changes during the DM.

The work is structured as follows: After Section 5.2, which described the state of the research and introduced some notation, Section 5.3 will provide a description of our model and our experiments. Section 5.4 focuses on the changes in surface temperatures and precipitation patterns caused by the different forcings. We further compare our model results to reconstructed temperature fields, and conclude in Section 5.5.

5.3 Sensitivity experiments and model description

5.3.1 AO-CCM SOCOL3-MPIOM

The AO-CCM SOCOL3-MPIOM emerges from a modification of CCM SOCOL version 3 (Stenke et al., 2013), which has been coupled with the OASIS3 coupler (Valcke, 2013) to the Max Planck Institute ocean model (Marsland et al., 2003). SOCOL3 is based on the GCM ECHAM5 (Roeckner et al., 2003) and includes the chemical part of the chemistry-transport model MEZON (Rozanov et al., 1999; Egorova et al., 2003;

Schraner et al., 2008). SOCOL3-MPIOM is applied in middle atmosphere mode (MA) extending from the ground to 0.01 hPa or around 80 km. Simultaneously with the radiation calculation, MA-ECHAM5 hands over temperature fields to MEZON, which takes into account interactions between 41 gas species - including 200 gas phase, 16 heterogeneous and 35 photolytic reactions. Those chemical fields are then handed back to MA-ECHAM5, which calculates all components of the general circulation and tracer advection.

All simulations have been executed using the model version with T31L39 resolution, which equals to an average horizontal grid space of $3.75°(\sim 400$ km) and an irregularly spaced vertical resolution of 39 levels. Due to the relatively coarse vertical resolution, the Quasi-Biennial-Oscillation is not reproduced autonomously. Hence, the equatorial zonal wind fields are nudged to reconstructed zonal mean wind datasets as in Giorgetta (1996).

It is known that the original MA-ECHAM5 code does not properly take into account radiative absorption by oxygen, neither in the Lyman-alpha line nor in the Schumann-Runge bands and also the absorption of ozone in the Hartley or Huggins bands is only coarsely resolved (Forster et al., 2011). Hence, the heating rate calculation has been improved to add the missing parts following the approach of Egorova et al. (2004) adapted to the spectral resolution of the ECHAM5 radiation code. The parameterizations for the ionization rates by GCR, SEP and LEE were introduced identically as in Rozanov et al. (2012b) and Anet et al. (2013a). HEE are not implemented due to absence of an easily applicable parameterization.

5.3.2 Boundary conditions

The applied boundary conditions are described in detail by Anet et al. (2013a). As a summary, the most important forcings are recapitulated subsequently.

The forcing caused by spectral solar irradiance changes is based on the mean values of the reconstruction by Shapiro et al. (2011) as illustrated in Figure 5.1a and b. This determines the photolysis and heating rates due to solar irradiance absorption by various air components. Shapiro et al. (2011) assumed that the minimum state of the quiet Sun corresponds to the observed quietest area on the present Sun, and then used available long-term proxies of the solar activity (i.e. [10]Be isotope concentrations in
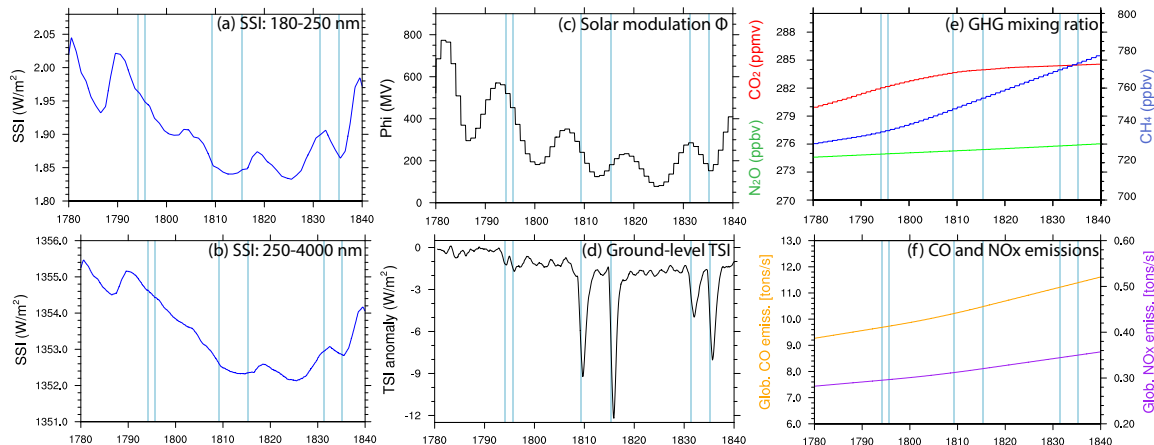
Figure 5.1: Model forcing data over the Dalton Minimum (1780-1840 AD). (a) Spectral solar irradiance in the UV-C at 180 nm $<\lambda<$ 250 nm. (b) Spectral solar irradiance at λ $>$250 nm. (c) Solar modulation potential following Steinhilber et al. (2008). (d) Ground-level TSI, showing anomalies relative to the 1780 unperturbed values. (e) Greenhouse gas mixing ratios for CO_2, CH_4 and N_2O. (f) Anthropogenic and natural CO and NO_x emissions from fossil fuel burning. Blue vertical lines highlight the years, at which a volcanic eruption occurred.

ice cores, 22-year smoothed neutron monitor data) to interpolate between the present quiet Sun and the minimum state of the quiet Sun. This determines the long-term trend in the solar variability, on which the 11-year activity cycle calculated from the sunspot number is then superposed. The time-dependent solar spectral irradiance is derived using a state-of-the-art radiation code COSI (Shapiro et al., 2010). The resulting spectral solar irradiance of this reconstruction is substantially lower during the MM than the one observed today, and the difference is larger than in the other recently published estimates. The advantage of this high-amplitude reconstruction is that it allows us to derive a maximum conceivable terrestrial climate response to solar changes, while other reconstructions leave hardly any fingerprint in the modeled climate.

For the EPPs, the A_p index reconstruction from Baumgaertner et al. (2009) is used for the LEE. For SEPs, return-period based datasets were created from an analysis of the last 45 years of the last century. The GCR ionization rates depend on Φ (Figure 5.1 c), which was reconstructed by Steinhilber et al. (2008). The geomagnetic dipole field strength and position is provided from paleomagnetic datasets from Finlay et al. (2010).

The volcanic forcing is based on simulations carried with a 2D aerosol microphysical model (Arfeuille et al., 2013a). It uses total aerosol injection values from Gao et al. (2008) and information on date/location of each eruptions. The stratospheric aerosols are prescribed in terms of extinction ratios, single scattering albedos and asymmetry factors for each of the 22 ECHAM5 radiation bands and in terms of surface area densities, for each latitude-altitude band of SOCOL (zonally averaged). Aerosol optical depth values derived from this forcing are documented in Table 5.1. The globally averaged effect on incoming surface shortwave radiation is shown in Figure 5.1 d.

The QBO was generated by means of a backwards extension of an already existing reconstruction, using an idealized QBO cycle which is superimposed onto the regular seasonal cycle (Brönnimann et al., 2007).

The greenhouse gas forcing (Figure 5.1 e) forcing for the period from 1780 to 1840 are based on the PMIP3 protocol (Etheridge et al., 1996, 1998; Ferretti et al., 2005; MacFarling-Meure et al., 2006; Meehl et al., 2009) while halogens are kept constant at preindustrial levels. The standard ECHAM5 land surface datasets by Hagemann et al. (1999) and Hagemann (2002) are used. Tropospheric aerosol fields were extracted from existing CAM3.5 simulations driven by CCSM3 (CMIP4) sea-surface temperatures and 1850-2000 CMIP5 emissions. These fields were then scaled as a function of the world population starting in the year 1850 going backwards, except for the 10% (relative to the 1990 values) of biomass burning, which were considered constant over time.

	Aerosol optical depth		
Year	NH	SH	Volcano, confirmed/tentative attrib.
1794	0.02	0.04	Unknown SH, no large eruption recorded
1796	0.12	0.02	Unknown NH, no large eruption recorded
1809	0.12	0.42	Unknown Tropics, eruption in February
1815	0.24	0.68	Tambora 8°S, Indonesia, 10 April
1831	0.22	0.06	Babuyan Claro 19.5°N, Philipp., date?
1835	0.36	0.23	Cosiguina 13°N, Nicaragua, 20 January

Table 5.1: Stratospheric aerosol optical depths at 550 nm derived from volcanic aerosol simulations Arfeuille et al. (2013a) using ice core measurements from Gao et al. (2008).

For the global CO and NO$_x$ emissions, the part emitted from shipping was calculated starting from the CMIP5 datasets, which were projected linearly backwards from 1850 on to the year 1800. Before 1800, no steamships existed, thus these emissions were set to zero. The natural biomass burning emissions were assumed to be constant over time, while the anthropogenic biomass burning emissions were scaled with the world population. The emissions are illustrated in Figure 5.1f.

5.3.3   Sensitivity experiments

We performed six sensitivity experiments covering the time period from 1780 to 1840 (Table 5.2), each with three ensemble members. These simulations are identical to those described by Anet et al. (2013a). The nomenclature is as follows: The run including all effects acting together on the climate system is named ALL. The sensitivity experiment "Top-Down" (TD, Meehl et al., 2008) experiment includes only the variations of solar irradiance with $\lambda <$250 nm and the corresponding extra heating (corrections for the Lyman-α line, the Schumann-Runge, Hartley and Huggins bands) and photolysis rates of photolytic chemical reactions. The "Bottom-Up" (BU) experiment (Meehl et al., 2008) allows only irradiance $\lambda >$250 nm to vary over time. The EPP experiment is exclusively forced by energetic particles. In the VOLC experiment, all other forcings except the stratospheric aerosols, which affect the radiation budget and heterogeneous chemistry via changes in surface area density (SAD), were kept constant. All runs were compared to a control run with perpetual 1780 conditions called CTRL1780.

Experiment	Process			
Name	ΔI ($\lambda<$250 nm)	ΔI ($\lambda>$250 nm)	ΔIoniz.	ΔSAD
CTRL1780	const	const	const	bckgrd
ALL	trans	trans	trans	trans
TD	trans	const	const	bckgrd
BU	const	trans	const	bckgrd
EPP	const	const	trans	bckgrd
VOLC	const	const	const	trans

Table 5.2: Dalton minimum experiments: *const* denotes constant 1780 conditions. *bckgrd* denotes background aerosol emissions and volcanic emissions off. *trans* denotes transient forcing. "Ioniz." stands for the parametrization for SPE, LEE and GCR.

The analysis of the data was done by comparing zonally and temporally averaged ensemble mean fields to the CTRL1780 ensemble mean.

In order to focus on the strongest signals (and following Anet et al., 2013a), the period from 1805 to 1825 is chosen for the temperature, precipitation and mass stream function analysis showing regional patterns on latitude-longitude or latitude-height plots, thus reducing the signal-to-noise ratio. Time evolution plots of the temperatures and ocean heat contents show ensemble means of the entire simulation period. Oceanic as well as surface temperature data has been smoothed with an 12-month full width-half maximum (FWHM) Gaussian filter. The statistical significance of the global distribution of the 2-m temperature anomalies were computed using a 2-sample Student's t-test (test of the ensemble mean for 20 years, n=20, df=38) on a 5% significance level, taking autocorrelation into account. The statistical analysis of the hydrological cycle was done similarly, with exception that the significance level was set to 10% (surface temperatures volcanic anomalies, precipitation, mass stream function).

5.4 Results

First, we discuss regional temperature differences between the specific sensitivity experiment and the CTRL1780 experiment averaged over the 1805-1825 AD period. Then we present the contribution of different forcing factors to the evolution of the mean surface temperature and ocean heat content during the entire integration period. Finally, changes of the precipitation are described in Sect. 3.3.

5.4.1 Temperature

The regional pattern of the 2-m temperature difference between the ALL and the CTRL1780 simulation is illustrated in Figure 5.2a. In particular the tropical and subtropical regions undergo a significant cooling by values ranging from 0.2 K to 1 K. The cooling is more pronounced over the land masses than over the oceans. Three small positive temperature anomalies appear over the Bering Sea, the western Antarctic, and over the north Atlantic regions. Significant deviations from the annual mean figure are a strong cooling during Northern Hemispheric (NH) winter over Siberia and Alaska, as well as the significant warming during polar winter over the respective
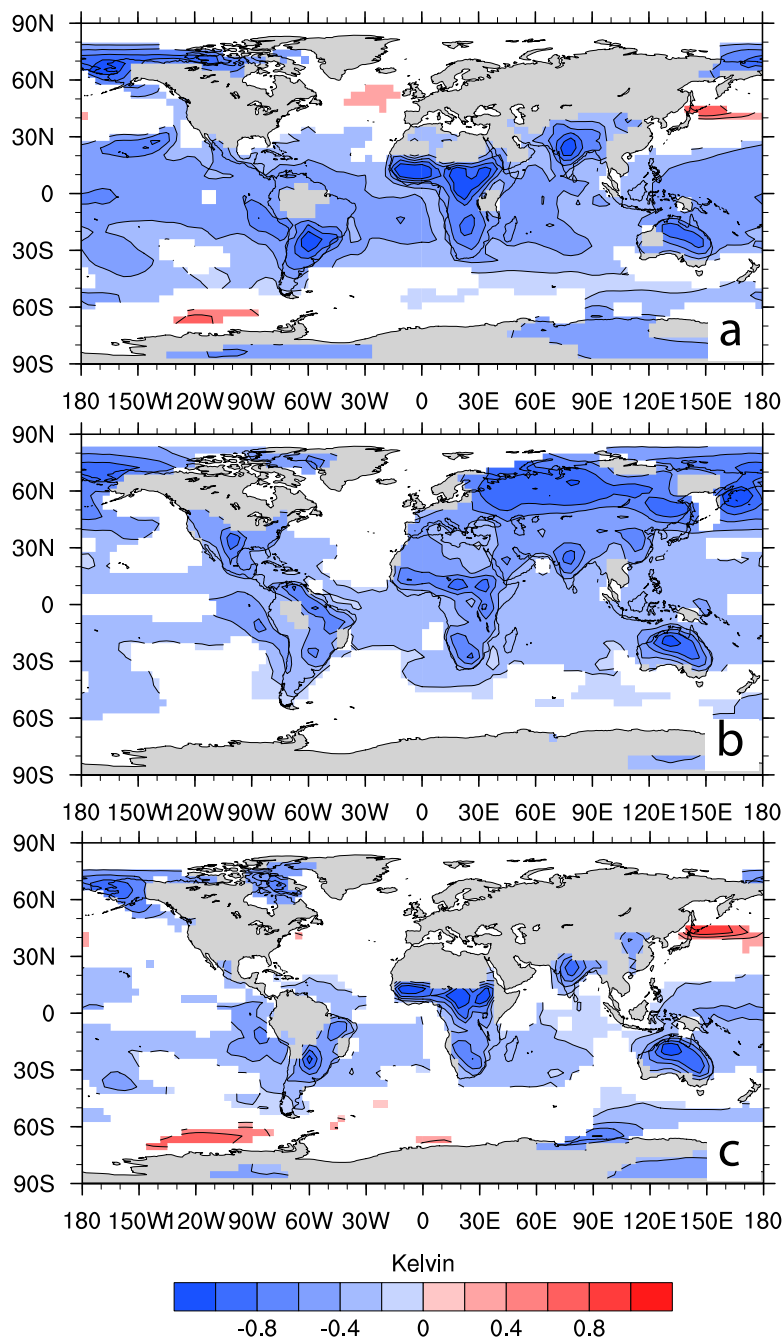
Figure 5.2: (a): Ensemble mean of 2m-Temperature differences, averaged over the 1805-1825 period for the ALL run. (b): Same for the "Bottom-Up" run. (c): Same for the VOLC run. Only areas which are significant at the 5% level are colored (two sided t-test).

polar hemisphere (Fig. S 5.1).

The cooling of the continents can be explained by the BU experiment shown in Figure 5.2 b, which simulates cooling patterns similar to the ALL ensemble mean, except over northern Asia and parts of Europe. The cooling is caused by the negative anomaly in solar irradiance at wavelengths $\lambda >$250 nm and subsequently by a reduced heating of the surface. The weaker ocean response is related to the large heat capacity of the ocean, partly compensating the reduced irradiance. The Siberian cold anomaly could be related to an increasing snow cover during the cold season, leading to a negative albedo feedback.

The slight warming anomalies over the Bering Sea and western Antarctic Peninsula regions can be explained with the VOLC simulation (Fig. 5.2 c). The warming pattern over the Bering Sea region, triggered by ocean upwelling (see later) is present during the whole year. In the western Antarctic Peninsula and north Atlantic regions, the patterns are predominant during the SH winter season (JJA). The western Antarctic Peninsula warming is associated with an enhanced transport of milder air masses from the subtropics. This is related to differential temperature anomalies from absorption and/or reflection of radiation by the volcanic aerosols, as shown in Anet et al. (2013a). The major warming over the Bering Sea originates from a strengthening of the northward surface winds inducing a positive meridional wind stress anomaly above the northwestern Pacific and the opposite – namely a weakening of the northward surface winds inducing a negative anomaly of the meridional wind stress – in the northeastern Pacific region (not shown). This facilitates ocean upwelling via the Ekman mechanism at this region, where deep water upwelling prevails (oceanic conveyor belt). The surface water of the northern Bering Sea region, cooling down during the winter season, is being replaced by deeper, older water from the thermocline region, which has no imprint of the volcanic signal yet, as indicated by a slight increase of the modeled vertical ocean mass transport in the winter season in that region. The warming signal is being so strong that it persists throughout the year. This result, though it seems consistent, should be confirmed by using a higher number of ensemble members to assure its robustness, which would go beyond the scope of this work. Both the BU and the VOLC simulations show a slight, but not significant warming over the north Atlantic. One might speculate that the warming pattern shown in ALL results from a combination of volcanic and solar influences

The TD experiment does not reveal any statistically significant temperature anomalies neither in the yearly, nor in the seasonal means. The EPP forcing does not produce any annual mean response, however, a strong winter warming pattern is simulated during the boreal winter over the northern polar regions (see Fig. S 5.2). The temperature response for the EPP case is much weaker and appears in a completely different location than in the previous studies (e.g., Calisto et al., 2011; Rozanov et al., 2012b). This can be explained by the fact that our EPP experiment is designed in a significantly different way: While in Calisto et al. (2011) and Rozanov et al. (2012b), the sensitivity study was done by comparing a simulation with enabled EPP parameterization to a simulation with disabled EPP parameterization, we compare a simulation with transient EPP to a simulation with constant 1780 EPP forcing. Hence the decreasing SEP and LEE ionization rates might compensate the effect of increasing GCRs.

Compared to the climate simulations of Calisto et al. (2011) or Rozanov et al. (2012b), the lower amplitude of the simulated anomalies is attributed to a different stratosphere–troposphere exchange behavior from SOCOL3-MPIOM, whose atmospheric transport model is based on ECHAM5, compared to SOCOL2, basing on ECHAM4. Especially the winter polar vortex represents a key factor determining how stratospheric influences can propagate down into the troposphere. Stratospherically induced disturbances in the polar vortex may lead to short-lived vortex breakdowns, facilitating the advection of warmer air masses from the midlatitudes into higher latitudes at the surface. A subsequent warm anomaly is the consequence. In both the before-mentioned works, strong warm 2-m temperature anomalies were found during the winter season over Europe and western Asia. This finding cannot be confirmed with our modeling results, which show a small, but significant warming over the polar region. The exact reason of this different behavior has not yet been found, but origins likely in a weaker winter vortex in SOCOL3-MPIOM. The deficiency is confirmed by the lack of any significant temperature response to the TD and EPP signal over Europe – which could possibly be improved by modifying the gravity wave parameterization in ECHAM5.

In agreement with Robock and Mao (1992), Kirchner et al. (1999), and Driscoll et al. (2012), or to the DM analysis of Fischer et al. (2007), we discern a significant winter warming pattern (WWP) over Europe, Russia and parts of Northern America in the years following the volcanic eruptions (Fig. 5.3 b) and a cool anomaly during the summer seasons following the volcanic eruptions (Fig. 5.3 a). The warming in DJF is caused by a slight shift of the NAO to a NAO+-like phase, enhancing the westerlies (see Fig. 5.3 d) and influences the precipitation patterns (see later). The
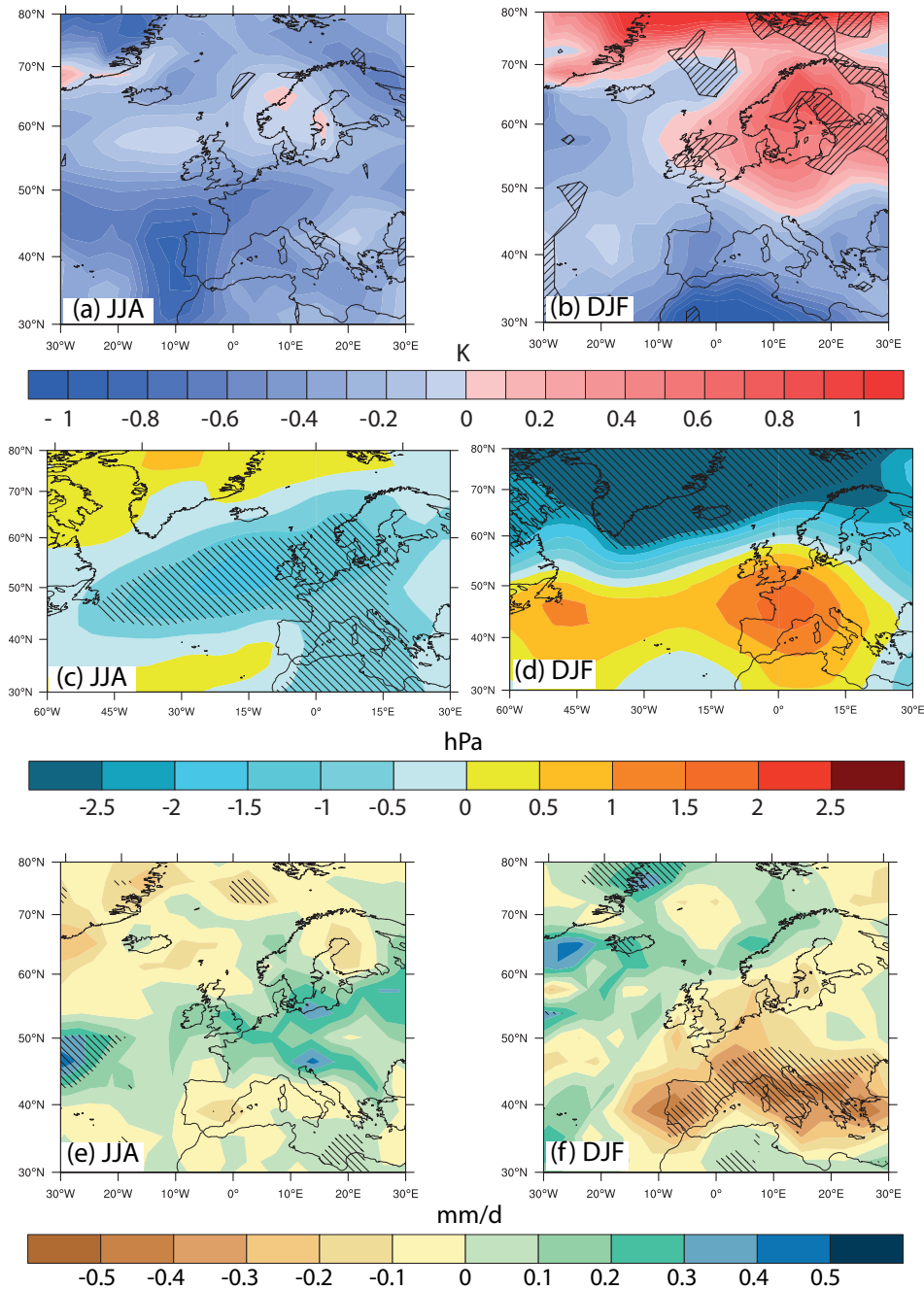
Figure 5.3: Ensemble mean of post-volcanic surface temperature (a, b), sea level pressure (c, d) and precipitation (e, f) anomalies, showing the difference between VOLC (4 years: 1810, 1816, 1832 and 1836) and CTRL1780 (60 years) in the JJA (left) and DJF (right) season. For all plots, dashed areas show significant changes on a 10% t-test (two sided t-test).

axis of the NAO pattern is slightly tilted counterclockwise (see climatology in Fig. S 5.3).

We now focus on the temporal evolution of the temperature anomalies during the DM (Fig. 5.4). For these illustrations, values of the CTRL1780 experiment were subtracted from the ALL, VOLC and BU time series. The internal variability of CTRL1780 is relatively small (σ global, annual ensemble mean (AEM) = 0.095, σ NH AEM = 0.154, σ SH AEM = 0.099).

Compared to CTRL1780 the ALL experiment (Fig. 5.4 a) shows a significant decrease in global mean temperatures starting in 1809. After the temperature minimum following the Tambora eruption (1815) the modeled temperatures show a slight recovery, but do not completely reach normal condition. After 1830, a second decrease in temperatures follows. We note that before 1809, all experiments show a very similar temperature evolution and that the strong volcanic eruptions (1809, 1815, 1831 and 1835), cause
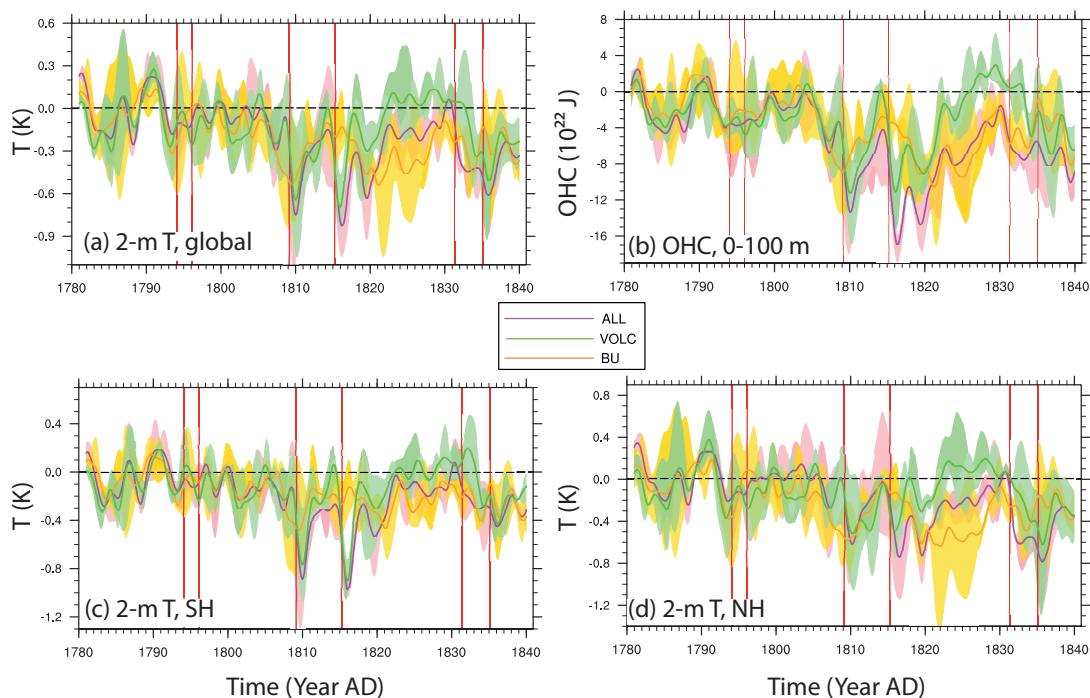
Figure 5.4: (a): Ensemble means of detrended anomalies of experiments ALL, VOLC and BU relative to CTRL1780 for (a): global 2-m temperatures; (b): global ocean heat content (OHC) of the upper ocean (first 100 m of depth); (c): SH 2-m temperatures; (d): NH 2-m temperatures. For all experiments, the envelope shows the min/max values. Red vertical lines highlight the years, at which a volcanic eruption occurred.

a clear excursion to low temperatures. These signals are clearly visible in the ocean heat content (Fig. 5.4 b). Again, four short-term reductions in the ALL run can be recognized after the volcanic eruptions, however with a delay of 2 to 4 years due to the thermal inertia of the ocean. Until 1830 the SH mean temperature evolution (Fig. 5.4 c) is very similar to the global mean. However, the volcanic eruptions after 1830 have a smaller influence on SH temperatures, as the Babuyan Claro (1831) and Cosiguina (1835) eruptions are of smaller size than the 1809 and 1815 eruptions and also characterized by a higher aerosol loading in the NH than in the SH. Due to the smaller direct aerosol forcing and to the much higher internal variability of the climate system in the NH than in the SH, the cooling signal after 1809 is far more difficult to recognize in Figure 5.4d. However, a significant decrease in temperatures of the ALL experiment is simulated after 1815 as well a second dip to lower temperatures drop after 1830.

The cooling after 1809 can be partially explained by the volcanic eruptions of 1809, 1815, 1831 and 1835. The green curve in Figure 5.4a and b of the VOLC experiment shows negative excursions at exactly those years. However, a clear recovery to pre-1809 temperatures is simulated after 1817. The next decrease in temperatures appears only after the 1831 volcanic eruption. Focusing on the volcanic response a clear inter-hemispheric difference is found: While in the SH, especially the 1809 and 1815 volcanic eruptions are well visible, the NH seems to be more responsive to the 1831 and 1835 volcanic eruptions. This is consistent with the different stratospheric aerosol loading. The temperature increase in the NH from 1813 to 1820 back to unperturbed temperature levels – and even positive anomalies in the 1820s –represents a supercompensation-like feature simulated by our model after each strong volcanic eruption. As it will be shown later, this warm anomaly pattern is caused by oceanic influence. The short-term warming right after preindustrial volcanic eruptions can be explained by a small, but significant increase in tropospheric ozone concentrations after the volcanic eruptions, acting as a greenhouse gas. This increase of ozone is related to a reduction of the production rate (less radiation, less water vapour) of the hydroxyl radical OH, which is a very efficient factor of the ozone destruction. This increase is especially pronounced over the NH due to larger CO concentrations.

In order to explain the rather low temperatures of ALL between 1817 and 1830, an additional mechanism to the volcanic eruptions only has to be considered: The BU ensemble mean in Figure 5.4 a and b describes a negative anomaly in temperatures and OHC from 1808 on. Those below-normal conditions persist until the year 1839, and are by far stronger in the NH (Fig. 5.4 d) than in the SH (Fig. 5.4 c) due to

greater amount of land masses. Our model results even suggest an unprecedented cool period in the NH in the 1820s following the BU scenario. This period would even have been colder than the simulated and reconstructed (see later) post-Tambora era (1816-1818), hence pointing at the importance of the volcanic eruptions during the DM, which interfered with the solar-only forcing effects.

In the ocean, a downward propagation of the signal from shallow to more deep layers is illustrated in Figures 5.5 a to c. While neither radiation with $\lambda <$250 nm nor EPP (Fig. S 5.4) seem to significantly influence the ocean heat content at any level, the radiation with $\lambda >$250 nm (Figure 5.5 b) and volcanic (Figure 5.5 c) signals propagate down to deeper ocean layers. In Figure 5.5 a, we note that while the
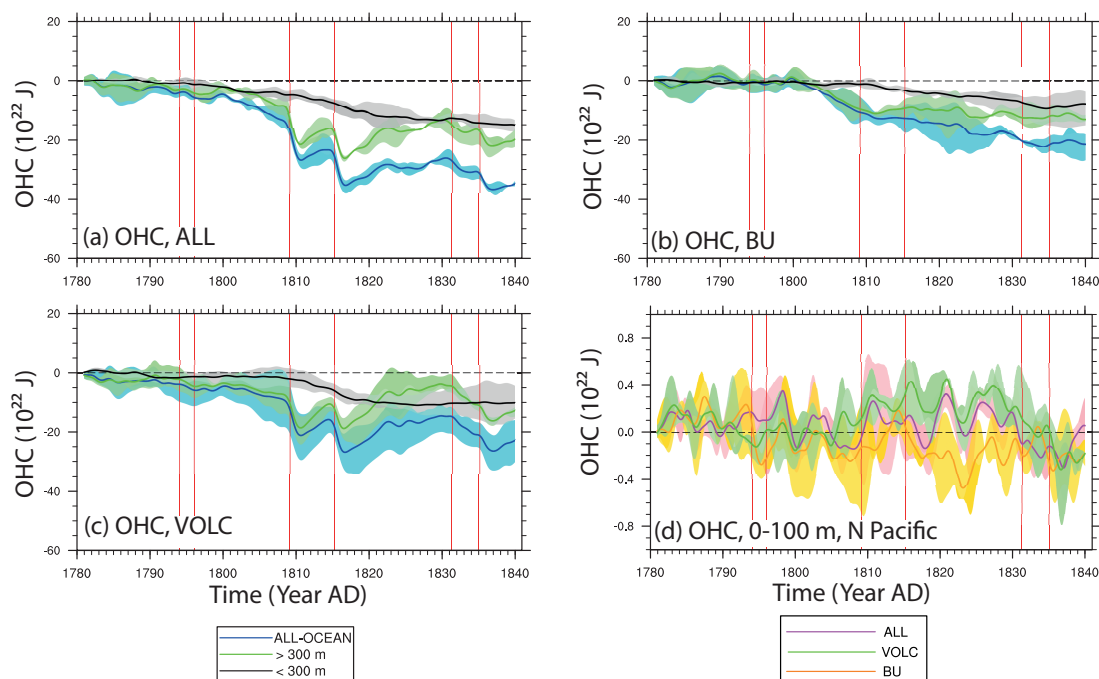
Figure 5.5: Ensemble mean of detrended global ocean heat content (OHC) anomalies relative to CTRL1780, plotting technique analogue to Stenchikov et al. (2009). For a-c: Black curve shows global total OHC (0 m–6020 m), green curve global OHC of the top 300 m, blue curve global OHC of the layers below 300 m (300 m–6020 m). (a): For ALL; (b): BU; (c): VOLC. (d): Ensemble mean of local OHC anomalies relative to CTRL1780 for the layers between 0 and 100 m of depth for the northern Pacific, Bering Sea region. Envelope shows the min/max values. Red vertical lines highlight the years, at which a volcanic eruption occurred.

upper layers (green curves) still show a small recovery after the volcanic eruptions, taking around 5–8 years, there is no signal of recovery in the deep ocean (black curves) during the DM period. Moreover, on one hand, the bottom-up signal (Fig. 5.5 b) takes more time to influence the ocean heat content in deeper layers than the volcanic eruptions (Fig. 5.5 c), which is due to the lower net irradiance anomaly in the solar forcing than in the volcanic forcing. On the other hand, the persistence of the BU-signal among all layers is more constant than the volcanic imprint due to the lack of "peaks" of activity. Still, the BU-scenario is only the second strongest contributor to changes in the deep-layer ocean heat content, ranging behind the volcanic eruptions. One should especially note that while the uppermost layers of the VOLC experiment recover quite quickly (Fig. 5.5 c, green curve), the signal stays memorized in the ocean, being rapidly transported into deeper layers (Fig. 5.5 c, black curve).

Globally, a superrecovery of OHC during the 1820s is simulated for the VOLC experiment: This positive anomaly can be explained when focusing on the Bering Sea region (Figure 5.5 d), which can explain more than half of the global ocean heat content increase by the volcanic contribution.

Stenchikov et al. (2009) also investigated the influence of the Tambora eruption on the ocean. For all layers our simulated OHC anomaly is more pronounced, which can be explained by the lack of the 1809 volcanic eruption in the work of Stenchikov et al. (2009), but also by the fact that the Tambora eruption in our study has a larger radiative impact on the SH (and thus on the oceans) than in Stenchikov et al. (2009). The half-life of the signals, however, is comparable to each other (Stenchikov et al. (2009): 16 years for 0.5 times the total OHC recovery. VOLC-experiment: 13 years needed for 0.45 times the total OHC recovery). The imprint of the lower OHC of Stenchikov et al. (2009) seems, however, to be much smaller than ours (10×10^{22} J versus 5.5×10^{22} J), even if one would subtract the effect of the 1809 volcano in our sensitivity study. A possible explanation would be a faster deep water formation in MPI-OM than in CM2.1. This goes however beyond the scope of this work.

As neither the EPP nor the TD curves show large significant changes in the OHC (Fig. S 5.4), we conclude that although volcanic eruptions most likely kicked in the colder DM period, it was the reduction in the radiation with $\lambda >$250 nm which maintained the low temperatures until the late 1830s.

5.4.2   Comparison to proxies

Back in the past, regular reliable temperature measurements were only done in some specific locations, especially in Europe, with some station records starting around 1750 (Jones et al., 2001). Further back, one has to rely on proxy-based reconstructions. Different techniques and sources for 2m-temperature reconstructions are available, and the absolute values and variability amplitudes differ amply from one to another data set. Most of the proxy data originates from tree rings. Not all techniques of tree-ring based (also known as "dendrochronological") temperature reconstructions are generally accepted by the scientific community (e.g. Cecile et al., 2013). Furthermore, there is ongoing discussion if dendrochronological proxies are at all a good basis for robust reconstructions of temperature anomalies during volcanic active periods (e.g. Tambora, 1815–1816, see also Mann et al., 2012; Anchukaitis et al., 2012). Moreover, the exact dating may not always be accurate enough to match exactly a specific (e.g. volcanic) event due to proximity effects ("wrong" exposition of the tree at that particular year, e.g. in the shadow). Here, we use the best-known NH temperature reconstructions published in the Intergovernmental Panel on Climate Change, IPCC, Climate change 2007 (2007), in order to allow comparison with other, similar modeling studies (e.g. Wagner and Zorita, 2005). We focus on NH temperature reconstructions since the density of proxy data is higher over the NH than over the SH and, therefore, NH data are expected to be more reliable. In Figure S4, the five different reconstructions of the NH temperatures used in this work are illustrated (Jones et al., 2001; Esper et al., 2002; D'Arrigo et al., 2006; Briffa et al., 2001; Mann et al., 1999).

In Figure 5.6, the temperature evolution of the NH 2-m temperatures of the ALL, VOLC and BU experiments is compared to reconstructions, represented by a grey envelope. The general anomaly pattern shown for the ALL experiment, that means, positive anomalies until the beginning of the 19th century, followed by a strong cooling between 1810 and 1820, a warmer period in the 1820s and a further temperature minimum around 1835, agrees very well with the reconstructed temperatures.

The first 30 years of the ALL time series are characterized by a slight temperature decrease, overlain by the 11-year solar cycle. As obvious from the sensitivity run BU, the temperatures follow the decline in solar irradiance of the Shapiro et al. (2011) forcing (Fig. 5.6, top panel). The cooling after the two smaller volcanic eruptions in the 1790s overcompensates the pure solar signal. While most of the reconstructions also show a 11-year-like cycle (Fig. S 5.5), the dating of the minima and maxima differs
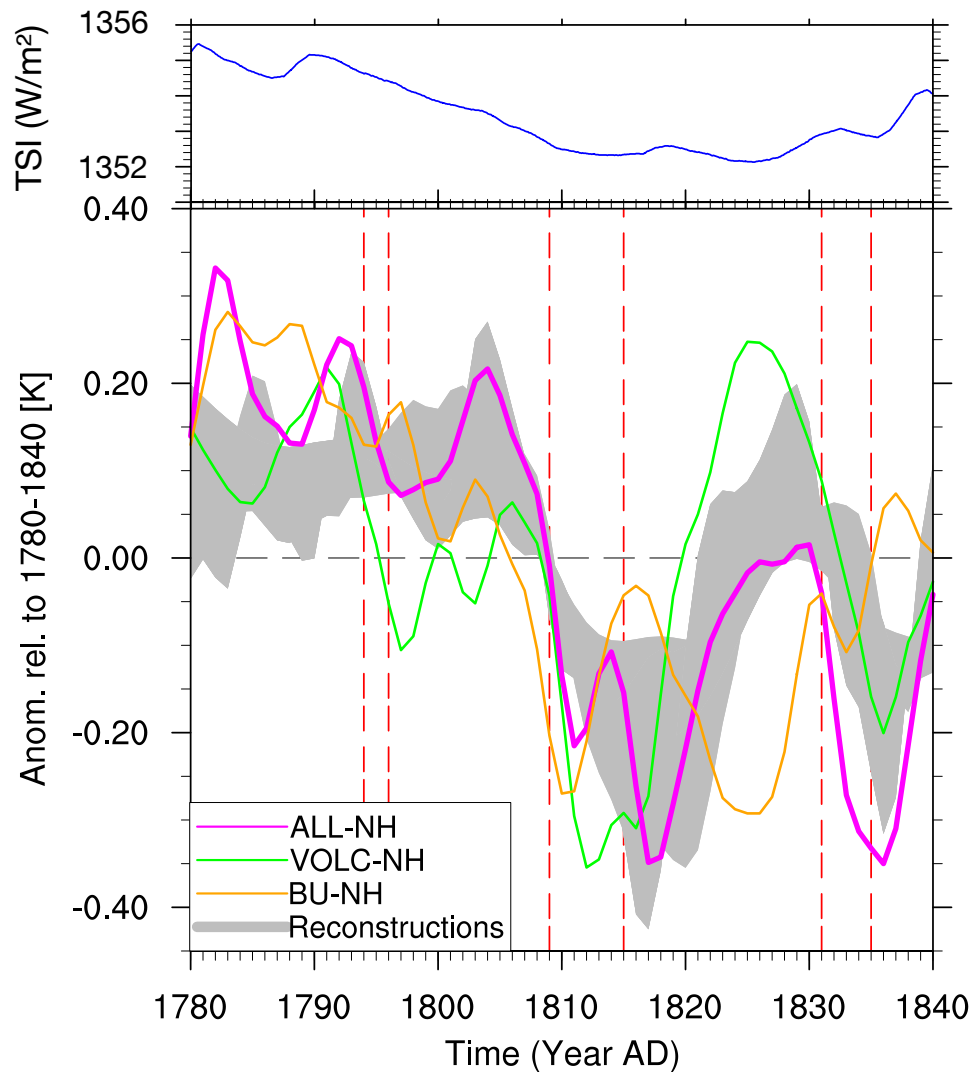
Figure 5.6: Top panel: Total solar irradiance from the Shapiro et al. (2011) forcing. Lower panel: Model comparison with five NH temperature reconstructions of the IPCC AR4 (averaged). Magenta, green and orange lines are model curves, the grey envelope the composite of a range of tree-ring-based reconstructions. Magenta thick: ensemble mean of NH temperatures (ALL-NH). Green: same, but for the VOLC experiment (VOLC-NH). Orange: same, but for the BU experiment (BU-NH). Grey region: Envelope of the five NH temperature reconstructions plotted in Figure S2 in the supplementary material. Smoothing of the model results: Gaussian 3 years FWHM, centered on year 1. Red vertical, dashed lines highlight the years, at which a volcanic eruption occurred.

among the data sets, leading to a rather diffuse picture.

Starting from around 1805 until 1816 both the reconstructions and the modeled temperatures show a strong cooling by up to 0.6 K. During that period, the ALL experiment is in very good agreement with the composite of the reconstructions, although a slight overestimation of the 1809 volcanic induced cooling in 1811-1812 is visible. After the two major volcanic eruptions in 1809 and 1815, the temperatures in the ALL experiment show a clear recovery until the year 1826. A very similar behavior is observed in the reconstructions, although the warming in the 1820s is stronger than in the ALL simulation. As can be seen from the sensitivity runs BU and VOLC, the simulated temperature behavior can be explained as a combination of solar and volcanic effects: The BU experiment shows that the solar-only driven cooling starts already around 1803, but the overall cooling is slightly postponed by a compensating warming by the earlier volcanic eruptions. The eruption of Mt. Tambora in 1815 overcompensates the solar induced warming after 1810, leading to a temperature minimum around 1816/17, while the solar minimum around 1822 (BU) prevents a more pronounced warming during the 1820s as visible in the model experiment VOLC.

The two volcanic eruptions of 1831 and 1835 with a predominant NH aerosol loading are followed by a second pronounced cold period, which is visible in the model simulations as well as in the reconstructions. Also, the simulated amplitude of this cooling with 0.3-0.4 K is similar to the reconstructions.

Finally, the model simulation shows a warming after 1836, which can be explained by a general increase in solar irradiance at the end of the DM as well as dilution and removal of volcanic aerosols in the stratosphere. The warming is also found in the reconstructions.

It should be mentioned that the separation of solar and volcanic effects as done in BU and VOLC neglects non-linear feedbacks. Nevertheless, we conclude that only the combination of both volcanic events and BU decrease is able to reproduce the reconstructed temperature patterns. Moreover, we suggest that a solar-only driven DM would have induced two cold periods in the 1810s and 1820s. Those were overcompensated by a strong VOLC warming signal in the ALL temperature pattern.

5.4.3 Precipitation and tropospheric circulation

Figure 5.7, illustrates the absolute difference in seasonal averaged precipitation (JJA and DJF) for the ALL and VOLC run relative to the constant forcing run CTRL1780. As can be recognized, the intertropical convergence zone (ITCZ) is shifted northwards to the equatorial Atlantic. Furthermore, a sharp decrease in precipitation both during the boreal summer and winter is modeled over the "El Niño" region, eastern Central America, and the maritime continent.

An interesting feature is the strong increase in precipitation over the Himalayan region as well as over the eastern part of the Indian Ocean. The surplus of precipitation in the Himalayan region is due to an increased northeasterly flow, coming from a northward shift of the ITCZ. In contrast, the precipitation anomaly over the western Pacific is related to a change in sea surface temperatures in the El Niño 3 region, which is consistent to a reduced evaporation, a modified circulation and a significant change in the ENSO signal, impacting – via the atmosphere – also the precipitation patterns in the Indopacific region - corresponding to the mechanism presented in McGregor and Timmermann (2011). The decomposition of the ALL forcing plot into the four different
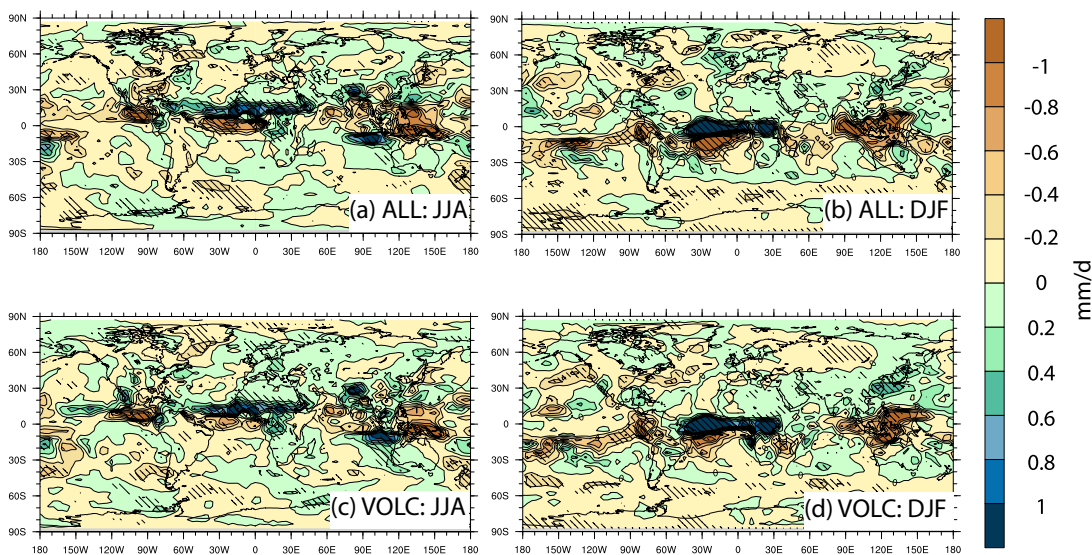
Figure 5.7: (a): Ensemble mean of precipitation anomalies, averaged over the 1805-1825 period for the ALL run, JJA season. (b): Same for DJF season. (c): Same for the VOLC run, JJA season. (d) Same for the VOLC run, DJF season. For all plots, dashed areas show significant changes on a 10% t-test.

forcing factors (EPP, $\lambda <$250 nm, $\lambda >$250 nm and VOLC) shows that neither the solar forcing ($\lambda <$250 nm, $\lambda >$250 nm) nor the energetic particles significantly influence the seasonal or annual precipitation patterns. Hence, only the volcanic run is illustrated here (Fig. 5.7 c, d) as it is the only run which shows a very similar precipitation anomaly pattern as in the ALL run.

A possible explanation for those precipitation anomalies lies both in the modified strength and width of the Hadley- and Ferrel cells. In Figure 5.8, the mass stream function (MSF) anomalies of the ALL and VOLC runs with respect to the CTRL1780 run are illustrated. During the boreal summer season (JJA), the Hadley cell is significantly weakened (Fig. 5.8 a) – most probably due to the volcanic eruptions (Fig. 5.8 c).
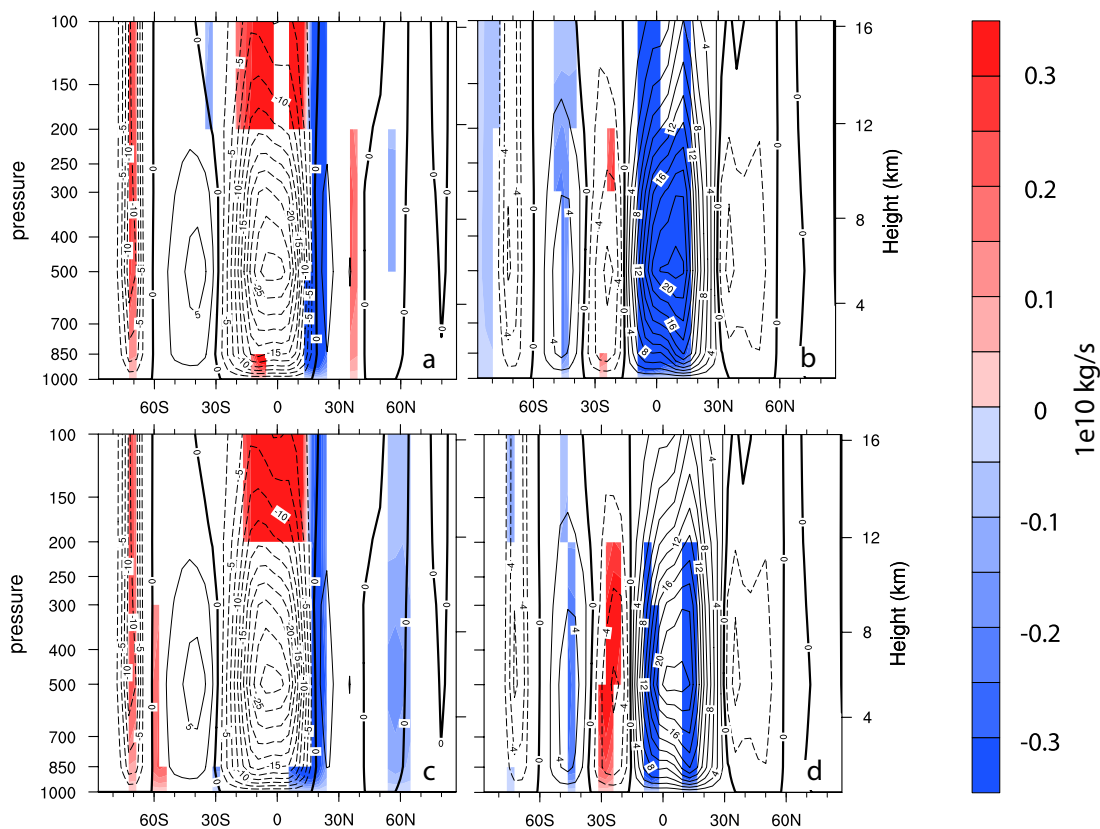
Figure 5.8: (a): Ensemble mean of mass stream function anomalies, averaged over the 1805-1825 period for the ALL run, JJA season. (b): Same for the DJF season. (c): Same, but for the VOLC run, JJA season. (d): Same, but for the VOLC run, DJF season. For all plots, coloured areas show significant changes on a 10% t-test. Black contour lines show the climatology for the two seasons.

Moreover, the Hadley cell expands in a northward direction (sharp decrease of the MSF field in Fig. 5.8 a and c at 20°N, meaning that the background climatology illustrated as contour lines would expand towards the NH). During the winter season (DJF), we find a significant weakening of the Hadley cell (Fig. 5.8 b and d) and a weak, yet significant decrease of the South hemispheric Ferrel cell. The size of the cells are not significantly modified during the boreal summer season.

A similar signal has been found in Wegmann et al. (2013), who investigated the temperature and precipitation patterns after volcanic eruptions in preindustrial times. They concluded that a changed monsoon pattern and a modified behavior of the tropospheric circulation cells right after the volcanic eruptions is able to modify the global circulation, influencing short-term (some years) climate patterns over continental Europe. Although our seasonal precipitation signal is rather weak over Europe, we investigate the short-term climate pattern changes right after the different tropical volcanic eruptions (1810, 1816, 1832, 1836). Over Europe, the boreal winter SLP field (Fig. 5.3 d) seems to switch to a more NAO+-like situation, facilitating the transport of moist air from the Atlantic to the British Islands and further to Scandinavia, while continental Europe stays in the slight influence of the anticyclonic pattern of the Azores. This NAO+-like pattern influences the precipitation distribution, triggering a significant decrease over continental Europe and a slight increase over the British islands (Fig. 5.3 f). The temperatures do change as well (Fig. 5.3 b), but only marginally over continental Northern Europe, and show a slightly positive anomaly, according to the known "winter warming pattern" (see e.g. Robock and Mao, 1992; Kirchner et al., 1999; Luterbacher et al., 2004). These results are in agreement to the work of e.g. Iles et al. (2013), which found dryer winters and wetter summers after volcanic eruptions, as we do. During the summer seasons following strong volcanic eruptions, a cold anomaly signal is found (Fig. 5.3 a), which is likely to be triggered by a significant low-pressure anomaly over continental Europe and the storm track region (Fig. 5.3 c), leading to a signal resembling to a wet anomaly over large parts of Europe (Fig. 5.3 e).

5.5 Conclusions

We have performed a series of sensitivity experiments over the DM with an AO-CCM, varying successively the solar radiation with $\lambda <$250 nm, the solar radiation with $\lambda >$250 nm, volcanic aerosols and energetic particles.

The results show that volcanic eruptions alone cannot explain the long-lasting negative surface air temperature anomaly during the DM found in different NH temperature reconstructions. Yet, while the long-term negative temperature trend in the DM can be explained by the "bottom-up" approach when reducing only radiation with $\lambda >$250 nm, the latter cannot explain the short and strong temperatures dips right after the volcanic eruptions. On the other hand, the volcanic eruptions cannot explain the cooler-than-average period in the 1820s.

We thus conclude that volcanic eruptions might have triggered the cold period from 1809 on, but that this cold time was maintained after 1816 by a lower solar irradiance. Without the decrease in solar irradiance, our model suggests that temperatures would have recovered to pre-1809 temperatures from 1820 on, except in the deep layer ocean, in which the volcanic signal seems to dominate over the solar signal.

The obtained results indicate that a strong solar irradiance changes suggested by Shapiro et al. (2011) do not cause unrealistically large surface temperature changes during the DM but rather help to reach a good agreement between simulated and reconstructed temperatures. This result contradicts the work of Feulner (2011a) which found a very large disagreement between surface temperature reconstructions and their model simulations using the solar irradiance forcing from Shapiro et al. (2011).

Our model results suggests moreover that without the two strong 1809 and 1815 volcanic eruptions, the NH would have suffered a very cold period in the 1820s, possibly putting the majority of the Earth's inhabitant into a problematic situation (famines). Only the "overcompensation" of the cold anomaly after 1816 by the VOLC scenario in the Bering Sea reagion seems to have prevented this solar-induced cool period.

Our sensitivity studies show that the solar influence on the tropospheric climate is related to the bottom-up mechanism, while the efficiency of the stop-down mechanism is negligible. We do not see any significant manifestations of the top-down mechanism (cooling in the lower tropical stratosphere (Anet et al., 2013a), modulation of the Hadley cell and surface temperature changes in the Northern Hemisphere during boreal winter). Moreover, the simulated wintertime warming over the northern landmasses after the major volcanic eruptions is not well pronounced and only marginally significant.

The reasons for the weak efficiency of the top-down mechanism in our results are not clear. It can be related to model deficiencies in the simulation of the vertical coupling, of the polar vortex state or of the wave generation and propagation. It is well possible that an interactive ocean damps the top-down and winter warming signal disproportionally, so that the signal disappears in the rather high noise of the NH temperature signal. The underestimation of the solar UV irradiance changes suggested by Shapiro et al. (2011) in comparison with the latest satellite measurements (Ermolli et al., 2013) could also be a reason, because a stronger UV forcing can make the top-down mechanism more efficient (see e.g. Ineson et al., 2011). The other unexpected result is the weak influence of energetic particles which can be explained by the absence of ozone response to the effects of low energy electrons discussed by Anet et al. (2013a) and probably some compensation between enhanced ionization by GCR and depressed ionization by electrons and protons during the DM.

We also show that due to volcanic eruptions, the hydrological cycle can be perturbed as such to decelerate the Hadley and Ferrel cells for a certain time. At the same time, the NAO is pushed into a NAO+-like phase in the winters following a volcanic eruption, leading to an increase in precipitation in northern Europe and a negative precipitation anomaly in southern Europe. Still, the precipitation anomaly is weaker than in other publications cited in our manuscript.

It is possible that our chosen timing in the volcanic forcing data (date of the year) of the 1809 and 1831 eruptions are wrong. This could of course influence the results discussed in the manuscript, as the timing (in the year) of the eruption determines in which hemisphere most of the volcanic aerosol will be transported. Moreover, characteristics of the stratospheric dynamics in the DM – such as the QBO which was nudged in our model and in the volcanic forcing calculation – are only reconstructed, and not observed. Also here, a certain margin of uncertainty persists, possibly influencing our results. The anomalies in temperature and precipitation might be more significant, as only two month of difference in the volcanic eruption lead to different results (as stated and shown in e.g. Kravitz and Robock, 2011; Toohey et al., 2011; Driscoll et al., 2012).

This is also a reason why the upwelling mechanism in the Bering Sea region, leading to the overcompensation-like temperature signal after the strong volcanic eruptions should be considered with interest, but with care. A different timing of the eruptions might lead to a different reaction not only of the tropospheric circulation cells, but also

of the ocean. Also, internal variability might be a reason for the simulated response of the Bering Sea region.

Future investigations should be done focusing on the downward propagation of the stratospheric perturbations in a model with prescribed sea surface temperatures versus a model with interactive ocean. As well future research should investigate to what extent the impact of decreasing SEP/LEE efficiency can compensate increasing GCR influences on regional temperature changes. The upwelling signal in the Bering Sea region should be confirmed with a different timing of the volcanic eruptions and another model setup. Moreover, the statistical testing procedures should be consolidated by increasing the number of ensemble members.

5.6   Acknowledgements

5.7   Appendix

Supplementary Material for CPD Manuscript

"Impact of solar and volcanic activity variations on tropospheric temperatures and precipitation during the Dalton Minimum" by J. G. Anet Institute for Atmospheric and Climate Science ETH, Zurich, Switzerland

S. Muthers Climate and Environment Physics, Physics Institute, University of Bern, Switzerland Oeschger Centre for Climate Change Research, University of Bern, Bern, Switzerland

E. V. Rozanov Physikalisch-Meteorologisches Observatorium Davos and World Radiation Center (PMOD/WRC), Davos, Switzerland

C. C. Raible Climate and Environment Physics, Physics Institute, University of Bern, Switzerland Oeschger Centre for Climate Change Research, University of Bern, Bern, Switzerland

A. Stenke Institute for Atmospheric and Climate Science ETH, Zurich, Switzerland

A. I. Shapiro Physikalisch-Meteorologisches Observatorium Davos and World Radiation Center (PMOD/WRC), Davos, Switzerland

S. Broennimann Institute of Geography, University of Bern, Switzerland Oeschger Centre for Climate Change Research, University of Bern, Bern, Switzerland

F. Arfeuille Institute of Geography, University of Bern, Switzerland Oeschger Centre for Climate Change Research, University of Bern, Bern, Switzerland

Y. Brugnara Institute of Geography, University of Bern, Switzerland Oeschger Centre for Climate Change Research, University of Bern, Bern, Switzerland

J. Beer Eawag, Surface Waters group, Switzerland

F. Steinhilber Eawag, Surface Waters group, Switzerland

W. Schmutz Physikalisch-Meteorologisches Observatorium Davos and World Radiation Center (PMOD/WRC), Davos, Switzerland

and

T. Peter Institute for Atmospheric and Climate Science ETH, Zurich, Switzerland

As supplementary electronic material, five (5) PDF figures are published online.
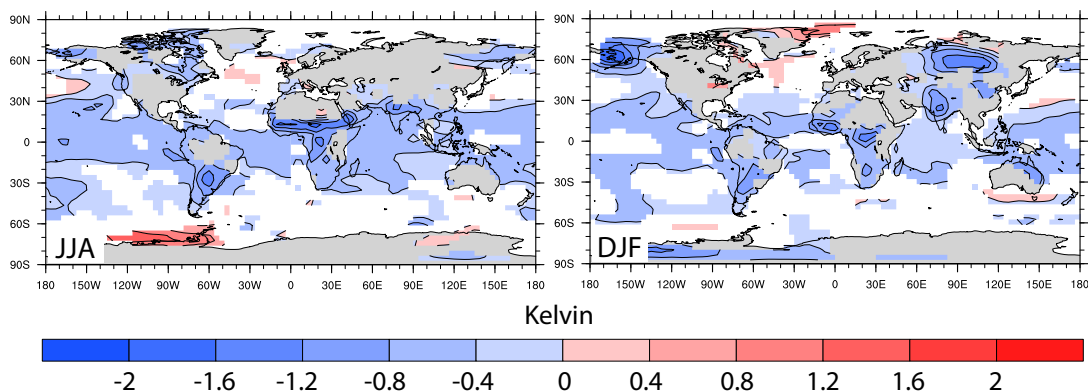
Figure S 5.1: Ensemble mean of 2m-Temperature differences, averaged over the 1805-1825 period for the ALL run, JJA (left) and DJF (right) seasons. Only areas which are significant at the 5% level are colored (two sided t-test).
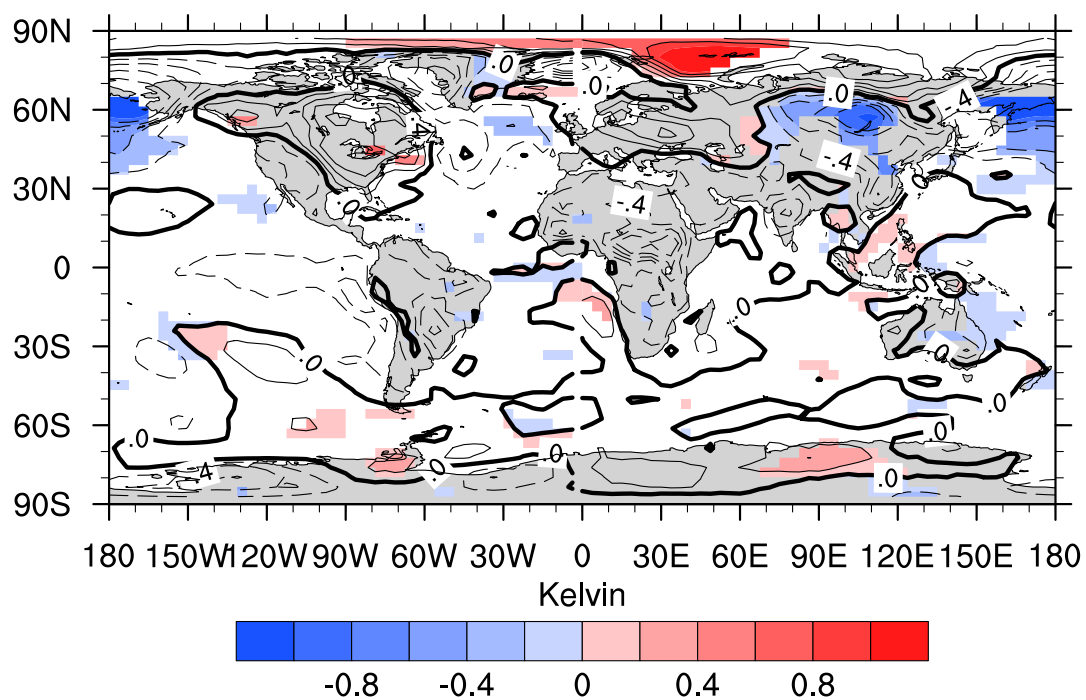
Figure S 5.2: Ensemble mean of 2m-Temperature differences, averaged over the 1805-1825 period for the EPP run, boreal winter season (DJF). Only areas which are significant at the 5% level are coloured (two sided t-test).
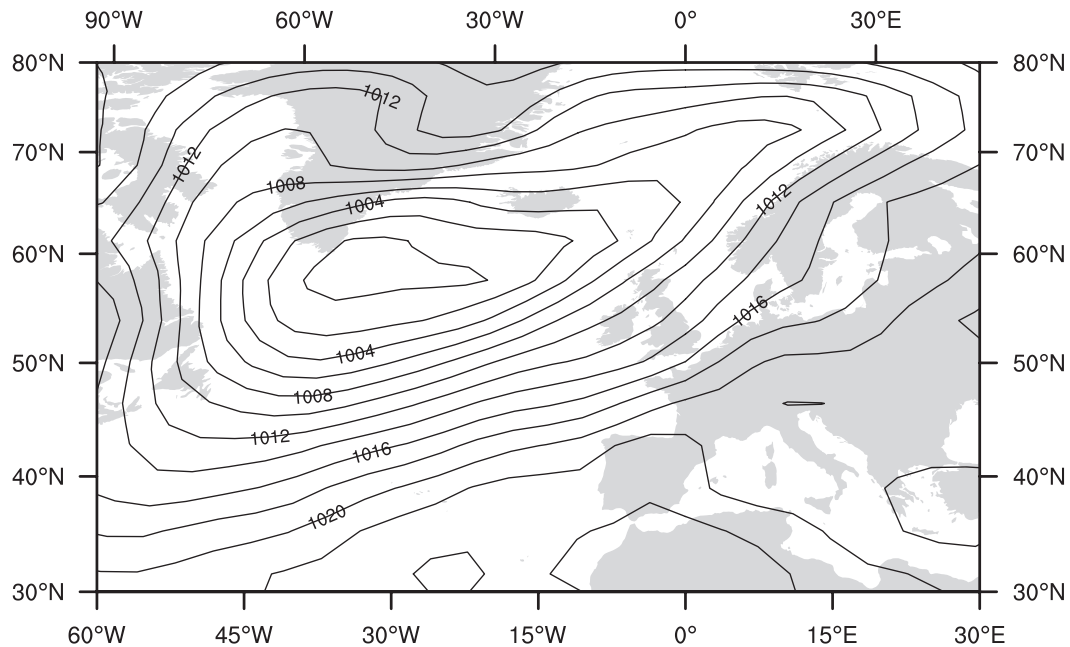
Figure S 5.3: Climatology of the sea level pressure patterns during the boreal winter season (DJF) of the ALL experiment.
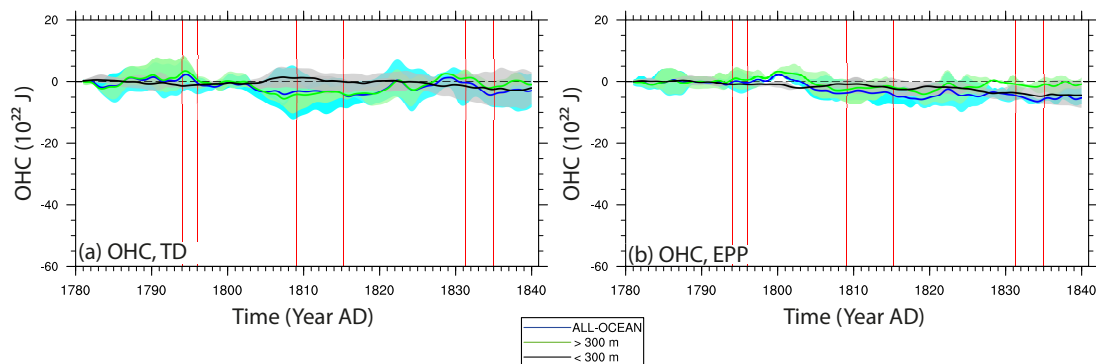
Figure S 5.4: Ensemble mean of detrended global ocean heat content (OHC) anomalies relative to CTRL1780, plotting technique analogue to Stenchikov 2009. For a and b: Black curve shows global total OHC (0 m-6020 m), green curve global OHC of the top 300 m, blue curve global OHC of the layers below 300 m (300 m-6020 m). Envelope shows the min/max values. (a): For TD; (b): for EPP. Red vertical lines highlight the years, at which a volcanic eruption occurred.
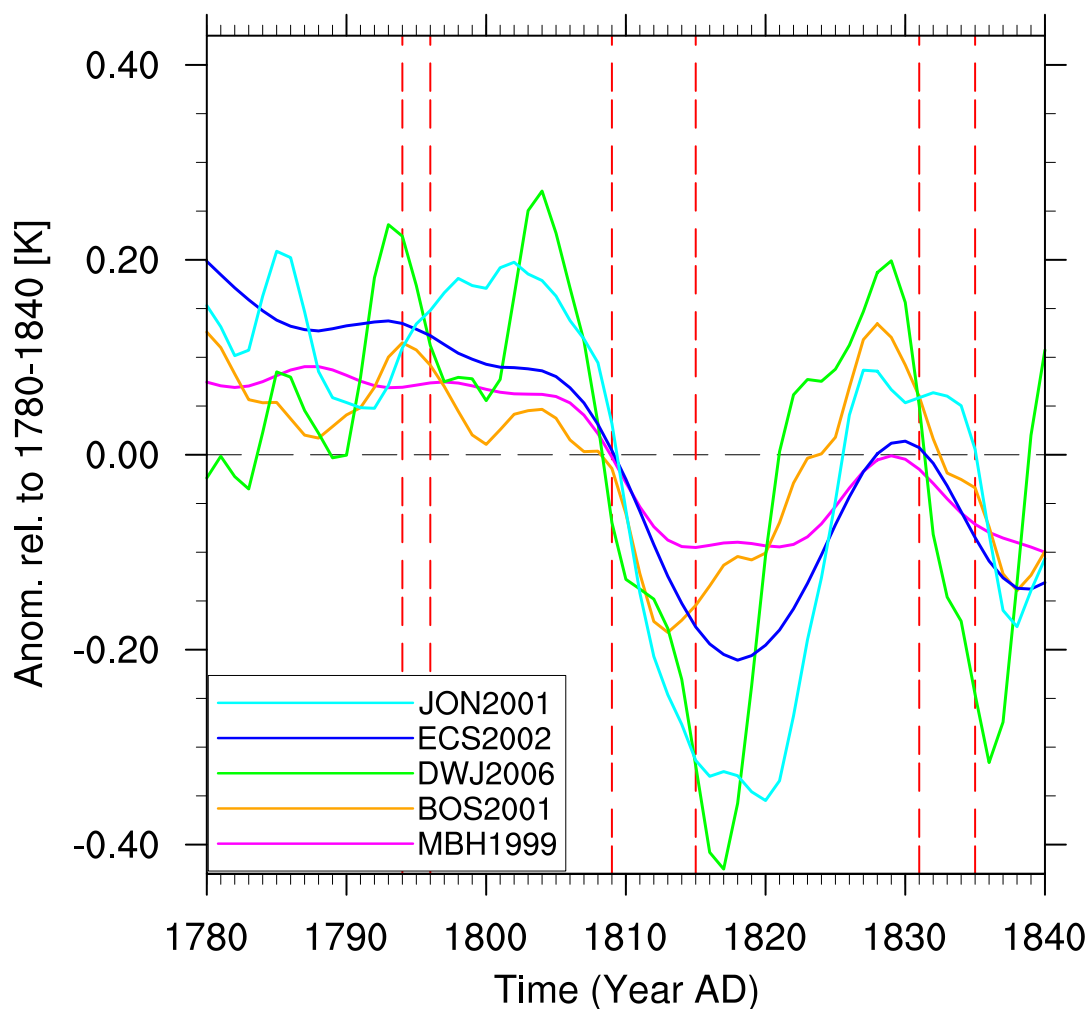
Figure S 5.5: Northern hemispheric temperature reconstructions following IPCC AR4. Cyan, JON2001: Jones et al. (2001); Blue, ECS2002: Esper et al. (2002); Green, DWJ2006: d'Arrigo et al. (2006); Orange, BOS2001: Briffa et al. (2001); Magenta, MBH1999: Mann et al. (1999). Red, dashed vertical lines highlight the years, at which a volcanic eruption occurred.

Chapter 6

Impact of a potential 21$^{\text{st}}$ century "Grand Solar Minimum" on surface temperatures and stratospheric ozone

J.G. Anet[1], E. Rozanov[1,2], S. Muthers[3,4], T. Peter[1], S. Brönnimann[4,5], F. Arfeuille[4,5], J. Beer[6], A.I. Shapiro[2], C.C. Raible[3,4], F. Steinhilber[6], W. Schmutz[2]

[1]Institute for Atmospheric and Climate Science ETH, Zurich, Switzerland
[2]Physikalisch-Meteorologisches Observatorium Davos and World Radiation Center (PMOD/WRC), Davos, Switzerland
[3]Climate and Environment Physics, Physics Institute, University of Bern, Bern, Switzerland
[4]Oeschger Centre for Climate Change Research, University of Bern, Bern, Switzerland
[5]Institute of Geography, University of Bern, Bern, Switzerland
[6]Eawag, Surface Waters group, Switzerland

6.1 Abstract

We investigate the effects of a recently proposed 21$^{\text{st}}$ century Dalton-minimum-like decline of solar activity on the evolution of Earths' climate and ozone layer. Three sets of 2-member ensemble simulations, radiatively forced by a mid-level emission scenario

(IPCC RCP4.5), are performed with the atmosphere-ocean chemistry climate model AOCCM SOCOL3-MPIOM, one with constant solar activity, the other two with reduced solar activity and different strength of the solar irradiance forcing. A future grand solar minimum will reduce the global mean surface warming of 2 K between 1986-2005 and 2081-2100 by 0.2 to 0.3 K. Furthermore, the decrease in solar UV radiation leads to a significant delay of stratospheric ozone recovery by 10 years and longer. Therefore, the effects of a solar activity minimum, should it occur, may interfere with international efforts for the protection of global climate and the ozone layer.

6.2　Introduction

Model simulations of 21ˢᵗ century climate undertaken under the CMIP5 project (e.g. Knutti and Sedláček, 2012) show global temperature increases of 1 ± 0.4 K for the RCP2.6 scenario, 1.8 ± 0.5 K for RCP4.5, 2.2 ± 0.5 K for RCP6.0 and 3.7 ± 0.7 K for RCP8.5 (Representative Concentration Pathways, e.g., van Vuuren et al., 2011). The ranges reflect inter-model differences for a given scenario, but do not include uncertainties in future natural forcings. In the CMIP5 protocol, volcanic effects are assumed to be negligible and solar activity is chosen to mimic the last solar cycle. Recently, the possibility of a future grand solar minimum was proposed to occur in the 21ˢᵗ century (Abreu et al., 2010; Lockwood et al., 2009; Steinhilber and Beer, 2013). The cooling associated with a potential solar activity decline might have implications for global warming, atmospheric dynamics, weather patterns, and for air chemistry in general and for stratospheric ozone in particular. Studies using different climate models and scenarios of solar activity changes (Feulner and Rahmstorf, 2010; Rozanov et al., 2012a; Meehl et al., 2013) concluded that global warming could be partially compensated by about 0.25 to 0.5 K.

Uncertainties in the magnitude of the solar contribution are partially related to different experimental designs: Feulner and Rahmstorf (2010) used a model of intermediate complexity with a simplified treatment of the stratospheric processes and obtain a reduction of the warming by 0.26 K. They adopted the greenhouse gas emissions following the SRES A1B scenario and applied solar activity changes without spectral resolution via a total solar irradiance (TSI) decrease by 0.08% and 0.25%. Resulting changes in ocean and land surface temperatures affect the entire atmosphere via the hydrological cycle. This mechanism is known as the bottom-up mechanism (e.g. Gray et al., 2010). On the other hand, the efficiency of the top-down mechanism (e.g. Gray et al., 2010) was probably underestimated because of the very low changes in the mid-

dle atmosphere induced by the small amplitude of the ultraviolet part of the spectrum (UV) and of the missing energetic particles. To overcome this shortcoming, Rozanov et al. (2012a) applied the CCM SOCOL in the time slice mode driven by the changes of energetic particle precipitation and spectral solar irradiance (SSI) taken from the reconstructions by Shapiro et al. (2011) for Dalton minimum conditions. However, these simulations were performed without interactive ocean. Meehl et al. (2013) used the atmosphere-ocean-chemistry-climate model (AOCCM) WACCM driven by a TSI drop by 0.25% during 50 years in the middle of the 21$^{\text{st}}$ century using the RCP4.5 emission scenario, and with an SSI decrease constructed by scaling of the solar irradiance from the NRLSSI data (Lean et al., 2005). They obtained a reduction of global warming by 0.24 K. There is presently a lively discussion of the very uncertain SSI variations over the recent past solar cycles (Haigh et al., 2010; Lean and DeLand, 2012). As Meehl et al. (2013) prescribed -0.25% less irradiance in the entire spectrum by taking the mean of the 1975, 1986 and 1996 solar minimum values of the NRLSSI data of Lean et al. (2005), the overall drop in UV is weaker than in the Shapiro et al. (2011) forcing, thus reducing the magnitude of the top-down mechanism. Shapiro et al. (2011) assumed that the minimum state of the quiet Sun in time corresponds to the observed quietest areas on the present Sun, which they represented by the "model of faint supergranule cell interior" from Fontenla et al. (1999). The resulting amplitudes of their secular solar irradiance change is larger than the other recently published estimates (see e.g. discussion in Lockwood, 2011a). This influence should be clearly seen in the ozone response and probably in the winter time temperature, but not much in the annual mean temperatues.

The potential drop in the solar UV activity can substantially affect the ozone layer (Anet et al., 2013a), which in turn affects stratospheric temperature, circulation, tropospheric climate, and the UV-intensity reaching the ground. The implications of a solar activity decline for the expected stratospheric ozone recovery later in this century (WMO, 2011) have not yet been considered in the literature. Here we analyse the influence of a strong UV decrease (Shapiro et al., 2011) and the concomitant changes in energetic particles on climate and global ozone. We use the results of transient 100-year long ensemble simulations with the AOCCM SOCOL-MPIOM. The model is driven by three scenarios of the future spectral solar irradiance, each with two members with identical anthropogenic forcing (RCP4.5, see van Vuuren et al., 2011). It uses a comprehensive middle-atmospheric chemical scheme, and a fully coupled deep ocean. Compared to Meehl et al. (2013), the applied solar forcing is much stronger in the UV spectrum and lasts for a longer time, because grand minima usually last for 70 to 110 years. Moreover, we improve the approach of Meehl et al. (2013) keeping the 11-year solar

cycle and decreasing the solar irradiance slowly to the new minimum, making it more realistic.

6.3   Model description and experimental design

The experiments are run with the AOCCM SOCOL-MPIOM which emerges from the CCM SOCOL v3 version (Stenke et al., 2013) coupled to the Max Plank Institute ocean model (Marsland et al., 2003) using the OASIS3 coupler (Valcke, 2013). The CCM SOCOL v3 is based on the GCM ECHAM5 (Roeckner et al., 2003) and includes the chemical module MEZON. The model is used in the middle atmosphere mode (MA) and does not include interactive vegetation. MA-ECHAM5 hands over temperature and tracer fields to MEZON, which calculates chemical transformations of 41 gas species participating in 200 gas phase, 16 heterogeneous and 35 photolytic reactions. The resulting tendencies of chemical species are then returned to MA-ECHAM5. Our experiments are performed with T31 spectral resolution, which equals to an average grid space of 3.75° ($\approx$400 km). In vertical direction the model domain is divided into 39 layers from the ground to 0.01 hPa. For more details see Stenke et al. (2013).

Three experiments are carried out, each consisting of two 100-year long simulations. The only difference between the experiments is the solar forcing. One experiment, named henceforward CONST, is forced by a perpetual repetition of the solar cycles 22 and 23 until the year 2100. The second and third experiments, thenceforth called WEAK and STRONG, follow the scenario of an oncoming grand solar minimum reaching its minimum in 2090, with TSI being 4 and 6 W/m^2 lower in WEAK and STRONG, respectively, as compared to CONST. In Figure 6.1, the grey curve shows the deviation of the total solar irradiance from the 1995-2005 averaged value (Shapiro et al., 2011). The oscillation shows the underlying 11-year solar cycle. These quantities are further used as proxies to calculate the future evolution of the SSI, the Ap index (describing the geomagnetic activity) and the ionization rate by galactic cosmic rays, which are necessary to drive the model (Rozanov et al., 2012b). The 4 and 6 W/m^2 lower TSI in WEAK and STRONG represent TSI decreases of 0.3% and 0.45%, respectively. The corresponding maximum changes of the spectral irradiance for the different bands of the ECHAM5 radiation code in WEAK are -10% for 180-250 nm, -1.5% for 240-440 nm, -0.2% for 440-690 nm, +0.01% for 690-1190 nm and 1190-2380 nm and -0.03% for 2380-4000 nm (Figure S 6.1 in the appendix). The SSI changes for STRONG are larger by roughly a factor 1.5. All simulations start from the year 2000. WEAK and STRONG are initialized by restart files for this year from four 400 year long transient simulation

starting from 1600, while CONST was branched from two of the 400 year long transient simulations at the year 2000. The concentrations of greenhouse gases (GHGs), ozone destroying substances (ODSs) as well as anthropogenic NO_x and CO emissions are set following the CMIP5 RCP4.5 scenario. The tropospheric aerosols are adapted from CAM3.5 simulations with a bulk aerosol model driven by CCSM3 (CMIP4) sea-surface temperatures and the 2000-2100 CMIP5 emissions (S. Bauer, pers. comm.). Stratospheric aerosols were kept at background levels excepted for four assigned volcanic eruptions (a Fuego-like volcanic eruption in 2024, a smaller volcanic eruption in 2033, an Agung-like volcanic eruption in 2060 and another smaller volcanic eruption in 2073, see Arfeuille et al. (2013a)).

6.4 Results

All runs follow a distinct warming path, yielding 1.96 ± 0.12 K (CONST), 1.75 ± 0.14 K (WEAK) and 1.61 ± 0.12 K (STRONG) change in the global annual mean surface temperature, averaged over the 2081-2100 period relative to the 1986-2005 reference period, respectively (Figure 6.1). The results of CONST is in a good agreement with the CMIP5 RCP4.5 multi-model mean global warming of 1.8 K (Knutti and Sedláček, 2012). While the warming trend of 0.24 ± 0.04 K/decade is very similar in all simulations from 2000 to 2045, the model projects a clear separation thereafter. While WEAK develops a reduced warming rate of 0.09 ± 0.04 K/decade for the second half of the century, STRONG enters a reduced warming phase of 0.08 ± 0.04 K/decade until the end of the century. Similar to WEAK, CONST shows a transition to a weaker warming rate phase of 0.11 ± 0.03 K/decade. The decrease of the global warming rate after 2045 in CONST is related to the declining CO_2 and CH_4 emission rates according to RCP4.5. The 2081-2100 mean temperatures are 0.21 ± 0.26 K higher in CONST than in WEAK and 0.35 ± 0.24 K higher than in STRONG. The decelerated global averaged warming is comparable to the results of Meehl et al. (2013) and also compares well to the simulation with strong solar forcing (-0.25% in TSI) of Feulner and Rahmstorf (2010). In our simulations, the major volcanic eruptions in 2023 and 2060 lead to a pronounced decrease in global temperatures right after the events, but temperatures recover in 2-5 years time. The two smaller eruptions have no detectable effect on temperatures. The simulated patterns of GHG warming are in good agreement with the results of other models (Meehl et al., 2005; Washington et al., 2009; Knutti and Sedláček, 2012, Figure S 6.2 in the appendix). The temperature difference between the period 2081-2100 and 1986-2005 of CONST shows the most pronounced positive

differences over the Arctic due to polar amplification (e.g. Serreze and Barry, 2011). Other strong temperature differences are found over Central Southern America, South Africa, the Himalayan region and Australia.

Figure 6.2a shows the differences in the regional pattern of surface air temperatures between STRONG and CONST for the period 2081-2100. The drop in solar activity leads to a significant cooling in the equatorial region and over most of the northern high latitudes. Due to the albedo effect from a positive sea ice anomaly, the northern polar region is cooled by up to 1 K, while the cooling over the southern polar region is less pronounced. The North Atlantic region reacts with a warming due to a 2 Sv stronger reduction of the Atlantic meridional overturning circulation in CONST compared with
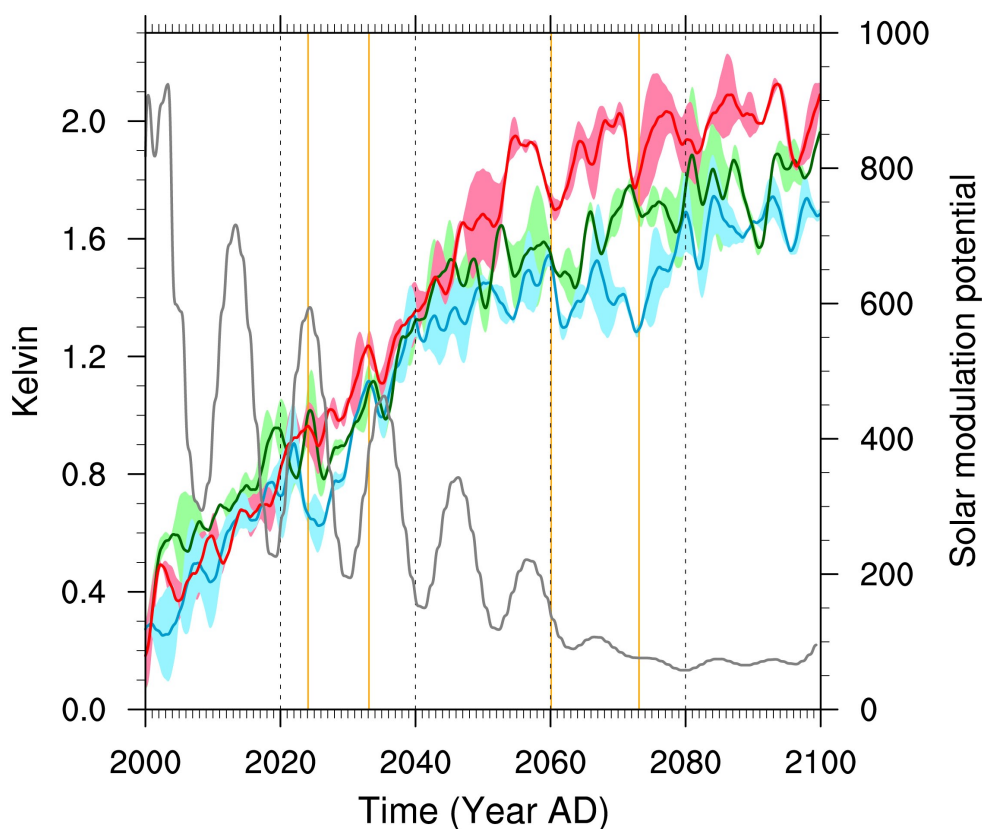
Figure 6.1: Globally averaged surface air temperature evolution for CONST (red); STRONG (blue) and WEAK (green) smoothed with a full width half maximum Gaussian filter over 24 months. Spread of the two runs per experiment are illustrated as pastel envelope. Anomalies (in Kelvin) are shown relative to the averaged 1986 - 2005 temperatures. Grey curve: Total solar irradiance following Shapiro et al. (2011). Orange vertical lines: Years of hypothetical volcanic eruptions.

STRONG. The reason for this reduction is the stronger external forcing in CONST and maybe also a change in the stratosphere-troposphere coupling as suggested by Reichler et al. (2012). Clearly this needs a more detailed analysis and is beyond the scope of this study. A cooling of up to 0.4 K takes place over the large parts of the Pacific, Atlantic, and Indian Oceans. The boreal winter pattern averaged over the same period of time (Figure S 6.3 in the appendix) shows an overall similar pattern as the annual mean, although the cooling over the northern polar region is stronger and temperature anomalies reach up to -1.4 K. The warming signal in the eastern part of the Antarctic Peninsula gets larger due to the sea ice melting process being stronger in CONST, leading to lower salinities. The patterns look very similar when comparing CONST to WEAK, just that the amplitudes of the temperature changes are smaller and less significant (see Figure S 6.4 in the appendix). Overall, a stronger cooling signal over land is evident especially over the Arctic region compared to Meehl et al. (2013) due to a stronger solar forcing.

The well-known pattern of recovery of the ozone layer (e.g. WMO, 2011) is shown in Figure S 6.5 in the appendix. Up to 33 DU more ozone over the northern polar region and up to 56 DU more ozone in the southern polar region is modelled in CONST by the end of this century compared to levels of the reference 1986-2005 period. However, the equatorial region and the subtropics of both hemispheres show much smaller or even slightly negative changes around 0 to -4 DU due to the increase of the meridional circulation in the future (e.g. WMO, 2011).

The differences in the total column ozone averaged over the last 20 years of the 21st century between STRONG and CONST are depicted in Figure 6.2b. Over all regions of the world, the model simulates a highly significant decrease of ozone (Student's t-test on the 1% significance level). The decrease is stronger over the midlatitudes than over the polar and equatorial regions, reaching negative total ozone column anomalies of up to -20 DU. Additionally, the equatorial region experiences loss of ozone of -12 DU on average, while the southern polar region suffers the smallest decrease of -8 DU. Over the northern polar region, a loss of -17 DU on average is simulated. The overall effect, illustrated in Figure S 6.6 in the appendix, shows the changes in total ozone column reached by the end of the century in STRONG compared to the 1986-2005 reference period.

Figure 6.3 shows the return date of the zonally averaged total column ozone compared to pre-2000 levels in CONST (Fig. 6.3a) and STRONG (Fig. 6.3b). While in CONST nearly full recovery to the 1960ies levels is reached in the extratropics and the poles, STRONG allows the total column ozone not even to reach the 1975 levels over the
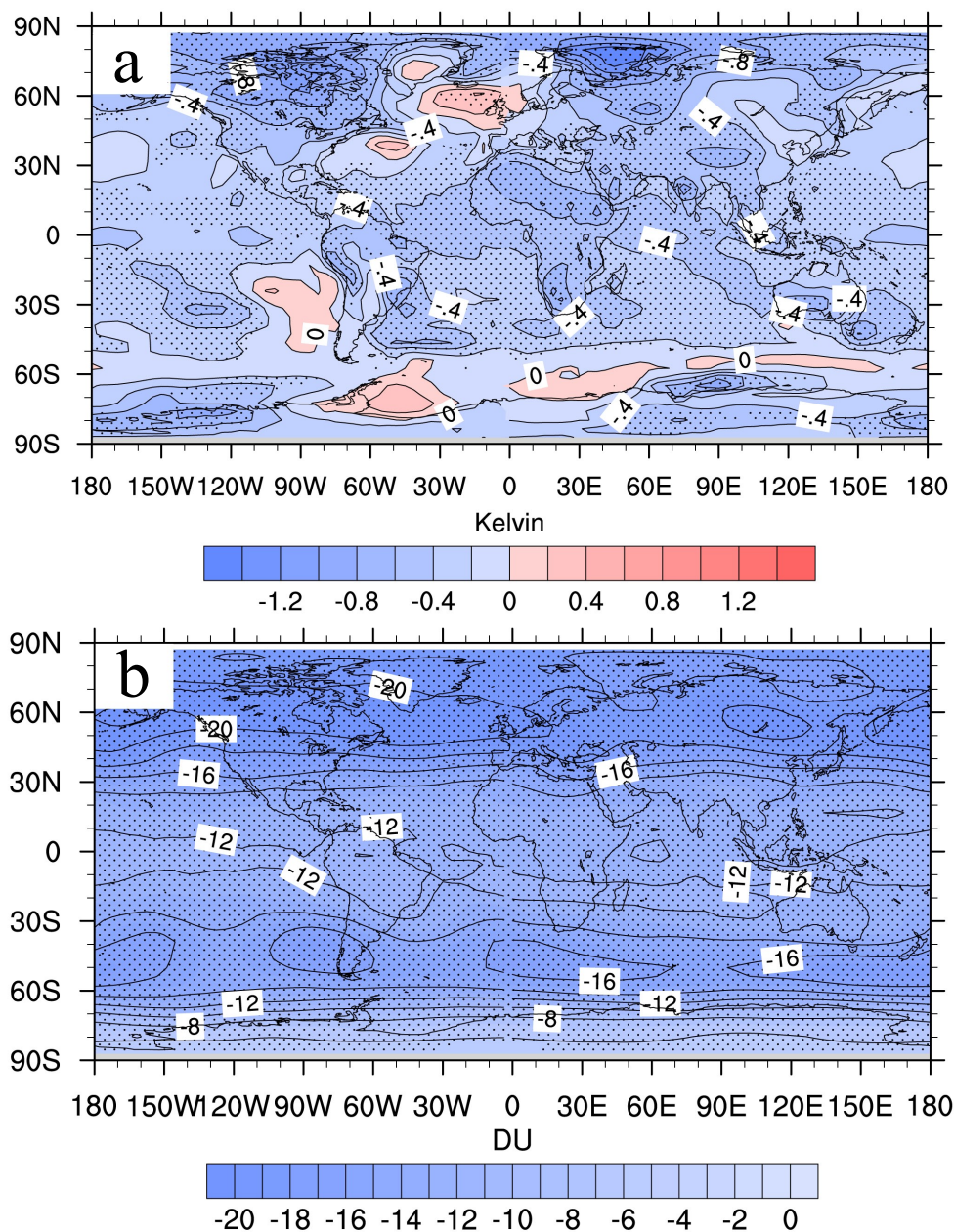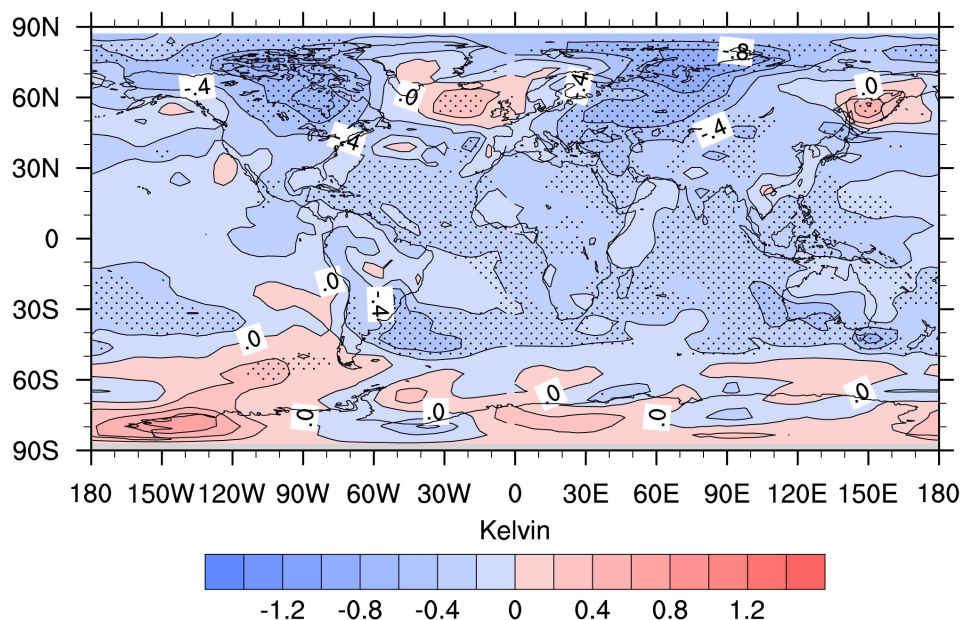
Figure 6.2: a) Surface air temperature difference between STRONG and CONST, averaged over the ensemble members in the 2081-2100 period. b) Total column ozone difference between STRONG and CONST, averaged over the ensemble members in the 2081-2100 period. Stippling denotes the areas where the differences are statistically significant at the 5% level using a t-test.

large areas of the northern subtropics, equatorial regions and southern hemisphere. The recovery to pre-seventies levels at the poles illustrated in Figure 6.3b thus sets in much later than in CONST.

6.5   Conclusions

The facts that during the past 10,000 years about 20 grand solar minima occurred and that the past decades correspond to a long lasting solar maximum make it very likely that a new grand minimum will occur. Spectral extrapolation indicates that it is likely that this minimum will occur within the next decades. However, it is not possible to predict whether it will be a Dalton or a Maunder minimum type.

Yet, by assuming a Dalton minimum-type solar minimum, we show in agreement with Meehl et al. (2013) that although the solar minimum results in a reduced global warming, it cannot compensate continuing anthropogenic impacts. Still, the modelled temperatures averaged over the last 20 years of the 21st century are lower by up to 0.3 K - depending on details of the solar minimum scenario - than the runs with solar constant forcing. Since the duration of the grand minimum assumed in the present work is longer than that of Meehl et al. (2013), the apparent weakening of the global warming is more pronounced. Yet, this should not distract from the fact that the general warming is due to anthropogenic emissions and that the grand minimum can at best lead to an episodic reduction of the warming.

Significant cooling pattern changes between the work of Meehl et al. (2013) and this one might be due to a stronger decrease in the UV spectrum - leading to a more important cooling especially over the Arctic region. In a future work, we will perform sensitivity experiments to investigate the contribution of the top-down mechanism to the temperature anomaly in the Arctic region.

Although the magnitude of the solar variability is still poorly constrained (see e.g. Judge et al., 2012; Solanki and Unruh, 2013; Shapiro et al., 2013) and remains a bottleneck for the climate studies, this study shows evidence that the strong decrease in UV radiation and in the photolysis rates leads to a significant decrease of ozone especially in the tropics. This reduction in UV slows down or even cancels the recovery of the ozone column, depending on the region. Moreover, due to the net decrease of the UV-absorbing ozone, photoactive radiation between 300 and 320 nm could be enhanced especially over the tropics and subtropics (40°S-40°N) during a future grand solar minimum. This could possibly increase the risk of skin cancer and other diseases (Setlow, 1974) in
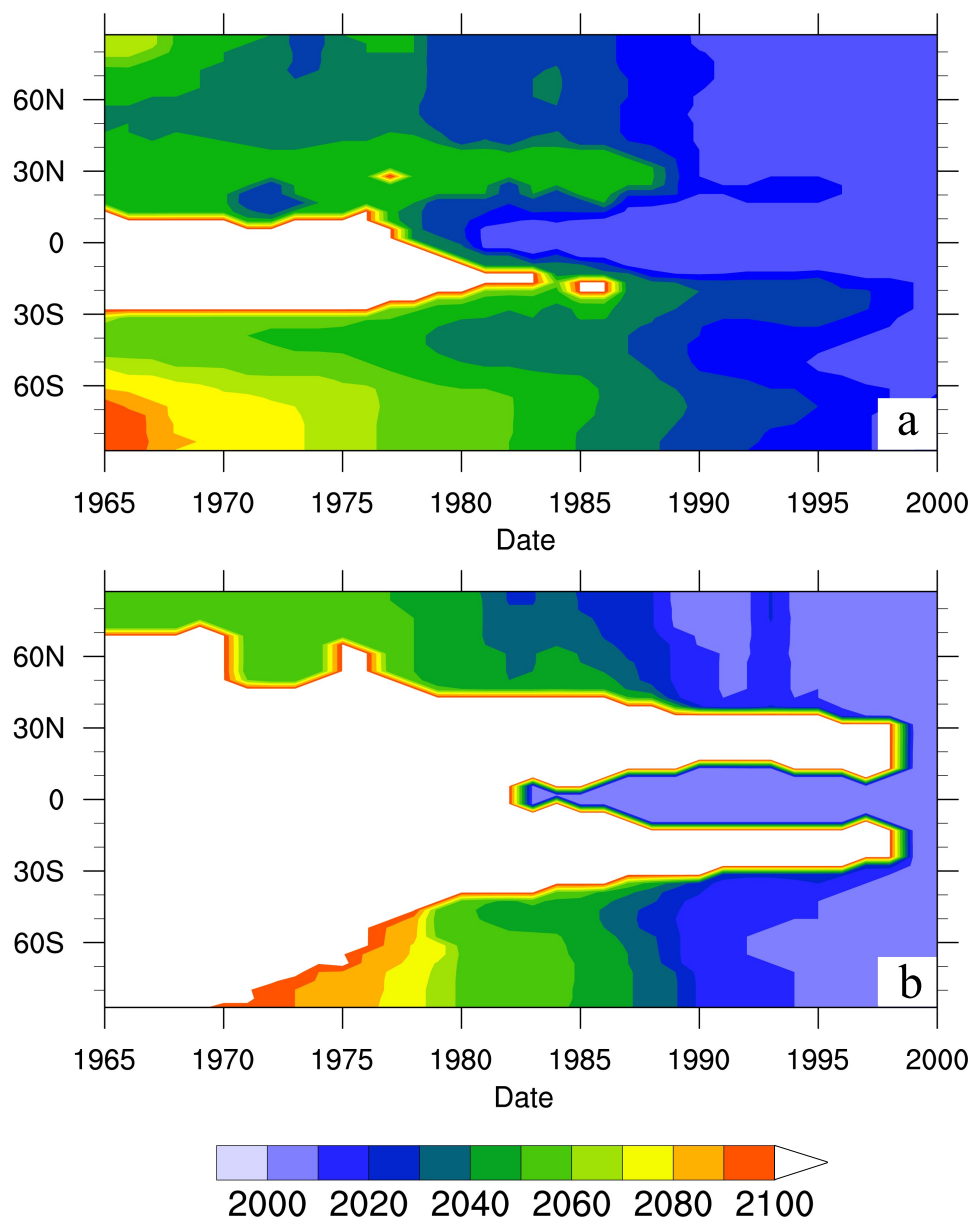
Figure 6.3: Timing of the total ozone column return date in the AOCCM SOCOL-MPIOM. Contours illustrate years of the simulation, in which the total ozone concentration shown on the abscissa is restored, similar to Figure 19, Austin et al. (2010). a: Mean of CONST. b: Mean of STRONG. Ozone column has been averaged with a running mean over 11 years (boxcar). White areas highlight ozone levels which are predicted not to recover to pre-2000 values before 2100. Reference ozone data are provided by the pre-2000 simulations.

WEAK and STRONG with respect to CONST - and also to present conditions. Future work is needed to investigate the change in erythemal radiation in order to specify health effects.

6.6 Acknowledgements

6.7 Appendix

Auxiliary Material for

Impact of a potential 21st century "Grand Solar Minimum" on surface temperatures and stratospheric ozone

Julien G. Anet Institute for Atmospheric and Climate Science ETH, Zurich, Switzerland

Eugene V. Rozanov Institute for Atmospheric and Climate Science ETH, Zurich, Switzerland Physikalisch-Meteorologisches Observatorium Davos and World Radiation Center (PMOD/WRC), Davos, Switzerland

Stefan Muthers Climate and Environment Physics, Physics Institute, University of Bern, Switzerland Oeschger Centre for Climate Change Research, University of Bern, Bern, Switzerland

Christoph C. Raible Climate and Environment Physics, Physics Institute, University of Bern, Switzerland Oeschger Centre for Climate Change Research, University of Bern, Bern, Switzerland

Stefan Brönnimann Institute of Geography, University of Bern, Switzerland Oeschger Centre for Climate Change Research, University of Bern, Bern, Switzerland

Florian Arfeuille Institute of Geography, University of Bern, Switzerland Oeschger Centre for Climate Change Research, University of Bern, Bern, Switzerland

Thomas Peter Institute for Atmospheric and Climate Science ETH, Zurich, Switzerland

Juerg Beer Eawag, Surface Waters group, Switzerland

Friedhelm Steinhilber Eawag, Surface Waters group, Switzerland

Werner K. Schmutz Physikalisch-Meteorologisches Observatorium Davos and World Radiation Center (PMOD/WRC), Davos, Switzerland

Geophysical research letters

Introduction

The auxiliary material for this article contains six figures illustrating the spectral solar forcing and differences in 2m temperatures and total column ozone between the experiments.

References:

Shapiro, A. I., W. Schmutz, E. Rozanov, M. Schoell, M. Haberreiter, A. V. Shapiro, and S. Nyeki (2011), A new approach to the long-term reconstruction of the solar irradiance leads to large historical solar forcing, A&A, 529 (A67), A67, doi:10.1051/0004-6361/201016173
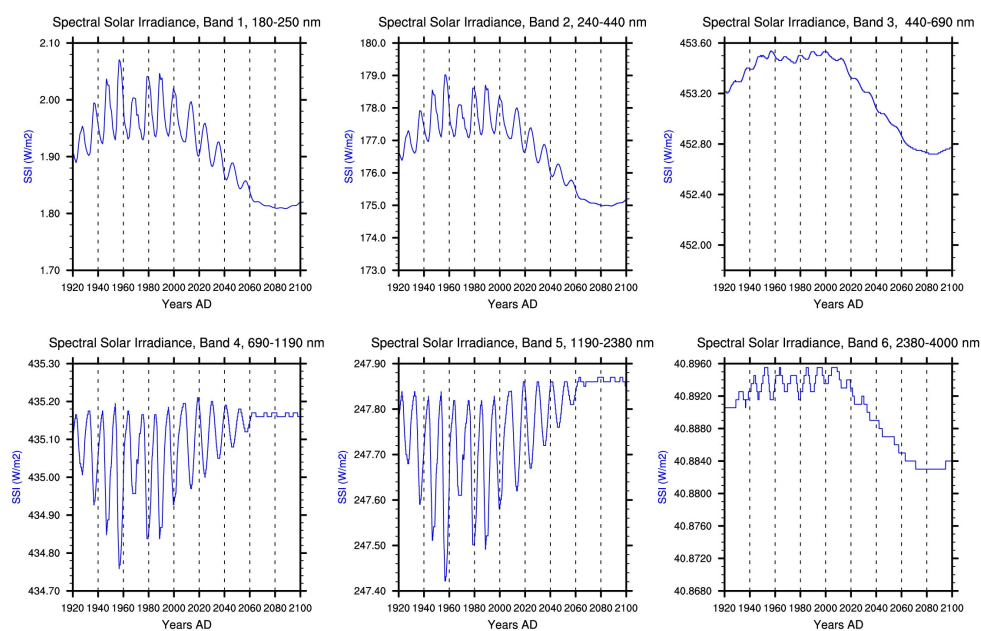
Figure S 6.1: Evolution of the spectral solar irradiance following Shapiro et al. (2011), split into the six ECHAM5 radiation bands.
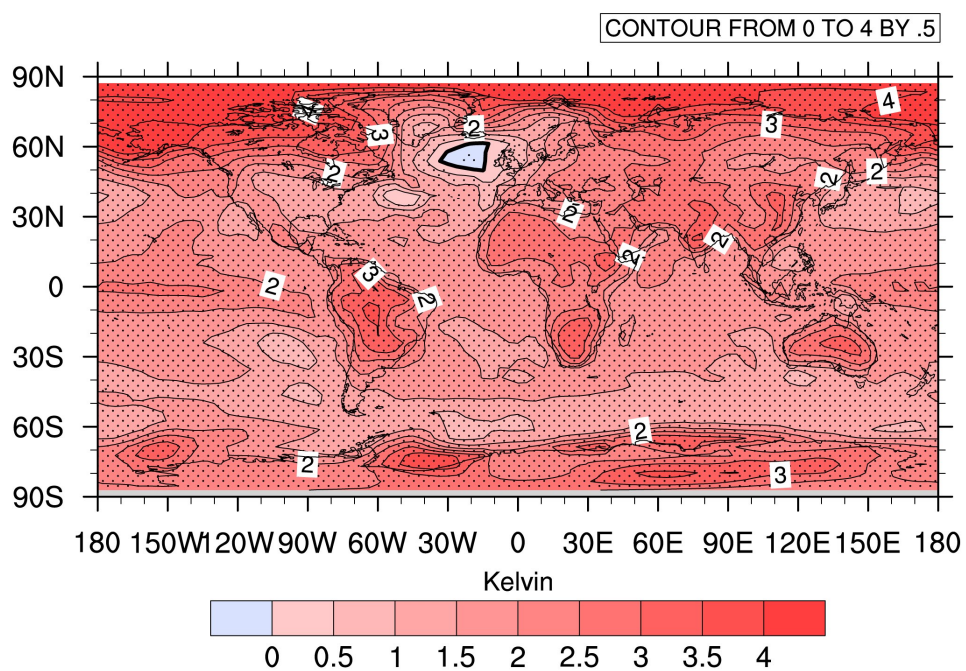
Figure S 6.2: Surface air temperature differences between CONST (2081-2100) and the reference period (1986-2005). Stippling: Differences significant based differences on a t-test with alpha=5%.
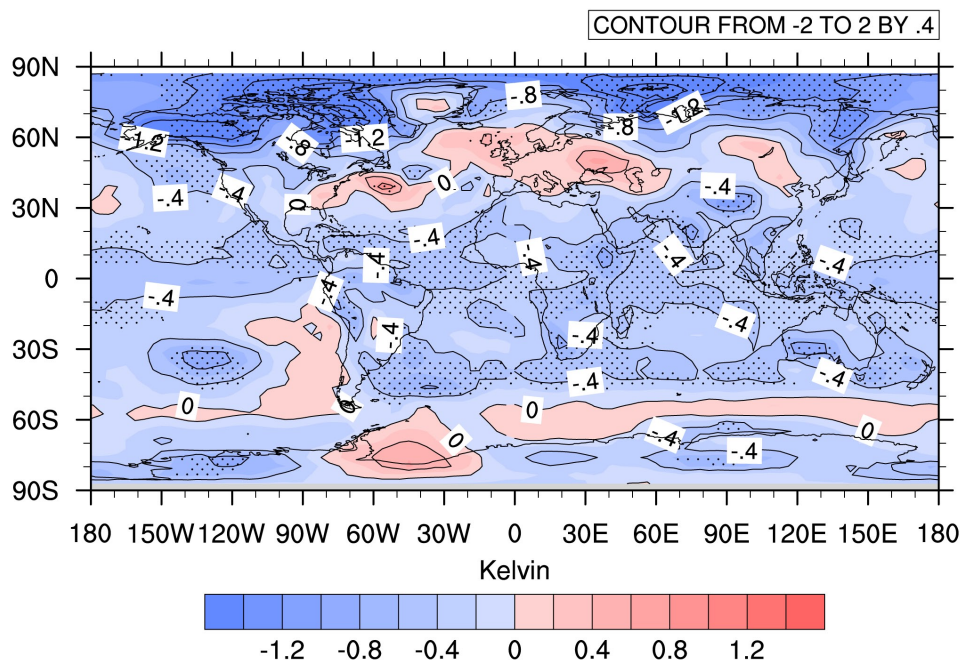
Figure S 6.3: 2m Temperature differences between STRONG and CONST (2081-2100) for the DJF season. Stippling: Differences significant based on a t-test with alpha=5%.

Figure S 6.4: Surface air temperature differences between WEAK and CONST, averaged over the ensemble members in the 2081-2100 period. Stippling: Differences significant based on a t-test with alpha=5%.
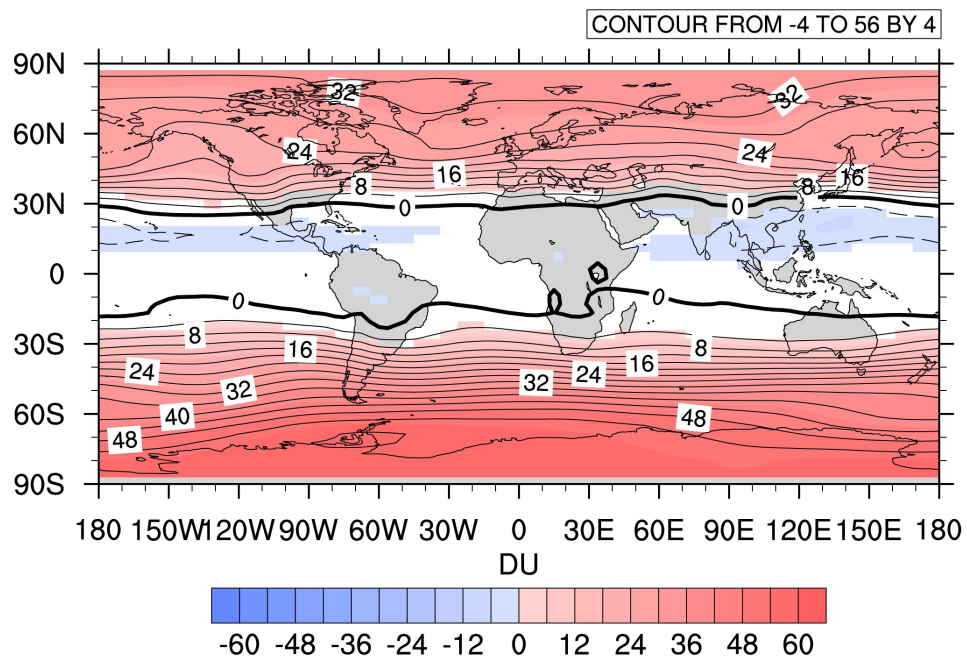
Figure S 6.5: Difference in total column ozone between CONST (2081-2100 period) and the reference period (1986-2005). Only areas which are significantly different on a 5% t-test are colored.
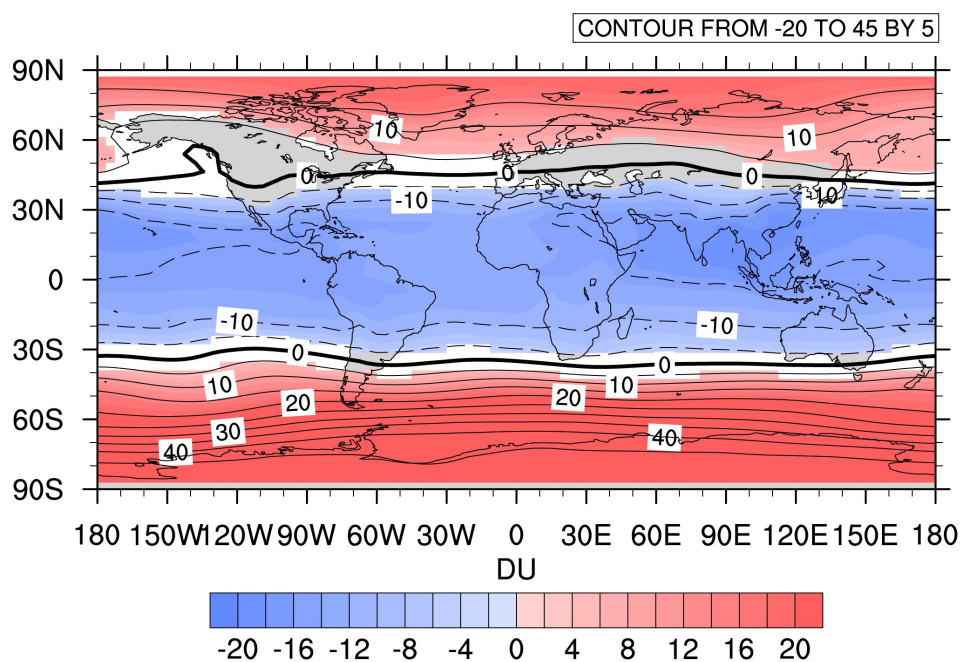
Figure S 6.6: Difference in total column ozone between STRONG (2081-2100 period) and the reference period (1986-2005). Only areas which are significantly different on a 5% t-test are colored.

Chapter 7

Conclusions and outlook

7.1 Conclusions

Realistic forecasts about climate change can only be made, if all external and internal natural forcings are known and sufficiently understood. As the last IPCC report AR4 stated in Table 2.11 of Chapter 2, the level of scientific understanding is still low with regard to the effect of variations in solar irradiance and volcanic aerosols, and very low in regard to the effect of cosmic rays.

In this thesis, the influence of the variability in solar irradiance (UV, visible and near-infrared), volcanic eruptions and energetic particles on past and future global climate was investigated. Using a 500-year long climate simulation from 1600 AD to 2100 AD, two series of sensitivity experiments were performed with the newly designed atmosphere-ocean chemistry-climate-model (AO-CCM) SOCOL3-MPIOM. Due to the expected analogous solar behavior during the last grand solar minimum (the Dalton minimum [DM]) and the hypothetical future solar minimum forecasted by e.g. Abreu et al. (2008) and Abreu et al. (2010), the DM was chosen as the first period for in-depth analysis. The hypothetical 21st century grand solar minimum was chosen as the second. All experiments were forced by the new Shapiro et al. (2011) spectral solar irradiance forcing, known for its high variability and especially strong decrease in the UV spectrum during grand solar minima.

After running the complete simulation from 1600 AD to 2100 AD, we learned that the greenhouse gas sensitivity of our model is rather high. We were nevertheless able to reproduce warming levels for the 21st century similar to those of the CMIP5

simulations. However, we failed to correctly reproduce the Maunder minimum (MM) despite the rather strong Shapiro et al. (2011) forcing. The DM, including the cold periods right after the 1809, 1815, 1831 and 1835 volcanic eruptions, was reproduced quite well. The anthropogenic global warming that began in the industrial era is also well-reproduced. The model's lack of sensitivity to the MM may be due to the long reaction time of our ocean, which was stabilized with a spin-up simulation of nearly 200 years. Had we started our simulations earlier, in 1500 AD, the ocean state could probably have been taken out of its "equilibrium state", likely better representing the MM after 130 years of transient simulations instead of only 30 years.

The second part of this thesis dealt with the climate feedbacks during the DM and was split into two parts. Our goal was to discern the effect of solar, energetic particle and volcanic forcing on stratospheric chemistry and climate, as well as on tropospheric temperature patterns. Both analyses were performed using data from six simulations. Two simulations were performed as reference simulations. In the first reference simulation, or the control run, all relevant forcing factors - solar irradiance, energetic particle precipitation and volcanic eruptions - were set to perpetually mimic the year 1780 AD. The other reference simulation, the "all forcings" run, had all forcing factors activated and varying over time. Two simulations focusing on the solar contribution of the DM climate change were also designed. One simulation was configured in such a way as to only allow UV irradiance to vary while keeping the remaining factors constant, while the other kept all factors except visible and near IR radiation constant. The volcanic contribution was analyzed with a run that was only forced by volcanic aerosols; the remaining forcing factors remained constant. The final sensitivity run focused on energetic particle precipitation. The energetic particles were allowed to vary in their ionization potential over time while all other factors were kept constant.

Two main effects were observed with regard to the stratospheric temperatures. First, a significant cooling in the middle and upper stratosphere of up to 4 K due to the reduction of solar UV irradiance and the subsequent drop in absorption of UV radiation by ozone was found. Second, a strong warming of up to 2 K in the tropical tropopause region due to the absorption of solar irradiance by the volcanic aerosols was observed. These findings are reflected in the stratospheric zonal wind fields. These fields show one important pattern in particular: A significant strengthening of the stratospheric extratropical zonal winds and a weakening of the subtropical jets. This is the result of key changes in the temperature gradients due to volcanic eruptions. Only minor changes in the wind patterns were due to the negative solar UV irradiance anomalies.

No strongly significant changes neither in temperature nor in the zonal wind field were found to result from a change in either visible and near IR radiation or in the energetic particle precipitation strength.

Three chemistry fields were most affected: ozone, water vapour and nitrogen oxide. Ozone in particular was influenced by decreasing UV radiation, which dropped by up to 20% in the middle stratosphere. In contrast, an increase in ozone of up to 16% was simulated in the volcanic scenario in the tropical tropopause region due to increasing HO_x and decreasing NO_x. Similar behavior was simulated in the water vapour field. While a decrease in the UV irradiance caused a decrease in water vapour of up to 4% in the middle stratosphere, an increase of up to 14% was caused by volcanic eruptions. Both changes originate from the negative and/or positive change in temperatures at the tropical tropopause region. While energetic particles did not noticeabbly influence the latter two chemical fields, NO_x concentrations were altered significantly in the lower polar mesosphere region. A drop of up to 80% was simulated due to the decrease in low energetic electron and solar proton events originating from the Sun. A slight increase in NO_x was simulated in the southern polar tropopause region due to an increase in GCRs. No significant changes resulting from a drop in the visible and infrared irradiance can be reported.

The analyses of the changes in the tropospheric climate were performed using the same experimental data. While neither decreasing UV irradiance nor changes in the energetic particle precipitation can explain the drop in temperatures observed in the proxy data, our volcanic eruption run at least partly explains the negative temperature anomalies following the years 1809, 1815, 1831 and 1835 in the northern hemisphere. However, it is only with the visible and near IR irradiance experiment that the sustained cold period between 1819 and 1830 can be interpreted. Our model results even suggest that a solar-only-DM would have lead to an unprecedented cold period in the 1820s, which only was avoided by a supercompensation-like feature triggered by the volcanic eruptions: A small region in the northern Bering Sea shows positive sea surface temperature anomalies, probably triggered by changes of the global wind patterns, influencing surface wind stress on the ocean and subsequent upwelling via the Ekman mechanism. The comparison with a set of temperature reconstructions shows that neither the volcanic eruptions, nor the visible and near-infrared solar forcing alone succeed in reproducing the temperature patterns. Only the combination of all factors is able to replicate the same temperature evolution than the one of the reconstructions. Moreover, we find that while the drop in solar irradiance does not,

the strong volcanic eruptions lead to a northward shift of the intertropical convergence zone and to modified temperature, sea level pressure and precipitation patterns over continental Europe especially during the boreal winter season.

We therefore conclude from this first series of sensitivity experiments that UV irradiance and volcanic eruptions are largely responsible for changes in the dynamics and chemistry of the stratosphere. Conversely, it is the decrease in visible and near IR irradiance, as well as volcanic eruptions, which explain the changes in dynamics in the troposphere during the DM. Only the combination of the latter two forcing factors are able to explain the temperature evolution observed from the reconstructions.

The second experiment explored the effects of a hypothetical grand solar minimum during the 21st century. Two simulations, one with a strong solar forcing and one with a weaker solar forcing, were launched from the year 2000 AD until the year 2100 AD. Two small volcanic eruptions in 2024 and 2031 and two strong eruptions in 2060 and 2075 were assumed in order to design the experiments as realistically as possible. Both experiments mimicked the last two solar cycles repeatedly; thus, the only difference between the two experiments was the solar forcing. The third experiment was designed to simulate a new grand solar minimum identical to the DM. All other forcing factors were identical to those in the first two experiments.

The experiments yielded two main results: First, global temperatures in the case of a new solar minimum case would be very similar to those in the experiments with a constant solar forcing. The new strong grand minimum simulation reaches a warming of 1.61 K by the end of this century relative to the 1986-2005 period. In comparison, the two experiments with either a constant solar forcing or a weak grand minimum solar forcing resulted in temperature increases of 1.96 K and 1.75 K, respectively. Due to a decrease in solar UV irradiance, the ozone layer is significantly thinner in the grand solar minimum run than in the solar constant runs. In the grand solar minimum run, anomalies of up to -12 DU in the equatorial region and -17 DU in the northern polar regions relative to the solar constant experiments are simulated.

We conclude from the second series of sensitivity experiments that a new grand solar minimum, even with the very strong solar forcing predicted by Shapiro et al. (2011), would at best lead to a less intense global warming but would not compensate for the anthropogenically driven changes. Moreover, due to a decrease in UV solar irradiance,

a significant decrease in ozone above the equatorial region would occur, possibly increasing the skin cancer risk at these latitudes.

7.2 Outlook

Although most of our research questions could be answered thanks to the numerous simulations, some questions remain open.

In contrast to the work of Calisto et al. (2011) and Rozanov et al. (2012a), our findings were much less in favour of the hypothesis that there is any influence by energetic particles on surface temperatures. We do however not exclude the possibility that a certain compensating effect from increasing GCRs by decreasing LEEs and SPEs persists. This should be investigated with a new series of model runs.

With regard to the effect of volcanic eruptions during the DM, we did only find a slightly significant winter warming after the major eruptions. Moreover, the shift in the NAO is hardly visible and lacks of significance. Although rather technical, the question to investigate here is if gravity wave parameterization in the model should be changed to improve this signal. A modification could possibly also enhance the downward propagation of the negative UV anomaly, possibly leading to a stronger cooling pattern over the northern polar hemisphere during winter time, as found in Meehl et al. (2009). As well, the response of the model to changes in the energetic particle precipitation could possibly be improved.

Finally, a very important question concerns the result of our future grand solar minimum simulation. If equatorial and subtropical ozone column values effectively drop by the amount which was simulated, by how much would the erythemal radiation increase? It is not clear if any change at all would be observed as UV irradiance decreases. However, if a change does occur, precautions could be taken to protect populations from this harmful radiation.

List of abbreviations

A$_a$ Geomagnetic disturbance index, based on two stations

A$_p$ Geomagnetic disturbance index, based on a set of specific stations

AD   Anno Domini, years after J.C. birth

AER   Atmospheric and Environmental Research Inc.

AO   Arctic oscillation

AO-CCM Atmosphere-Ocean chemistry climate model

AO-GCM Atmosphere-Ocean general circulation model

AR   Assessment report of the IPCC

BCKGRD Background

BDC   Brewer-Dobson circulation

Be   Beryllium

BU   Bottom-Up mechanism

CAM   Community Atmosphere Model

CCM   Chemistry climate model

CCSM Community Climate System Model

CFC   Chlorofluorocarbon, an ODS

CMIP Coupled Model Intercomparison Project

CO   Carbon monoxide

CONST Constant

CTRL Control run

DJF   December-January-February

DM   Dalton Minimum

DU   Dobson Unit

EAWAG Eidgenössische Anstalt für Wasserversorgung, Abwasserreinigung und
       Gewässerschutz

ECHAM5 ECMWF-HAMburg GCM model version 5

ENSO El Niño southern oscillation

EPP   Energetic particle precipitation

Ga   A million year

GCM   General circulation model

GCR   Galactic cosmic rays

GHG   Greenhouse gas

GIUB   Geographisches Institut Universität Bern

Gt   Gigaton, is equal to 1 Tg

HEE   High energy electrons

HO_x Hydroxides

hPa   100 Pascals

IAC   Institute for Atmosphere and Climate

IPCC   Intergovernmental Panel on Climate Change

IR   Infrared

J   Joules

JJA   June-July-August

K   Kelvin

ky   Thousand years

LEE   Low energy electrons

MA   Middle atmosphere

MeV   Megaelectronvolts

MEZON Model for Evaluation of oZONe trends, a CCM model

MM   Maunder Minimum

MPIOM Max Plank Institute Ocean Model

Mt   Mega tons

NAO   North atlantic oscillation

NH   North hemisphere

nm   Nanometers

NO_x Nitrogen oxides

OASIS A program allowing to couple atmosphere and ocean together

ODS   Ozone depleting substances

OHC   Ocean heat content

PCA   Principal component analysis

PDO   Pacific decadal oscillation

PMIP3 Paleoclimate Modelling Intercomparison Project Phase III

PMOD/WRC Physikalisch-Meteorologisches Institut Davos/World Radiation Centre

QBO   Quasi-biennial oscillation

RCS   Regional curve standardization

SEP   Solar energetic particles

SH   South hemisphere

SNF   Schweizerischer Nationalfonds

SOCOL3 SOlar Climate Ozone Links: A chemical model

SON   September-October-November

SPE   Solar proton events, see also SEP

SSI   Spectral solar irradiance

SSW Sudden stratospheric warming

TD   Top-Down mechanism

Tg   Teragram, is equal to 1 Gt

TRANS Transient

TSI   Total solar irradiance

UT/LS Upper troposphere/Lower stratosphere: A broader region of the tropopause

UV   Ultraviolet

VIS   Visible spectrum

VOC   Volatile organic carbon

WMO World Meteorological Organization

List of Tables

List of Figures

Bibliography

Abreu, J., Beer, J., and Ferriz-Mas, A. Past and future solar activity from cosmogenic radionuclides. In K.J.A.S.o.t.P.C.S..U. eds Cranmer SR Hoeksema JT, editor, *SOHO-23: Understanding a Peculiar Solar Minimum*, volume 428, page 287. Past and future solar activity from cosmogenic radionuclides. Astronomical Society of the Pacific Conference Series: SOHO-23: understanding a peculiar solar minimum, 2010.

Abreu, J., Beer, J., Steinhilber, F., Tobias, S.M., and Weiss, N.O. For how long will the current grand maximum of solar activity persist? *Geophys. Res. Lett.*, 35(20):L20109, 2008. ISSN 1944-8007. doi:10.1029/2008GL035442.

Adams, J.B., Mann, M.E., and Ammann, C.M. Proxy evidence for an El Niño-like response to volcanic forcing. *Nature*, 426(6964):274–278, 2003. doi:10.1038/nature02101.

Aikin, A. Energetic particle-induced enhancements of stratospheric nitric acid. *Geophys. Res. Lett.*, 21(10):859–862, 1994. doi:10.1029/94GL00914.

Ammann, C., Joos, F., Schimel, D., Otto-Bliesner, B., and Tomas, R. Solar influence on climate during the past millennium: Results from transient simulations with the ncar climate system model. *P. Natl. Acad. Sci. USA*, 104(10):3713–3718, 2007. doi:10.1073/pnas.0605064103.

Anchukaitis, K.J., Breitenmoser, P., Briffa, K.R., Buchwal, A., Büntgen, U., Cook, E.R., D'Arrigo, R.D., Esper, J., Evans, M.N., Frank, D., et al. Tree rings and volcanic cooling. *Nature Geoscience*, 5(12):836–837, 2012. doi:10.1038/ngeo1645.

Andrews, D.G., Holton, J.R., and Leovy, C.B. *Middle atmosphere dynamics*. Academic Press, Orlando, USA, 1987. ISBN 0120585758 0120585766.

Anet, J.G., Muthers, S., Rozanov, E., Raible, C.C., Peter, T., Stenke, A., Shapiro, A.I., Beer, J., Steinhilber, F., Brönnimann, S., Arfeuille, F., Brugnara, Y., and Schmutz, W.

Forcing of stratospheric chemistry and dynamics during the dalton minimum. *Atmos. Chem. Phys. Discuss.*, 13(6):15061–15104, 2013a. doi:10.5194/acpd-13-15061-2013.

Anet, J.G., Rozanov, E.V., Muthers, S., Peter, T., Brnnimann, S., Arfeuille, F., Beer, J., Shapiro, A.I., Raible, C.C., Steinhilber, F., and Schmutz, W.K. Impact of a potential 21st century grand solar minimum on surface temperatures and stratospheric ozone. *Geophysical Research Letters*, pages n/a–n/a, 2013b. ISSN 1944-8007. doi:10.1002/grl.50806.

Arfeuille, F. *Impacts of large volcanic eruptions on the stratosphere and climate*. (Doctoral Dissertation) ETH Zürich, 2012. doi:10.3929/ethz-a-007577656.

Arfeuille, F., Luo, B.P., Heckendorn, P., Weisenstein, D., Sheng, J.X., Rozanov, E., Schraner, M., Brönnimann, S., Thomason, L.W., and Peter, T. Uncertainties in modelling the stratospheric warming following Mt. Pinatubo eruption. *Atmos. Chem. Phys. Discuss.*, 13:4601–4635, 2013b. doi:10.5194/acpd-13-4601-2013.

Arfeuille, F., Weisenstein, D., Mack, H., Rozanov, E., Peter, T., and Brönnimann, S. Volcanic forcing for climate modeling: A new microphysics-based dataset covering years 1600-present. *Clim. Past Discuss.*, 9:967–1012, 2013a. doi:10.5194/cpd-9-967-2013.

Auchmann, R., Brönnimann, S., Breda, L., Bühler, M., Spadin, R., and Stickler, A. Extreme climate, not extreme weather: the summer of 1816 in Geneva, Switzerland. *Clim. Past*, 8:325–335, 2012. doi:10.5194/cp-8-325-2012.

Austin, J., Struthers, H., Scinocca, J., Plummer, D.A., Akiyoshi, H., Baumgaertner, A.J.G., Bekki, S., Bodeker, G.E., Braesicke, P., Brühl, C., Butchart, N., Chipperfield, M.P., Cugnet, D., Dameris, M., Dhomse, S., Frith, S., Garny, H., Gettelman, A., Hardiman, S.C., Jöckel, P., Kinnison, D., Kubin, A., Lamarque, J.F., Langematz, U., Mancini, E., Marchand, M., Michou, M., Morgenstern, O., Nakamura, T., Nielsen, J.E., Pitari, G., Pyle, J., Rozanov, E., Shepherd, T.G., Shibata, K., Smale, D., Teyssedre, H., and Yamashita, Y. Chemistry-climate model simulations of spring antarctic ozone. *J. Geophys. Res.*, 115(D3), 2010. ISSN 2156-2202. doi:10.1029/2009JD013577.

Bard, E., Raisbeck, G., Yiou, F., and Jouzel, J. Solar irradiance during the last 1200 years based on cosmogenic nuclides. *Tellus*, 52B:985–992, 2000. doi:10.1034/j.1600-0889.2000.d01-7.x.

Bates, D.R. and Nicolet, M. The photochemistry of atmospheric water vapor. *J. Geophys. Res.*, 55(3):301–327, 1950. doi:10.1029/JZ055i003p00301.

Bauer, E., Claussen, M., Brovkin, V., and Huenerbein, A. Assessing climate forcings of the earth system for the past millennium. *Geophys. Res. Lett.*, 30(6):1276, 2003. doi:10.1029/2002GL016639.

Baumgaertner, A.J.G., Joeckel, P., and Bruehl, C. Energetic particle precipitation in ECHAM5/MESSy1, Part 1: Downward transport of upper atmospheric NOx produced by low energy electrons. *Atmos. Chem. Phys.*, 9:2729–2740, 2009. doi:10.5194/acp-9-2729-2009.

Bazilevskaya, G., Usoskin, I., Flückiger, E., Harrison, R., Desorgher, L., Bütikofer, R., Krainev, M., Makhmutov, V., Stozhkov, Y., Svirzhevskaya, A., Svirzhevsky, N., and Kovaltsov, G. Cosmic ray induced ion production in the atmosphere. In F. Leblanc, K. Aplin, Y. Yair, R. Harrison, J. Lebreton, and M. Blanc, editors, *Planetary Atmospheric Electricity*, volume 30 of *Space Sciences Series of ISSI*, pages 149–173. Springer New York, 2008. ISBN 978-0-387-87663-4. doi:10.1007/978-0-387-87664-1_10.

Beer, J., Baumgartner, S., Dittrich-Hannen, B., Hauenstein, J., Kubik, P., Lukasczyk, C., Mende, W., Stellmacher, B., and Suter, M. Solar variability traced by cosmogenic isotopes. In *Poster Proceedings from IAU Colloquium 143: The Sun as a Variable Star: Solar and Stellar Irradiance Variations*, volume 1, page 291. 1994.

Beer, J., Mende, W., and Stellmacher, R. The role of the sun in climate forcing. *Quaternary Science Reviews*, 19(1):403–415, 2000. doi:10.1016/S0277-3791(99)00072-4.

Beer, J., Raisbeck, G., and Yiou, F. Time variations of Be-10 and solar activity. In *The sun in time*, volume 1, pages 343–359. 1991.

Bragg, W. and Kleeman, R. On the α particles of radium, and their loss of range in passing through various atoms and molecules. *Philos. Mag.*, 10(57):318–340, 1905. doi:10.1080/14786440509463378.

Brasseur, G. and Solomon, S. *Aeronomy of the Middle Atmosphere*. Springer Netherlands, Dordrecht, 2005. doi:10.1007/1-4020-3824-0.

Briffa, K.R., Osborn, T.J., Schweingruber, F.H., Harris, I.C., Jones, P.D., Shiyatov, S.G., and Vaganov, E.A. Low-frequency temperature variations from a northern tree ring density network. *J. Geophys. Res.*, 106(D3):2929–2941, 2001. doi:10.1029/2000JD900617.

Brönnimann, S., Annis, J.L., Vogler, C., and Jones, P.D. Reconstructing the quasi-biennial oscillation back to the early 1900s. *Geophys. Res. Lett.*, 34(22), 2007. ISSN 1944-8007. doi:10.1029/2007GL031354.

Brugnara, Y., Brönnimann, S., Luterbacher, J., and Rozanov, E. Influence of the sunspot cycle on the northern hemisphere wintertime circulation from long upper-air data sets. *Atmospheric Chemistry and Physics*, 13(13):6275–6288, 2013. doi:10.5194/acp-13-6275-2013.

Budich, R., Giorgetta, M., Jungclaus, J., Redler, R., and Reick, C. The MPI-M Millennium Earth System Model: An Assembling Guide for the COSMOS Configuration. Technical report, MPI-Hamburg, 2010.

Buhaug, O., Corbett, J., Endresen, O., Eyring, V., Faber, J., Hanayama, S., Lee, D., Lee, D., Lindstad, H., Markowska, A., Mjelde, A., Nelissen, D., Nilsen, J., Palsson, C., Winebrake, J., Wu, W., and Yoshida, K. *Second IMO greenhouse gas study*. International Maritime Organization, London, 2009.

Calisto, M. *Influence of energetic particle precipitation on atmospheric chemistry and climate*. Ph.D. thesis, Eidgenössische Technische Hochschule ETH Zürich, 2011. doi:10.3929/ethz-a-006382983.

Calisto, M., Usoskin, I., Rozanov, E., and Peter, T. Influence of galactic cosmic rays on atmospheric composition and dynamics. *Atmos. Chem. Phys.*, 11:4547–4556, 2011. doi:10.5194/acp-11-4547-2011.

Callis, L., Natarajan, M., Evans, D., and Lambeth, J. Solar atmospheric coupling by electrons (SOLACE) 1. Effects of the May 12, 1997 solar event on the middle atmosphere. *J. Geophys. Res.*, 103(D21):28405–28, 1998. doi:10.1029/98JD02408.

Callis, L.B., Baker, D., Blake, J., Lambeth, J., Boughner, R., Natarajan, M., Klebesadel, R., and Gorney, D. Precipitating relativistic electrons: Their long-term effect on stratospheric odd nitrogen levels. *J. Geophys. Res.*, 96(D2):2939–2976, 1991. doi:10.1029/90JD02184.

Casadevall, T.J., Rose, W.I., Fuller, W.H., Hunt, W.H., Hart, M.A., Moyers, J.L., Woods, D.C., Chuan, R.L., and Friend, J.P. Sulfur dioxide and particles in quiescent volcanic plumes from Poas, Arenal, and Colima volcanos, Costa Rica and Mexico. *J. Geophys. Res.*, 89(D6):9633–9641, 1984. doi:10.1029/JD089iD06p09633.

Cecile, J., Pagnutti, C., and Anand, M. A likelihood perspective on tree-ring standardization: eliminating modern sample bias. *Climate of the Past Discussions*, 9(4):4499–4551, 2013. doi:10.5194/cpd-9-4499-2013.

Chapman, S. *A theory of upper-atmospheric ozone*, volume 3. Edward Stanford, 1930.

Christiansen, B. Volcanic Eruptions, Large-Scale Modes in the Northern Hemisphere, and the El Niño Southern Oscillation. *J. Climate*, 21:910–922, 2007. doi:10.1175/2007JCLI1657.1.

Clark, S. Saved by the sun. *New Scientist*, 191(2569):32–36, 2006. ISSN 0262-4079. doi:10.1016/S0262-4079(06)60496-X.

Coriolis, G.G. *Mémoire sur les équations du mouvement relatif des systèmes de corps*. Bachelier, 1835.

Crutzen, P.J. Determination of parameters appearing in the dry and the wet photochemical theories for ozone in the stratosphere. *Tellus*, 21(3):368–388, 1969. doi:10.1111/j.2153-3490.1969.tb00450.x.

Crutzen, P.J. The influence of nitrogen oxides on the atmospheric ozone content. *Quart. J. Roy. Meteor. Soc.*, 96(408):320–325, 1970. doi:10.1002/qj.49709640815.

Crutzen, P.J., Isaksen, I.S., and Reid, G.C. Solar proton events: Stratospheric sources of nitric oxide. *Science*, 189(4201):457–459, 1975. doi:10.1126/science.189.4201.457.

D'Arrigo, R., Wilson, R., and Jacoby, G. On the long-term context for late twentieth century warming. *J. Geophys. Res.*, 111(D3):D03103, 2006. doi:10.1029/2005JD006352.

Drdla, K. and Müller, R. Temperature thresholds for chlorine activation and ozone loss in the polar stratosphere. *Annales Geophysicae-Atmospheres Hydrospheres and Space Sciences*, 30(7):1055, 2012. doi:10.5194/angeo-30-1055-2012.

Driscoll, S., Bozzo, A., Gray, L.J., Robock, A., and Stenchikov, G. Coupled model intercomparison project 5 (cmip5) simulations of climate following volcanic eruptions. *Journal of Geophysical Research: Atmospheres*, 117(D17):n/a–n/a, 2012. ISSN 2156-2202. doi:10.1029/2012JD017607.

Dutton, E.G. and Christy, J.R. Solar radiative forcing at selected locations and evidence for global lower tropospheric cooling following the eruptions of El Chichón and Pinatubo. *Geophys. Res. Lett.*, 19(23):2313–2316, 1992. ISSN 1944-8007. doi:10.1029/92GL02495.

Easterbrook, D.J. The looming threat of global cooling. In *Heartland Conference on Climate Change*, volume 4. 2010.

Egorova, T., Rozanov, E., Manzini, E., Haberreiter, M., Schmutz, W., Zubov, V., and Peter, T. Chemical and dynamical response to the 11-year variability of the solar irradiance simulated with a chemistry-climate model. *Geophys. Res. Lett.*, 31:4 PP., 2004. doi:10.1029/2003GL019294.

Egorova, T., Rozanov, E., Ozolin, Y., Shapiro, A.I., Calisto, M., Peter, T., and Schmutz, W. The atmospheric effects of october 2003 solar proton event simulated with the chemistry-climate model socol using complete and parameterized ion chemistry. *J. Atmos. Sol-Terr. Phy.*, 73(2-3):356 – 365, 2011. ISSN 1364-6826. doi:10.1016/j.jastp.2010.01.009. Space Climate.

Egorova, T., Rozanov, E., Zubov, V., and Karol, I. Model for investigating ozone trends (mezon). *Izvestiia Akademii Nauk SSSR. Seria Fizika Atmosfery i Okeana*, 39:310–326, 2003. Translated by MAIK "Nauka/Interperiodica" (Russia).

Erlykin, A., Sloan, T., and Wolfendale, A. A review of the relevance of the cloud results and other recent observations to the possible effect of cosmic rays on the terrestrial climate. *Meteorology and Atmospheric Physics*, 121(3-4):137–142, 2013. ISSN 0177-7971. doi:10.1007/s00703-013-0260-x.

Ermolli, I., Matthes, K., Dudok de Wit, T., Krivova, N.A., Tourpali, K., Weber, M., Unruh, Y.C., Gray, L., Langematz, U., Pilewskie, P., Rozanov, E., Schmutz, W., Shapiro, A., Solanki, S.K., and Woods, T.N. Recent variability of the solar spectral irradiance and its impact on climate modelling. *Atmospheric Chemistry and Physics*, 13(8):3945–3977, 2013. doi:10.5194/acp-13-3945-2013.

Esper, J., Cook, E.R., and Schweingruber, F.H. Low-frequency signals in long tree-ring chronologies for reconstructing past temperature variability. *Science*, 295(5563):2250–2253, 2002. doi:10.1126/science.1066208.

Etheridge, D., Steele, L., Langenfelds, R., Francey, R., Barnola, J., and Morgan, V. Natural and anthropogenic changes in atmospheric CO2 over the last 1000 years from air in Antarctic ice and firn. *J. Geophys. Res.*, 101(D2):4115–4128, 1996. doi:10.1029/95JD03410.

Etheridge, D.M., Steele, L.P., Francey, R.J., and Langenfelds, R.L. Atmospheric methane between 1000 A.D. and present: Evidence of anthropogenic emissions and

climatic variability. *J. Geophys. Res.*, 103(D13):15979–15993, 1998. ISSN 2156-2202. doi:10.1029/98JD00923.

Ewert, F.K. Die Fallgruben der Klimawandler. *Europäisches Institut für Klima und Energie e.V.*, pages 1–15, 2011.

Eyring, V., Butchart, N., Waugh, D.W., Akiyoshi, H., Austin, J., Bekki, S., Bodeker, G.E., Boville, B.A., Brühl, C., Chipperfield, M.P., Cordero, E., Dameris, M., Deushi, M., Fioletov, V.E., Frith, S.M., Garcia, R.R., Gettelman, A., Giorgetta, M.A., Grewe, V., Jourdain, L., Kinnison, D.E., Mancini, E., Manzini, E., Marchand, M., Marsh, D.R., Nagashima, T., Newman, P.A., Nielsen, J.E., Pawson, S., Pitari, G., Plummer, D.A., Rozanov, E., Schraner, M., Shepherd, T.G., Shibata, K., Stolarski, R.S., Struthers, H., Tian, W., and Yoshiki, M. Assessment of temperature, trace species, and ozone in chemistry-climate model simulations of the recent past. *J. Geophys. Res.*, 111(D10):D22308, 2006. doi:10.1029/2006JD007327.

Eyring, V., Isaksen, I.S., Berntsen, T., Collins, W.J., Corbett, J.J., Endresen, O., Grainger, R.G., Moldanova, J., Schlager, H., and Stevenson, D.S. Transport impacts on atmosphere and climate: Shipping. *Atmos. Environ.*, 44(37):4735–4771, 2010. doi:10.1016/j.atmosenv.2009.04.059.

Fahey, D., Kawa, S., Woodbridge, E., Tin, P., Wilson, J., Jonsson, H., Dye, J., Baumgardner, D., Borrmann, S., Toohey, D., Awallone, L., Proffitt, M., Margitan, J., Loewenstein, M., Podolske, J., Salawitch, R., Wofsy, S., Ko, M., Anderson, D., Schoeber, M., and Chan, K. In situ measurements constraining the role of sulphate aerosols in mid-latitude ozone depletion. *Nature*, 363:509 – 514, 1993. doi:10.1038/363509a0.

Ferretti, D., Miller, J., White, J., Etheridge, D., Lassey, K., Lowe, D., Meure, C., Dreier, M., Trudinger, C., Van Ommen, T., and Langenfelds, R. Unexpected changes to the global methane budget over the past 2000 years. *Science*, 309(5741):1714–1717, 2005. doi:10.1126/science.1115193.

Feulner, G. Are the most recent estimates for maunder minimum solar irradiance in agreement with temperature reconstructions? *Geophysical Research Letters*, 38(16):n/a–n/a, 2011a. ISSN 1944-8007. doi:10.1029/2011GL048529.

Feulner, G. The smithsonian solar constant data revisited: no evidence for a strong effect of solar activity in ground-based insolation data. *Atmos. Chem. Phys*, 11(7):3291–3301, 2011b. doi:10.5194/acp-11-3291-2011.

Feulner, G. and Rahmstorf, S. On the effect of a new grand minimum of solar activity on the future climate on Earth. *Geophys. Res. Lett.*, 37(5):L05707, 2010. doi:10.1029/2010GL042710.

Finlay, C.C., Maus, S., Beggan, C.D., Bondar, T.N., Chambodut, A., Chernova, T.A., Chulliat, A., Golovkov, V.P., Hamilton, B., Hamoudi, M., Holme, R., Hulot, G., Kuang, W., Langlais, B., Lesur, V., Lowes, F.J., Lühr, H., Macmillan, S., Mandea, M., McLean, S., Manoj, C., Menvielle, M., Michaelis, I., Olsen, N., Rauberg, J., Rother, M., Sabaka, T.J., Tangborn, A., Tffner-Clausen, L., Thebault, E., Thomson, A.W.P., Wardinski, I., Wei, Z., and Zvereva, T.I. International geomagnetic reference field: the eleventh generation. *Geophys. J. Int.*, 183(3):1216–1230, 2010. ISSN 1365-246X. doi:10.1111/j.1365-246X.2010.04804.x.

Fischer, E.M., Luterbacher, J., Zorita, E., Tett, S.F.B., Casty, C., and Wanner, H. European climate response to tropical volcanic eruptions over the last half millennium. *Geophys. Res. Lett.*, 34(5), 2007. ISSN 1944-8007. doi:10.1029/2006GL027992.

Flückiger, J., Dällenbach, A., Blunier, T., Stauffer, B., Stocker, T., Raynaud, D., and Barnola, J.M. Variations in atmospheric N2O concentration during abrupt climatic changes. *Science*, 285(5425):227–230, 1999. doi:10.1126/science.285.5425.227.

Flückiger, J., Monnin, E., Stauffer, B., Schwander, J., Stocker, T.F., Chappellaz, J., Raynaud, D., and Barnola, J.M. High-resolution Holocene N2O ice core record and its relationship with CH4 and CO2. *Global Biogeochem. Cycles*, 16(1):10–1, 2002. doi:10.1029/2001GB001417.

Fontenla, J., White, O.R., Fox, P.A., Avrett, E.H., and Kurucz, R.L. Calculation of Solar Irradiances. I. Synthesis of the Solar Spectrum. *The Astrophysical Journal*, 518:480–499, 1999. doi:10.1086/307258.

Forbush, S.E. World-wide cosmic ray variations, 1937–1952. *J. Geophys. Res.*, 59(4):525–542, 1954. doi:10.1029/SP037p0183.

Forster, P., Ramaswamy, V., Artaxo, P., Berntsen, T., Betts, R., Fahey, D., Haywood, J., Lean, J., Lowe, D., Myhre, G., Nganga, J., Prinn, R., Raga, G., Schulz, M., and Van Dorland, R. Changes in atmospheric constituents and in radiative forcing. In S. Solomon, D. Qin, M. Manning, Z. Chen, M. Marquis, K. Averyt, M. Tignor, and H. Miller, editors, *Climate Change 2007: The Physical Science Basis. Contribution of Working Group I to the Fourth Assessment Report of the Intergovernmental Panel on Climate Change*. Cambridge University Press, Cambridge, United Kingdom and New York, NY, USA, 2007.

Forster, P.M., Fomichev, V.I., Rozanov, E., Cagnazzo, C., Jonsson, A.I., Langematz, U., Fomin, B., Iacono, M.J., Mayer, B., Mlawer, E., Myhre, G., Portmann, R.W., Akiyoshi, H., Falaleeva, V., Gillett, N., Karpechko, A., Li, J., Lemennais, P., Morgenstern, O., Oberländer, S., Sigmond, M., and Shibata, K. Evaluation of radiation scheme performance within chemistry climate models. *J. Geophys. Res.*, 116(D10), 2011. ISSN 2156-2202. doi:10.1029/2010JD015361.

Franklin, B. Meteorological imagination's and conjectures. *Manchester Lit. Philos. Soc.*, 2:122, 1784.

Fröhlich, C. Solar irradiance variability since 1978. *Space Science Reviews*, 125(1-4):53–65, 2006. doi:10.1007/s11214-006-9046-5.

Funke, B., Baumgaertner, A., Calisto, M., Egorova, T., Jackman, C.H., Kieser, J., Krivolutsky, A., López-Puertas, M., Marsh, D.R., Reddmann, T., Rozanov, E., Salmi, S.M., Sinnhuber, M., Stiller, G.P., Verronen, P.T., Versick, S., von Clarmann, T., Vyushkova, T.Y., Wieters, N., and Wissing, J.M. Composition changes after the "Halloween" solar proton event: the High Energy Particle Precipitation in the Atmosphere (HEPPA) model versus MIPAS data intercomparison study. *Atmos. Chem. Phys.*, 11(17):9089–9139, 2011. doi:10.5194/acp-11-9089-2011.

Gaines, E., Chenette, D., Imhof, W., Jackman, C., and Winningham, J. Relativistic electron fluxes in May 1992 and their effect on the middle atmosphere. *J. Geophys. Res.*, 100(D1):1027–1033, 1995. doi:10.1029/94JD02615.

Gao, C., Robock, A., and Ammann, C. Volcanic forcing of climate over the past 1500 years: An improved ice core-based index for climate models. *J. Geophys. Res.*, 113(D23):D23, 2008. ISSN 2156-2202. doi:10.1029/2008JD010239.

Gao, C., Robock, A., and Ammann, C. Correction to volcanic forcing of climate over the past 1500 years: An improved ice core-based index for climate models. *J. Geophys. Res.*, 117(D16):D16, 2012. ISSN 2156-2202. doi:10.1029/2012JD018052.

Garcia, R.R. and Solomon, S. A numerical model of the zonally averaged dynamical and chemical structure of the middle atmosphere. *J. Geophys. Res.*, 88(C2):1379–1400, 1983. doi:10.1029/JC088iC02p01379.

Garcia, R.R. and Solomon, S. A new numerical model of the middle atmosphere: 2. Ozone and related species. *J. Geophys. Res.*, 99(D6):12937–12951, 1994. doi: 10.1029/94JD00725.

Giorgetta, M. *Der Einfluss der quasi-zweijaehrigen Oszillation: Modellrechnungen mit ECHAM4*. Ph.D. thesis, Max-Planck-Institut für Meteorologie, Hamburg, 1996.

Gosling, J.T. The solar flare myth. *J. Geophys. Res.*, 98(A11):18937–18949, 1993. doi:10.1029/93JA01896.

Granier, C. and Brasseur, G. Impact of heterogeneous chemistry on model predictions of ozone changes. *J. Geophys. Res.*, 97(D16):18015–18033, 1992. doi:10.1029/92JD02021.

Gray, L.J., Beer, J., Geller, M., Haigh, J.D., Lockwood, M., Matthes, K., Cubasch, U., Fleitmann, D., Harrison, G., Hood, L., Luterbacher, J., Meehl, G.A., Shindell, D., van Geel, B., and White, W. Solar influences on climate. *Rev. Geophys.*, 48(4), 2010. ISSN 1944-9208. doi:10.1029/2009RG000282.

Hagemann, S. *An improved land surface parameter dataset for global and regional climate models*. Max-Planck-Institut für Meteorologie, Hamburg, 2002.

Hagemann, S., Botzet, M., Dümenil, L., and Machenhauer, B. *Derivation of global GCM boundary conditions from 1 km land use satellite data*. Max-Planck-Institut für Meteorologie, 1999.

Hagemann, S. and Dümenil, L. A parametrization of the lateral waterflow for the global scale. *Climate Dyn.*, 14(1):17–31, 1997. doi:10.1007/s003820050205.

Haigh, J., Winning, A., Toumi, R., and Harder, J. An influence of solar spectral variations on radiative forcing of climate. *Nature*, 467(7316):696–699, 2010. doi:10.1038/nature09426.

Haigh, J.D. The impact of solar variability on climate. *Science*, 272(5264):981–984, 1996. doi:10.1126/science.272.5264.981. eprint:http://www.sciencemag.org/content/272/5264/981.full.pdf.

Haigh, J.D. The effects of solar variability on the earth's climate. *Phil. Trans. R. Soc. Lond*, 361(1802):95–111, 2003. doi:10.1098/rsta.2002.1111.

Halmer, M., Schmincke, H.U., and Graf, H.F. The annual volcanic gas input into the atmosphere, in particular into the stratosphere: a global data set for the past 100 years. *J. Volcanol. Geotherm. Res.*, 115(3):511–528, 2002. doi:10.1016/S0377-0273(01)00318-3.

Hampson, J. *Photochemical behaviour of the ozone layer*. Canadian Armament Research and Development Establishment, 1964.

Hansen, J., Lacis, A., Ruedy, R., and Sato, M. Potential climate impact of Mount Pinatubo eruption. *Geophys. Res. Lett.*, 19(2):215–218, 1992. ISSN 1944-8007. doi:10.1029/91GL02788.

Hanson, D.R. and Ravishankara, A. The reaction probabilities of ClONO2 and N2O5 on 40 to 75% sulfuric acid solutions. *J. Geophys. Res.*, 96(D9):17307–17314, 1991. doi:10.1029/91JD01750.

Harington, C. The year without a summer. In C. Harington, editor, *World Climate in 1816*. Ottawa: Canadian Museum of Nature, 1992.

Hays, J.D., Imbrie, J., and Shackleton, N.J. Variations in the Earth's orbit: Pacemaker of the ice ages. *Science*, 194(4270):1121–1132, 1976. doi:10.1126/science.194.4270.1121.

Heikkilä, U. *Modeling of the Atmospheric Transport of the Cosmogenic Radionuclides 10Be and 7Be Using the ECHAM5-HAM General Circulation Model*. Ph.D. thesis, ETH, 2007.

Hoerandel, J.R. On the knee in the energy spectrum of cosmic rays. *Astroparticle Physics*, 19(2):193–220, 2003. eprint:astro-ph/0210453v1.

Holton, J.R. and Hakim, G.J. *An introduction to dynamic meteorology*. Academic press, Elsevier, Burlington, MA, USA, 2012.

Hoyt, D.V. and Schatten, K.H. Group sunspot numbers: A new solar activity reconstruction. *Sol. Phys.*, 181:491–512, 1998. doi:10.1023/A:1005007527816.

Hunt, B.G. Photochemistry of ozone in a moist atmosphere. *J. Geophys. Res.*, 71(5):1385–1398, 1966. doi:10.1029/JZ071i005p01385.

Iles, C.E., Hegerl, G.C., Schurer, A.P., and Zhang, X. The effect of volcanic eruptions on global precipitation. *J. Geophys. Res.*, 118(16):8770–8786, 2013. ISSN 2169-8996. doi:10.1002/jgrd.50678.

Imbrie, J., Berger, A., Boyle, E.A., Clemens, S.C., Duffy, A., Howard, W.R., Kukla, G., Kutzbach, J., Martinson, D.G., McIntyre, A., Mix, A.C., Molfino, B., Morley, J.J., Peterson, L.C., Pisias, N.G., Prell, W.L., Raymo, M.E., Shackleton, N.J., and Toggweiler, J.R. On the structure and origin of major glaciation cycles 2. The 100,000-year cycle. *Paleoceanography*, 8(6):699–735, 1993. ISSN 1944-9186. doi:10.1029/93PA02751.

Ineson, S., Scaife, A.A., Knight, J.R., Manners, J.C., Dunstone, N.J., Gray, L.J., and Haigh, J.D. Solar forcing of winter climate variability in the Northern Hemisphere. *Nature*, 4(11):753–757, 2011. ISSN 1752-0894. doi:10.1038/NGEO1282.

Intergovernmental Panel on Climate Change, IPCC, Climate change 2007. The physical science basis. contribution of working group i to the fourth assessment report of the intergovernmental panel on climate change. In S. Solomon, D. Qin, M. Manning, Z. Chen, M. Marquis, K. Averyt, H. Tignor, and H. Miller, editors, *AR4*. Cambridge University Press, Cambridge, United Kingdom and New York, NY, USA, 2007.

Jackman, C.H. Ionization rates for 1963-2005 from solar proton events. Technical report, SPARC report, SOLARIS, 2006.

Jackman, C.H., Douglass, A.R., Rood, R., McPeters, R.D., and Meade, P. Effect of solar proton events on the middle atmosphere during the past two solar cycles as computed using a two-dimensional model. *J. Geophys. Res.*, 95 (D6):7417–7428, 1990. doi:10.1029/JD095iD06p07417.

Jackman, C.H., Marsh, D.R., Vitt, F.M., Garcia, R.R., Fleming, E.L., Labow, G.J., Randall, C.E., López-Puertas, M., Funke, B., Von Clarmann, T., and Stiller, G.P. Short- and medium-term atmospheric constituent effects of very large solar proton events. *Atmos. Chem. Phys.*, 8(3):765–785, 2008. doi:10.5194/acp-8-765-2008.

Jackman, C.H., Marsh, D.R., Vitt, F.M., Garcia, R.R., Randall, C.E., Fleming, E.L., and Frith, S.M. Long-term middle atmospheric influence of very large solar proton events. *J. Geophys. Res.*, 114(D11), 2009. ISSN 2156-2202. doi:10.1029/2008JD011415.

Jackson, A., Jonkers, A.R., and Walker, M.R. Four centuries of geomagnetic secular variation from historical records. *Philosophical Transactions of the Royal Society of London. Series A: Mathematical, Physical and Engineering Sciences*, 358(1768):957–990, 2000. doi:10.1098/rsta.2000.0569.

Jones, G.S., Lockwood, M., and Stott, P.A. What influence will future solar activity changes over the 21st century have on projected global near-surface temperature changes? *J. Geophys. Res.*, 117(D5), 2012. ISSN 2156-2202. doi:10.1029/2011JD017013.

Jones, P.D., Ogilvie, A.E., Davies, T.D., and Briffa, K.R. *History and climate: memories of the future?* Springer, 2001.

Judge, P.G., Lockwood, G.W., Radick, R.R., Henry, G.W., Shapiro, A.I., Schmutz, W., and Lindsey, C. Confronting a solar irradiance reconstruction with solar and stellar data. *Astron. & Astrophys.*, 544:A88, 2012. doi:10.1051/0004-6361/201218903.

Jungclaus, J.H., Lorenz, S.J., Timmreck, C., Reick, C.H., Brovkin, V., Six, K., Segschneider, J., Giorgetta, M.A., Crowley, T.J., Pongratz, J., Krivova, N.A., Vieira, L.E., Solanki, S.K., Klocke, D., Botzet, M., Esch, M., Gayler, V., Haak, H., Raddatz, T.J., Roeckner, E., Schnur, R., Widmann, H., Claussen, M., Stevens, B., and Marotzke, J. Climate and carbon-cycle variability over the last millennium. *Clim. Past*, 6(5):723–737, 2010. doi:10.5194/cp-6-723-2010.

Kahler, S. Solar flares and coronal mass ejections. *Annu. Rev. Astron. Astr.*, 30:113–141, 1992. doi:10.1146/annurev.aa.30.090192.000553.

Karl, T.R. and Trenberth, K.E. Modern global climate change. *Science*, 302(5651):1719–1723, 2003. doi:10.1126/science.1090228.

Kerrick, D.M. Present and past nonanthropogenic CO2 degassing from the solid Earth. *Rev. Geophys.*, 39(4):565–585, 2001. doi:10.1029/2001RG000105.

Kirchner, I., Stenchikov, G.L., Graf, H.F., Robock, A., and Antuna, J.C. Climate model simulation of winter warming and summer cooling following the 1991 Mount Pinatubo volcanic eruption. *J. Geophys. Res.*, 104(D16):19039–19055, 1999. doi:10.1029/1999JD900213.

Knutti, R. and Sedláček, J. Robustness and uncertainties in the new CMIP5 climate model projections. *Nat. Clim. Chang.*, 3:369–373, 2012. doi:10.1038/nclimate1716.

Kodera, K. and Kuroda, Y. Dynamical response to the solar cycle. *J. Geophys. Res.*, 107:4749–4761, 2002. doi:10.1029/2002JD002224.

Kopp, G. and Lean, J.L. A new, lower value of total solar irradiance: Evidence and climate significance. *Geophys. Res. Lett.*, 38(1), 2011. doi:10.1029/2010GL045777.

Korte, M., Donadini, F., and Constable, C. Geomagnetic field for 0–3 ka: 2. A new series of time-varying global models. *Geochem. Geophys. Geosyst.*, 10(6), 2009. doi:10.1029/2008gc002297.

Kosovichev, A., Schou, J., Scherrer, P., Bogart, R., Bush, R., Hoeksema, J., Aloise, J., Bacon, L., Burnette, A., Forest, C., Giles, P., Leibrand, K., Nigam, R., Rubin, M., Scott, K., Williams, S., Basu, S., Christensen-Dalsgaard, J., Däppen, W., Rhodes, E.J., J., Duvall, T.L., J., Howe, R., Thompson, M., Gough, D., Sekii, T., Toomre,

J., Tarbell, T., Title, A., Mathur, D., Morrison, M., Saba, J., Wolfson, C., Zayer, I., and Milford, P. Structure and Rotation of the Solar Interior: Initial Results from the MDI Medium-L Program. In B. Fleck and Z. Łvestka, editors, *The First Results from SOHO*, pages 43–61. Springer Netherlands, 1997. ISBN 978-94-010-6204-6. doi: 10.1007/978-94-011-5236-5_3.

Kravitz, B. and Robock, A. Climate effects of high-latitude volcanic eruptions: Role of the time of year. *J. Geophys. Res.*, 116(D1):n/a–n/a, 2011. ISSN 2156-2202. doi:10.1029/2010JD014448.

Labitzke, K., Austin, J., Butchardt, N., Knight, J., Takahashi, M., Nakamoto, M., Nagashima, T., Haigh, J., and Williams, V. The global signal of the 11-year solar cycle in the stratosphere: observations and models. *J. Atmos. Sol.-Terr. Phy.*, 64:203–210, 2002. doi:10.1016/S1364-6826(01)00084-0.

Lamarque, J.F., Bond, T.C., Eyring, V., Granier, C., Heil, A., Klimont, Z., Lee, D., Liousse, C., Mieville, A., Owen, B., Schultz, M.G., Shindell, D., Smith, S.J., Stehfest, E., Van Aardenne, J., Cooper, O.R., Kainuma, M., Mahowald, N., McConnell, J.R., Naik, V., Riahi, K., and van Vuuren, D.P. Historical (18502000) gridded anthropogenic and biomass burning emissions of reactive gases and aerosols: methodology and application. *Atmos. Chem. Phys.*, 10(15):7017–7039, 2010. doi:10.5194/acp-10-7017-2010.

Lang, K.R. *The Cambridge encyclopedia of the Sun*, volume 1. Cambridge University Press, Cambridge, UK, 2001.

Lanzante, J.R. Diagnosis of Radiosonde Vertical Temperature Trend Profiles: Comparing the Influence of Data Homogenization versus Model Forcings. *Journal of Climate*, 20:5356, 2007. doi:10.1175/2007JCLI1827.1.

Laut, P. Solar activity and terrestrial climate: an analysis of some purported correlations. *Journal of Atmospheric and Solar-Terrestrial Physics*, 65(7):801 – 812, 2003. ISSN 1364-6826. doi:10.1016/S1364-6826(03)00041-5.

Lean, J., Beer, J., and Bradley, R. Reconstruction of solar irradiance since 1610: Implications for climate change. *Geophys. Res. Lett.*, 22(23):3195–3198, 1995. doi: 10.1029/95GL03093.

Lean, J., Rottman, G., Harder, J., and Kopp, G. SORCE contributions to new understanding of global change and solar variability. *Sol. Phys.*, 230:27–53, 2005. doi: 10.1007/s11207-005-1527-2.

Lean, J.L. and DeLand, M.T. How Does the Sun's Spectrum Vary? *J. Climate*, 25(7):2555–2560, 2012. doi:10.1175/JCLI-D-11-00571.1.

Lee, D.S., Fahey, D.W., Forster, P.M., Newton, P.J., Wit, R.C., Lim, L.L., Owen, B., and Sausen, R. Aviation and global climate change in the 21st century. *Atmos. Environ.*, 43(22):3520–3537, 2009. doi:10.1016/j.atmosenv.2009.04.024.

Lisiecki, L.E. and Raymo, M.E. A Pliocene-Pleistocene stack of 57 globally distributed benthic δ18O records. *Paleoceanography*, 20(1), 2005. doi:10.1029/2004PA001071.

Ljungqvist, F. A new reconstruction of temperature variability in the extra-tropical northern hemisphere during the last two millenia. *Geogr. Ann. A*, 92(3):339–351, 2010. ISSN 1468-0459. doi:10.1111/j.1468-0459.2010.00399.x.

Lockwood, M. Solar physics: Shining a light on solar impacts. *Nature Climate Change*, 1:98–99, 2011a. doi:10.1038/nclimate1096.

Lockwood, M. and Fröhlich, C. Recent oppositely directed trends in solar climate forcings and the global mean surface air temperature. *Proceedings of the Royal Society A: Mathematical, Physical and Engineering Science*, 463(2086):2447–2460, 2007. doi:10.1098/rspa.2007.1880.

Lockwood, M., Owens, M., Barnard, L., Davis, C., and Steinhilber, F. The persistence of solar activity indicators and the descent of the sun into maunder minimum conditions. *Geophysical Research Letters*, 38(22), 2011b. doi:10.1029/2011GL049811.

Lockwood, M., Rouillard, A., and Finch, I. The rise and fall of open solar flux during the current grand solar maximum. *Astrophys. J.*, 700(2):937, 2009. doi:10.1088/0004-637X/700/2/937.

Lohmann, U. and Roeckner, E. Design and performance of a new cloud microphysics scheme developed for the ECHAM general circulation model. *Clim. Dyn.*, 12(8):557–572, 1996. doi:10.1007/BF00207939.

London, J. Radiative energy sources and sinks in the stratosphere and mesosphere. In M. Nicolet and A.C. Aikin, editors, *Atmospheric Ozone and its Variation and Human Influences*, page 703. 1980.

Lorenz, E.N. A study of the general circulation and a possible theory suggested by it. *Scientific Proceedings of the International Association of Meteorology, Rome*, 1954.

Lorius, C., Jouzel, J., Raynaud, D., Hansen, J., and Le Treut, H. The ice-core record: climate sensitivity and future greenhouse warming. *Nature*, 347(6289):139–145, 1990. doi:10.1038/347139a0.

Lüdecke, H.J. Long-term instrumental and reconstructed temperature records contradict anthropogenic global warming. *Energy & Environment*, 22(6):723–745, 2011b. eprint:1110.1841v1.

Lüdecke, H.J., Link, R., and Ewert, F.K. How natural is the recent centennial warming? an analysis of 2249 surface temperature records. *International Journal of Modern Physics C*, 22(10):1139–1159, 2011a. doi:10.1142/S0129183111016798.

Luterbacher, J., Dietrich, D., Xoplaki, E., Grosjean, M., and Wanner, H. European Seasonal and Annual Temperature Variability, Trends, and Extremes Since 1500. *Science*, 303:1499–1503, 2004. doi:10.1126/science.1093877.

MacFarling-Meure, C. *The natural and anthropogenic variations of carbon dioxide, methane and nitrous oxide during the Holocene from ice core analysis*. Ph.D. thesis, University of Melbourne, 2004.

MacFarling-Meure, C., Etheridge, D., Trudinger, C., Steele, P., Langenfelds, R., Van Ommen, T., Smith, A., and Elkins, J. Law Dome CO_2, CH_4 and N_2O ice core records extended to 2000 years BP. *Geophys. Res. Lett.*, 33(14), 2006. doi:10.1029/2006GL026152.

Machida, T., Nakazawa, T., Fujii, Y., Aoki, S., and Watanabe, O. Increase in the atmospheric nitrous oxide concentration during the last 250 years. *Geophys. Res. Lett.*, 22(21):2921–2924, 1995. doi:10.1029/95GL02822.

Mann, M., Bradley, S., and Hughes, M. Northern hemisphere temperatures during the past millennium: inferences, uncertainties, and limitations. *Geophys. Res. Lett.*, 26(6):759–762, 1999. doi:10.1029/1999GL900070.

Mann, M.E., Fuentes, J.D., and Rutherford, S. Underestimation of volcanic cooling in tree-ring-based reconstructions of hemispheric temperatures. *Nature Geoscience*, 5:202–205, 2012. doi:10.1038/ngeo1394.

Manzini, E., Giorgetta, M., Esch, M., Kornblueh, L., and Roeckner, E. The influence of sea surface temperatures on the northern winter stratosphere: Ensemble simulations with the MAECHAM5 model. *J. Climate*, 19(16):3863–3881, 2006. doi:10.1175/JCLI3826.1.

Margitan, J.J. Mechanism of the atmospheric oxidation of sulfur dioxide. catalysis by hydroxyl radicals. *J. Phys. Chem.*, 88(15):3314–3318, 1984. doi:10.1021/j150659a035.

Marsh, N. and Svensmark, H. Cosmic rays, clouds, and climate. *Space Science Reviews*, 94(1-2):215–230, 2000. doi:10.1023/A:1026723423896.

Marsland, S., Haak, H., Jungclaus, J., Latif, M., and Roske, F. The Max-Planck-Institute global ocean/sea ice model with orthogonal curvilinear coordinate. *Ocean Model.*, 5:91–27, 2003. doi:10.1016/S1463-5003(02)00015-X.

Maunder, E.W. Note on the distribution of sun-spots in heliographic latitude, 1874-1902. *Monthly Notices of the Royal Astronomical Society*, 64:747–761, 1904.

Mayewski, P.A., Meeker, L.D., Twickler, M.S., Whitlow, S., Yang, Q., Lyons, W.B., and Prentice, M. Major features and forcing of high-latitude northern hemisphere atmospheric circulation using a 110,000-year-long glaciochemical series. *J. Geophys. Res.*, 102(C12):26345–26, 1997. doi:10.1029/96JC03365.

McGregor, S. and Timmermann, A. The effect of explosive tropical volcanism on enso. *Journal of Climate*, 24(8):2178–2191, 2011. doi:10.1175/2010JCLI3990.1.

Meehl, G., Arblaster, J., Branstator, G., and Van Loon, H. A coupled air-sea response mechanism to solar forcing in the pacific region. *J. Clim.*, 21:2883–2897, 2008. doi:10.1175/2007JCLI1776.1.

Meehl, G.A., Arblaster, J.M., and Marsh, D.R. Could a future Grand Solar Minimum like the Maunder Minimum stop global warming? *Geophys. Res. Lett.*, 40(9):1789–1793, 2013. ISSN 1944-8007. doi:10.1002/grl.50361.

Meehl, G.A., Arblaster, J.M., Matthes, K., Sassi, F., and van Loon, H. Amplifying the pacific climate system response to a small 11-year solar cycle forcing. *Science*, 325(5944):1114–1118, 2009. doi:10.1126/science.1172872. eprint:http://www.sciencemag.org/content/325/5944/1114.full.pdf.

Meehl, G.A., Washington, W.M., Collins, W.D., Arblaster, J.M., Hu, A., Buja, L.E., Strand, W.G., and Teng, H. How much more global warming and sea level rise? *Science*, 307(5716):1769–1772, 2005. doi:10.1126/science.1106663.

Meehl, G.A., Washington, W.M., Wigley, T., Arblaster, J.M., and Dai, A. Solar and greenhouse gas forcing and climate response in the twentieth century. *J. Clim.*, 16(3):426–444, 2003. doi:10.1175/1520-0442.

Milanković, M. Mathematische Klimalehre und astronomische Theorie der Klimaschwankungen. In:. *Koeppen, W., Geiger, R. (Eds.), Handbuch der Klimatologie. Bd. I, Teil A. Berlin, Verlag Borntraeger*, pages 1–176, 1930.

Milham, W. The year 1816 - the causes of abnormalities. *Mon. Wea. Rev.*, 52:563–570, 1924. doi:10.1175/1520-0493(1924)52.

Minnis, P., Harrison, E., Stowe, L., Gibson, G., Denn, F., Doelling, D., and Smith, W. Radiative climate forcing by the Mount Pinatubo eruption. *Science*, 259:1411–1415, 1993. doi:10.1126/science.259.5100.1411.

Mitler, H.E. Cosmic-ray production of deuterium, He3, lithium, beryllium, and boron in the Galaxy. *Astrophys. Space Sci.*, 17(1):186–218, 1972. doi:10.1007/BF00642551.

Mlawer, E.J., Taubman, S.J., Brown, P.D., Iacono, M.J., and Clough, S.A. Radiative transfer for inhomogeneous atmospheres: RRTM, a validated correlated-k model for the longwave. *J. Geophys. Res.*, 102(D14):16663–16, 1997. doi:10.1029/97JD00237.

Molina, L. and Molina, M. Production of chlorine oxide (Cl2O2) from the self-reaction of the chlorine oxide (ClO) radical. *J. Phys. Chem.*, 91(2):433–436, 1987. doi:10.1021/j100286a035.

Molina, M.J. and Rowland, F.S. Stratospheric sink for chlorofluoromethanes: chlorine atom-catalysed destruction of ozone. *Nature*, 249(28):810–812, 1974. doi:doi:10.1038/249810a0.

Mörner, N.A. Solar Minima, Earth's rotation and Little Ice Ages in the past and in the future: The North AtlanticEuropean case. *Global and Planetary Change*, 72(4):282 – 293, 2010. ISSN 0921-8181. doi:http://dx.doi.org/10.1016/j.gloplacha.2010.01.004. Quaternary and Global Change: Review and Issues Special issue in memory of Hugues FAURE.

NCAR/CISL/VETS. The NCAR Command Language (Version 6.0.0) [Software], Boulder, USA. 2012.

Nesme-Ribes, E., Sokoloff, D., and Sadourny, B. Solar rotation, irradiance changes and climate. In *Poster Proceedings from IAU Colloquium 143: The Sun as a Variable Star: Solar and Stellar Irradiance Variations*, volume 1, page 244. 1994.

Newhall, C.G. and Self, S. The Volcanic Explosivity Index (VEI) an estimate of explosive magnitude for historical volcanism. *J. Geophys. Res.*, 87(C2):1231–1238, 1982. doi:10.1029/JC087iC02p01231.

Nordeng, T.E. *Extended versions of the convective parametrization scheme at ECMWF and their impact on the mean and transient activity of the model in the tropics*. European Centre for Medium-Range Weather Forecasts, 1994.

Norval, M., Cullen, A., De Gruijl, F., Longstreth, J., Takizawa, Y., Lucas, R., Noonan, F., and Van Der Leun, J. The effects on human health from stratospheric ozone depletion and its interactions with climate change. *Photochem. Photobiol. Sci.*, 6(3):232–251, 2007. doi:10.1039/B700018A.

Olson, D.W., Doescher, R.L., and Olson, M.S. The blood-red sky of the scream. *American Physical Society*, 13(5), 2004.

Oman, L., Robock, A., Stenchikov, G., Schmidt, G.A., and Ruedy, R. Climatic response to high-latitude volcanic eruptions. *J. Geophys. Res.*, 110(D13), 2005. doi:10.1029/2004JD005487.

Oreskes, N. The scientific consensus on climate change. *Science*, 306(5702):1686–1686, 2004. doi:10.1126/science.1103618.

Pagani, M., Freeman, K.H., and Arthur, M.A. Late Miocene atmospheric CO2 concentrations and the expansion of C4 grasses. *Science*, 285(5429):876–879, 1999. doi:10.1126/science.285.5429.876.

Parker, E. Acceleration of cosmic rays in solar flares. *Phys. Rev.*, 107(3):830, 1957. doi:10.1103/PhysRev.107.830.

Petit, J.R., Jouzel, J., Raynaud, D., Barkov, N., Barnola, J.M., Basile, I., Bender, M., Chappellaz, J., Davis, M., Delaygue, G., Delmotte, M., Kotlyakov, V., Legrand, M., Lipenkov, V., Lorius, C., Pepin, L., Ritz, C., Saltzman, E., and Stievenhard, M. Climate and atmospheric history of the past 420,000 years from the vostok ice core, antarctica. *Nature*, 399(6735):429–436, 1999. doi:10.1038/20859.

Pickering, K.E., Wang, Y., Tao, W.K., Price, C., and Müller, J.F. Vertical distributions of lightning NOx for use in regional and global chemical transport models. *J. Geophys. Res.*, 103(D23):31203–31, 1998. doi:10.1029/98JD02651.

Pitari, G. and Rizi, V. An estimate of the chemical and radiative perturbation of stratospheric ozone following the eruption of Mt. Pinatubo. *J. Atmos. Sci.*, 50(19), 1993.

Pongratz, J., Reick, C., Raddatz, T., and Claussen, M. A reconstruction of global agricultural areas and land cover for the last millennium. *Global Biogeochem. Cycles*, 22(3), 2008. doi:10.1029/2007GB003153.

Porter, H., Jackman, C., and Green, A. Efficiencies for production of atomic nitrogen and oxygen by relativistic proton impact in air. *J. Chem. Phys.*, 65:154, 1976.

Raisbeck, G., Yiou, F., Jouzel, J., Petit, J., Weiss, N., Allsop, J., and Robin, G.d.Q. 10Be and d2H in Polar Ice Cores as a Probe of the Solar Variability's Influence on Climate [and Discussion]. *Phil. Trans. R. Soc. A*, 330(1615):463–470, 1990. doi: 10.1098/rsta.1990.0027.

Ramankutty, N. and Foley, J.A. Estimating historical changes in land cover: North American croplands from 1850 to 1992. *Global Ecology and Biogeography*, 8(5):381–396, 1999. doi:10.1046/j.1365-2699.1999.00141.x.

Ravishankara, A., Daniel, J.S., and Portmann, R.W. Nitrous oxide (N2O): The dominant ozone-depleting substance emitted in the 21st century. *Science*, 326(5949):123–125, 2009. doi:10.1126/science.1176985.

Reichler, T., Kim, J., Manzini, E., and Kröger, J. A stratospheric connection to atlantic climate variability. *Nature Geoscience*, 5:783–787, 2012. doi:10.1038/ngeo1586.

Robock, A. Review of year without a summer? world climate in 1816. *Climatic Change*, 26:105–108, 1994.

Robock, A. Volcanic eruptions and climate. *Rev. Geophys.*, 38:191–219, 2000. doi: 10.1029/1998RG000054.

Robock, A. and Mao, J. Winter warming from large volcanic eruptions. *Geophys. Res. Lett.*, 19(24):2405–2408, 1992. doi:10.1029/92GL02627.

Robock, A. and Mao, J. The volcanic signal in surface temperature observations. *J. Climate*, 8(5):1086–1103, 1995. doi:10.1175/1520-0442(1995)008.

Roeckner, E., Baeuml, G., Bonaventura, L., Brokopf, R., Esch, M., Giorgetta, M., Hagemann, S., Kirchner, I., Kornblueh, L., Manzini, E., Rhodin, A., Schlese, U., Schulzweida, U., and Tompkins, A. The atmospheric general circulation model ECHAM 5. PART I: Model description. *Max-Plank-Institut für Meteorologie, Hamburg, Report No. 349*, 2003.

Roeckner, E., Dümenil, L., Kirk, E., Lunkeit, F., Ponater, M., Rockel, B., Sausen, R., and Schlese, U. The Hamburg version of the ECMWF model (ECHAM). *Research activities in atmospheric and oceanic modelling. CAS/JSC Working Group on Numerical Experimentation*, 13:7–1, 1989.

Rozanov, E., Calisto, M., Egorova, T., Peter, T., and Schmutz, W. Influence of the precipitating energetic particles on atmospheric chemistry and climate. *Surveys in Geophysics*, 33:483–501, 2012b. ISSN 0169-3298. doi:10.1007/s10712-012-9192-0.

Rozanov, E., Schlesinger, M., and Zubov, V. The University of Illinois, Urbana-Champaign three-dimensional stratosphere-troposphere general circulation model with interactive ozone photochemistry: Fifteen-year control run climatology. *J. Geophys. Res.*, 106(D21):27233–27254, 2001. doi:10.1029/2000JD000058.

Rozanov, E., Schlesinger, M.E., Zubov, V., Yang, F., and Andronova, N.G. The UIUC three-dimensional stratospheric chemical transport model: Description and evaluation of the simulated source gases and ozone. *J. Geophys. Res.*, 104:755–781, 1999. doi:10.1029/1999JD900138.

Rozanov, E.V., Egorova, T.A., Shapiro, A.I., and Schmutz, W.K. Modeling of the atmospheric response to a strong decrease of the solar activity. *Proc. Int. Astron. Union*, 7(S286):215–224, 2012a. doi:10.1017/S1743921312004863.

Sander, S.P., Friedl, R., Barker, J., Golden, D., Kurylo, M., Wine, P., Abatt, J., Burkholder, J., Kolb, C., Moortgat, GK Huie, R., and Orkin, V. Chemical kinetics and photochemical data for use in atmospheric studies, evaluation number 17. *JPL Publication 10-6*, 17:1–684, 2011.

Scherer, K., Fahr, H.J., Fichtner, H., and Heber, B. Long-term modulation of cosmic rays in the heliosphere and its influence at earth. *Solar Physics*, 224(1-2):305–316, 2004. ISSN 0038-0938. doi:10.1007/s11207-005-5687-x.

Schraner, M., Rozanov, E., Schnadt Poberaj, C., Kenzelmann, P., Fischer, A.M., Zubov, V., Luo, B.P., Hoyle, C.R., Egorova, T., Füglistaler, S., Brönnimann, S., Schmutz, W., and Peter, T. Technical Note: Chemistry-climate model SOCOL: version 2.0 with improved transport and chemistry/microphysics schemes. *Atmos. Chem. Phys.*, 8:5957–5974, 2008. doi:10.5194/acp-8-5957-2008.

Schrijver, C., Beer, J., Baltensperger, U., Cliver, E., Güdel, M., Hudson, H., McCracken, K., Osten, R., Peter, T., Soderblom, D., R., D., Usoskin, I.G., and Wolff, E.W. Estimating the frequency of extremely energetic solar events, based on solar, stellar, lunar, and terrestrial records. *J. Geophys. Res.*, 117(A8):A8, 2012. ISSN 2156-2202. doi:10.1029/2012JA017706.

Schwabe, M. Sonnenbeobachtungen im Jahre 1843. Von Herrn Hofrath Schwabe in Dessau. *Astronomische Nachrichten*, 21:233–236, 1844.

Semeniuk, K., Fomichev, V.I., McConnell, J.C., Fu, C., Melo, S.M.L., and Usoskin, I.G. Middle atmosphere response to the solar cycle in irradiance and ionizing particle precipitation. *Atmospheric Chemistry and Physics*, 11(10):5045–5077, 2011. doi: 10.5194/acp-11-5045-2011.

Serreze, M.C. and Barry, R.G. Processes and impacts of arctic amplification: A research synthesis. *Global and Planetary Change*, 77(1):85–96, 2011. doi:10.1016/j.gloplacha.2011.03.004.

Setlow, R.B. The wavelengths in sunlight effective in producing skin cancer: a theoretical analysis. *P. Natl. Acad. Sci. USA*, 71(9):3363–3366, 1974. doi:10.1073/pnas.71.9.3363.

Shackleton, N.J. The 100,000-year ice-age cycle identified and found to lag temperature, carbon dioxide, and orbital eccentricity. *Science*, 289(5486):1897–1902, 2000. doi:10.1126/science.289.5486.1897.

Shapiro, A.I., Schmutz, W., Cessateur, G., and Rozanov, E. The place of the Sun among the Sun-like stars. *Astron. & Astrophys.*, 552:A114, 2013. doi:10.1051/0004-6361/201220512. eprint:1303.2245.

Shapiro, A.I., Schmutz, W., Rozanov, E., Schoell, M., Haberreiter, M., Shapiro, A.V., and Nyeki, S. A new approach to the long-term reconstruction of the solar irradiance leads to large historical solar forcing. *Astron. & Astrophys.*, 529(A67), 2011. eprint: arXiv:1102.4763v1.

Shapiro, A.I., Schmutz, W., Schoell, M., Haberreiter, M., and Rozanov, E. NLTE solar irradiance modeling with the COSI code. *Astron. & Astrophys.*, 517:A48+, 2010. doi: 10.1051/0004-6361/200913987. eprint:1004.3048.

Shea, M., Smart, D., McCracken, K., Dreschhoff, G., and Spence, H. Solar proton events for 450 years: The Carrington event in perspective. *Adv. Space Res.*, 38(2):232 – 238, 2006. ISSN 0273-1177. doi:10.1016/j.asr.2005.02.100. The Great Historical Geomagnetic Storm of 1859: A Modern Look.

Shindell, D., Rind, D., Balachandran, N., Lean, J., and Lonergan, P. Solar cycle variability, ozone, and climate. *Science*, 284(5412):305–308, 1999. doi:10.1126/science.284.5412.305.

Shindell, D., Schmidt, G., Miller, R., and Mann, M. Volcanic and solar forcing of climate change during the preindustrial era. *J. Climate*, 16:4094–4107, 2000. doi:10.1175/1520-0442(2003)016⟨4094:VASFOC⟩2.0.CO;2.

Sinnhuber, M., Nieder, H., and Wieters, N. Energetic Particle Precipitation and the Chemistry of the Mesosphere/Lower Thermosphere. *Surveys in Geophysics*, 33:1281–1334, 2012. doi:10.1007/s10712-012-9201-3.

Solanki, S. and Unruh, Y. Solar irradiance variability. *Astronomische Nachrichten*, 334(1-2):145–150, 2013. ISSN 1521-3994. doi:10.1002/asna.201211752.

Solanki, S.K., Krivova, N.A., and Haigh, J.D. Solar Irradiance Variability and Climate. *Astron. & Astrophys.*, 51:311–351, 2013. doi:10.1146/annurev-astro-082812-141007. eprint:1306.2770.

Solomon, S., Daniel, J., Neely, R., Vernier, J.P., Dutton, E., and Thomason, L. The persistently variable background stratospheric aerosol layer and global climate change. *Science*, 333(6044):866–870, 2011. doi:10.1126/science.1206027.

Solomon, S., Rusch, D., Gérard, J.C., Reid, G., and Crutzen, P. The effect of particle precipitation events on the neutral and ion chemistry of the middle atmosphere: II. Odd hydrogen. *Planet. Space Sci.*, 29(8):885–893, 1981. doi:10.1016/0032-0633(81)90078-7.

Sonett, C. and Suess, H. Correlation of bristlecone pine ring widths with atmospheric 14C variations: a climate–sun relation. *Nature*, 307:141–143, 1984. doi:10.1038/307141a0.

Spahni, R., Chappellaz, J., Stocker, T.F., Loulergue, L., Hausammann, G., Kawamura, K., Flückiger, J., Schwander, J., Raynaud, D., Masson-Delmotte, V., and Jouzel, J. Atmospheric methane and nitrous oxide of the late pleistocene from antarctic ice cores. *Science*, 310(5752):1317–1321, 2005. doi:10.1126/science.1120132. eprint: http://www.sciencemag.org/content/310/5752/1317.full.pdf.

Spangehl, T., Cubasch, U., and Langematz, U. Änderung der NAO im Maunder Minimum und einem zukünftigen Klima in Modellsimulationen mit EGMAM. *Copernicus meetings*, 2007. [Accessed June 5th, 2013].

Spangehl, T., Cubasch, U., Raible, C., Schimanke, S., Körper, J., and Hofer, D. Transient climate simulations from the Maunder Minimum to present day: role of the stratosphere. *J. Geophys. Res.*, 115(D1):D00I10, 2010.

Steinhilber, F., Abreu, J.A., and Beer, J. Solar modulation during the holocene. *Astrophys. Space Sci.*, 4(1):1–6, 2008. doi:10.5194/astra-4-1-2008.

Steinhilber, F. and Beer, J. Prediction of solar activity for the next 500 years. *J. Geophys. Res.*, 2013. doi:10.1002/jgra.50210.

Steinhilber, F., Beer, J., and Fröhlich, C. Total solar irradiance during the holocene. *Geophys. Res. Lett.*, 36(19):L19704, 2009. doi:10.1029/2009GL040142.

Stenchikov, G., Delworth, T.L., Ramaswamy, V., Stouffer, R.J., Wittenberg, A., and Zeng, F. Volcanic signals in oceans. *J. Geophys. Res.*, 114(D16), 2009. ISSN 2156-2202. doi:10.1029/2008JD011673.

Stenchikov, G., Kirchner, I., Robock, A., Graf, H., Antuna, J., Grainger, R., Lambert, A., and Thomason, L. Radiative forcing from the 1991 Mount Pinatubo volcanic eruption. *J. Geophys. Res.*, 103:837–857, 1998. doi:10.1029/98JD00693.

Stenchikov, G., Robock, A., Ramaswamy, V., Schwarzkopf, M.D., Hamilton, K., and Ramachandran, S. Arctic Oscillation response to the 1991 Mount Pinatubo eruption: Effects of volcanic aerosols and ozone depletion. *J. Geophys. Res.*, 107(D24):ACL 28–1–ACL 28–16, 2002. ISSN 2156-2202. doi:10.1029/2002JD002090.

Stenke, A., Schraner, M., Rozanov, E., Egorova, T., Luo, B., and Peter, T. The socol version 3.0 chemistryclimate model: description, evaluation, and implications from an advanced transport algorithm. *Geoscientific Model Development*, 6(5):1407–1427, 2013. doi:10.5194/gmd-6-1407-2013.

Stockwell, W.R. and Calvert, J.G. The mechanism of the HO-SO2 reaction. *Atmos. Environ.*, 17(11):2231–2235, 1983. doi:10.1016/0004-6981(83)90220-2.

Swider, W. and Keneshea, T. Decrease of ozone and atomic oxygen in the lower mesosphere during a PCA event. *Planet. Space Sci.*, 21(11):1969–1973, 1973. doi:10.1016/0032-0633(73)90126-8.

Tie, X. and Brasseur, G. The response of stratospheric ozone to volcanic eruptions: Sensitivity to atmospheric chlorine loading. *Geophys. Res. Lett.*, 22(22):3035–3038, 1995.

Tiedtke, M. A comprehensive mass flux scheme for cumulus parameterization in large-scale models. *Mon. Wea. Rev.*, 117(8):1779–1800, 1989. doi:10.1175/1520-0493(1989)117.

Tompkins, A.M. A prognostic parameterization for the subgrid-scale variability of water vapor and clouds in large-scale models and its use to diagnose cloud cover. *J. Atmos. Sci.*, 59(12):1917–1942, 2002. doi:10.1175/1520-0469(2002)059.

Toohey, M., Krüger, K., Niemeier, U., and Timmreck, C. The influence of eruption season on the global aerosol evolution and radiative impact of tropical volcanic eruptions. *Atmospheric Chemistry and Physics*, 11(23):12351–12367, 2011. doi: 10.5194/acp-11-12351-2011.

Tratt, D. and Menzies, R. Evolution of the Pinatubo Volcanic Aerosol Column Above Pasadena, California Observed With a Mid-Infrared Backscatter Lidar. Technical report, Jet Propulsion Laboratory, California Institute of Technology, 1994.

Turman, B. and Edgar, B. Global lightning distributions at dawn and dusk. *J. Geophys. Res.*, 87(C2):1191–1206, 1982. doi:10.1029/JC087iC02p01191.

Usoskin, I., Gladysheva, O., and Kovaltsov, G. Cosmic ray-induced ionization in the atmosphere: spatial and temporal changes. *J. Atmos. Sol-Terr. Phy.*, 66(18):1791–1796, 2004. doi:10.1016/j.jastp.2004.07.037.

Usoskin, I.G. and Kovaltsov, G. Cosmic ray induced ionization in the atmosphere: Full modeling and practical applications. *J. Geophys. Res.*, 111:21206, 2006. doi:10.1029/2006JD007150.

Usoskin, I.G., Kovaltsov, G.A., and Mironova, I.A. Cosmic ray induced ionization model CRAC:CRII: An extension to the upper atmosphere. *J. Geophys. Res.*, 115(D10):D10, 2010. ISSN 2156-2202. doi:10.1029/2009JD013142.

Valcke, S. The OASIS3 coupler: a European climate modelling community software. *Geosci. Model Dev.*, 6(2):373–388, 2013. doi:10.5194/gmd-6-373-2013.

van Vuuren, D.P., Edmonds, J., Kainuma, M., Riahi, K., Thomson, A., Hibbard, K., Hurtt, G.C., Kram, T., Krey, V., Lamarque, J.F., Masui, T., Meinshausen, M., Na-kicenovic, N., Smith, S.J., and Rose, S.K. The representative concentration pathways: an overview. *Climatic Change*, 109(1-2):5–31, 2011. ISSN 0165-0009. doi: 10.1007/s10584-011-0148-z.

Varma, V, Prange, M., Lamy, F., Merkel, U., and Schulz, M. Solar-forced shifts of the southern hemisphere westerlies during the holocene. *Clim. past*, 7(2):339–347, 2011. doi:10.5194/cp-7-339-2011.

Varma, V., Prange, M., Spangehl, T., Lamy, F., Cubasch, U., and Schulz, M. Impact of solar-induced stratospheric ozone decline on southern hemisphere westerlies during the late maunder minimum. *Geophys. Res. Letters*, 39:20704, 2012. doi:10.1029/2012GL053403.

Vernier, J.P., Thomason, L.W., Pommereau, J.P., Bourassa, A., Pelon, J., Garnier, A., Hauchecorne, A., Blanot, L., Trepte, C., Degenstein, D., and Vargas, F. Major influence of tropical volcanic eruptions on the stratospheric aerosol layer during the last decade. *Geophys. Res. Lett.*, 38(12), 2011. ISSN 1944-8007. doi: 10.1029/2011GL047563.

Wagner, S. and Zorita, E. The influence of volcanic, solar and CO2 forcing on the temperatures in the Dalton Minimum (1790-1830): a model study. *Clim. Dyn.*, 25:205–218, 2005.

Warneck, P. Cosmic radiation as a source of odd nitrogen in the stratosphere. *J. Geophys. Res.*, 77(33):6589–6591, 1972. doi:10.1029/JC077i033p06589.

Washington, W.M., Knutti, R., Meehl, G.A., Teng, H., Tebaldi, C., Lawrence, D., Buja, L., and Strand, W.G. How much climate change can be avoided by mitigation? *Geophys. Res. Lett.*, 36(8):L08703, 2009. doi:10.1029/2008GL037074.

Wegmann, M., Brönnimann, S., Bhend, J., Franke, J., Folini, D., Wild, M., and Luterbacher, J. Volcanic influence on european summer precipitation though monsoons: Possible cause for "years without a summer". *J. Climate*, subm.:subm., 2013.

Weisenstein, D., Yue, G., Ko, M., Sze, N., Rodriguez, J., and Scott, C. A two-dimensional model of sulfur species and aerosols. *J. Geophys. Res*, 102(11D):13019–13035, 1997. doi:10.1029/97JD00901.

White, W.B. and Liu, Z. Non-linear alignment of El Niño to the 11-yr solar cycle. *Geophys. Res. Lett.*, 35(19), 2008. doi:10.1029/2008GL034831.

Whitehouse, D. Ray of hope: Can the sun save us from global warming? The Independent, online, 2007. eprint:http://www.independent.co.uk/news/science/ray-of-hope-can-the-sun-save-us-from-global-warming-762878.html.

Whitten, R., Toon, O., and Rurco, R. The stratospheric sulfate aerosol layer: Processes, models, observations, and simulations. *Pure Appl. Geophys.*, 118(1):86–127, 1980. doi:10.1007/BF01586447.

WMO. Scientific assessment of ozone depletion, global ozone research and monitoring project - report no. 52. Technical report, Geneva, Switzerland, 2011.

Wofsy, S.C., McElroy, M.B., and Yung, Y.L. The chemistry of atmospheric bromine. *Geophys. Res. Lett.*, 2(6):215–218, 1975. doi:10.1029/GL002i006p00215.

Wolf, R. Mittheilungen über die Sonnenflecken I. *Astronomische Mitteilungen der Ei-denössischen Sternwarte Zurich*, 1:3–13, 1850.

Wolf, R. Abstract of his latest results. *Mon. Not. R. Astron. Soc.*, 21:77, 1861.

Wolff, E., Bigler, M., Curran, M., Dibb, J., Frey, M., Legrand, M., and McConnell, J. The Carrington event not observed in most ice core nitrate records. *Geophys. Res. Lett.*, 39(8), 2012. doi:10.1029/2012GL051603.

Wolff, E., Jones, A.E., Bauguitte, S., and Salmon, R.A. The interpretation of spikes and trends in concentration of nitrate in polar ice cores, based on evidence from snow and atmospheric measurements. *Atmos. Chem. Phys*, 8(18):5627–5634, 2008. doi: 10.5194/acp-8-5627-2008.

Yoshimori, M., Stocker, T., Raible, C., and Renold, M. Externally forced and internal variability in ensemble climate simulations of the maunder minimum. *J. Climate*, 18(20):4253–4270, 2005. doi:10.1175/JCLI3537.1.

Yung, Y., Pinto, J., Watson, R., and Sander, S. Atmospheric bromine and ozone perturbations in the lower stratosphere. *J. Atmos. Sci.*, 37(2):339–353, 1980. doi: 10.1175/1520-0469(1980)037.

Zachos, J., Pagani, M., Sloan, L., Thomas, E., and Billups, K. Trends, rhythms, and aberrations in global climate 65 Ma to present. *Science*, 292(5517):686–693, 2001. doi:10.1126/science.1059412.

Zhu, X. An accurate and efficient radiation algorithm for middle atmosphere models. *J. Atmos. Sci.*, 51(24):3593–3614, 1994. doi:10.1175/1520-0469(1994)051.

Acknowledgements

Julien Gérard Anet

Regensbergstr. 81, CH-8050 Zürich
Tel.: +41 78 611 23 26
E-Mail: julien.anet@env.ethz.ch

Date of birth: November 27, 1986
Citizenship: Swiss, Geneva (GE)

EDUCATION	07/2010 – today	PhD in Atmospheric and Climate Sciences, *ETH Zürich*
	09/2008 – 07/2010	**Master in Atmospheric and Climate Sciences**, *ETH Zürich* Grade point average 5.2 Master thesis about "*Using the Community land model in air pollution modeling*" *(Grade 5.25)*
	09/2005 – 06/2008	**Bachelor in Earth Sciences**, *ETH Zürich* Grade point average 5.3 Bachelor thesis about "*Understanding the role of Potential-Vorticity-Streamers affecting rainfall in Northern Switzerland*" *(Grade 5.5)*
	10/2007 – 12/2007	**ERASMUS Studies in Earth Sciences/Climatology** *Leeds University (GB)*
	06/2005	**High school degree** with honors
PROFESSIONAL EXPERIENCE	Since 08/2007	**Forecaster**, *WetterInfo.ch* (own start-up)
	Since 07/2005	**Guide at St-Luc Observatory**, as well as IT administrator and telescope operator (voluntary)
	09/2011 – 05/2012	**Weather forecaster,** *Meteotest*
	09/2009 – 06/2010	**Assistant** in Mathematics, *ETH Zürich*
	10/2008 – 07/2009	**Weather forecasting and wind measurement, *Meteotest*** 4 months internship (PHP-scripting, MySQL, WebServices, weather charts analysis) followed by 6 months of work as assistant in programming
	02/2008 – 05/2008	**Assistant** in Statistics, *ETH Zürich*

FURTHER EDUCATION	02/2011 – 04/2011	**CCES Winter School:** Science Meets Practice
	09/2010	**Fortran for Scientific Computing** (one-week course at HLRS)
LANGUAGES	French German English Spanish	Native language Fluent (Bilingual) Proficient Moderate
IT	Excel, Word Linux / HPC MATLAB, Maple, R Fortran PHP, MySQL Java	Very good knowledge Very good knowledge Good knowledge Good knowledge Good knowledge Basic knowledge
OTHER ACTIVITIES	04/2012 – today	**Akademischer Sportverband Zürich**, Trainer/Guide for outdoor road cycling activities
	01/2011 – 01/2013	**careAct** (youth empowerment for sustainability), Cashier/Co-initiator
	Summer 2009/2010	**Summer camp co-counsellor**, weekly treks with teenagers
INTERESTS	Road cycling	Especially steep roads, climbing passes but less for races
	Mountainbike	Benefit from nature without the inconveniences of the road traffic
	Trekking and alpine ski	Enjoying the nature and its beauty, finding the optimal path
	Astronomy	Astrophotography with digital cameras, including picture editing
	Singing	After 7 years in a choir, taking private lessons for a band-workshop
REFERENCES	Prof. Dr. Thomas Peter ETH Zürich	thomas.peter@env.ethz.ch
	Dr. Stefan Kunz Meteotest Bern	stefan.kunz@meteotest.ch